Durham University

Durham E-Theses

Geomorphology of active fold-and-thrust belts and plateaux: unravelling tectonic and climatic controls

GROVES, KATHARINE

How to cite:

GROVES, KATHARINE (2022) *Geomorphology of active fold-and-thrust belts and plateaux: unravelling tectonic and climatic controls* , Durham theses, Durham University. Available at Durham E-Theses Online: http://etheses.dur.ac.uk/14327/

Use policy

The full-text may be used and/or reproduced, and given to third parties in any format or medium, without prior permission or charge, for personal research or study, educational, or not-for-profit purposes provided that:

- a full bibliographic reference is made to the original source
- a link is made to the metadata record in Durham E-Theses
- the full-text is not changed in any way

The full-text must not be sold in any format or medium without the formal permission of the copyright holders.

Please consult the full Durham E-Theses policy for further details.

Academic Support Office, The Palatine Centre, Durham University, Stockton Road, Durham, DH1 3LE
e-mail: e-theses.admin@durham.ac.uk Tel: +44 0191 334 6107
http://etheses.dur.ac.uk

Geomorphology of active fold-and-thrust belts and plateaux:

unravelling tectonic and climatic controls

Katharine Groves

A thesis submitted for the degree of

Doctor of Philosophy (PhD)

Department of Earth Sciences

Durham University

2021

Abstract

Orogenic belts on Earth are varied, complex and are areas of seismic and landslide hazard. Understanding them means assessing relative tectonic (active faulting, deformation style, strain rate), climatic (precipitation, glaciation) and erosional (fluvial erosion, lithology) controls. Climatic and tectonic controls are interlinked and understanding the relative importance of each is important for understanding the global landscape system.

Geomorphic indices capture the landscape response to competition between climate and tectonics and reflect the spatial distribution of erosion. They can be applied over remote and large-scale geographic areas. I use geomorphic indices (hypsometric integral (HI), elevation-relief ratio (ZR), surface roughness (SR) and normalised channel steepness (k_{sn})) to identify areas of active deformation and erosion, highlight landscape variations and I interpret the results for potential tectonic and climatic drivers. Geomorphic indices are also compared to active strain rate, calculated from published geodetic data. High HI, SR and low ZR are found to occur in landscapes overlying areas of brittle crustal deformation (seismogenic faulting) in the Qilian Shan, Himalaya, Andes and Zagros.

In the central-eastern Tibetan Plateau geomorphic indices and precipitation data are used to identify a broad ˜WSW-ENE trending transition in the landscape where changes in landscape and precipitation are grouped and in alignment. I argue that this geomorphic-climatic transition zone represents a change from incised to non-incised landscapes, the location of which is controlled by the western extent of the East Asian summer monsoon rainfall. This modern pattern is consistent with a model of early Cenozoic growth of the eastern Tibetan Plateau, superimposed by incision driven by Miocene monsoon intensification; this model is supported by published erosion rate and thermochronology data.

Precipitation and strain rate are found to be strong controls on landscapes when fold-and-thrust belts are compared but are not found to be major controls on landscape within individual fold-and-thrust belts. Climate (precipitation) is found to be more strongly correlated with geomorphic indices than tectonics (strain rate) and this result has implications for further work in understanding climate-tectonic-landscape relationships.

Contents

Abstract 1
Declaration 5
Acknowledgements 6
Chapter 1: Introduction 7
1.1 Fold-and-thrust belts 7
1.2 Tectonics and Climate 9
1.3 Methods 11
1.4 Aims and Importance 13
1.5 Outline 14
Chapter 2: Geomorphic expressions of collisional tectonics in the Qilian Shan, north eastern Tibetan Plateau 17
2.1 Introduction 17
2.1.1 Introduction 17
2.1.2 Background 20
2.1.3 Tectonic geomorphology in the Qilian Shan 23
2.2 Methods 25
2.2.1 Hypsometric Integral (HI) 25
2.2.2 Normalised Channel steepness (k_{sn}) 31
2.2.3 ZR (Elevation-Relief Ratio 33
2.2.4 Surface Roughness: Standard Deviation of Slope 33
2.2.5 Swath Profiles 35
2.3 Results 35
2.3.1 Hypsometric Integral 35
2.3.2 Normalised Channel Steepness 38
2.3.3 ZR (Elevation Relief Ratio) 38
2.3.4 Surface Roughness 38
2.3.5 Swath Profiles 41
2.4 Discussion 41
2.4.1 Morphology of the Qilian Shan 41
2.4.2 Precipitation, Lithology and Geomorphic Indices 45
2.4.3 Underlying Structure and Geomorphic Indices 50
2.5 Conclusions 54
Chapter 3: Monsoon-driven Incision and Exhumation of the Eastern Tibetan Plateau 57
3.1 Introduction 57

3.2 Methods 62
3.2.1 Hypsometric Integral 62
3.2.2 Surface Roughness 63
3.2.3 Elevation-Relief Ratio 63
3.2.4 Swath Profiles 64
3.2.5 Thermochronology and Erosion Rate Data 70
3.3 Results 73
3.3.1 Results of Geomorphic Analysis 73
3.3.2 Thermochronology 75
3.3.3 Erosion Rate 76
3.4 Discussion 80
3.5 Conclusions 85
Chapter 4: Geomorphic indices compared to underlying structure and strain rate in fold-and-thrust belts 87
4.1 Introduction 87
4.2 Methods 89
4.2.1 Geomorphic Indices 89
4.2.2 Strain Rate 90
4.3 Himalaya 91
4.3.1 Introduction 91
4.3.2 Results 95
4.3.3 Discussion 99
4.4 Qilian Shan 102
4.4.1 Introduction 102
4.4.2 Results 103
4.4.3 Discussion 106
4.5 Andes 106
4.5.1 Introduction 106
4.5.2 Results 110
4.5.3 Discussion 114
4.6 Zagros 115
4.6.1 Introduction 115
4.6.2 Results 119
4.6.3 Discussion 123
4.7 Discussion 124
4.7.1 Geomorphology and climatic, lithological and drainage controls 124

4.7.2 Geomorphology and strain rate 126
4.7.3 Geomorphology and underlying structure 127
4.8 Conclusion 128
Chapter 5: Does the rain or the strain shape the mountain chain? Correlations between climate, tectonics and landscape 129
5.1 Introduction 129
5.2 Methods 131
5.3 Results 132
5.4 Discussion 139
5.5 Conclusion 141
Chapter 6: Discussion, Suggestions for Further Work and Conclusions 143
6.1 Discussion 143
6.1.1 Tectonic Geomorphology 143
6.1.2 Tectonic Understanding 145
6.1.3 Climate and Tectonics 146
6.2 Conclusions 148
6.3 Suggestions for Further Work 149
Appendix 151
References 165

Declaration

I declare that this thesis, which I submit for the degree of Doctor of Philosophy at Durham University, is my own work and not substantially the same as any which has previously been submitted at this or any other university.

Where appropriate, work in this thesis which has already been published is clearly indicated.

Katharine Groves

October 2021

The copyright of this thesis rests with the author. No quotation from it should be published without the author's prior written consent and information derived from it should be acknowledged.

Acknowledgements

Firstly, I would like to thank my supervisors. A huge thanks to Mark Allen for all of his support as a supervisor. He has provided great input and enthusiasm at every stage of the project which has led to really great discussions and ideas. He always makes time in his busy schedule for me and congratulated me on every small win. Throughout the past 4 years and particularly during the Covid lockdowns he has looked out for me, made sure that I was doing okay and has always been supportive, and this all helped me to keep going. For all of this I am really grateful. Thank you to my other supervisors: Chris Saville, Martin Hurst and Stuart Jones for all of their support, discussions, input and feedback. Thanks also to Rich Walters for his help with the calculation of strain rate.

Thank you to Iapetus DTP, for funding this project and for the many training courses and conferences provided. It was always good to meet people from other subject areas and universities.

Thank you to the friends I have met along the way, with lots of fun and laughter over tea breaks and lunchtimes, weekends away, demonstrating and fieldwork: thanks to Eloïse, Emma, Lena, Jack, Bob, Madeline, Katy, Ayu, Becca, Tim, Olly, Chris, Pavlos, Miles, Laura, Izzy, Jack, Tom and everyone else. Thanks to my Mary's friends Fliss and Jenny, who were back in Durham too, for all of the fun and the chance to spend time outside of Earth Sciences. Thank you also to other friends, further afield including Beth and Eleanor.

I owe a huge amount of thanks to my Mum, Dad and Jennifer, for always being there for me and encouraging me, including supporting me in my work, inspiring my love of the Earth, providing distractions at times of worry and for having us to stay during the lockdowns. Finally, thank you to Adrian, for his never-ending love, support and belief in me.

Chapter 1: Introduction

Deformation of fold-and-thrust belts and orogenic plateaux is a complex and active area of research. The convergence of tectonic plates produces a variety of behaviours and resulting structures (e.g. Tapponnier et al., 2001). The interaction between climate and tectonic processes is also a key area of research within Earth Sciences (e.g. Whipple, 2009). Landscapes of orogenic belts are controlled by tectonics, climate and surface processes and react to changes in these controls. Tectonic geomorphology is the study of the competition between the tectonic processes building topography and the surface processes wearing them down (Burbank and Anderson, 2001). In this thesis, regions of active convergence and uplift are studied within Eurasia (Zagros and the Tibetan Plateau and its margins) and the eastern Andes in South America. By studying such zones of active deformation, it is possible to understand continental tectonics in ways that are not possible in inactive regions.

1.1 Fold-and-thrust belts

A variety of landscape features can be produced by tectonic collision, varying due to the strength and rheology of the continental lithosphere and its response to collision (Kearey et al., 2013). The landforms also evolve and change over time (Whipple, 2009). Landscapes formed by continental collision are commonly mountainous regions located in the fold-and-thrust belts. The thrusts and associated folds create crustal thickening, which produces elevation via isostasy. These elevated areas are prone to erosion so their landscapes are steeper than neighbouring areas. Drainage can be deflected around or cut through the areas of uplift. Crustal shortening is mostly accommodated in the fold-and-thrust belts, with the highest regional elevations in the areas of active thrust faulting (Keller and Pinter, 1996).

This work studies 5 orogenic belts and their plateau regions (Figure 1.1a) formed by ocean-continent subduction (Central Andes) and by continent-continent collision (Himalaya, Qilian Shan, Longmen Shan and Zagros). The crustal deformation style is different in different mountain belts, with some belts shortening on a basal detachment onto which thrust faults sole (Qilian Shan, Himalaya, Andes). At depth, deformation on the detachment changes from brittle (seismogenic) to ductile and the location of this change has been modelled by shortening models that use GPS data (e.g. McFarland et al., 2017; Stevens and Avouac, 2005). In the Zagros there is no evidence of a detachment, instead there is discrete thrust faulting, which also has a seismogenic limit identified (Nissen et al., 2011), i.e there are very few major thrust earthquakes above the regional 1250 m

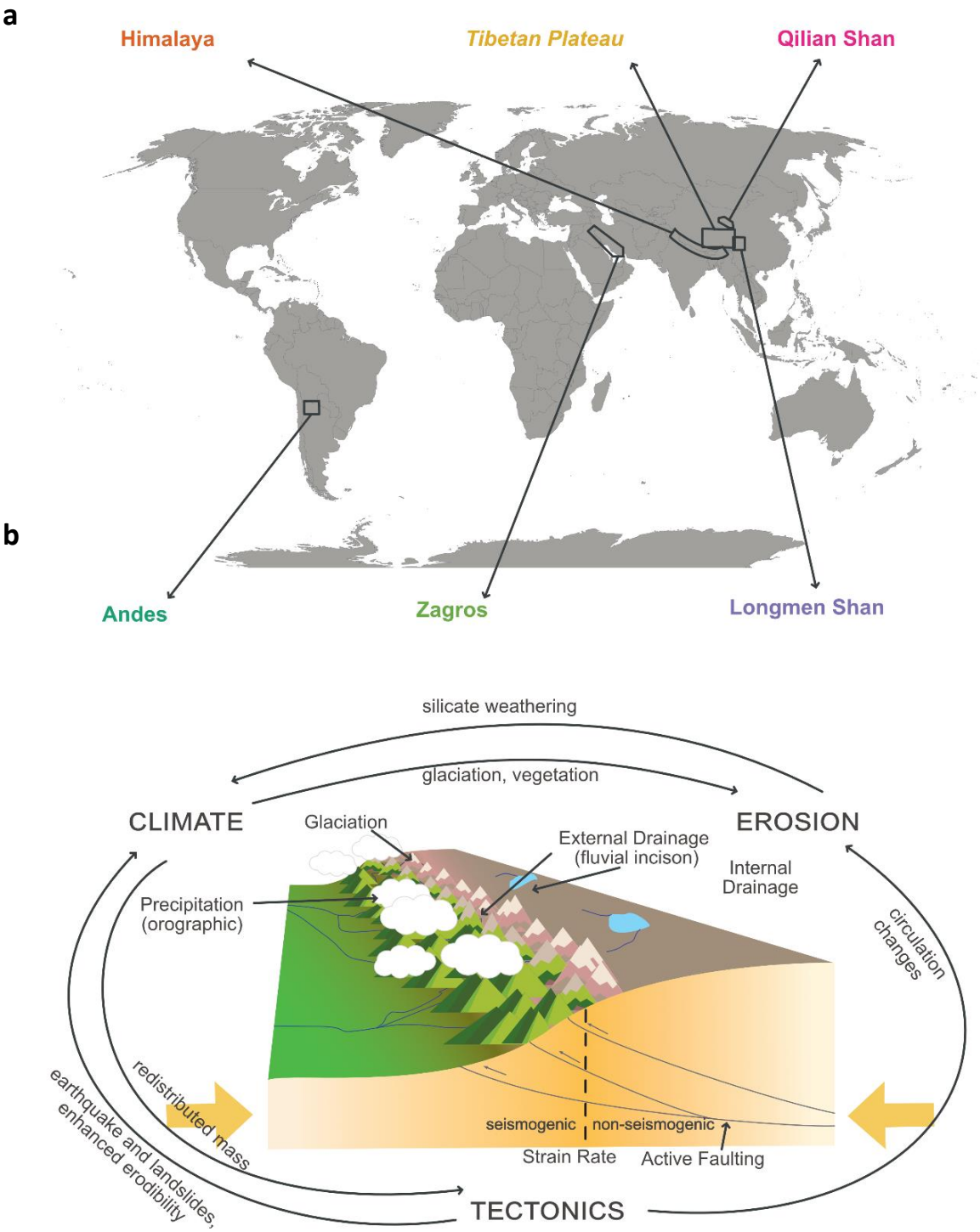

Figure 1: a) Map showing the locations of fold-and-thrust belts and the Tibetan Plateau which are analysed in this thesis. b) Stylised mountain belt showing the factors controlling mountain belt morphology studied (strain rate, active faulting, drainage, precipitation and glaciation) and the ways in which climate, tectonics and erosion are inter-related.

elevation contour. Each study area is actively shortening and erosion is largely by landsliding and fluvial incision, with erosion mainly from externally drained rivers (Korup and Weidinger, 2011). Each area experiences orographic precipitation and precipitation also varies along the mountain belts; these climatic variations are described and discussed within the main chapters.

Plateaux form when tectonic-driven crustal thickening and surface uplift occur with relatively low erosion and incision. Further thickening is resisted as the thickened crust has relatively high gravitational potential energy (England and Houseman, 1998). Internal drainage aids plateau formation as erosion within the basins also leads to deposition within the basin, resulting in overall relief reduction in a process known as bathtub fill (Liu-Zeng et al., 2008). The formation of plateaux is debated, (e.g. England and Houseman, 1989; Tapponnier et al., 2001; Royden et al., 2008; C. Wang et al., 2014; Y. Li et al., 2015). For example, suggested Tibetan Plateau formation mechanisms are early crustal thickening at the time of collision (Tapponnier et al., 2001) followed by relief reduction (Liu-Zeng et al., 2008) or a later phase of lower crustal channel flow (Clark and Royden, 2000).

1.2 Tectonics and Climate

Tectonics, climate and landscape are interlinked by a variety of factors (Burbank and Anderson, 2001; Figure 1.1b). Erosion affects climate as increased silicate weathering leads to CO_2 drawdown and therefore cooling. Burial of organic material is also important (Hilley and Porder, 2008; Raymo and Ruddiman, 1992). Erosion affects tectonics by redistributing mass, which changes gravitational stress and therefore changes the location of tectonic deformation (Whipple, 2009). Tectonics affect climate as surface uplift can change both global and local climate patterns. For example, Cenozoic cooling has been attributed to uplift of the Tibetan Plateau, as Tibetan Plateau uplift led to jet stream deflection, intense monsoon circulation, increased rainfall on slopes, greater rates of chemical weathering and lower CO_2 concentrations and therefore global cooling (Raymo and Ruddiman, 1992). Active tectonics increases erosion and therefore alters landscapes by enhancing relief, erodibility and basin size. Climate affects erosion, for example by i) controlling the amount of glaciation, with larger degrees of glaciation giving high erosion rates (Jiao et al., 2017), ii) controlling the amount of vegetation, which stabilises land surface and therefore lowers denudation rates (Acosta et al., 2015), and iii) by affecting precipitation patterns, with higher precipitation meaning higher river incision rates (Ferrier et al., 2013). Climate also affects tectonics, with warmer and wetter climates having higher exhumation rates, meaning deformation is concentrated over a narrower region which absorbs much of the shortening (Whipple, 2009). These

relations are preserved within the landscapes. The landscapes can therefore be studied to gain insights into the process-form relationships (Montgomery et al., 2001; Dietrich et al. 2003; Wobus et al., 2003).

These climate, tectonic and erosional factors are intrinsically linked. For example, increased erosion, perhaps due to increased precipitation, leads to lowering of the landscape surface, but this is partially compensated by surface uplift due to isostasy. These factors provide both positive and negative feedbacks. Feedbacks are complicated, but in general climate is kept in balance by a negative feedback of warmer climates leading to greater chemical weathering, more CO_2 drawdown and therefore cooling. An example of a positive feedback is colder temperatures leading to higher glacial weathering, CO_2 drawdown and therefore further temperature cooling. The link between these tectonic, climatic and erosion factors make it difficult to assess the relative importance of each factor in fold-and-thrust belts. It has been suggested that fold-and-thrust belt mountain height can be explained by tectonic forcing alone, expressed as the underlying shear force (Dielforder et al., 2020). Calculation of the predicted tectonically-supported elevation from shear force on megathrusts for multiple mountain belts in convergent settings is shown to match the true elevation, regardless of the climate conditions, suggesting that the climate conditions are not important (Dielforder et al., 2020). However, most studies agree that the landscape of mountain belts is a combination of tectonic, climatic and erosional factors (Whipple et al., 2009). Champagnac et al., (2012) attempted to quantify the relative effect of these factors and concluded that both tectonic (shortening rates) and climatic (precipitation and latitude) factors control topographic relief at mountain belts worldwide, with shortening alone accounting for less than 25 % of the variance of relief and mean and maximum elevations, while the tectonics and climate together account for up to 50 % of the mean and maximum elevation. These proportions show that many other factors are influencing landscape relief, and therefore further research is needed to understand the controls.

Landscapes give qualitative insights into the tectonic-climatic system of an area, but not quantitative results, such as absolute rates of surface uplift (Whittaker, 2012). Geomorphic studies are therefore frequently combined with erosion rate or thermochronology data. Thermochronology data are commonly inverted into long-term erosion rates in order to study tectonic, climatic and geomorphic correlations. Herman et al., (2013) use worldwide thermochronology to show an increase in erosion rates in the last 6 Ma as global cooling occurred, mainly in glaciated areas. They also show that the areas with the highest erosion rates (2-7 mm/yr) occur in tectonically active areas which also have high precipitation and have threshold hillslopes

dominated by landslides or are glaciated. Jiao et al., (2017) also use thermochronology derived exhumation rates and show exhumation rates in New Zealand are highest (5 mm/yr) where tectonic deformation and precipitation are high, lower (0.5 – 3 mm/yr) where crustal deformation is low but the area is glaciated and exhumation rates are lowest (> 0.5 mm/yr) where deformation is low and the area is non-glaciated. Bermúdez et al., (2013) find that long-term exhumation rates in the Venezuelan Andes correlate strongly with landscape relief but weakly with precipitation, decadal erosion rates and seismic energy, including no variation in exhumation rate between the NW and SE parts of the mountain belt despite a three-fold difference in precipitation. Reiners et al., (2003) show coupled spatial variation in precipitation and thermochronology-derived erosion rate in the Cascades. In contrast, Burbank et al., (2003) find no correlation between thermochronology-derived erosion rates and precipitation in the Himalaya, despite a five-fold variation in precipitation. Erosion rate variations are instead attributed to variations in hillslope steepness, channel width and sediment concentration.

Other studies of tectonics and climate compared to erosion rates also show varied results. Erosion rates from the past 1.5 Ma in the Himalaya show a 50-70 km wide focussed area of erosion which corresponds spatially with the location of highest precipitation (Thiede et al., 2004). This suggests a climatic control on erosion which may then be compensated by faulting and uplift. Adams et al., (2020) also show that erosion rate is proportionally related to precipitation, with the precipitation moderating relief. However, in a further study in the Himalaya, a five-fold difference in denudation rates is found despite no variation in precipitation, suggesting that landscapes adjust quickly to climate variations and that denudation is limited by sediment variability due to tectonic uplift (Godard et al., 2014). Decadal erosion rates do not correlate with relief or runoff in Taiwan (Dadson et al., 2003).

1.3 Methods

Geomorphic indices capture the landscape response to competition between tectonics and climate, reflecting the spatial distribution of erosion. Landscapes are affected by tectonics, climate, underlying lithology and surface processes and react to changes in these controls (Burbank and Anderson, 2001; Kirby and Whipple, 2012; D'Arcy and Whittaker, 2014). In this thesis I use geomorphic indices to identify areas of active deformation and erosion, highlight landscape variations and interpret the results for potential tectonic and climatic drivers. The geomorphic indices used in this work are the hypsometric integral (HI) which is the distribution of relief (high HI highlights more rugged landscapes, where elevation values within an area are skewed towards

higher elevations); normalised channel steepness (k_{sn}; high k_{sn} shows steep channels); surface roughness (SR; high SR indicates a rough landscape) and the elevation-relief ratio (ZR; low ZR highlights areas of high elevation and low relief, i.e. "plateauness"). Tectonic geomorphology techniques can be used to study landscapes on a wide range of scales, for example for a single fault scarp, basin or stretch of river, or can be used on a much broader scale, as in the case of this work, where geomorphic indices are calculated for entire mountain belts and plateaux. Availability of high resolution, free global datasets of topography and climate (e.g. Shuttle Radar Topography Mission (SRTM) and Global Precipitation Measurement (GPM)) mean that large geographical areas can be analysed, including remote areas which would be costly or difficult to access.

Geomorphic indices are powerful tools for analysing patterns in the landscape of fold-and-thrust belts and interpreting them with regard to tectonics. For example, studies identify patterns such as faults acting as major boundaries between high and low HI regions (Gao et al., 2016), high HI and normalised channel steepness in the hanging walls of thrust faults (Gao et al., 2016; Nennewitz et al., 2018), active faults using channel steepness (Boulton and Whittaker, 2009), high HI and k_{sn} at the limit of seismogenic thrusting (Obaid and Allen, 2019), identification of a shear zone by identifying high concavity streams (Wobus et al., 2006), channel steepness identifying variations in rock uplift rates across a fault-bend fold (Kirby and Whipple, 2001), identification of incised valleys (Tejero et al., 2006), changes in tectonic uplift rate shown by changes in river long profiles (Whittaker et al., 2008) and correlation of high long-term erosion rates to high channel steepness (Wobus et al., 2006). The geomorphic indices may also identify features such as underlying changes in deformation, as well as variations between fault parallel and fault transverse valleys.

Most geomorphic analysis focusses on rivers, particularly using measures of channel steepness and identification of knickpoints (e.g. Wobus 2006; Mudd et al., 2014; Whittaker and Boulton., 2012). Geomorphic methods can also use a whole-landscape approach, studying either the entire area or hillslope areas (e.g. Liu-Zeng et al., 2008; Gao et al., 2016; H. Zhang et al., 2017; Obaid and Allen, 2019). In this thesis whole-landscape metrics are mostly used, as profile analysis has been carried out extensively in the study areas (e.g. Hodges et al., (2004); Cannon and Murphy (2014); Sinclair et al., (2017); in the Himalaya; Obaid (2018); Obaid and Allen (2019) in the Zagros; Hoke et al., (2007); Bookhagen and Strecker (2012) in the Andes; H. Zhang et al., (2017) in the Qilian Shan; Ouimet et al., (2010); Kirby and Ouimet (2011) in the Eastern Tibetan Plateau) and hillslopes are controlled by river erosion, therefore methods give complementary results (Hurst et al., 2013).

Each chapter of this thesis uses geomorphic indices calculated for the individual mountain belts, the Tibetan Plateau and makes comparisons within and between these different areas. In order to

interpret the results, the geomorphic indices are compared to a range of other datasets. For each mountain belt the geomorphic indices are compared to the underlying tectonic structures and active faulting from published studies. The indices are also compared to the mean annual precipitation, the amount of glaciation within the areas and the strain rate, which is calculated from a global GPS database. A compilation of published erosion rates and thermochronology ages is used to compare the geomorphic indices to the short-term and long-term exhumation patterns in the central-eastern Tibetan Plateau. More detail on these datasets is given in the individual chapters. These comparisons compare the present-day landscape to the present-day climate and strain rate and the longer-term exhumation patterns, but landscape response times mean that landscapes represent different timescales (e.g. 0.9-2.5 Myr for the Himalaya; Huntington et al., 2006) and not simply current tectonic and climate conditions. However, the fold-and-thrust belts included in the study have not undergone significant tectonic reorganisation in this timescale, and changes in climate are plausibly changes in absolute climate values, but not spatial changes along or across the fold-and-thrust belt.

1.4 Aims and Importance

This work aims to: identify changes in geomorphic indices and relate them to changes in crustal deformation style identified from published studies; identify climate (precipitation) controls on landscape in mountain belts and plateaux; compare landscapes, climatic and tectonic controls within and between mountain belts; use geomorphic indices to assess models of Tibetan Plateau uplift mechanisms.

These analyses are regional studies, over entire mountain belts. Many tectonic geomorphology studies are more localised, focussing in detail on individual rivers, basins, faults and river terraces for example. The study is quasi-global: although only 5 fold-and-thrust belts and the Tibetan Plateau are studied, these are from the three largest convergent settings on the Earth at present, formed by the India-Eurasia collision, Arabia-Eurasia collision and Andean subduction. Comparisons between these regions are rare, and most published studies focus on localised areas within single fold-and-thrust belts. The landscape is compared to active crustal strain rate, calculated from decadal GPS data. Exhumation data are often used as a proxy for tectonic uplift (e.g. Herman et al., 2013; Jiao et al., 2017) which means comparisons are for different timescales in these previous studies, with the exhumation data not necessarily corresponding to the modern landscapes. An advantage of the approach used in this thesis is that enough geodetic data are available to permit the calculation of active strain rates within the same areas that are analysed for geomorphic

metrics. A potential caveat for this approach is the possibility that landscapes result from longer-term controls than are represented by the active strain rate, due to landscape response times. These issues are discussed at appropriate points in the thesis.

1.5 Outline

Chapters 2-5 are written in the style of papers, with each chapter including introduction, methods, results, discussion and conclusions. There is no separate methods chapter. Instead, new methods are introduced in each chapter. Chapter 2 introduces the geomorphic methods (HI, SR, ZR, k_{sn}) and the calculation of strain rate is introduced in Chapter 4. The study locations are also introduced in the first relevant chapter: the Qilian Shan in Chapter 2, the Tibetan Plateau in Chapter 3, the Himalaya, Longmen Shan, and Central Andes in Chapter 4 and the Longmen Shan in Chapters 3 and 5.

Chapter 2 introduces the geomorphic methods used throughout the thesis, using the Qilian Shan in the north east Tibetan Plateau as an example. Changes in geomorphic indices identify active faults and the largest change in geomorphic indices occur across the Haiyuan Fault which is the locked-creeping transition on the underlying detachment, as identified in published work (Allen et al., 2017). This is used to demonstrate the sensitivity of geomorphic indices to active tectonics. The geomorphic indices are also compared to erosion rates, lithology and precipitation. This chapter is published (Groves et al., 2020) with minor changes made from the published format. I carried out the data collection, analysis and wrote the paper. Co-author contributions are in-line with normal PhD supervision duties These changes are to include the supplementary figures within the main text and a more detailed comparison of methods.

Chapter 3 uses a series of swath profiles drawn across the central and eastern Tibetan Plateau to identify a continuous landscape change in geomorphic indices, and annual precipitation. This landscape change is compared to modern day precipitation patterns and a compilation of published erosion rates and thermochronology ages, thereby allowing a comparison of short and long timescales. The landscape change is attributed to erosion by the East Asian Summer Monsoon, since the time of monsoon intensification in the early Miocene. This chapter also highlights the climatic control on landscapes in an area where tectonics has previously built up a thick, elevated crust, although active thrusting is now confined to the easternmost margin of the eastern plateau, in the Longmen Shan.

Chapter 4 compares variation in geomorphic indices to calculated strain rate, precipitation patterns, internal-external drainage divides, thrust faults and published crustal structure and deformation. Four fold-and-thrust-belts are studied: Qilian Shan, Himalaya, Zagros and Central Andes. These fold-and-thrust belts each have different deformation styles, tectonic settings, climate and scales. Within each area there are changes in geomorphic indices which correspond spatially with changes in strain rate and structure.

Chapter 5 compares climate (precipitation and glaciation), tectonic (strain rate) and geomorphic (HI and SR) data from quadrats spaced along the mountain belts (Qilian Shan, Himalaya, Longmen Shan, Zagros and Central Andes). Data from the central Tibetan Plateau (Chapter 3) are also considered. This chapter uses the datasets from Chapter 4, but instead of considering variations within each range it is focussed on comparing the different ranges. Correlations are used to identify the relative importance of these climatic and tectonic controls on landscape.

Chapter 6 contains a discussion and conclusion of the results presented in this thesis, and suggestions of ways in which this work could be extended.

Chapter 2: Geomorphic expressions of collisional tectonics in the Qilian Shan, north eastern Tibetan Plateau

2.1 Introduction

2.1.1 Introduction

The India-Eurasia and Arabia-Eurasia collisions are by far the largest active continental collisions on Earth. Processes and structures vary among the fold-and-thrust belts produced by these collisions (Tapponnier et al., 2001; Poblet and Lisle, 2011; Royden et al., 2008; Lacombe and Bellahsen, 2016; Kapp and DeCelles, 2019). By studying such zones of active deformation, it is possible to understand continental tectonics in ways that are not possible in inactive regions. One method that can be used to gain insights into underlying tectonic structure is tectonic geomorphology: the analysis of landscapes to help understand the underlying tectonics. Landscapes are affected by tectonics, climate, underlying lithology and surface processes and react to changes in these controls (Burbank and Anderson, 2001; Kirby and Whipple, 2012).

The geomorphic methods used in this study are the hypsometric integral (HI) which is the distribution of relief, normalised channel steepness (k_{sn}), surface roughness (SR) and the elevation-relief ratio (ZR) which highlights areas of high elevation and low relief. Geomorphic indices are powerful tools for analysing patterns in the landscape of fold-and-thrust belts and interpreting them with regard to tectonics.

The Qilian Shan fold-and-thrust belt is used here as a case study for the use of tectonic geomorphology to study continental-scale processes. The Qilian Shan is at the northern margin of the Tibetan Plateau and is considered to be the youngest area to have deformed within the plateau (Figure 2.1), currently absorbing ~20% of the active convergence and is therefore able to tell us about the effects of upward and outward growth of the orogenic plateau and large scale tectonic processes (Tapponnier et al. 1990; 2001; Meyer et al., 1998; Yin et al., 2008; Yuan et al., 2013; Zuza et al., 2018). It is therefore a good location for studying continental tectonics and the development of intracontinental fold-and-thrust belts in particular. The structure of the Qilian Shan is broadly agreed to be divergent thrusts and a subdued interior, overlying a south-dipping detachment (Figure 2.1; Meyer et al., 1998; Allen et al., 2017; Cheng et al., 2019). Compressional deformation across the range is oblique (transpressional) (Figure 2.2), expressed by strain partitioning on the thrust faults and the strike-slip Haiyuan Fault (Gaudemer et al., 1995; Zheng et al., 2013). Therefore

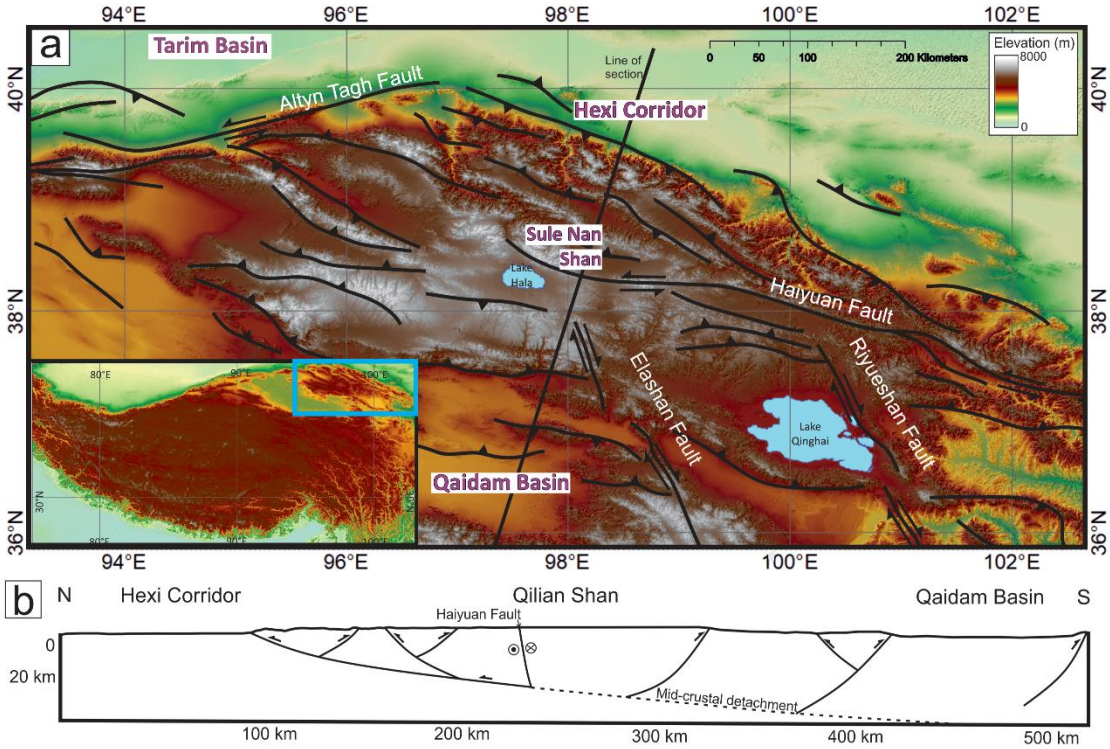

Figure 2.1: a) The regional structure and topography (SRTM) of the Qilian Shan and b) cross section of Qilian Shan. Thrust faults mainly strike WNW-ESE (Allen et al., 2017). Major strike-slip faults are labelled. Inset shows the location of the Qilian Shan, at the north east of the Tibetan Plateau.

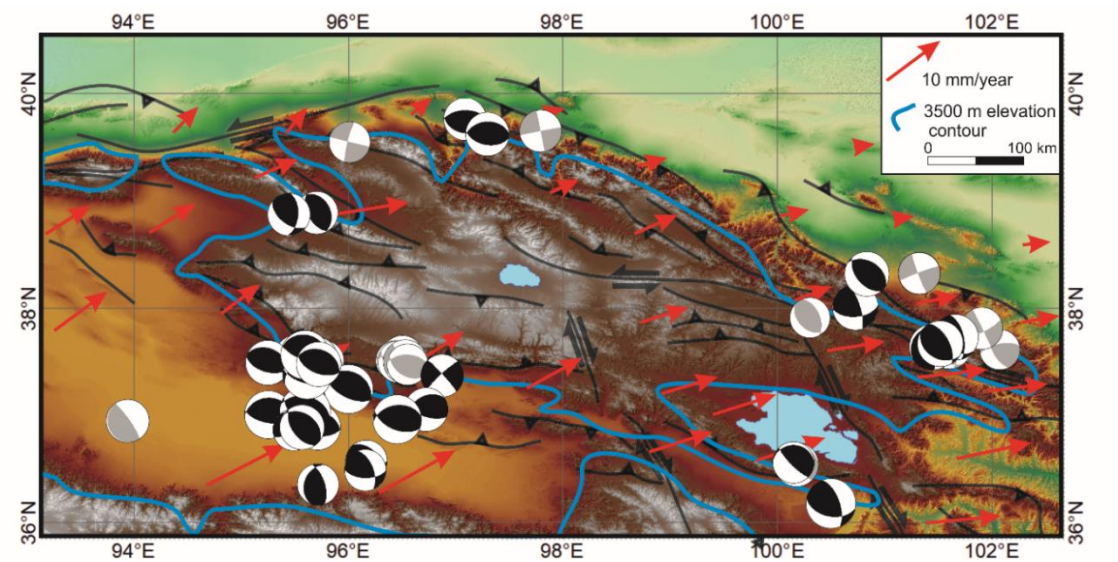

Figure 2.2: Seismicity and GPS velocities of the Qilian Shan. The black focal mechanisms are from body wave modelling (Molnar and Lyon-caen, 1989; Elliott et al., 2010) or the Global CMT catalogue where *M* >5.3 and there is >70% double couple (data to 2016). The grey focal mechanisms are from the Global CMT catalogue where *M* <5.3 and/or there is <70% double couple. Epicentres are clustered at and below the regional 3500 m contour line. GPS velocities are shown with respect to stable Eurasia, taken from Liang et al. (2013) and are oblique to the general WNW-ESE trend of the thrust faults.

the Qilian Shan is also important as a study area for understanding strain partitioning, its expression in the geomorphology and how landscapes can be interpreted to understand the underlying structure.

I use tectonic geomorphology to study the landscape of the Qilian Shan and to assess the evidence for this structure. Identification of the tectonic controls using these methods could point the way for future studies to assess how structures and processes differ in other fold-and-thrust belts (Chapter 4). Another driver for this study is to assess the role of precipitation on landscape evolution. The Qilian Shan has an along strike variation in precipitation of ~600 mm/yr in the east due to influence of the East Asian monsoon, to <100 mm/yr in the west (Hu et al., 2010; Geng et al., 2017; Figure 2.3), whereas most mountain belts show more variation across strike, in the form of orographic precipitation. As precipitation varies in a different direction to tectonics, the Qilian Shan provides a good area to analyse the impact of precipitation relative to tectonics on landscape morphology. Catchment averaged precipitation in Hawaii was found to correlate with bedrock river incision rates by Ferrier et al. (2013), who postulated that this relationship would apply on a global scale. If a similar correlation applies to the Qilian Shan, it predicts that the range will exhibit higher SR and HI in the eastern region due to higher precipitation and therefore incision, with a gradual decrease to lower values SR and HI towards the west due to lower precipitation and therefore lower incision.

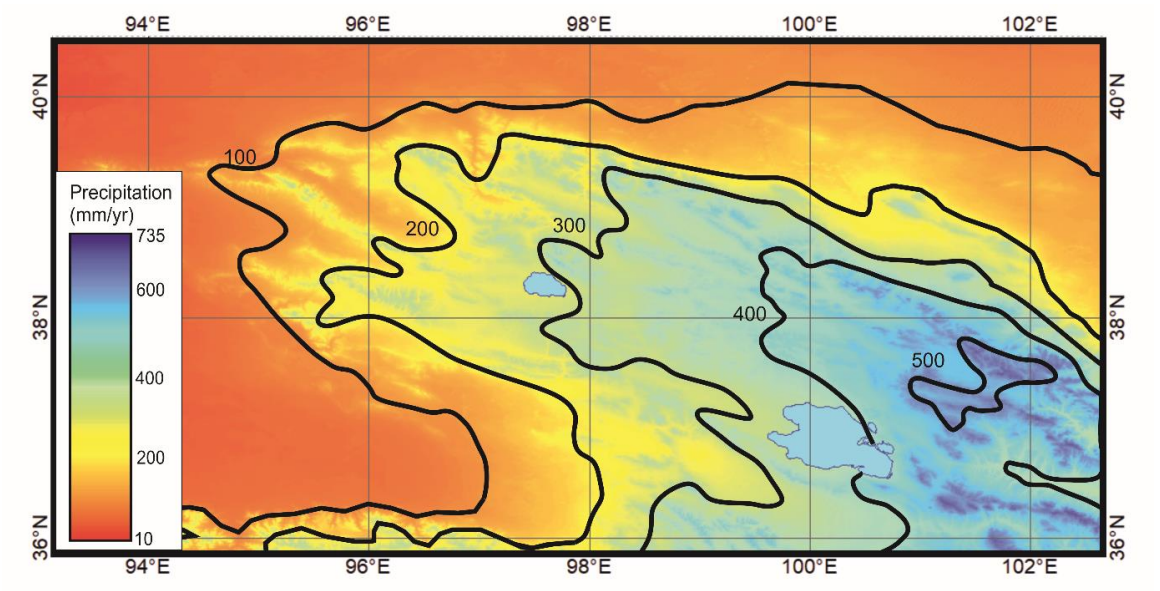

Figure 2.3: Mean annual precipitation (mm) for the study area from the years 1970-2000. Data from WorldClim, version 2 (Fick and Hijmans, 2017) shown overlain by smoothed contours. Precipitation generally decreases East (> 500 mm) to West (< 100 mm), across the Qilian Shan.

Studies which find rainfall to be a good predictor of erosion rates are based in regions of low tectonically-driven uplift, whereas studies in tectonically active regions suggest relief to be the best predictor of erosion rates (Henck et al., 2011). If the latter is the case, there would be no relationship between the geomorphic index patterns and precipitation, but high HI and SR would be concentrated in areas of active rock uplift. Wang et al., (2019) found no correlation between k_{sn} and precipitation in the Qilian Shan at the scale of the main drainage basins. There is very little variation (< 10°) in mean annual temperature in the Qilian Shan, with temperatures decreasing with increasing elevation (Pan et al., 2010) but with no change east-west or north-south.

2.1.2 Background

The Tibetan Plateau and its margins, including the Himalaya, accommodate over 90% of the active India-Eurasia plate convergence (Wang et al., 2001). The timing, rate and pattern of uplift of the Plateau are subjects of intense research (Wang et al., 2014a). Models for growth include continuous lateral growth (England and Houseman, 1989), stepwise growth (Tapponnier et al., 2001) and outward growth from central Tibet (Wang et al., 2014a). Models of lower crustal channel flow (Royden et al., 2008) predict crustal thickening and surface uplift without crustal shortening, focussed on eastern and south-eastern Tibet. Many studies have been carried out across the region, including the Qilian Shan, with the aim of constraining the timing of uplift, using approaches such as low temperature thermochronology, stable isotope-based palaeoaltimetry, lithology and/or provenance shifts and magmatic records (Wang et al., 2014a and references within). These methods suggest that the timing of the onset of uplift was at or shortly after initial collision at ~50-60 Ma (e.g. Yin et al., 2002; Clark et al., 2010; Qi et al., 2016; Bush et al., 2016) and continued into the Pliocene-Quaternary (e.g. Tapponnier et al., 2001).

The timing of Qilian Shan uplift is also linked to the debated pattern of Tibetan surface uplift after collision: progressive plateau growth, stepwise growth, or rapid regional uplift long after initial collision (summarised in Law and Allen, 2020). There is some thermochronology and other evidence for exhumation and deformation in the early Cenozoic in northern Tibet i.e. not long after the initial India-Eurasia collision and there is also increasing evidence for renewed exhumation in the Early Miocene or later (e.g. Zhu et al., 2006; Zheng et al., 2010; Lease et al., 2011; Zhang et al., 2012; Bush et al., 2016; Duvall et al., 2013; Zuza et al., 2016, Qi et al., 2016; Liu et al., 2017; Zheng et al., 2017; Pang et al., 2019). It is not clear whether these data collectively record deformation progressing northwards across the Qilian Shan, a more regional and synchronous deformation across the range, or deformation and exhumation stepping outwards from the interior of the range to both the north and south, in a pattern that might be predicted if the range operated as a large-

scale flower structure. No clear spatial pattern is clear in the recent summary of thermochronology data by Tong et al. (2019), although the distinction seems clear between clusters of early (largely Eocene) and late Cenozoic (largely Miocene) exhumation ages. Yuan et al. (2013) noted that, whatever the exact pattern of deformation and exhumation across the Qilian Shan, there are sufficient data to suggest growth initiated prior to the Pliocene.

The Qilian Shan consists of a series of WNW-ESE trending ridges, each ~700 km long and ~50 km wide, with an overall area of 250,000 km². The Qilian Shan is bounded by the Qaidam Basin to the south, the Hexi Corridor to the north and the Tarim Basin to the northwest (Figure 2.1). Peaks are over 5000 m and average elevation is 3500-4000 m. This compares to elevations of ~2750 m in the Qaidam Basin and 900-1200 m in the Tarim Basin. Crustal thickness in the area is ~60-70 km, compared to ~55 km in the interior of the Qaidam Basin and 45-50 km in the Tarim Basin and Hexi Corridor areas, derived from the crustal P- and S-wave structure (Wang et al. 2013). The area is seismically active (Figure 2.2), with destructive historical earthquakes and earthquake-induced landsliding (Tang et al., 2012; Xu et al., 2010; Gaudemer et al., 1995).

Lower Palaeozoic and Proterozoic basement formed during accretion of several arcs and microcontinents to each other and the southwest margin of the North China Craton (Song et al., 2013; Zuza et al., 2018). These rocks were deformed and metamorphosed before the deposition of an Upper Palaeozoic cover sequence, which was then itself overlain by Mesozoic non-marine clastic rocks. Cenozoic alluvial, fluvial and lacustrine sediments have been deposited in intermontane basins (Horton et al., 2004).

The series of linear, Cenozoic thrust-fault-bounded ridges that collectively form the Qilian Shan accommodate most of the uplift in the area and trend WNW-ESE (Figure 2.1; Tapponnier et al., 1990; Van der Woerd et al., 2001). Thrusts emerge at the base of the ranges, typically dipping >30°, with the marginal thrusts at the northern range front dipping south and thrusts at the southern margin dipping north (H. Zhang et al., 2017). Total GPS-derived convergence rates across the range are ~7-8 mm/yr (Wang et al., 2001). The frontal thrust in the region of the Shule River (Figure 2.4) accommodates 15 - 20 % of Qilian Shan shortening, as calculated from river terrace uplift (Yang et al., 2018). Oblique convergence across the range is partitioned into dip-slip (~6.7 mm/yr) and strike-slip (4.2 mm/yr) components (Allen et al., 2017).

Left-lateral strike-slip faulting occurs in the area, mainly on the Haiyuan Fault. The Haiyuan Fault slips at ~5 mm/yr in its centre, measured from GPS data (Allen et al. 2017) and 2.7-3 mm/yr at the left-stepping restraining bend to the north of Hala Lake (Figure 2.1), from ^{10}Be-^{26}Al cosmogenic

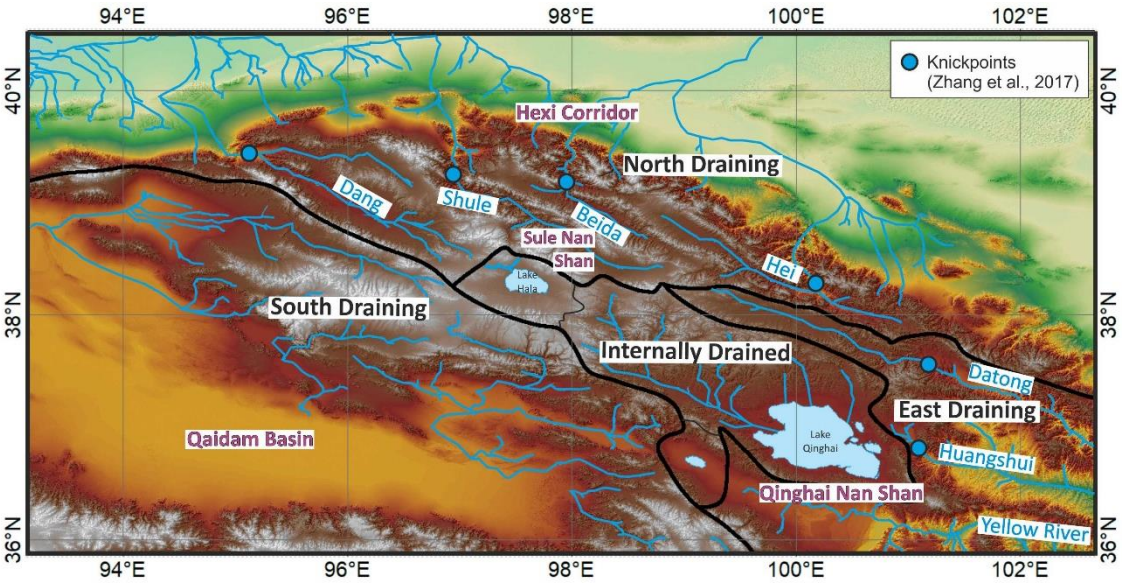

Figure 2.4: Major drainage divides and rivers of the Qilian Shan, extracted from SRTM data using the D8 algorithm. The major rivers, used in Figure 2.10 are labelled. These rivers are broadly divided into North Draining, East Draining, South Draining and Internally Drained rivers; divides are shown in black. Locations of knickpoints from H. Zhang et al., 2017 are shown.

nuclide dating (Li et al., 2017). Strike-slip faulting contributes to surface uplift via restraining bends and thrusting at the western tip of the Haiyuan Fault at the Sule Nan Shan (H. Zhang et al. 2017; Figure 2.1). The Altyn Tagh Fault marks the northwestern boundary of the Tibetan Plateau, with a length of over 1200 km and a slip rate that varies along its length, but is thought to be typically ˜9 mm/yr decreasing to ˜2 mm/yr at its east end (Figure 2.1; Shen et al., 2001; Yin et al., 2002; Zheng et al., 2013). Dextral faulting occurs, trending NNW-SSE, in the south east region of the Qilian Shan, near Qinghai Lake, with slip rates of ~1 mm/yr on the Elashan and Riyueshan faults (Yuan et al. 2011).

Large ($M_W \geq 7$) earthquakes occur in the north of the Qilian Shan, on strike-slip and thrust faults, but are scarce in the southern Qilian Shan (Xu et al., 2010). Thrust earthquakes occur at the lower elevation margins of the Qilian Shan, but rarely in the interior; thrust earthquake epicentres $M_W \geq$ ~5.3 are not seen above the regional 3500 m elevation contour (Allen et al., 2017; Figure 2.2). This indicates that active seismogenic thrusting is not occurring in the high elevation, central area, with non-seismic shortening building elevations above 3500 m. Strain is highest in the north of the Qilian Shan (Zuza et al., 2016).

The structure of the Qilian Shan contributes to our knowledge of the Tibetan Plateau formation. Geodetic data are consistent with the Qilian Shan deforming via a low angle (17°) detachment thrust, which dips to the south under the range (Allen et al., 2017). This thrust is modelled to have

oblique slip below seismogenic depths (~26 ± 8 km) and slip is partitioned into separate strike-slip (Haiyuan Fault) and thrust faults in the shallow crust (Figure 2.1). Decreasing rock uplift rates from the Qilian Shan frontal thrusts to the south west are interpreted as a decrease in the angle of the frontal thrust as it flattens with depth and soles onto the detachment (Hetzel, 2013). Yin et al., (2008) emphasised the importance of a north-dipping detachment thrust under the Qilian Shan, which is emergent on the southern side of the range. Another suggested deformation mechanism is distributed shortening on crustal thrust faults across the Qilian Shan (England and Houseman, 1986). The Haiyuan Fault has been suggested to act as a root to a flower structure (Pang et al., 2019). Estimates of the magnitude of Cenozoic shortening across the Qilian Shan-Nan Shan thrust belt, compared to the strain distribution, indicate that the magnitude of shortening is produced by a combination of distributed shortening and minor southward underthrusting of Asian lithosphere (Zuza et al., 2016). Each shortening mechanism would show higher erosion in the hanging walls of thrust faults and therefore higher HI, k_{sn} and SR. However, these different structures and shortening mechanisms would produce different spatial patterns of geomorphic indices in the Qilian Shan, therefore I study the entire range to ascertain which mechanism most closely matches my results. The underlying detachment thrust would lead to a relatively high relief landscape above the locked portion of the fault, because this part of the fault produces major earthquakes. These earthquakes in turn produce landslides and episodic rock uplift. In comparison, above the creeping portion of the thrust, uplift rates would be more constant, creating a lower relief landscape with high ZR values. Distributed shortening across a flower structure, or with southward underthrusting would produce greater HI, SR and k_{sn} in the north of the Qilian Shan, due to higher strain in this region.

2.1.3 Tectonic geomorphology in the Qilian Shan

High topographic relief of the Qilian Shan coincides spatially with the location of faults (Figure 2.1) and can be termed 'structural relief' (Liu-Zeng et al., 2008). Rivers draining the Qilian Shan, mainly flow parallel to thrust faults, along topographic lows between the mountain ridges (Figure 2.4). Some rivers cross thrusts, especially at the southern and northern range fronts. The northern range front is steep with broad, northward draining, gently sloping alluvial fans with active channel braiding and deeply incised channels (Tapponnier et al. 1990). In the eastern Qilian Shan, rivers drain into the Yellow River (Huang He) which flows to its outlet in Bohai Bay (Wang et al. 1986). Rivers that drain the south of the Qilian Shan enter the internally-drained Qaidam Basin. The central region of the Qilian Shan is internally drained. Zhang et al., (2014) used cosmogenic nuclide dating and analysis of basin fill deposits to show that Qinghai Lake was cut off from the Yellow River external drainage between 0.5 and 1.2 Ma by the isostatic response to Yellow River excavation.

Landslide scarps are common in the Qilian Shan, from modern and ancient tectonically-induced landslides (Tang et al., 2012; Xu et al., 2010).

Under pre-steady state, rock uplift outstrips erosion and in steady-state conditions rates of erosion or extension balance rock uplift over a long period (Burbank and Anderson, 2001). Pan et al. (2010) identify a linear relationship between local relief and catchment-scale decadal erosion rates, as estimated from sediment load records in the Qilian Shan. The northern Qilian Shan has been suggested to have reached topographic steady state (Hetzel, 2013) as erosion rates are similar to millennial throw rates (Hetzel et al., 2004) and long-term vertical slip rates of 0.4 – 0.6 mm/yr in the frontal thrusts of the Qilian Shan (Zheng et al., 2010), although more recent millennial vertical slip-rates of 0.9 ±1 mm/yr in the northern Qilian Shan (Yang et al., 2018) suggest pre-steady state conditions. 20 km to the south west of the frontal thrust lower erosion rates (0.02 -0.25 mm/yr) have occurred for ˜10 Myr, suggesting much lower rock uplift rates have occurred in this area since the initiation of thrust faulting (Zheng et al., 2010). Su et al. (2019) use hypsometric curves and slope area plots and suggest that the topographic evolution of the eastern Qilian Shan is in pre-steady state, where denudation will soon match with rock uplift from mountain building. In areas where erosion outpaces soil production rates, landscapes respond to erosion by bedrock landsliding (Montgomery, 2001). OSL and AMS ^{14}C Dating of strath terraces of the Xie River, eastern Qilian Shan shows the proximal fault of the North Frontal Thrust system to have remained active as deformation propagated basinwards (Xiong et al., 2017).

Previous work on tectonic geomorphology of the Qilian Shan has provided insights into plateau formation processes and rock uplift variations and fault displacements. For example, high resolution topography has been used to calculate displacements on thrust and strike slip faults (Bi et al., 2018; the Heli Shan thrust fault, northern Qilian Shan). Wang et al., (2019) assessed the channel steepness and concavity variations across the major rivers of the northern and western Qilian Shan. Variations were attributed to rock uplift rather than precipitation or underlying lithology and they concluded that the channel steepness is greatest at the frontal thrusts of the Qilian Shan and decreases to the South and suggested that this is due to distributed crustal shortening in this area, concentrated on the thrust fault bounded ranges and underthrusting of Asian lithosphere (Wang et al., 2019), consistent with Zuza et al., (2016). Decadal erosion rates have been correlated with local topographic gradient, rock fracture density and rainstorm intensity for 11 drainage basins in the northern Qilian Shan (Pan et al., 2010; Wang et al., 2014b). Rock uplift along the northern margin of the Qilian Shan is shown to be greater in the middle and western portions than the east, as calculated from channel steepness (Hu et al., 2010; Q. Li et al., 2019) and

catchment wide erosion rates (Palumbo et al., 2011). All of these studies were carried out in the northern Qilian Shan and therefore provide no means of testing for spatial variations in geomorphology across the Haiyuan Fault, as are predicted by the model of change from locked to creeping deformation on the underlying detachment (Allen et al., 2017). H. Zhang et al., (2017) used river longitudinal profiles and geomorphic indices of topographic slope, local relief and channel steepness in the northern Qilian Shan to identify a plateau-like structure, with suggested relict erosional surfaces to the south of the Haiyuan Fault and intermontane aggradation forming the landscape to the north of the Haiyuan Fault. They calculated one knickpoint for each of the 6 major rivers of the Qilian Shan (Figure 2.4), using the SRTM dataset and conventional methods. The knickpoints are close to active faults and confirm the Qilian Shan to be in a transient state, but do not show a systematic pattern with elevation. The results were not considered in relation to an underlying detachment. To build on these previous studies, I use a broader range of geomorphic indices, each providing complementary results and apply the techniques to the whole of the Qilian Shan, rather than localised areas.

I use digital topography from the 3 arc second (~90 m pixel size), Shuttle Radar Topography Mission (SRTM) (http://www2.jpl.nasa.gov/srtm/) to analyse Qilian Shan geomorphology at the regional scale. Sensitivity testing (Figure 2.5) shows similar results for use of 30 m or 90 m data, therefore 90 m was used throughout for faster processing speed. The geomorphic indices of hypsometric integral (HI), elevation-relief ratio (ZR), surface roughness (SR) and normalised channel steepness (k_{sn}) are analysed.

This work integrates geomorphic indices with recent structural and geodetic results in the Qilian Shan (Zheng et al., 2013; Zuza et al., 2016; Allen et al., 2017). The work aims to help to constrain the underlying structure of the Qilian Shan, which gives insights into the wider Tibetan Plateau formation, whilst also considering the relative roles of tectonics, precipitation and surface processes (Liu-Zeng et al., 2008) on the Qilian Shan formation. More broadly, the work shows the potential of these geomorphic indices to constrain fault locations and deep structure in other fold-and-thrust belts (Gao et al., 2016; Nennewitz et al., 2018).

2.2 Methods

2.2.1 Hypsometric Integral (HI)

Hypsometry describes the distribution of elevation within an area (Pike and Wilson, 1971). The hypsometric integral (HI) is a method of differentiating between landscapes at different stages of

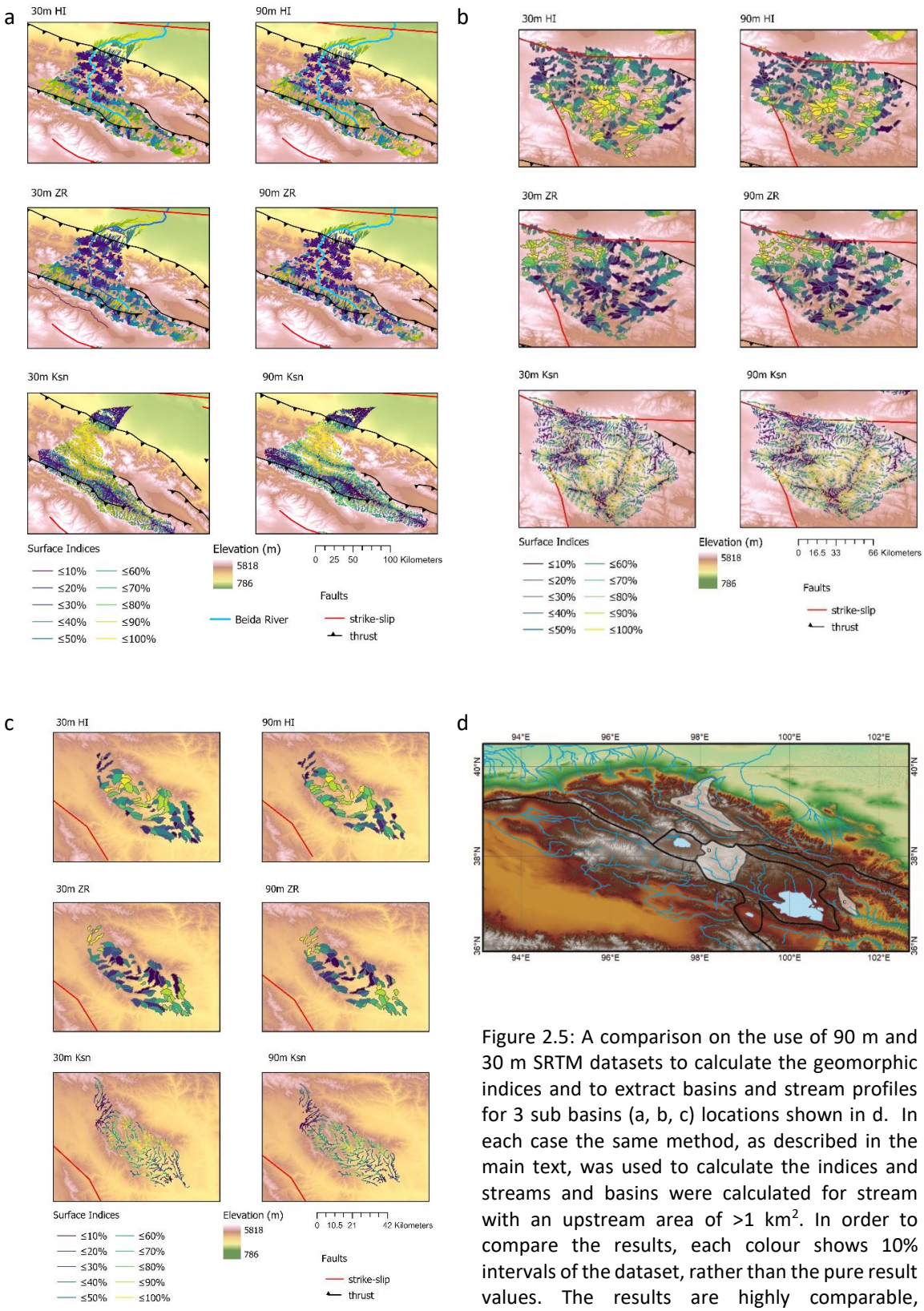

Figure 2.5: A comparison on the use of 90 m and 30 m SRTM datasets to calculate the geomorphic indices and to extract basins and stream profiles for 3 sub basins (a, b, c) locations shown in d. In each case the same method, as described in the main text, was used to calculate the indices and streams and basins were calculated for stream with an upstream area of >1 km^2. In order to compare the results, each colour shows 10% intervals of the dataset, rather than the pure result values. The results are highly comparable, therefore the 90 m dataset has been used throughout this study, as this provides faster processing times, with no discernible loss of accuracy.

landscape evolution (Strahler et al. 1952). HI is calculated as the integral of a hypsometric curve: a plot of normalised elevation against normalised drainage area for each drainage basin. Where surface uplift rate is greater than erosion within a catchment there is a greater range of elevation in the area, giving a high HI. Therefore, high HI values are typically found in areas of rapid uplift, although values can also be controlled by external factors, including rock type and precipitation.

Different methods of calculating HI are compared in Figure 2.6. HI can be approximated as the hypsometric index, which is calculated using the formula:

$$Hypsometric\ Index = \frac{(mean\ elevation - \text{minimum}\ elevation)}{(maximum\ elevation - minimum\ elevation)}$$

Hypsometric index is calculated using moving windows of 35 and 50 km surrounding each point (Figure 2.6.a. and b.) The smaller sized moving window provides greater detail.

Both the hypsometric index and the hypsometric integral can also be calculated for drainage basins (Figure 2.6.c-h). The rationale of using drainage basins is that the boundaries of drainage basins may be controlled by tectonic and geological features and are therefore natural boundaries between different uplift and river characteristics. Therefore, mapping HI by drainage basin avoids smoothing values over spatial boundaries such as faults, compared to other approaches such as the moving windows (e.g. Obaid and Allen, 2019). The drainage basins are extracted from the SRTM data using TecDEM software (Shahzad and Gloaguen, 2011), based on a stream network defined with an upstream drainage area threshold of >1 km². This method produced an accurate stream pattern when compared to satellite imagery. Flat areas were removed after processing, to remove spurious results derived for lakes. A comparison is shown between the hypsometric index calculated using zonal statistics in ArcGIS and HI values calculated in TecDEM both for second order drainage basins is shown in Figure 2.6.c-d. The method of calculating the HI used by TecDEM produces lower values of HI than using simple integration and the values are also lower than those calculated using the hypsometric index. I have reproduced the HI values produced by TecDEM by extracting the elevation data for individual basins. These values are shown to be linearly related to the hypsometric index values (Figure 2.6.e) with variation due to hypsometric index being an estimation of the area under the hypsometric curve. HI calculated in TecDEM is used throughout this work as this provides a more accurate value of HI, particularly in areas where the hypsometric curve is highly variable. Comparison of the HI calculated using the TecDEM software was calculated for drainage basins of different orders, from 2nd Strahler order to 6th Strahler order (Figures 2.6.d and f-h). The patterns of high and low HI regions are similar for each order, but 2nd order basins are

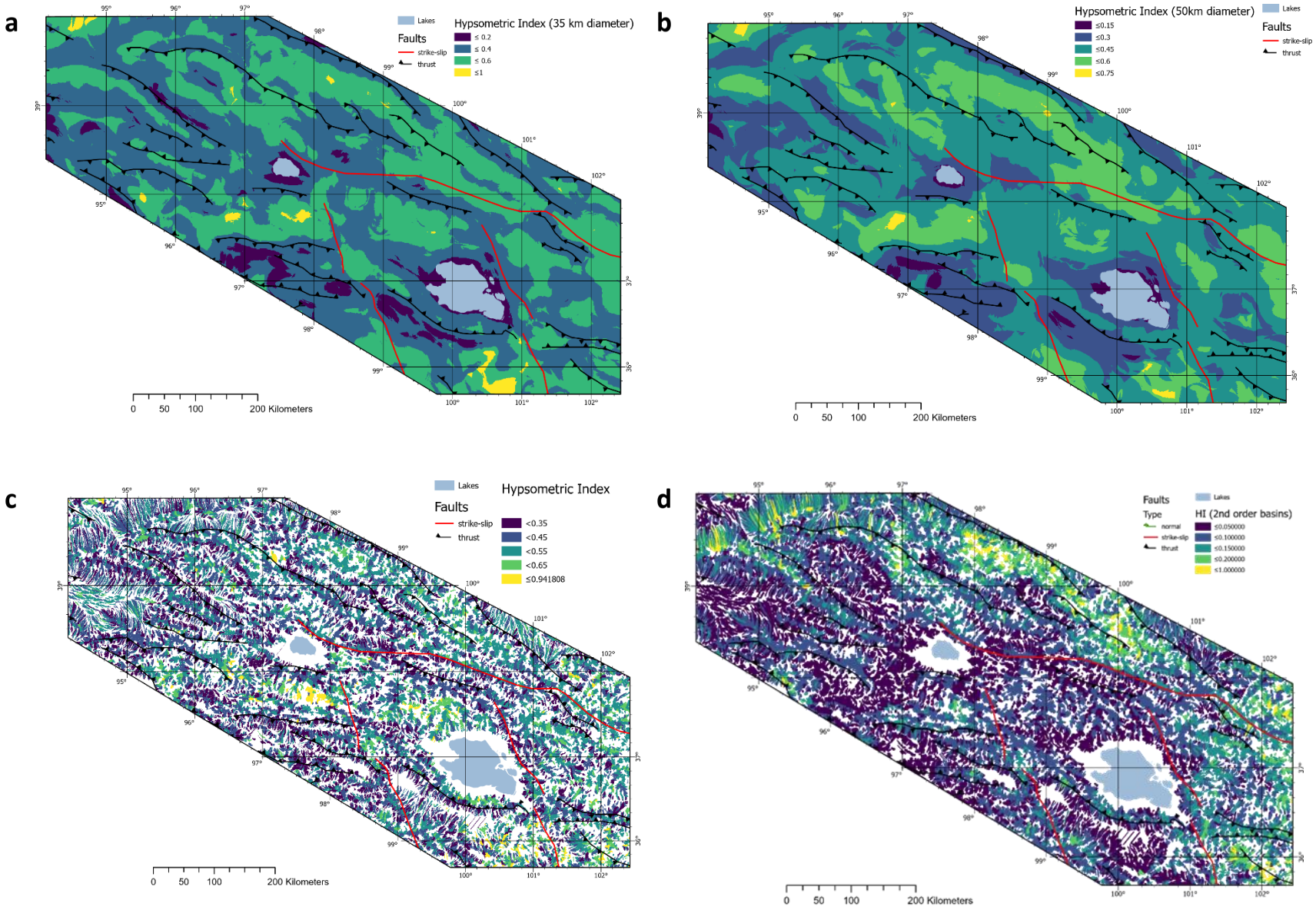
a
Lakes
Hypsometric Index (35 km diameter)
Faults
strike-slip
thrust
≤ 0.2
≤ 0.4
≤ 0.6
≤1
0 50 100 200 Kilometers
b
Hypsometric Index (50km diameter)
Lakes
Faults
strike-slip
thrust
≤0.15
≤0.3
≤0.45
≤0.6
≤0.75
0 50 100 200 Kilometers
c
Lakes
Hypsometric Index
Faults
strike-slip
thrust
<0.35
<0.45
<0.55
<0.65
≤0.941808
0 50 100 200 Kilometers
d
Faults
Type
normal
strike-slip
thrust
Lakes
HI (2nd order basins)
≤0.050000
≤0.100000
≤0.150000
≤0.200000
≤1.000000
0 50 100 200 Kilometers

e

Hypsometric Integral (TecDEM)	Hypsometric Integral (zonal statistics in ArcGIS)
0.299	0.67
0.2	0.5
0.18	0.5
0.14	0.38
0.13	0.4
0.13	0.4
0.11	0.3
0.088	0.28

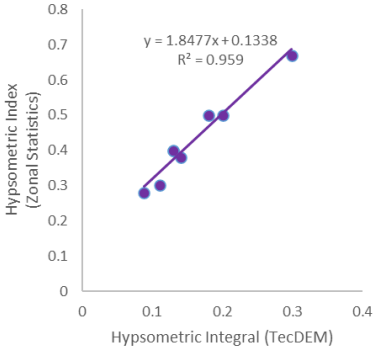

f

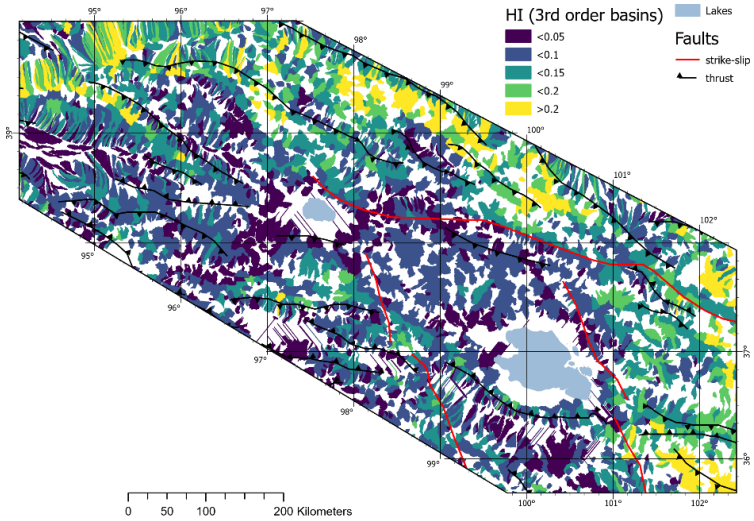

g

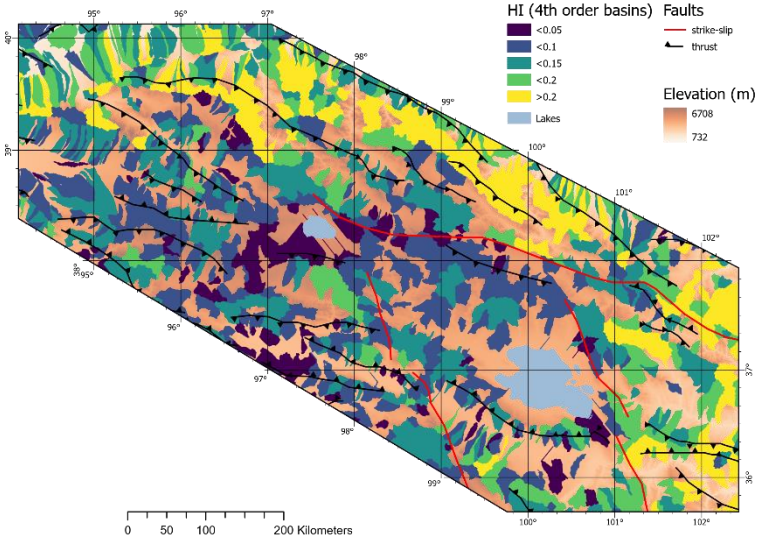

h

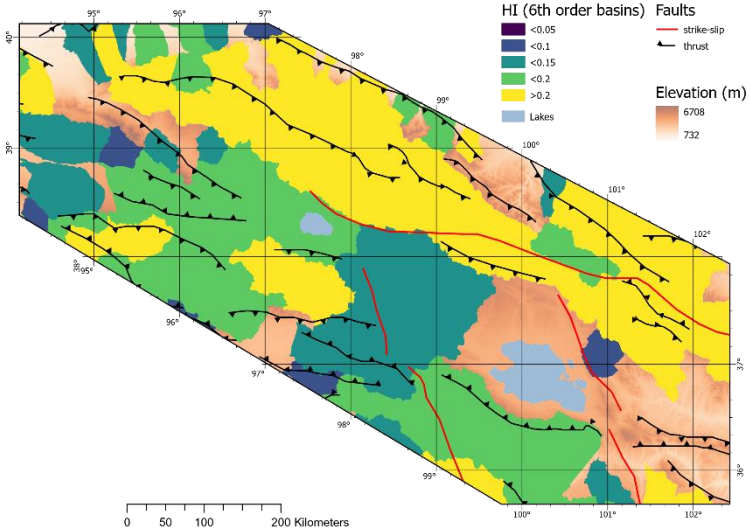

Figure 2.6: Hypsometric index calculated for (a) 35 km and (b) 50 km diameter moving windows using 3 arc second SRTM data and the focal statistics tool in ArcGIS software. Results show relatively high hypsometric index values in the hanging walls of the faults and low in the central Qilian Shan near to the lakes. The changes in the hypsometric index across the faults are not sharp due to the smoothing produced by this method.

All basins in figures (c, d f-h) were extracted using an upstream area of >1km^2 and HI was calculated using the TecDEM software (Shahzad and Gloaguen, 2011).

(c) shows the hypsometric index calculated for second order drainage basin using the zonal statistics tool in ArcGIS software.

(d) **is the HI calculated for the second order drainage basins using the TecDEM algorithm. This method is used throughout this thesis and this figure is repeated as Figure 2.12**.

(e) shows a manual comparison of 8 basins following the methods used in (c) and (d): the two methods are linearly related, with variations from this linear trend due to the assumptions used in the calculation of the hypsometric index.

Figures show basins of (f) 3rd, (g) 4th and (h) 6th Strahler order basins. The same colour divisions are used for comparison. The results show the same a comparable pattern of high and low values, for example high values across the North of the range and lower in the South. However, the larger basins do not show the same level of detail as the smaller basins. The smallest, second order basins were therefore used (Figure 2.12).

used throughout this work as these provide the most detail. Larger basins span fault traces and therefore obscure the changes in HI across fault boundaries.

In this chapter and throughout this thesis HI was calculated using TecDEM software for second order drainage basins using the TecDEM software as the HI method in TecDEM is more accurate than calculating hypsometric index. The use of drainage basins rather than a moving window approach reduces smoothing over different basins and faults and the second order basins provide the most detailed information.

2.2.2 Normalised Channel steepness (k_{sn})

Local channel slope for a steady-state river profile can be expressed as a power-law function of contributing drainage area e.g. Wobus et al., (2006):

$$S=k_s A^{-\Theta}$$

where S=Slope, k_s=steepness index, A=upstream drainage area and Θ≈concavity. The slope and area of the drainage basin is calculated. Channel steepness is calculated here based on a reference concavity to determine a normalised steepness index, k_{sn} (Wobus et al., 2006) allowing comparison of values between different basin sizes.

SRTM data was pre-processed and rivers extracted, using the TopoToolbox set of Matlab scripts (Schwanghart and Scherler, 2014). The TopoToolbox methodology is built upon the integral method of river process analysis, after Perron and Royden (2013). Rivers were extracted with a minimum upslope area of >1 km² in order to remove areas of hillslope areas. Pixels of the area of lakes were then removed.

Both a calculated best-fit theta value and the most commonly used value of Θ=0.45 were used (Kirby et al., 2003) for comparison with previous studies. The averaged best-fit theta value was calculated by taking the best-fit values of theta for each of the major drainage basins of the Qilian Shan. The best-fit theta value is calculated as the gradient of a slope-area plot for each drainage basin as calculated by the TopoToolbox. The weighted average theta value was then calculated, weighted by catchment areas measured in ArcMap. The best-fit theta value was Θ=0.29. The results of these two analyses show the same pattern of k_{sn} on a map scale, but different values (see Figure 2.7). The value of Θ=0.45 is used for analysis in this paper as results can then be compared to other areas.

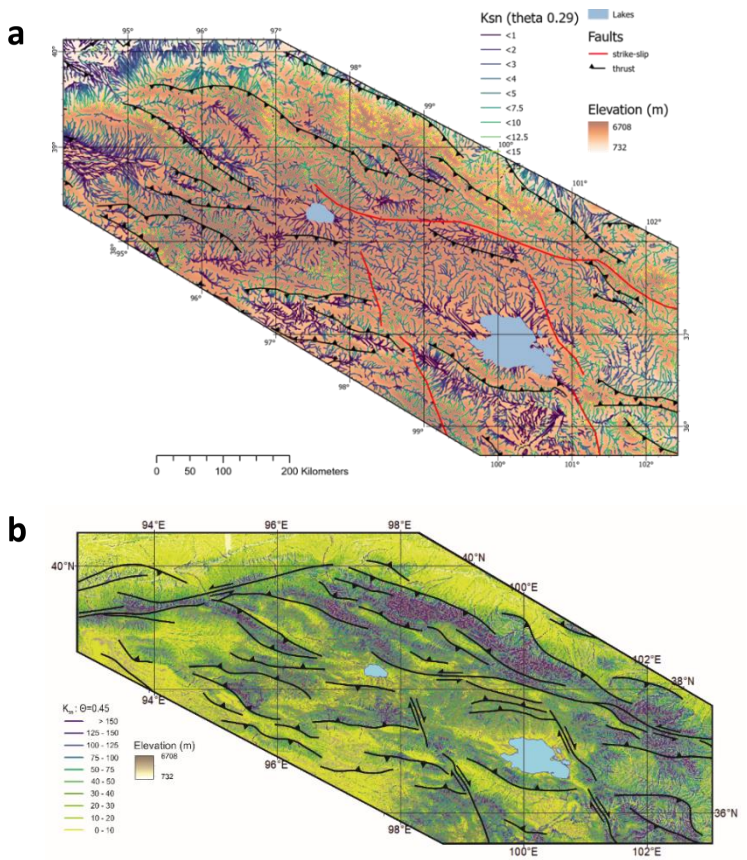

Figure 2.7: k_{sn} calculated using a theta (Θ) value of a) 0.29 and b) 0.45. Θ values were calculated in TopoToolbox (Schwanghart and Scherler, 2014) for each drainage basin, using slope area plots. The value of Θ = 0.29 is the mean Θ for the Qilian Shan, weighted by catchment areas measured in ArcMap. The results of k_{sn} calculated using Θ = 0.45 (Figure 2.13) and Θ = 0.29 show the same pattern of k_{sn} on a map scale, but different absolute values. Θ = 0.45 was therefore used as results can then be compared to other areas and studies. **This preferred method is shown in Figure 2.13** and is a repeat of Figure 2.7b.

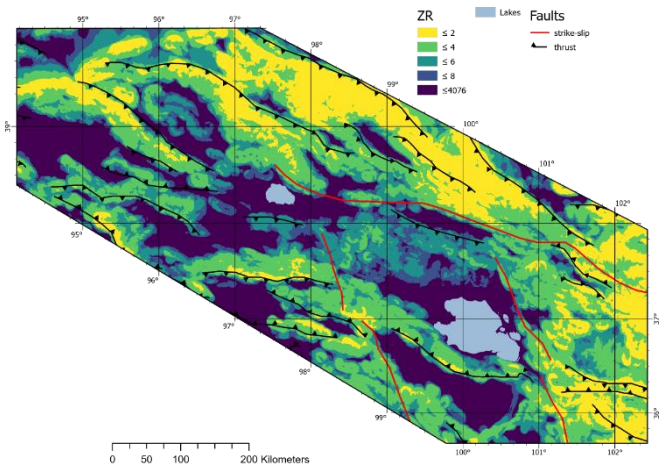

Figure 2.8: ZR calculated by moving window. Elevation was calculated as the mean elevation within a moving window of 10 km diameter. This was then divided by the relief which is also calculated using a 10 km diameter moving window. Using a moving window technique is beneficial as all data in the area is included in the analysis. However, the moving windows smooth out details across different zones, e.g. across faults or drainage divides. **ZR calculated for second order basins (Figure 2.14) was therefore used in preference** to this moving window technique as the drainage divides naturally define boundary conditions.

2.2.3 ZR (Elevation-Relief Ratio)

The elevation-relief ratio (ZR ratio), calculated using the equation below, can be used to identify plateau-like areas: areas with high elevation and low relief (Formento-Truglio and Pazzaglia, 1998; Andronicos et al., 2007).

$$ZR = \frac{Mean\ Elevation\ (m)}{Maximum\ elevation\ (m) - minimum\ elevation\ (m)}$$

Second order stream basins were used, in line with the reasoning in section 2a. The mean elevation and range of elevation were calculated for each drainage basin in order to calculate the ZR. The ZR was also calculated by moving window, see Figure 2.8.

2.2.4 Surface Roughness: Standard Deviation of Slope

Surface roughness (SR) shows the variability of a topographic surface and is one of the most commonly used indices in geomorphology as it can be used to identify surface processes, uplift, feature type and material properties (e.g. Grohmann et al., 2010; Shahzad and Gloaguen, 2011; Domínguez-González et al., 2015). There are multiple methods of characterising surface roughness, with Grohmann et al. (2010) concluding that the most appropriate measurement of the roughness of regional topography is the standard deviation of slope, as this correctly identified breaks of slope and smooth-sloping areas.

Figure 2.9 shows a comparison of different calculations of SR: terrain ruggedness index, standard deviation of elevation and standard deviation of slope, each calculated for moving windows. In this thesis SR is calculated for each second order drainage basin, calculating the standard deviation of the slope from 90 m resolution data, within each basin. The results of the moving window and the by basin approach were similar, but the by basin approach is used throughout this thesis (see Section 2.2a) and calculating using the standard deviation of slope produced the best map of regional SR, rather than high values within valleys (Figure 2.9).

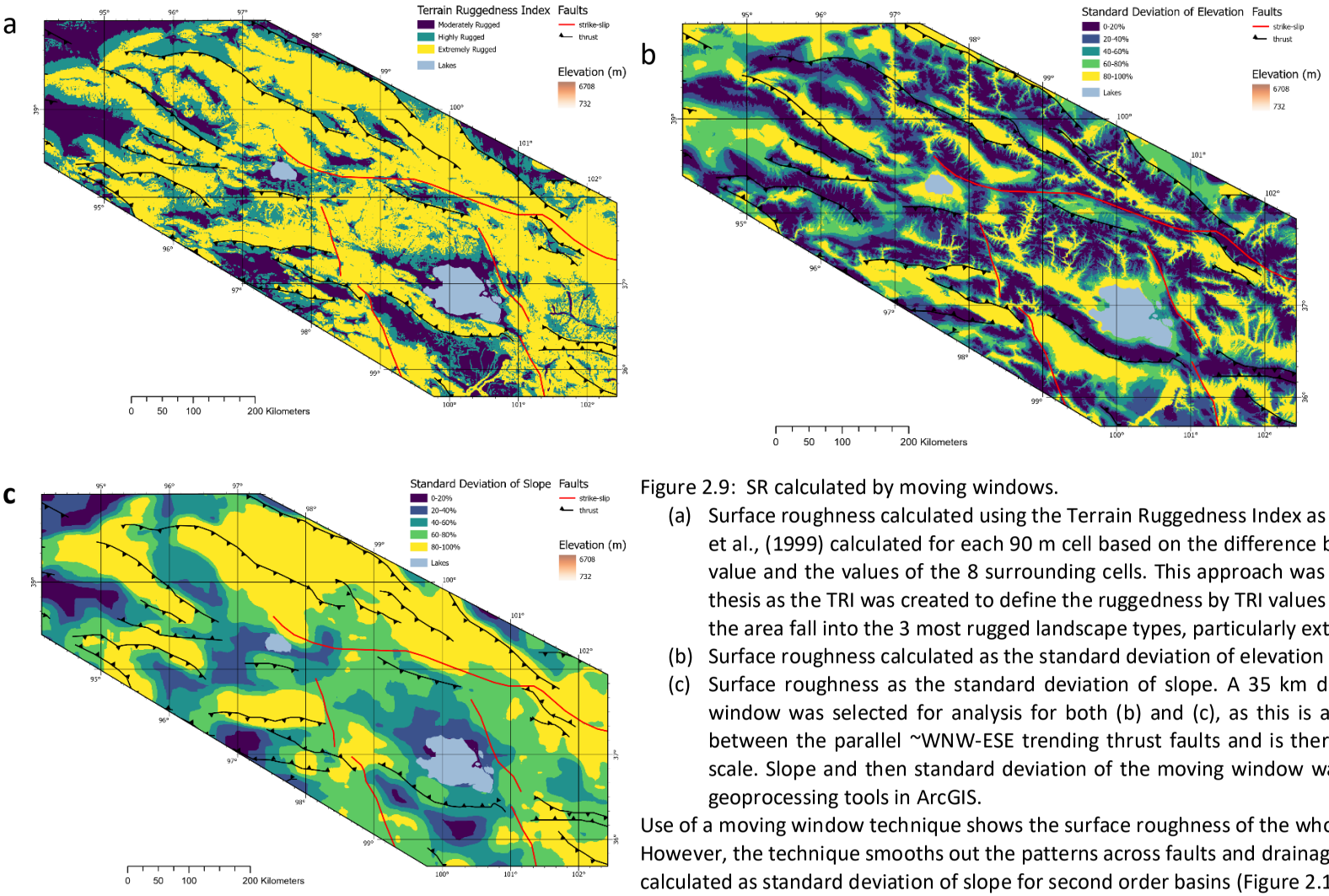

Figure 2.9: SR calculated by moving windows.

(a) Surface roughness calculated using the Terrain Ruggedness Index as defined by Riley et al., (1999) calculated for each 90 m cell based on the difference between the cell value and the values of the 8 surrounding cells. This approach was not used in this thesis as the TRI was created to define the ruggedness by TRI values and all values in the area fall into the 3 most rugged landscape types, particularly extremely rugged.

(b) Surface roughness calculated as the standard deviation of elevation *and*

(c) Surface roughness as the standard deviation of slope. A 35 km diameter moving window was selected for analysis for both (b) and (c), as this is average distance between the parallel ~WNW-ESE trending thrust faults and is therefore a suitable scale. Slope and then standard deviation of the moving window was calculated by geoprocessing tools in ArcGIS.

Use of a moving window technique shows the surface roughness of the whole area. However, the technique smooths out the patterns across faults and drainage divides. SR calculated as standard deviation of slope for second order basins (Figure 2.15) was therefore used in preference as the drainage divides naturally define boundary conditions. The basins also sample comparable areas of the landscape, for example excluding all upper hillslopes.

2.2.5 Swath Profiles

Swath profiles show the variation of topography across a region. Spatial data is taken for a rectangular corridor of a given width and across this width minimum, maximum and mean values are extracted and condensed onto a single profile. Topographic swath profiles, of 30 km width, were created for 7 segments, trending NNE-SSW, perpendicular to the direction general WNW-ESE strike of the thrust faulting. Elevation data were extracted from the 90 m SRTM data with no smoothing. Maximum values represent the highest peaks and minimum values, the valleys. The difference between the maximum and the minimum values is also shown, which represents the relief. Integration of the maximum-minimum difference gives the integrated relief (Obaid and Allen, 2019) which allows for comparison of relief across the range.

2.3 Results

I split the Qilian Shan into 5 main parts in terms of morphology and geomorphic indices patterns. These are: the Central, internally drained region; the Northern region, with south-dipping thrust faults and rivers draining north into the Hexi Corridor; the Southern region, with north-dipping thrust faults and rivers draining south into the Qaidam Basin; the Western region, affected by the Altyn Tagh Fault and the Eastern Qilian Shan which is drained by tributaries of the Yellow River (Figure 2.10). Four of these 5 areas are delineated by major drainage divides and therefore are natural boundaries between different conditions. The Western region of the Altyn Tagh Fault was considered separately, as this is a major structure which affects the landscape. Field photos of landscape variations in the areas of the Qilian Shan are shown in Figure 2.11.

2.3.1 Hypsometric Integral

Variations in HI values highlight the active faults of the area, particularly the active, WNW-ESE trending thrust faults (Figure 2.12). There are sharp boundaries along the fault traces, with abrupt changes from higher values in the hanging walls to lower values in the footwalls. In some areas a sharp change in values does not occur along a fault trace: in the Western region, high HI values occur on both sides of the Altyn Tagh Fault. In this study HI values range from 0 - 0.31, with values > 0.2 considered as high.

HI distributions show a distinct pattern of higher HI (> 0.2) in the north and east of the Qilian Shan than in the south and west. Values of HI > 0.15 are largely at or below 3500 m elevation. The overall

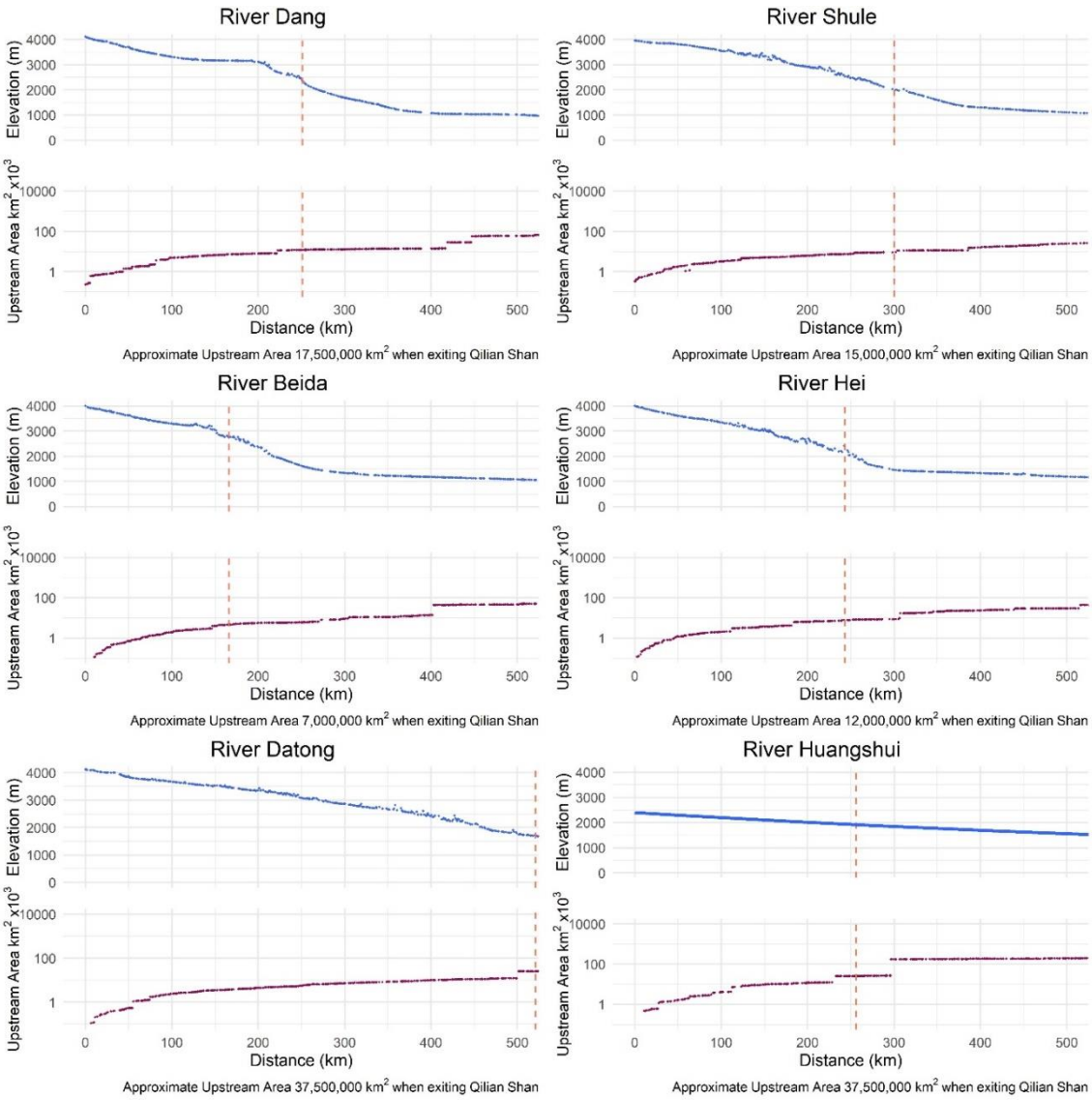

Figure 2.10: River profiles and upstream area of 6 major rivers draining the Qilian Shan, located in Figure 2.4. Upstream area is calculated by flow accumulation, multiplied by cell size. Vertical dashed line indicates the approximate extent of the Qilian Shan. The profiles show the stream profile morphology within the Qilian Shan to be largely similar. However the upstream areas vary from 7 million-17.5 million km^2 in the rivers flowing across the strike of the range (Dang, Shule, Beida and Hei) compared to 37.5 million km^2 for the range parallel tributaries of the Yellow River (Datong and Huangshui). This difference in upstream area may account for higher HI and SR values in the Yellow River tributaries.

pattern shows a boundary between the high and low values aligned with the Haiyuan Fault. There is also a pattern of high HI values across the margins of the mountain chain and low values in the

central region, which is indicative of the plateau morphology.

The pattern of HI is strongly linked to the drainage pattern of the Qilian Shan. Low values of HI (< 0.1) occur in the central Qilian Shan, centred around the areas of internal drainage of Lake Hala and Lake Qinghai. Low values are also seen in the rivers draining to the south into the Qaidam Basin. Higher values (> 0.15) occur in the Eastern region, along the basins draining into the Datong and Huangshui rivers, which are tributaries of the Yellow River.

The 5 areas of the Qilian Shan discussed here were statistically analysed. The Kruskal-Wallis test (p value < 0.05) shows that there are significant differences between the HI values of the 5 areas. Mann-Whitney U test analyses compared the data of the 10 combinations of areas, with results showing all areas to be distinct from each other ($p < 0.05$).

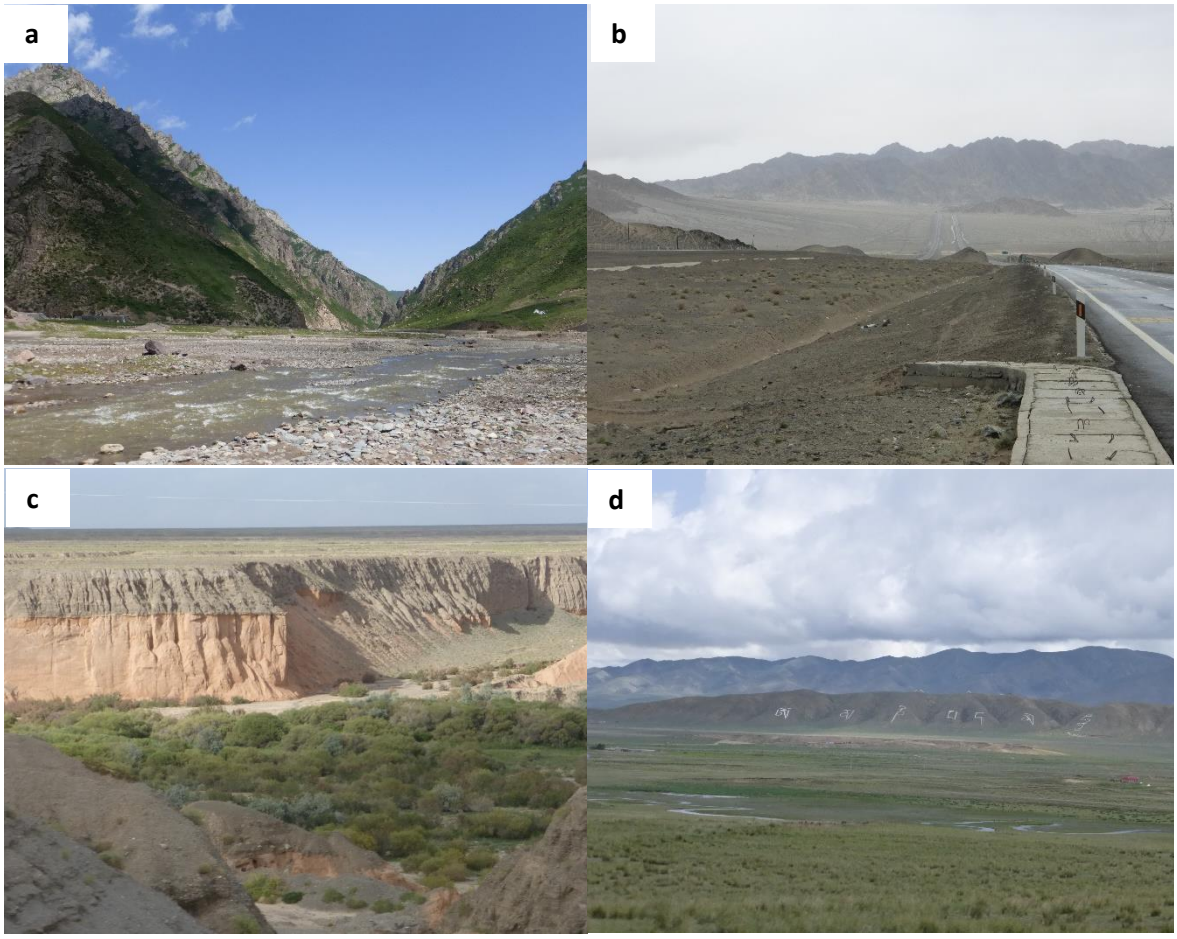

Figure 2.11: Field photos, courtesy of M. Allen, of landscape variations in the Qilian Shan. a) a steep and narrow valley in the Northern Qilian Shan. b) Rugged topography in an arid area of the Southern Qilian Shan. c) Steep sided gullies in the area of the Altyn Tagh fault, North West Qilian Shan. d) The low relief landscape of the central, internally drained region of the Qilian Shan, near Qinghai Lake.

2.3.2 Normalised Channel Steepness

K_{sn} values vary with climatic setting, rock strength and erosion/rock uplift (Kirby and Whipple, 2012). Underlying lithology and precipitation control are discussed in section 4.2 and are found to not be first order controls on k_{sn},. I therefore interpret the k_{sn} results with respect to changes in erosion and/or surface uplift.

The regions of highest k_{sn} are in the north and east of the Qilian Shan (Figure 2.13). Localised regions of high k_{sn} occur at major faults, as for the HI distributions. The k_{sn} values show a pattern of higher values (k_{sn} > 50) in the hanging wall of thrust faults. The width of the high k_{sn} regions varies, with wider regions (40 km wide where k_{sn} > 50) along the WNW-ESE trending thrust faults in the north, but 25 km wide in the south.

Rivers draining across active thrust faults in the northern Qilian Shan show some of the highest regional values of k_{sn} (> 100). Values are highest at the locations where the rivers cross the range fronts. The upper reaches of some of these rivers, such as the Beida River (Figure 2.5a, location shown in Figure 2.4), have lower k_{sn} values where they flow parallel to the ranges. High k_{sn} (> 50) values are also seen in the East Qilian Shan, representing rivers that flow into the Yellow River. The region of internal drainage has low values of k_{sn} (<50), indicating less steep rivers. The highest values of k_{sn} within the internally drained basins occur in the rivers draining into Lake Qinghai, which is the largest of the three internal basins. High values of k_{sn} are found below the regional 3500 m elevation contour.

2.3.3 ZR (Elevation Relief Ratio)

A high ZR ratio (in this study ZR > 6) indicates a low relief at higher elevation, mainly >3500 m, which is indicative of a plateau geomorphology. The Central Qilian Shan, around Hala Lake shows ZR above 6, showing plateau-like relief. There are low values (ZR < 4) on the northern and southern margins (Figure 2.14). Anonymously high values are also seen in very flat basins, such as the Qaidam Basin to the south of the Qilian Shan, simply due to their very low relief.

2.3.4 Surface Roughness

The standard deviation of slope (Figure 2.15) shows a similar pattern to the HI values, with high values (SR >10) in the hanging walls of the thrust faults. The lowest values (SR <4) are seen in the lowlands surrounding the mountain chain and in the centre of the Qilian Shan, around Qinghai and

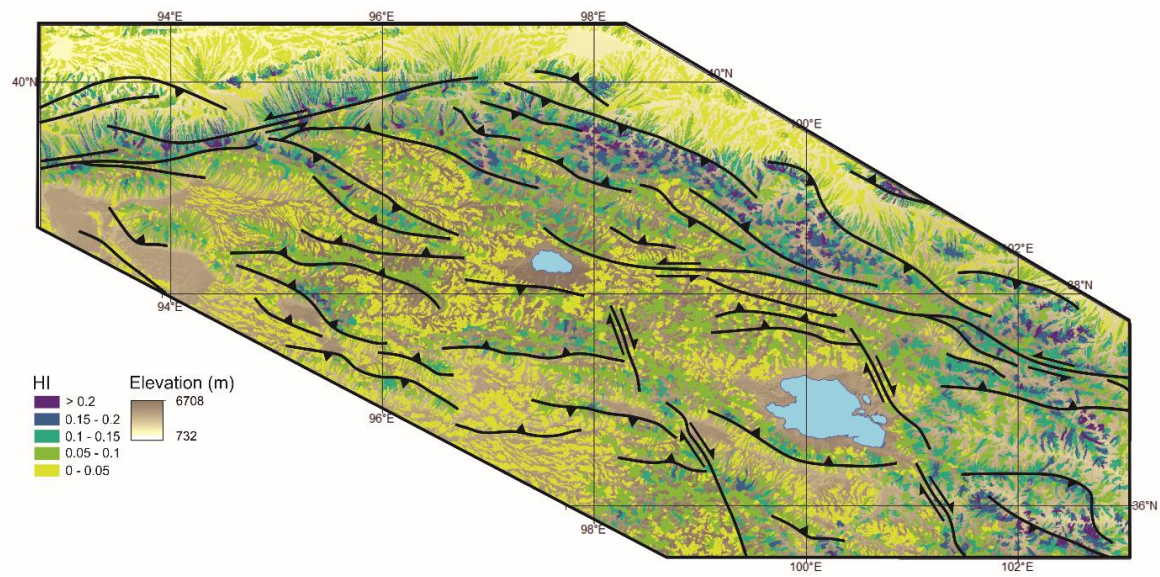

Figure 2.12: HI (Mean: 0.06; Maximum; 0.32 Standard Deviation: 0.04) for second Strahler order drainage basins, with fault traces shown. High HI (> 0.2) indicates landscapes with high rock and surface uplift and low HI (> 0.05) flatter landscapes. HI is sensitive to active faulting in the area, with high HI in the hangingwalls of thrust faults and along the Altyn Tagh Fault. HI values are higher in the North and East of the region, with a distinct increase in HI from south to north across the Haiyuan Fault.

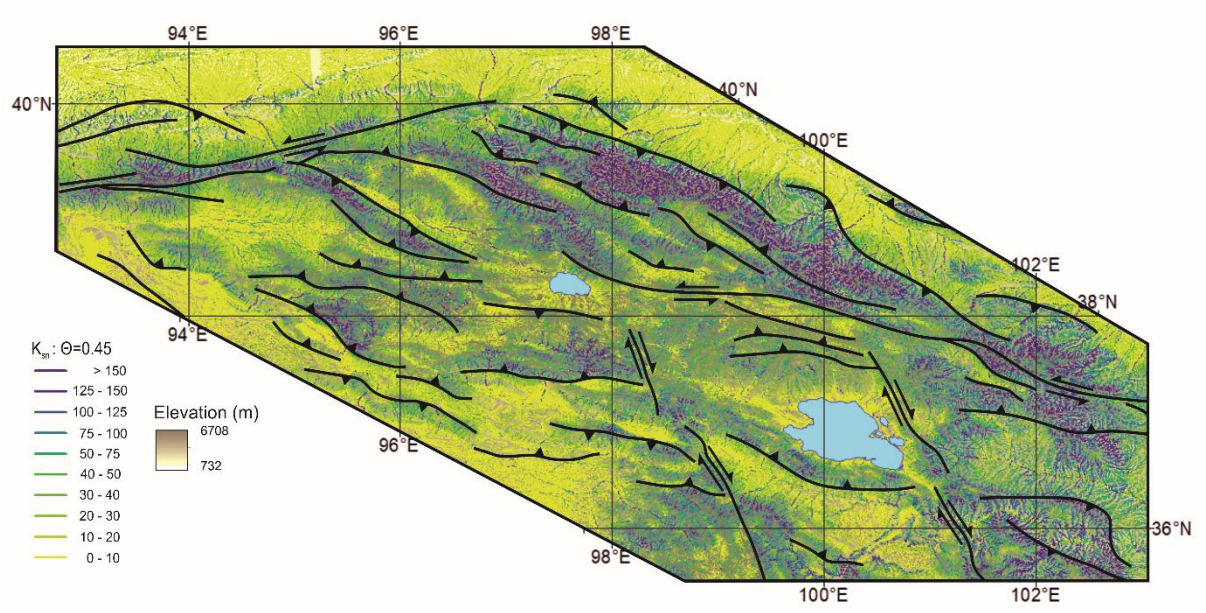

Figure 2.13: K_{sn} (Mean: 56; Maximum; 670 Standard Deviation: 83) of streams across the region, calculated with a reference concavity of Θ=0.45. Fault traces are also shown. High k_{sn} values (>75) occur in the north and south of the region, again with high values in the hangingwalls of active thrust faults.

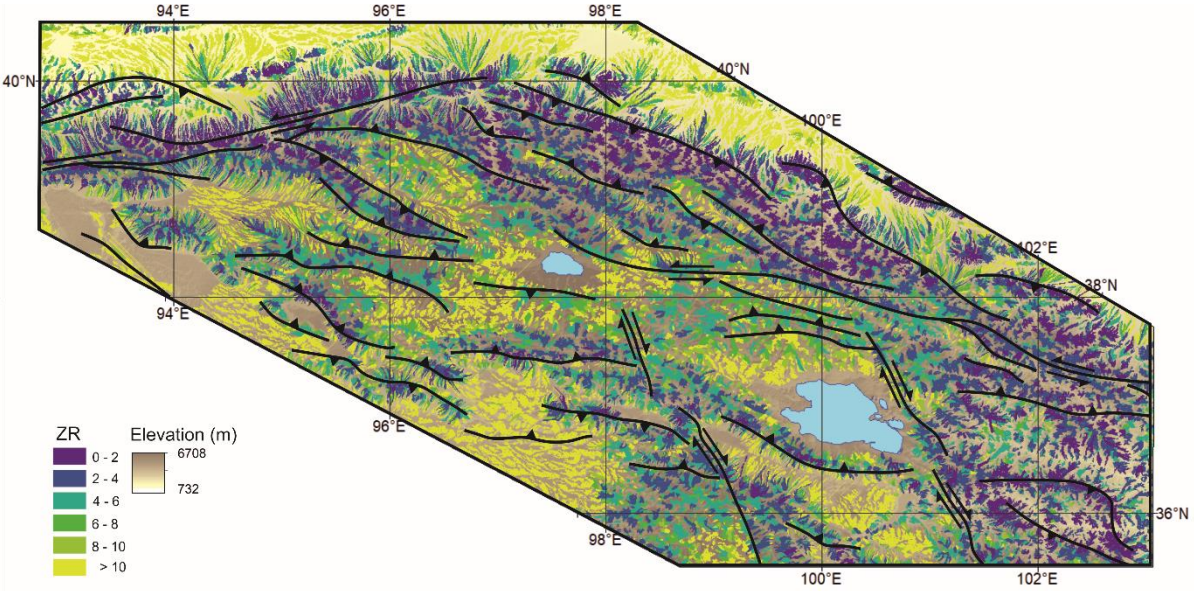

Figure 2.14: ZR (Mean: 19; Maximum; 351 Standard Deviation: 42) calculated for second Strahler order basins, shown with the faults of the area. High ZR (> 6) values are created by a combination of high elevation and low relief. The highest values occur in the flat basins surrounding the Qilian Shan, due to their low relief. High values also occur in the central region of the Qilian Shan, surrounding the lakes, showing these areas have a plateau-like morphology. Low ZR values (< 2) show low elevation and/or high relief. These areas are again in the north and east of the region and in the hangingwalls of thrust faults.

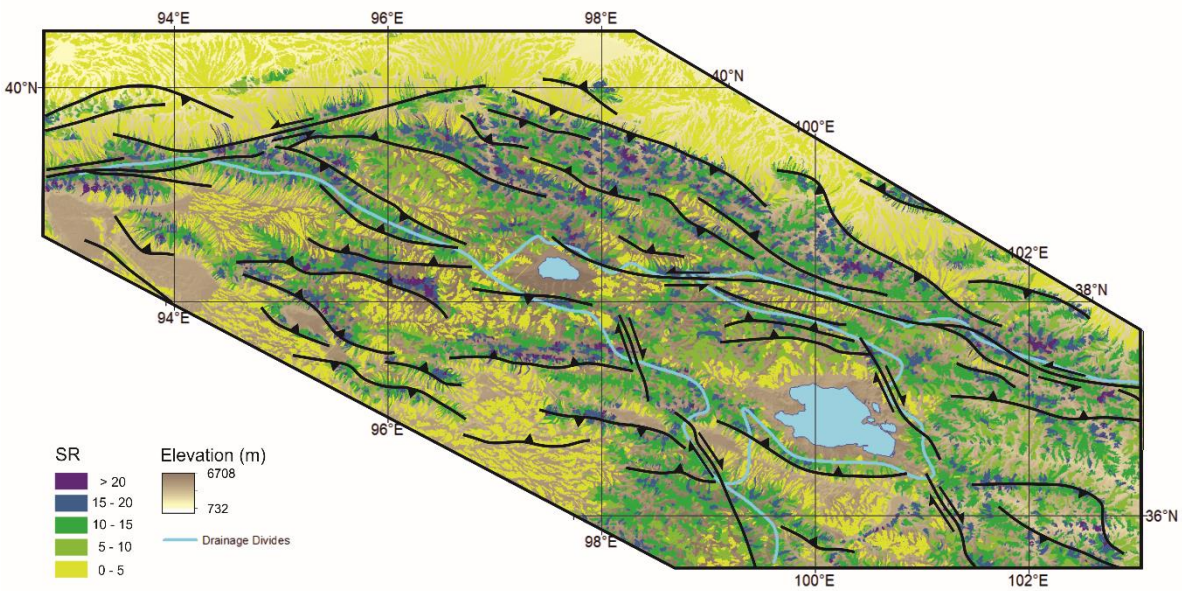

Figure 2.15: Surface roughness (SR - Mean: 9; Maximum; 33 Standard Deviation: 6) calculated for second Strahler order basins, shown with the major drainage divides and faults of the Qilian Shan. High SR values (>10) occur in the hangingwalls of active thrust faults and in the regions of major strike-slip faulting, such as the Altyn Tagh Fault. Lower SR values are present in the lowlands surrounding the Qilian Shan and also in the central, internally drained regions, where the rivers drain into the lakes.

Hala lakes. Surface roughness shows a less clear relationship with the drainage divides and regions of >3500 m elevation.

2.3.5 Swath Profiles

The elevation profiles (Figure 2.16) show the plateau morphology of the interior of the Qilian Shan, with swaths 2-6 showing the clearest plateau morphology: shallower slopes in the south, a flatter area in the centre with maximum elevations of ~5500 m and steeper slopes at the northern mountain front. There appears to be a sharper transition from the range front to the internally-drained plateau region in the north than the south. Swath 1 shows a similar trend, but with a steeper southern margin and a shallower northern margin. This difference may be due to the curvature of the mountain front, which in this region is not parallel to the swaths. Swath 7 shows high relief throughout. The relief curves of swaths 1-6, calculated as the difference between the maximum and minimum elevations, show an overall increase in relief from south to north.

2.4 Discussion

2.4.1 Morphology of the Qilian Shan

The Northern region shows bands of high HI, k_{sn} and SR and low ZR values (HI >0.15, k_{sn} >100, SR >10, ZR <2). These bands are in the hanging wall of the thrust faults. This pattern suggests that the thrust faults are actively uplifting. It is unlikely that changes are due to lithological contrasts (section 2.4.2). The rivers draining these regions are steepened by the rock uplift, forming deeply incised valleys. The plan-view width of these incised landscape regions in the hanging walls of each fault decrease to the south, as discussed in section 2.3.1. This may indicate a combination of lower uplift rates towards the central plateau and/or steeper dipping faults and/or a different duration of fault activity. In the west of this region, the Dang and Shule rivers (Figure 2.4) have been diverted to flow parallel to the thrust faults and exit the mountain chains parallel to these faults, giving lower values of HI <0.15, k_{sn} <75, SR <10 and higher ZR values (ZR >6).

The Southern region shows the same pattern of geomorphic indices as the Northern region, with high values of HI, k_{sn} and SR and low ZR in the hanging walls of thrust faults. The width of these regions are narrower than the northern margin, at ~35 km compared with ~60 km. This may be due to lower topographic slopes in the south Qilian Shan compared to the north, or due to variation in rock uplift. If these changes are attributed to rock uplift, the results suggest that the Qilian Shan

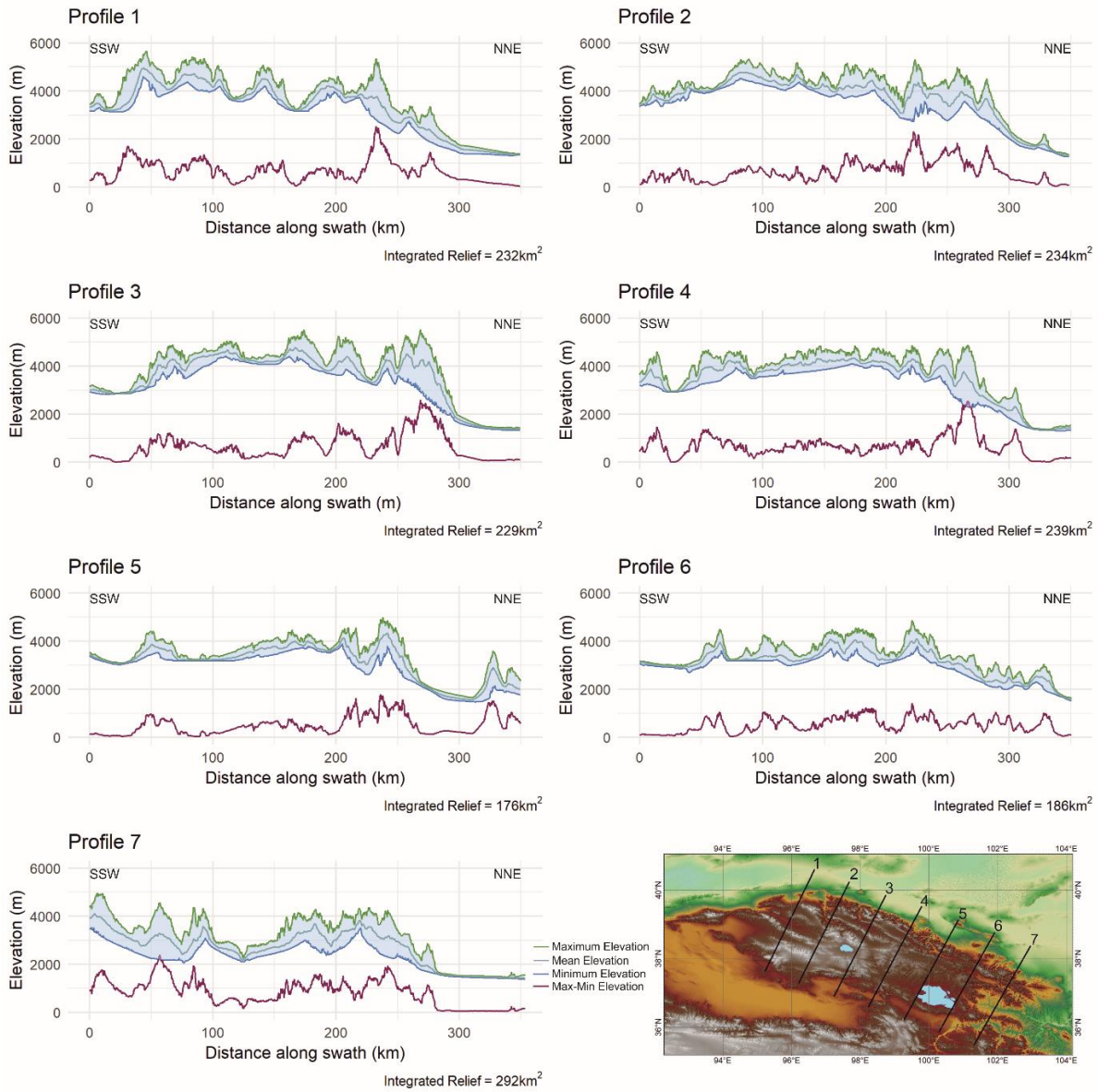

Figure 2.16: Swath profiles of elevation, each of total width 30 km and drawn from South West to North East. The location of the profiles is shown. The area between the maximum and minimum values (shaded and also shown in purple) is summed to give the integrated relief. Profiles 1-6 are orthogonal to the WNW-ESE trending thrust faults and near parallel to the rivers draining across the strike of the mountains. These show the plateau like morphology of the Qilian Shan. Profile 7 is orthogonal to the WNW-ESE trending thrust faults, but also orthogonal to the along strike rivers (Huangshui and Datong rivers) accounting for the more dissected swath profile, with the location of the river channel identifiable. Integrated relief is largely similar across the region.

shows an asymmetric pattern of deformation, with a broader region of active uplift at the northern margin.

The Altyn Tagh Fault affects drainage patterns in this area. Rivers in the area are deflected left-laterally by the fault and the area is characterised by braided rivers and alluvial fans (Mériaux et al., 2005). The Altyn Tagh Fault region has values of HI >0.15, k_{sn} >75, SR >8, ZR <4 and Figure 2.12 shows that the second order basins are elongated perpendicular to the fault and parallel to the rivers that pass into the Tarim Basin to the north. The high HI values here occur where there are deeply incised gorges cut into alluvial fans, due to the differences in elevation between the fan surfaces and the active channels. I suggest that there may be a climatic control on the high HI values in this region and that downcutting of the fan surfaces is a response to base level fall, itself produced by aridification of the Tarim Basin. The timescales are not constrained.

The central area, between the north and south sets of WNW-ESE trending thrust faults has the characteristics of a plateau landscape, with low relief (Figures 2.15 - 17), high elevation (Figure 2.16), high ZR (ZR > 6) Figure 2.14), low k_{sn} (< 50, Figure 2.13) and low HI (HI <0.1, Figure 2.12) and internal drainage. The geomorphic indices indicate a flatter landscape which is not being incised to the same extent as surrounding regions. This result is consistent with the work of Liu-Zeng et al. (2008), who used relief patterns to delineate the plateau-like landscape in the interior of the Qilian Shan.

The East region of the Qilian Shan drains into tributaries of the Yellow River (Figure 2.4), which is the only river in the area which reaches the sea. The South and Central areas are internally drained – rivers in the Central region drain into the lakes and rivers in the southern region into the Qaidam Basin, at ~2750 m elevation. The west and north fringes of the Qilian Shan drain further into the interior of Asia, to elevations of ~1400 m. The East region drains to the Bohai Sea. Swath profile 7 (Figure 2.16) shows that the morphology of the Eastern area varies from the plateau-like morphology of the central Qilian Shan. There is no high flat, central region. Instead there is a large variation in each of the indices which simply represents the location of river channels, where the rivers incised deep valleys. This is attributed to the Datong and Huangshui rivers running parallel to the range, in contrast to the other major rivers of the Qilian Shan, particularly the Northern Qilian Shan, which flow orthogonal to the range, crossing the faults. The rivers are orthogonal to swath 7, therefore showing a different morphology in the swath profile (Figure 2.16, 2.17). The area shows relatively high values of HI (>0.15), k_{sn} (>100), SR (>8) and low (ZR <6). This may be due to the relative ease of excavating the valleys parallel to the major thrust faults.

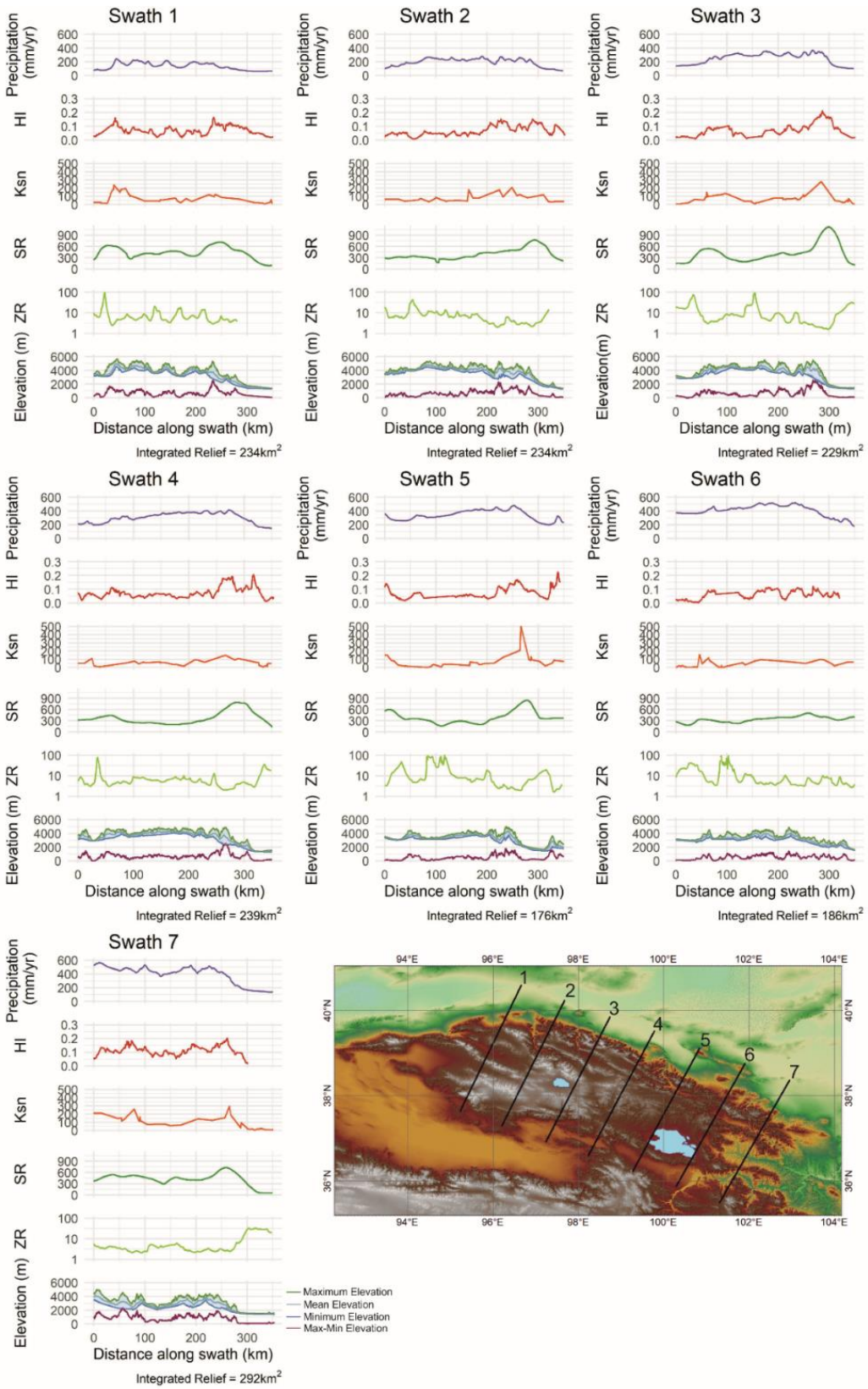

Figure 2.17: Swath profiles showing variations in geomorphic indices and elevation across the strike of the range, including elevation profiles as in Figure 2.16.

Headward erosion due to base-level changes (Shi, 2019) and the larger, externally-drained, upstream area may also account for high HI and SR (Figure 2.10). As there is no correlation between geomorphic indices and precipitation the higher values are not due to greater precipitation (Figures 2.18, 2.19).

Drainage divides can be produced by tectonics, including both strike-slip and thrust faulting. The major basins are mostly defined by strike slip faulting: the left-lateral Altyn Tagh Fault, the North-East and North-Central by the left-lateral Haiyuan Fault, the Central-East by the right-lateral Riyueshan Fault and the Central-South by the right-lateral Elashan Fault (Figure 2.15). Strike-slip faulting often offsets and defeats rivers (Burbank and Anderson, 2001) and this process is crucial in plateau formation. The coincidence of drainage boundaries and strike slip faulting suggests that the faulting is aiding plateau formation in the Qilian Shan and therefore is a major control on the overall landscape of the Qilian Shan. Plateau formation will be in competition with externally drained rivers cutting back into the internally drained areas. The North-South and Central-East drainage boundaries (south of Qinghai Lake) are controlled by thrust fault location.

Integration of the relief of the profiles shows a variation in results (Figure 2.16) of 66 % (176 km² to 292 km² - a difference of 116 km²). The largest integrated relief (Profile 7) is in the east of the Qilian Shan, with the swath sampling the area drained by the Yellow River tributaries. Excluding this swath, the variation of swaths 1-6 is 36 %. Obaid and Allen (2019) found variations of < 25% across the Zagros, which they suggest to be a low value considering the variation in structure and climate across the range and therefore the integrated relief value is more likely controlled by factors that are similar across the strike of the range, such as strain rate, overall shortening and elevation differences between plateau and foreland. The value of 36 % suggests that broadly similar factors may be controlling the relief in this area, apart from in the location of swath 7.

2.4.2 Precipitation, Lithology and Geomorphic Indices

Previous studies in other regions have shown that precipitation is positively correlated with erosion rates in areas with relatively low rates of tectonic rock uplift and high precipitation would therefore produce higher values of HI and SR and low ZR and k_{sn} (Montgomery and Brandon, 2002; Henck et al., 2011). Annual precipitation (WorldClim version 2) for 1970-2000 for the Qilian Shan is shown in Figure 2.3. There is a precipitation gradient parallel to the Qilian Shan, with precipitation decreasing from east to west. Precipitation is also higher in the northern margin of the Qilian Shan than the southern margin, which is likely to be due to higher elevations in the north, but may partially

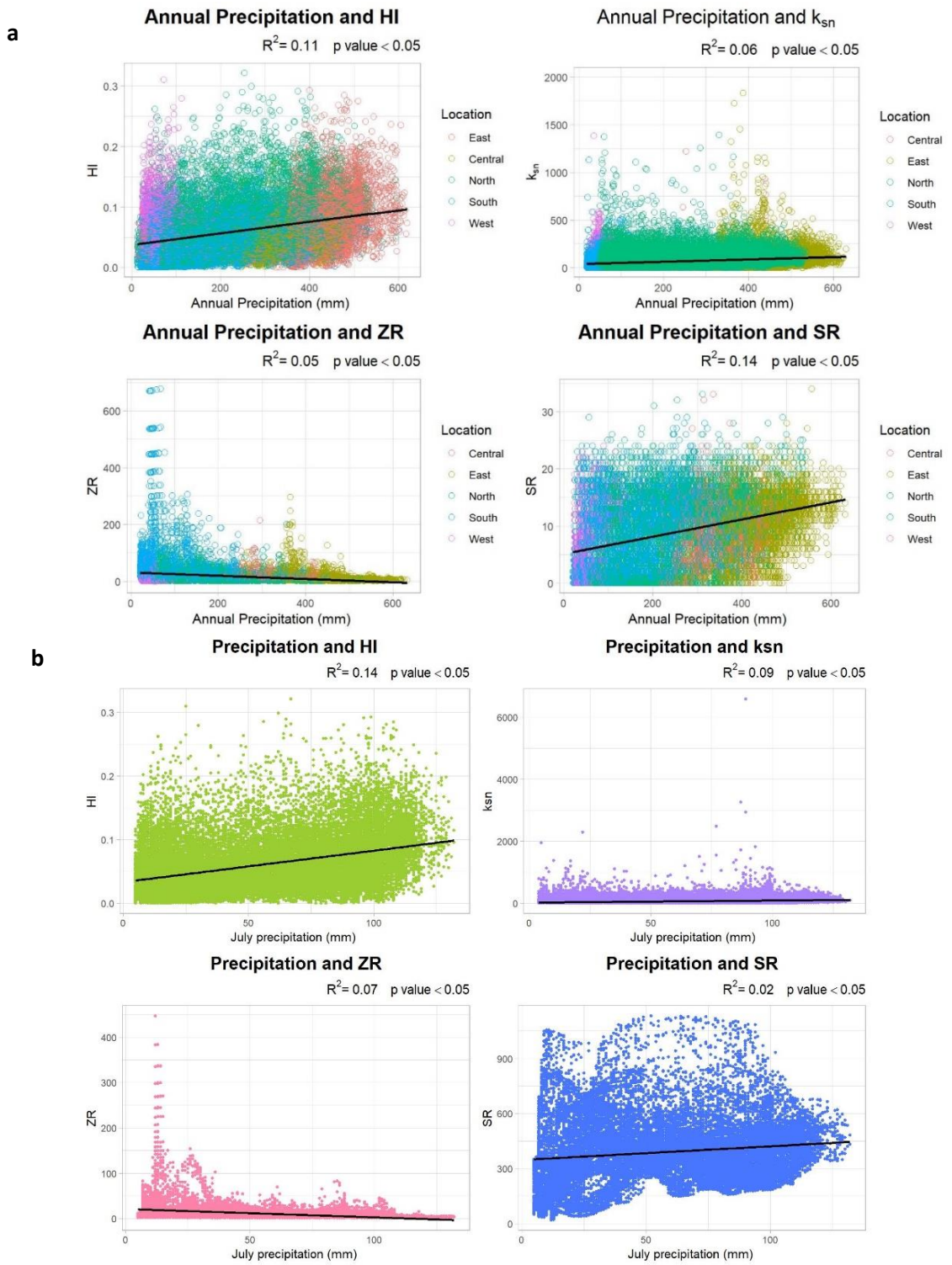

Figure 2.18: a). Scatter graphs of geomorphic indices against mean annual precipitation. The colours represent the 5 areas studied: East, North, South and Central regions defined by major drainage divides and the West defined as the area around the Altyn Tagh Fault (Figure 2.20a). b) Scatter graphs of geomorphic indices for mean July precipitation, which is the wettest month in the Qilian Shan. Each comparison in both a) and b) has low R^2 values showing a low correlation between the indices and precipitation, suggesting that precipitation is not a major control on the landscape of the Qilian Shan.

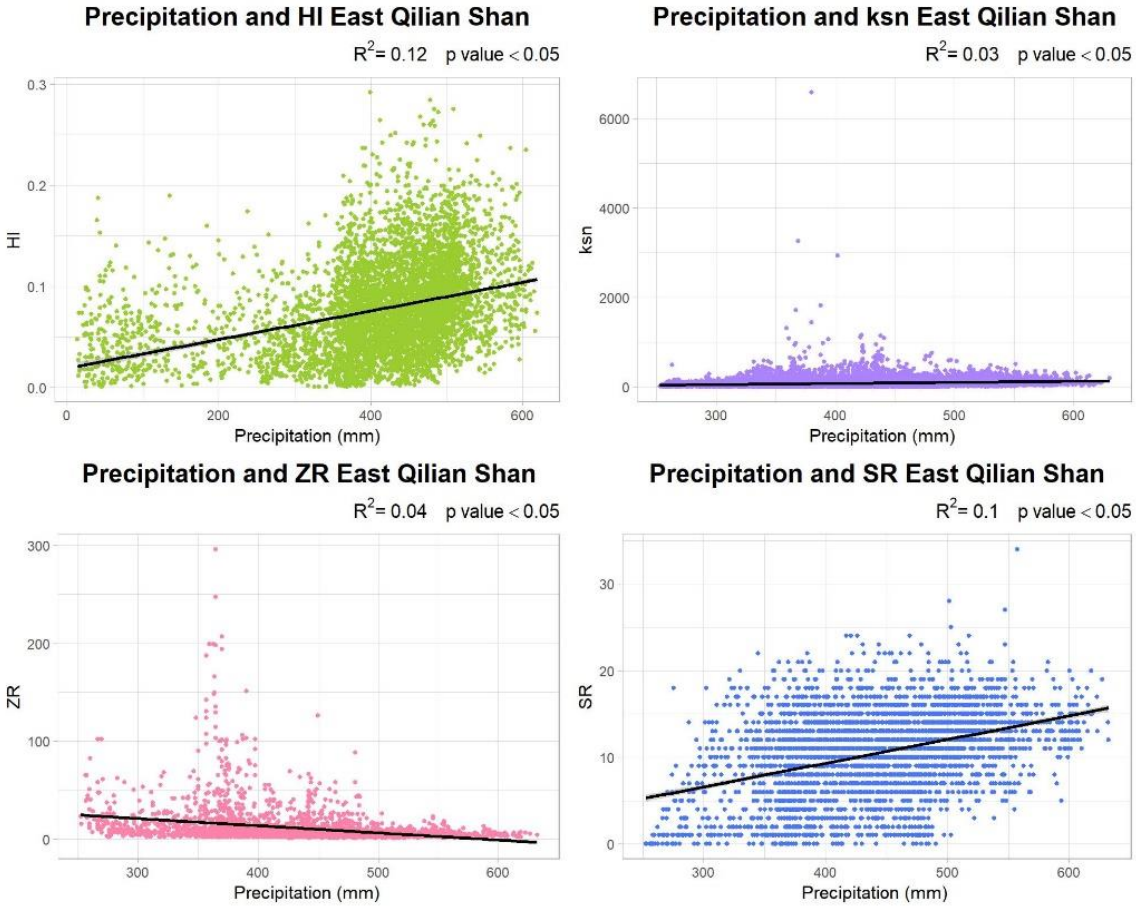

Figure 2.19: Scatter graphs of geomorphic indices against mean annual precipitation in the East draining region of the Qilian Shan, the area defined in Figure 2.4. There is poor correlation between the indices and precipitation.

account for higher HI, k_{sn} and SR in the north. However, overall in the Qilian Shan, there is a very weak relationship between annual precipitation and HI, k_{sn} SR and ZR respectively (r^2 = 0.11, 0.06, 0.14, 0.05 respectively all p values < 0.05; see Figure 2.18.a) and between precipitation in July and the indices (r^2 = 0.14, 0.05, 0.07, 0.02, p values < 0.05; Figure 2.18.b) which is the wettest month and accounts for 24% of the annual precipitation. No east-west variation is observed in the HI, k_{sn} or SR or ZR, apart from in the Eastern region, with the higher HI, k_{sn} and SR and lower ZR values here attributed the range parallel rivers in this area (section 4.1). Within the East region there is also a poor correlation between indices and precipitation (r^2 = 0.12, 0.03, 0.1, 0.04, p values < 0.05; Figure 2.19).Figure 2.20, shows an east-to-west decrease in precipitation but no east-to-west change in any of the indices, with HI shown in the figure. There is also poor correlation between the indices and storminess as calculated as the runoff coefficient of variation by Wang et al., (2014b) for areas steeper than 20° for 11 basins in the northern Qilian Shan (r^2 = 0.17, 0.002, 0.03,

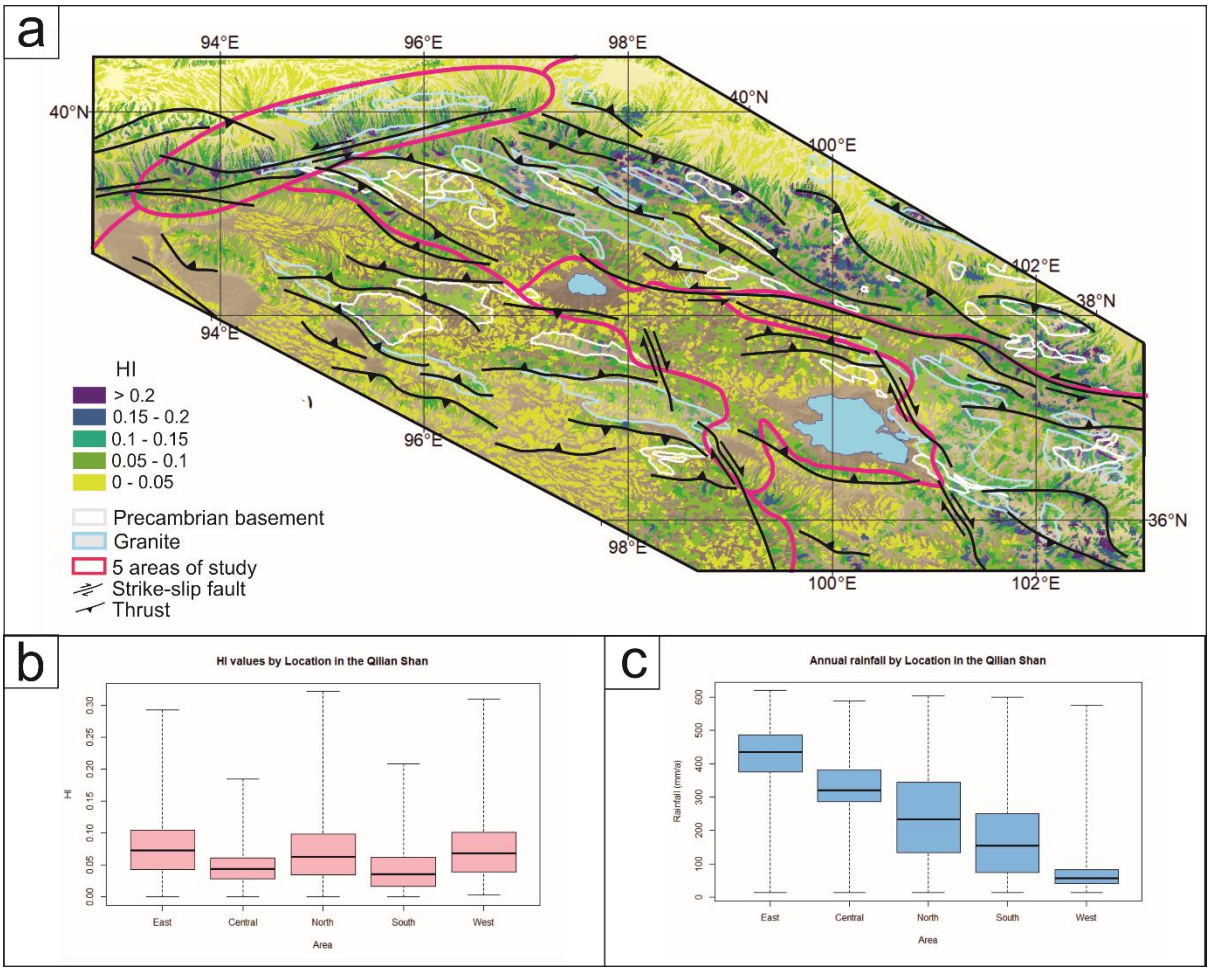

Figure 2.20: a) Areas of underlying crystalline basement and granites (Y. Zhang et al., 2017) are highlighted, overlain over the HI results. The underlying lithology appears to have no control on geomorphic index values (Figure 2.22) as the same value distributions are found, regardless of lithology. b) Distribution of HI values across the 5 areas of the Qilian Shan. The box and whisker diagrams show the medians, interquartile ranges and range of data. c) Distribution of annual precipitation (mm) across the 5 areas of the Qilian Shan, shown as a box and whisker diagram. Precipitation decreases in general from East to West, with no systematic change in HI values.

0.2, p values < 0.05). HI is more sensitive to storminess than the other indices. Decadal erosion is low in the Qilian Shan compared to other regions of active shortening such as the Himalaya (Li et al., 2014) and is weakly correlated to the geomorphic indices (Figure 2.21; r^2 = 0.34, 0.39, 0.53, 0.35, p values < 0.05). Pan et al., (2010) found no relationship between decadal erosion rates and precipitation on a catchment scale in the northern Qilian Shan, although variables such as discharge and runoff may account for some of the variation in erosion rates and may therefore account for variations in the geomorphic indices. I therefore conclude that precipitation variation and storminess do not control the geomorphic indices calculated in this study and are therefore not a first order control on landscape in the area. Decadal erosion rates, which are likely to be partially controlled by precipitation shows a stronger relationship with geomorphic indices. Su et al. (2017) also found no correlation between k_{sn} and precipitation in the Qinghai Nanshan (Figure 2.4), in the

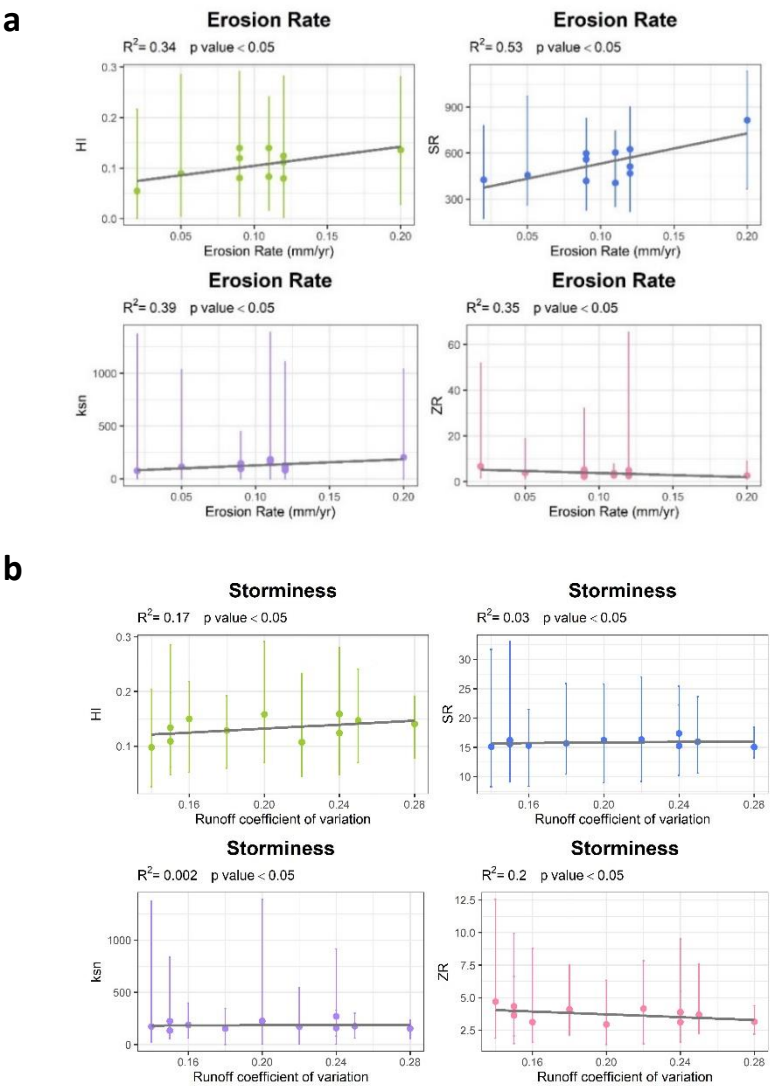

Figure 2.21: a) Correlation between decadal erosion rate and geomorphic indices for 11 drainage basins in the Qilian Shan, as defined in Pan et al., 2010. Data is taken as the mean for the entire drainage basins and error bars represent the minimum and maximum geomorphic indice values within the basin.
b) Storminess calculated as the standard deviation of runoff divided by mean runoff, for the 11 drainage basins, as calculated by Wang et al., (2014) compared to the mean geomorphic indices for the drainage basin, where slope is greater than 20°. Error bars represent the maximum and minimum geomorphic indice values.

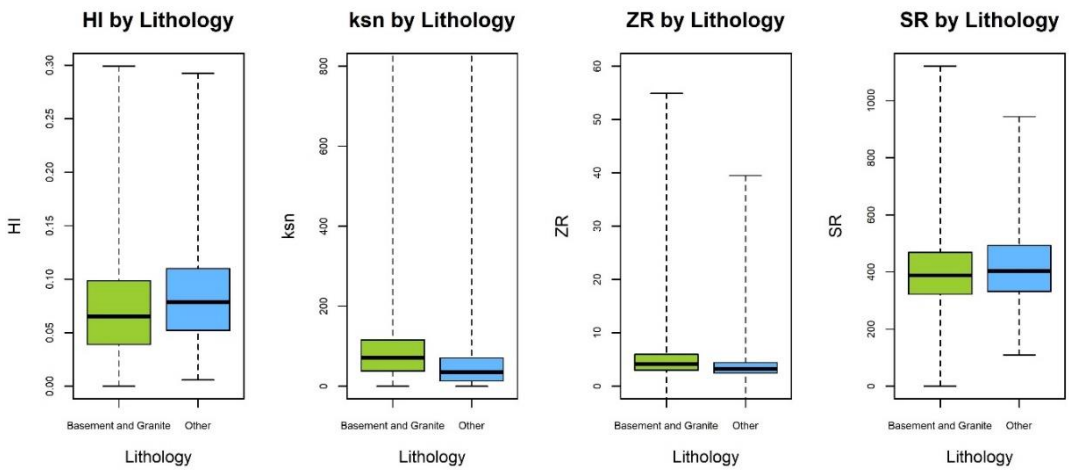

Figure 2.22: Boxplots showing the distribution of geomorphic index values, for areas of basement and non-basement lithologies. Basement rocks are distributed across the Qilian Shan, including areas of active channels and active faulting and areas with no active faulting. The non-basement rocks are largely non-crystalline. Mean values (not plotted) are near identical (HI 0.06 and HI 0.05; k_{sn}79 and k_{sn} 54; ZR 10 and ZR 20; SR 10 and SR 8) for basement and non-basement respectively. The results show that the rock type has little control on the landscape in the Qilian Shan.

south of our area of study and therefore concluded that precipitation is not the main control on geomorphological evolution. My finding that precipitation does not exert a major control on landscape despite a five-fold difference along the Qilian Shan therefore seems to be robust and in line with previous studies. This result is of interest as many studies in other regions conclude that precipitation is a major control on geomorphology (e.g. Ferrier et al., 2013; D'Arcy and Whittaker, 2014; Han et al., 2015). The key point of difference may be the relatively low rates of precipitation in the Qilian Shan, compared with regions in previous studies.

The underlying lithology of the area can also potentially influence landscape. Figure 2.20.a shows the distributions of Precambrian basement and granite (Y. Zhang et al., 2017), in comparison to the pattern of HI. In terms of erodibility, these lithologies are the most resistant to erosion, compared to other lithologies in the area (Moosdorf et al., 2018). Basement and granite outcrops are coincident with a range of values of the geomorphic indices and geomorphic index values overlying these lithologies are near identical to those for all other lithologies (Figure 2.22). This suggests that lithology is not a major control on changes in HI and the other geomorphic indices. Changes in values across thrust faults (Section 4.1) are therefore attributed to changes in uplift rates and their consequences, rather than lithological changes. Comparison of underlying lithology and precipitation with channel steepness for major rivers in the northern Qilian Shan by Hu et al. (2010) also shows no relationship between them.

2.4.3 Underlying Structure and Geomorphic Indices

As precipitation and underlying lithology are not controlling the geomorphic index values, the results can be analysed in terms of tectonic control. Overall, the results of this study highlight active thrust faulting, with stepped increases in index values across the thrust faults. In general, thrust faults in the north of the Qilian Shan dip to the south and thrust faults in the south dip to the north. There is also a south-to-north increase in HI and k_{sn} coincident with the Haiyuan Fault. This increase is statistically significant (p value < 0.05) as calculated by a t-test on a moving area of 60 x 60 km, the extent of which is shown in Figure 2.23. A t-test was used as the data were shown by Q-Q plots to be normally distributed. 60 km was chosen, as this is the crustal thickness (Tian and Zhang, 2013) and a wide (larger than 60 km), straight section of the fault was selected to give a representative region. This area was also selected as this is within the area where geodetic data was modelled by Allen et al., (2017). The best fitting lines, with the highest t-value, are shown to be within 2.5 km of the Haiyuan Fault in this area.

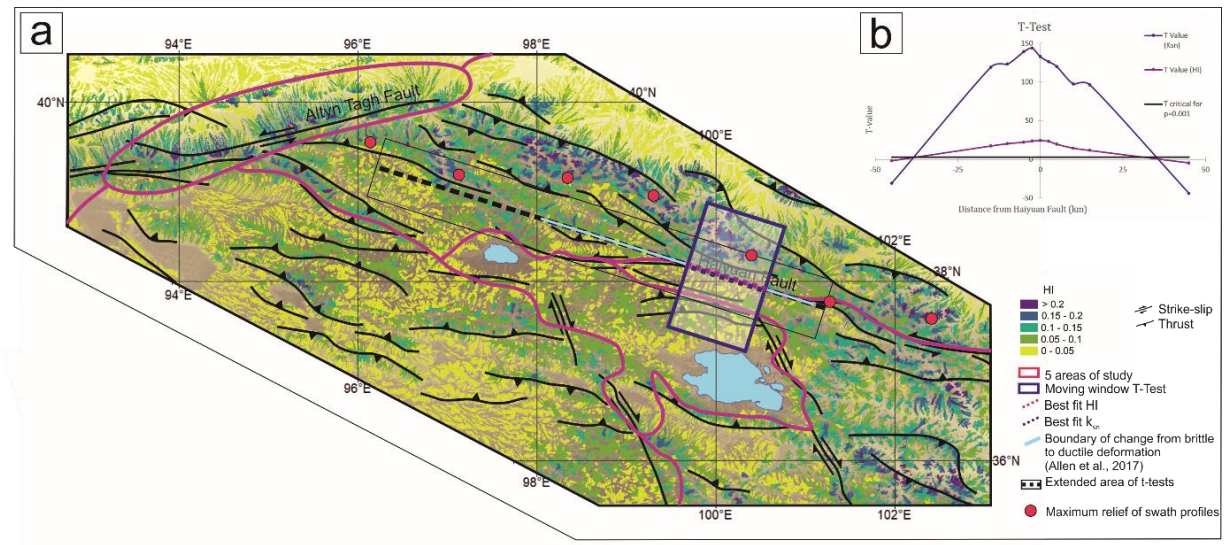

Figure 2.23: a) The moving window t-test in b) is calculated over the area in the purple box and shows the greatest change in values to occur across the Haiyuan Fault. The pale blue line represents the width of the region of geodetic data used in the model of Allen et al., (2017), with the line representing a change from locked to creeping deformation on an underlying detachment. A second t-test across the width of the Qilian Shan, 550 km wide (black line) indicates that HI and K_{sn} is distinctly higher in the north of the region than the south, suggesting that the locked-creeping transition extends across the region. The location of maximum relief, calculated from the swath profiles in Figure 2.16, is shown to occur to the north of this black line. b) Results of the moving window t-test, showing the largest change in HI and K_{sn} to be within 2.5 km of the Haiyuan Fault, with the location of the change shown with the coloured lines in a).

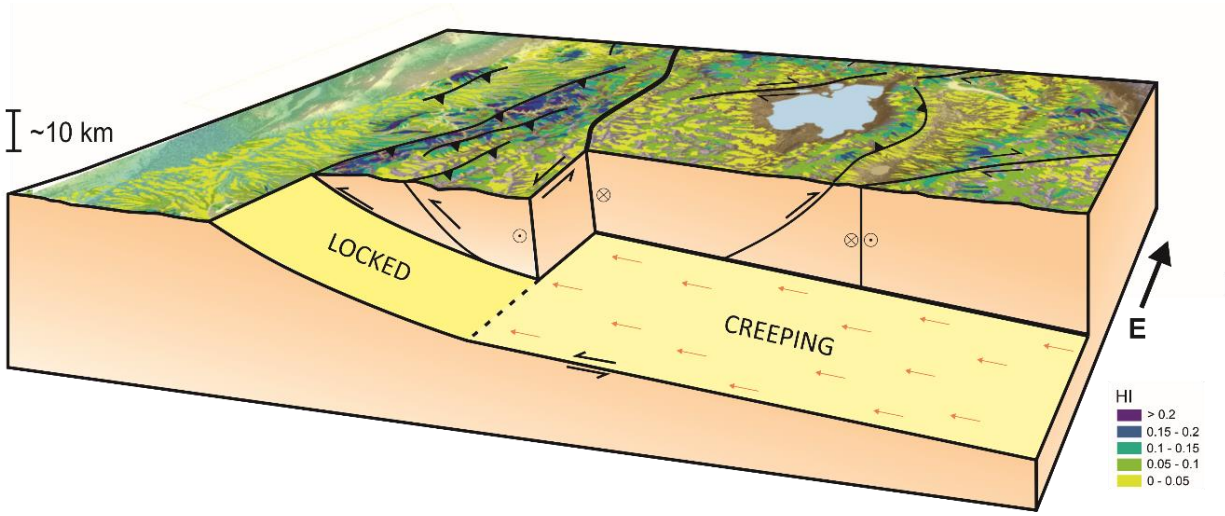

Figure 2.24: Schematic diagram showing inferred structure of Qilian Shan, underlain by a southwards-dipping detachment. A transition from locked to creeping behaviour is coincident with the location of the left-lateral Haiyuan Fault (Allen et al., 2017). This change is also coincident with the statistically significant change in our calculated surface indices, showing these results to be sensitive to underlying tectonics. The colours and values shown are the HI from Figure 2.12.

This distinct change in values of geomorphic indices from south to north across the Haiyuan Fault does not represent the location of maximum relief. The location of maximum relief for each of the 7 swath profiles (Figure 2.23.a) shows the location the maximum value of the maximum-minus-minimum swath. These maximum relief values occur to the north of the Haiyuan Fault transition. The geomorphic index change is also coincident with the restraining bend of the Haiyuan Fault, but the change is seen to extend beyond this region and therefore the restraining bend cannot account for the regional pattern of geomorphic indices.

The abrupt change in geomorphic indices across the Haiyuan Fault may be due to drainage patterns, as drainage divides are reflective of boundary conditions. The drainage divide between the northern-draining and east-draining region is controlled by the strike-slip Haiyuan Fault. This drainage divide is therefore coincident with the change in geomorphic index values and could be the cause of the change in geomorphic indices across the fault. However, I argue that as the drainage divide is between two externally-drained regions there should not be a large variation in index values. I would expect the largest change in values to be further to the south, between the Eastern region that drains into the Yellow River and the internally drained Central region, but there is no significant change in values across this boundary.

Uplift on inward-dipping thrust faults is consistent with the Qilian Shan having an overall flower structure at upper crustal levels (Yin et al., 2008 ; Pang et al., 2019), with wider regions of high HI, SR and k_{sn} in the north than the south possibly due to higher strain on the northern margin (Zuza et al., 2016). However, this model would not produce the observed change in values across the Haiyuan Fault and therefore does not fully explain the geomorphic signals seen at the regional scale. This model is also not consistent with the locked-creeping transition identified by analysis of geodetic data in the area by Allen et al., (2017).

The patterns of the geomorphic indices are consistent with inward-dipping thrust faults, rooting onto a south-dipping detachment thrust (Meyer et al., 1998; Allen et al., 2017). The overall higher values of HI, k_{sn} and SR in the north of the Qilian Shan could represent higher uplift rates at the steepest portion of the detachment thrust, which is suggested to occur in this region (Hetzel, 2013). However, due to the statistically significant change in HI and k_{sn} values across the Haiyuan Fault, calculated by the moving window t-test, I suggest that the increased HI and k_{sn} values to the north of the fault relate to the transition from the up-dip limit of creep on the underlying detachment thrust, as suggested by Allen et al. (2017) on the basis of elastic dislocation modelling of GPS data. They proposed that the left-lateral, strike-slip Haiyuan Fault marks the surface boundary of the transition from oblique creep below the seismogenic depth (~26 km) on a south-dipping

detachment, to partitioned strike-slip and thrust faulting above i.e. from seismogenic faulting in the upper crust to ductile deformation below it. (Figure 2.24). This work constrains the geometry of the detachment, but not of the other faults in the area. The structure shown in Figure 2.24 is schematic, but is consistent with the geomorphic indices of this study.

Geodetic data was modelled by Allen et al (2017) from a wider region than that of the t-test (pale blue line, Figure 2.23), but sparse data meant that the analysis was not extended further to the east or west. A second t-test, over a 550 km extent of the Qilian Shan, of 30 km width, reveals the pattern of high values to the north of the black dashed line (Figure 2.23) and lower values to the south (p value < 0.05) to be continuous across the Qilian Shan. High values in this area partially correspond to the hanging wall of a thrust fault, but the pattern of high values to the north is not confined to this region. The geomorphic indices therefore suggest that the transition from locked to creeping deformation may extend across the area, not just in the region of the Haiyuan Fault. I suggest the change from locked to creeping can be said to be partially coincident with the Haiyuan Fault. The use of geomorphic indices, which can be calculated across the whole range, is therefore used to infer a continuation of the structure predicted by the geodetic analysis, where GPS data were too sparse.

Assuming deformation on an underlying detachment, the central portion of the Qilian Shan, where the statistically significant value changes are coincident with the Haiyuan Fault (HI from < 0.05 to > 0.1, k_{sn} from < 20 to > 75), is shown to be deforming remarkably simply under oblique convergence conditions. The deformation mechanism is more complicated to the west, where the change is to the north of the Haiyuan Fault, but a plateau morphology is still forming (Figure 2.16). This is likely to be due to internal drainage, with erosion on steep slopes and deposition within the basins creating a flatter landscape. The western margin is also deforming more complexly, due to strike-slip movement of the Altyn Tagh Fault deflecting structures and to some degree controlling the location and intensity of thrusting within the interior of the Qilian Shan (Meyer et al., 1998; Cheng et al., 2015). The historical earthquake record is also consistent with an underlying detachment. The locked-creeping transition is the likely southern limit for the largest earthquakes in the range (Allen et al., 2017) and therefore to the north of the Haiyuan Fault there is likely to be more seismic-induced landsliding, promoting high HI, SR and k_{sn} values and low ZR values. It is notable that the only *M* ~7 earthquakes recorded in the Qilian Shan are historic events along the northern margin of the range (Xu et al., 2010), or along the Haiyuan Fault (Gaudemer et al., 1995). Such major earthquakes may dominate the erosion budgets of the region, by analogy with other seismically active areas such as Taiwan (Dadson et al., 2003; Xu et al., 2010) although only a weak positive

correlation was found with erosion rate and accumulative seismic moment in the northern Qilian Shan (Wang et al., 2014b). This may be due to lower precipitation in the Qilian Shan meaning that landslide mass is not transported out of the basins as rapidly as in Taiwan, or because the 60 year time period used for the seismic moment did not include any earthquakes with $M_W \geq 7$. Above the creeping portion of the fault earthquakes and seismic-induced landsliding are less likely to occur, with more constant uplift, leading to flatter landscapes with higher ZR values.

The geomorphic indices are sensitive to drivers on a tectonic scale, showing the effect of the deep structure on the surface morphology. The results provide independent support for slip partitioning on an underlying detachment at depth, underneath the Haiyuan Fault (Allen et al., 2017; Bowman et al., 2003; Figure 2.24), while also confirming the development of lower relief, plateau-like landscape in the interior of the Qilian Shan (Liu-Zeng et al., 2008).

Application of the geomorphic indices in this study, combined with geodetic data analysis, to other fold-and-thrust belts can be used to assess whether the area is underlain by a detachment thrust e.g. Himalaya (Stevens and Avouac, 2015) or a set of individual thrust faults e.g. Zagros fold-and-thrust belt (Allen et al., 2013). This analysis is carried out in Chapter 4. It is predicted that the Himalaya and similar "detached" systems should be similar to the Qilian Shan, in terms of a geomorphic transition above the underlying change from creeping to locked thrust behaviour. More distributed systems, like the Zagros, should lack such a geomorphic transition.

2.5 Conclusions

The east-west precipitation gradient of the Qilian Shan, which is orthogonal to the direction of shortening, provides an opportunity to assess the effect of precipitation on geomorphic indices in this area: precipitation is shown to not have a first order control on landscape. This result shows that a larger precipitation variation than the ~50 mm/yr to ~650 mm/yr variation along the Qilian Shan is needed to see an effect of precipitation on landscape, given the other parameters for this region such as strain rate, finite strain and landscape maturity (see Henck et al., 2011). Lithology variations are also not a first order control on landscape evolution.

The pattern of high HI, k_{sn} and SR in the hanging walls of the inwardly-dipping thrust faults and to the north of the left-lateral Haiyuan Fault is consistent with shortening on an underlying south-dipping detachment thrust, which changes behaviour from creeping to locked at the location of the Haiyuan Fault, as suggested by Allen et al., (2017). The geomorphic indices suggest this shortening mechanism to also be operating further to the west of the Haiyuan Fault , across the width of the

Qilian Shan, in an area with sparse GPS data, showing how the geomorphic indices can help our understanding of less accessible or less well monitored areas. The geomorphic indices used are sensitive to the underlying tectonic structure of the area and provide independent support for this structure, which was previously defined by modelling of geodetic data. The geomorphic changes across the Haiyuan fault and published geodetic analysis of Allen et al., (2017) do not support the idea that the Qilian Shan operates now as a flower structure (Pang et al., 2019), but does not rule out such a scenario operating at previous times.

These geomorphology approaches and in particular the combination with geodetic modelling, are used in Chapter 4 to assess how processes and structures vary among different fold-and-thrust belts and tectonic settings. In particular, this work aims to test the potential for differences between landscapes of fold-and-thrust belts where an underlying thrust detachment has been recognised, such as the Himalaya (Stevens and Avouac, 2015) and where this structural style may not apply, such as the Zagros (Allen et al., 2013).

Chapter 3: Monsoon-driven Incision and Exhumation of the Eastern Tibetan Plateau

3.1 Introduction

The relative importance of tectonic and climatic control on mountain building and geomorphology is widely studied and debated (e.g. Whipple, 2009; Godard et al., 2014). The Tibetan Plateau, formed by the India-Eurasia collision, is the largest and highest elevation plateau on the earth but the surface uplift mechanism is debated (e.g. England and Houseman, 1988; Magni et al., 2017). The Tibetan Plateau has affected both local and global climate systems and contributed to the formation of the Asian monsoon systems and central Asian deserts (An et al., 2001; Miao et al., 2012). In this chapter, I identify a spatial change in landscape in the central-eastern Tibetan Plateau and relate this to a spatial change in precipitation, erosion rates and exhumation. I suggest that this provides evidence for Pre-Miocene plateau growth followed by monsoon-driven incision.

The timing of formation of the Proto-Tibetan Plateau occurred from 55-35 Ma, with the central plateau gaining its present elevation of ˜5000 m and 70 km crustal thickness (Wang et al., 2008; C. Wang et al., 2014). Evidence for this includes paleo-elevation studies, rapid cooling between 85 and 43 Ma in central Tibet followed by slow cooling (Rohrmann et al., 2012) and evidence based on regional geology (Kapp et al., 2003; Kapp et al., 2007). Palaeoaltimetry studies give insights into the evolution of the plateau but give varied results. For example, Rowley and Currie (2006) used $\delta^{18}O$ of Cenozoic carbonate sediments to show that the central plateau was at over 4000 m elevation since at least 35 Ma. B. Sun et al., (2015) suggested a much lower Miocene elevation in the central Tibetan Plateau, using an early Miocene fossil leaf physiognomy, with 2-3 km surface uplift in the last 17 Myr. Overall, there is a consensus that the surface elevation of the central and southern Tibetan Plateau was > 4000 m by as early as the Eocene (Kapp and DeCelles (2019) and references within). There was a deceleration in erosion rates in the central plateau in the Mid-Eocene (Hetzel et al., 2011; Rohrmann et al., 2012), which Han et al., (2019) attributed to the initiation of internal drainage in the region. In the Early Miocene vast interconnected systems (>150 000 km^2 area) of internally drained lakes extended across the central Tibetan Plateau over the modern internally-drained area and extended eastwards to ˜98° (Wu et al., 2008). Deposition in lakes in the area began at ˜23.5 Ma and ended before 13.5 Ma, as evidenced by field relations, fossils, magnetostratigraphy and Ar-Ar and K-Ar dating (see Wu et al., 2008), with little deformation since this time. Analysis of sedimentary successions near to the modern internal-external drainage divide suggest that the area has been internally drained since ˜35Ma and became flat in the Early

Miocene (˜23Ma), sustaining this low relief until the modern day (Han et al., 2019). The elevation history of the southern and eastern Tibetan Plateau is harder to define (e.g. Shen and Poulsen, 2019) but there are multiple suggestions of high elevations by the Miocene in the south eastern (S. Li et al., 2015; Hoke et al., 2014) and eastern Tibetan Plateau (Xu et al., 2016).

The south eastern margin of the Tibetan Plateau has a relatively gradual topographic transition from the high elevation plateau interior to the steep front at the Longmen Shan (Figure 3.1), compared to the other Tibetan Plateau margins. The formation mechanism of the active plateau margin is debated, with two major hypotheses. The first is the suggestion that pre-Miocene growth of the Tibetan Plateau to near present-day extent and elevation occurred (Figure 3.2). This may have formed by crustal shortening and thickening and surface uplift, following the initial India-Eurasia collision (Tapponnier et al., 2001). The east and southeast plateau margin is then suggested to have undergone relief reduction and retreat (Liu-Zeng et al., 2008). Evidence for this model includes thermochronological ages in the eastern plateau, which are older than the Miocene (Liu-Zeng et al., 2018), geological evidence of a long-lived margin in the area of the present-day Longmen Shan (Tian et al., 2016) and evidence of rapid denudation in the Sichuan Basin beginning in the Eocene-Oligocene (˜40-35 Ma) caused by incision of the Three Rivers/Gorges region driving incision into the plateau (Richardson et al., 2008). The second major model is the channel flow model (Figure 3.2) which suggests a late phase (12-10 Ma) of crustal thickening, surface uplift and plateau growth driven by lower crustal flow outwards from the central plateau (Clark and Royden, 2000). Lower crustal flow is suggested to occur due to lateral pressure gradients within the crust after crustal thickening of the Proto-Tibetan Plateau. This model suggests that prior to 12 Ma low relief landscapes formed at low elevations at the present-day eastern plateau margin. Evidence for this model includes: the identification of remnant plateau surfaces in interfluves in eastern Tibet ("relict landscapes" of Clark et al., 2004; 2006; Figure 3.1b); the landscape not having equilibrated to regional uplift (Clark et al., 2004) and low-temperature thermochronology studies showing increased river incision and rapid exhumation since the late Miocene, between 8-13 Ma (Clark et al., 2005; Ouimet et al., 2010). However, further studies have now suggested an Oligocene to Miocene initiation of river incision (Shen et al., 2016; Tian et al., 2014a).

The central Tibetan Plateau is characterised by a high elevation, low relief landscape which is internally drained (Figure 3.1a), with river systems draining into lakes of the central plateau. River systems draining the southeastern Tibetan Plateau include the major Salween, Mekong and Yangtze rivers. Active faulting in the eastern Tibetan Plateau is largely strike-slip and trends largely NW-SE (Figure 3.1a), near-parallel to the modern-day river systems. In the central plateau, normal

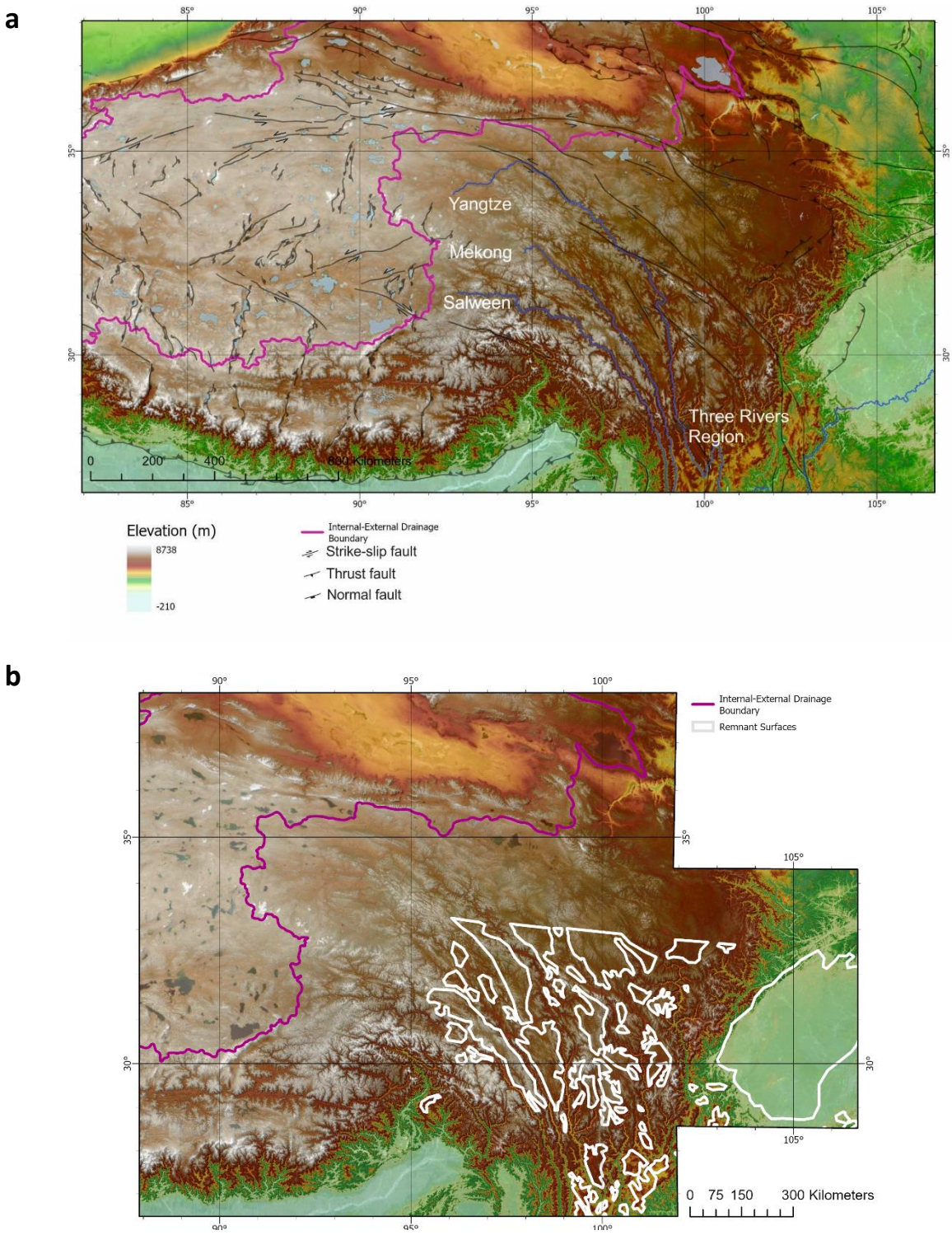

Figure 3.1: a) Map showing the study area of this work. The major channels of the major rivers draining the plateau are shown in blue. The purple line shows the boundary between the internal and external drainage. Major faults of the area are shown. b) Map showing the outlines of the "remnant surfaces" identified by Clark et al 2004, 2006 in the interfluves in the south easter Tibetan Plateau.

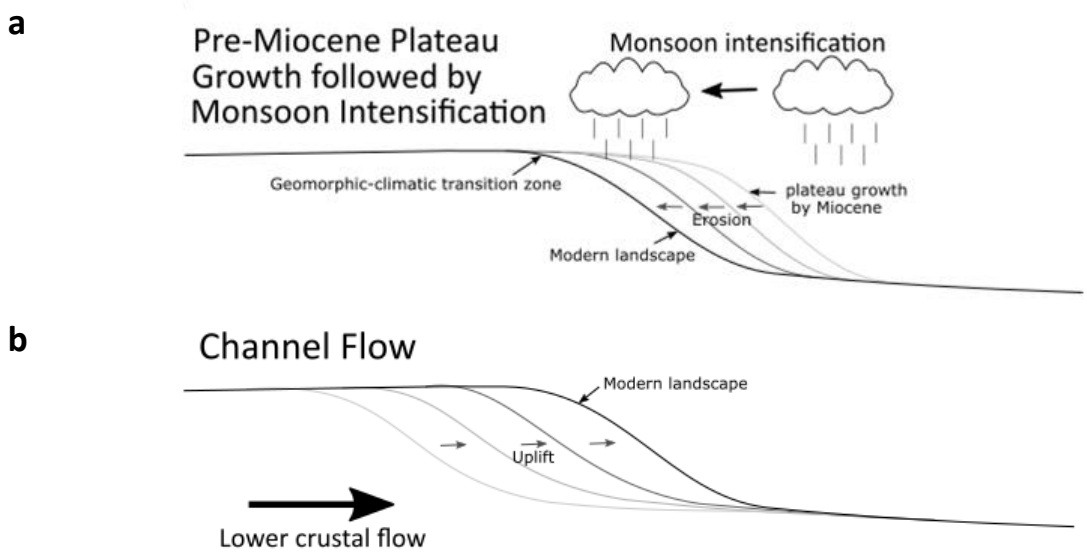

Figure 3.2: a) Simple sketch showing a model of plateau growth followed by monsoon intensification. This model suggests pre-Miocene growth of the plateau, followed by east-to-west erosion of the landscape due to fluvial erosion driven by increased monsoonal precipitation. The landscape transition identified in this study is the western limit of monsoon-driven incision. b) Simple sketch showing the channel flow model of Tibetan Plateau uplift. This model suggests an outward growth of the plateau due to lower crustal flow.

faulting trends ˜NNE-SSW. Extension was initiated in the mid Miocene (14 - 8 Ma), with a change from crustal shortening to extension in the central plateau (Blisniuk et al., 2001; Y. Li et al., 2015). Terrane boundaries caused by Mesozoic collisions trend ˜E-W and define first order tectonic boundaries in the plateau region (e.g. Zhu et al., 2013).

The modern climate of central Asia is strongly seasonal, with the margins of the Tibetan Plateau trapping moisture from the Pacific and Indian Oceans, forming the East Asian Monsoon and the South Asian Monsoon respectively (Saylor et al., 2009). Strong continent-scale circulation leads to increased summer monsoon precipitation, due to latent and sensible heating focused on and over the slopes of the high plateau (Kutzbach et al., 1993; An et al., 2001). The high mountains of the Himalaya cut off moisture transport from the Pacific and Indian Oceans, leading to the arid climate of the Tibetan Plateau interior (Miao et al., 2012) and moisture in this region is transported from westerlies (Dong et al., 2017). Tibetan Plateau uplift and climate systems are related. Many studies show that Tibetan Plateau growth controls monsoon intensity by influencing atmospheric circulation and precipitation due to an increased land-sea thermal contrast and increased pressure gradient (R. Zhang et al., 2015; Liu and Yin, 2002).

Analysis of vegetation changes in the central Tibetan Plateau suggest a change in climate from warm and dry in the Oligocene, to become colder and higher elevation throughout the Miocene

and into the Early Pliocene (Wu et al., 2008). The climate of East Asia in the Paleogene was characterised by a latitudinally zonal climate (Guo et al., 2008). The onset of a strong monsoonal system during the Early Miocene was followed by generally decreasing temperature and precipitation, related to global cooling and linked to Antarctic glaciation (Ao et al., 2016; Zhang et al., 2018; Nie et al., 2017). The Mid-Miocene Climatic Optimum (MMCO), from 17-14 Ma was characterised by a warm climate and enhanced East Asian Summer Monsoon precipitation with large variability (Guo et al., 2002; 2008). The highest CO_2 levels in the past 20 Ma were at this time (Tripati et al., 2009; Zachos et al., 2001). There was increased summer monsoon precipitation in stage HT3 in the Late Miocene (An et al., 2001).

Many thermochronology studies have been carried out in the central and eastern Tibetan Plateau, with much focus on the Longmen Shan region. Data are sparser in the less accessible plateau interior. Studies located within major river valleys and those away from the valleys give complementary information. These data can be considered separately or can be considered together to give information on regional tectonic exhumation. Thermochronology studies of the eastern Tibetan Plateau suggest an increase in exhumation over time, which is likely to be due to incision of the rivers. Erosion rates in the area have been studied using cosmogenic nuclides. The Tibetan Plateau interior experiences low erosion rates (<0.037 mm/yr; Li et al., 2014) with Strobl et al., (2012) finding lower rates in stable peneplains (mean = 0.008 mm/yr) than in the plateau interior rivers (mean = 0.018 mm/yr). The east Tibetan Plateau margin experiences higher erosion rates (˜0.3 – 1 mm/yr; Liu-Zeng et al., 2011; Godard et al., 2010; Ouimet et al., 2009) and intermediate rates at the northern margin at the Kunlun (< 0.1 mm/yr) which may be lower than the eastern margin due to the drier climate (Li et al., 2014). Erosion rate has been locally correlated to channel steepness (Harkins et al., 2007) and rock uplift (Henck et al., 2011).

The landscape of the region has been studied using geomorphological methods. Liu-Zeng et al., (2008) studied the landscape of the entire Tibetan Plateau and its margins using analysis of elevation data, surface relief and slope and from this suggested that the evolution of the river systems in the area have shaped the plateau. For example, they suggest that the high elevation, low relief landscape of the plateau interior is formed by the erosion of tectonic-related relief and by deposition into internally drained basins. The south eastern margin of the plateau is suggested to have formed in this manner and subsequently have been dissected by headward retreat of externally drained rivers. Other studies of tectonic geomorphology in the central and eastern Tibetan Plateau are more regionally focused. In the Three Rivers region in the southeast of the main plateau, erosion rates were found to correlate with high elevations and high channel steepness of

the Mekong and Salween rivers (Yang et al., 2016) but were found to correlate more strongly to rock uplift rates than to landscape relief or precipitation (Henck et al., 2011). Channel steepness shows a non-linear relationship with erosion rates in the eastern margin of the Tibetan Plateau, whereas hillslope steepness and erosion rates show a non-linear relationship up to a slope-stability related threshold. This suggests that channels drive the landscape adjustments to base-level fall (Ouimet et al., 2009). Channel steepness was also seen to reflect rock uplift rather than slip distribution following the 2008 Wenchuan Earthquake (Kirby and Ouimet, 2011). In this study I use tectonic geomorphologic indices over the entire central and eastern Tibetan plateau to identify spatial changes. Results are then related to spatial changes in precipitation, erosion rates and exhumation. I use this comparison to assess the Late Miocene channel flow mechanism and the Pre-Miocene early growth mechanism of eastern Tibetan Plateau topographic formation (Figure 3.2). The results provide evidence for Pre-Miocene plateau growth followed by monsoon-driven incision.

3.2 Methods

The analysis focusses on the Eastern Tibetan Plateau, from the internally drained central plateau, to ˜105° E. 3 arc second SRTM data are used throughout this work. Precipitation data are mean annual precipitation in mm, taken from the Global Precipitation Mission (GPM) IMERG dataset from 2000 to 2018 (Figure 3.3). In each case, the geomorphic indices were calculated for second Strahler order drainage basins. Drainage basins are natural boundaries between areas of different uplift and erosion characteristics and therefore by calculating geomorphic indices by drainage basin we avoid smoothing values over features such as faults and drainage divides. Basins were extracted from SRTM data based upon a stream network calculated with a threshold of > 1 km^2 in order to exclude hillslopes from the analysis. Second order drainage basins were selected as these are found to provide the most detail, as they are large enough to exclude hillslopes from the calculation but small enough to minimise smoothing of data across the spatial variations (see Chapter 2 for more details, including on the methods described below).

3.2.1 Hypsometric Integral

The hypsometric integral (HI; Figure 3.4) describes the distribution of elevation within an area, in this case within each drainage basin. HI is the integral of a hypsometric curve, which is a plot of normalised elevation against normalised drainage area (Pike and Wilson, 1971). High HI occurs when the distribution of elevation within an area is skewed towards higher values and high HI

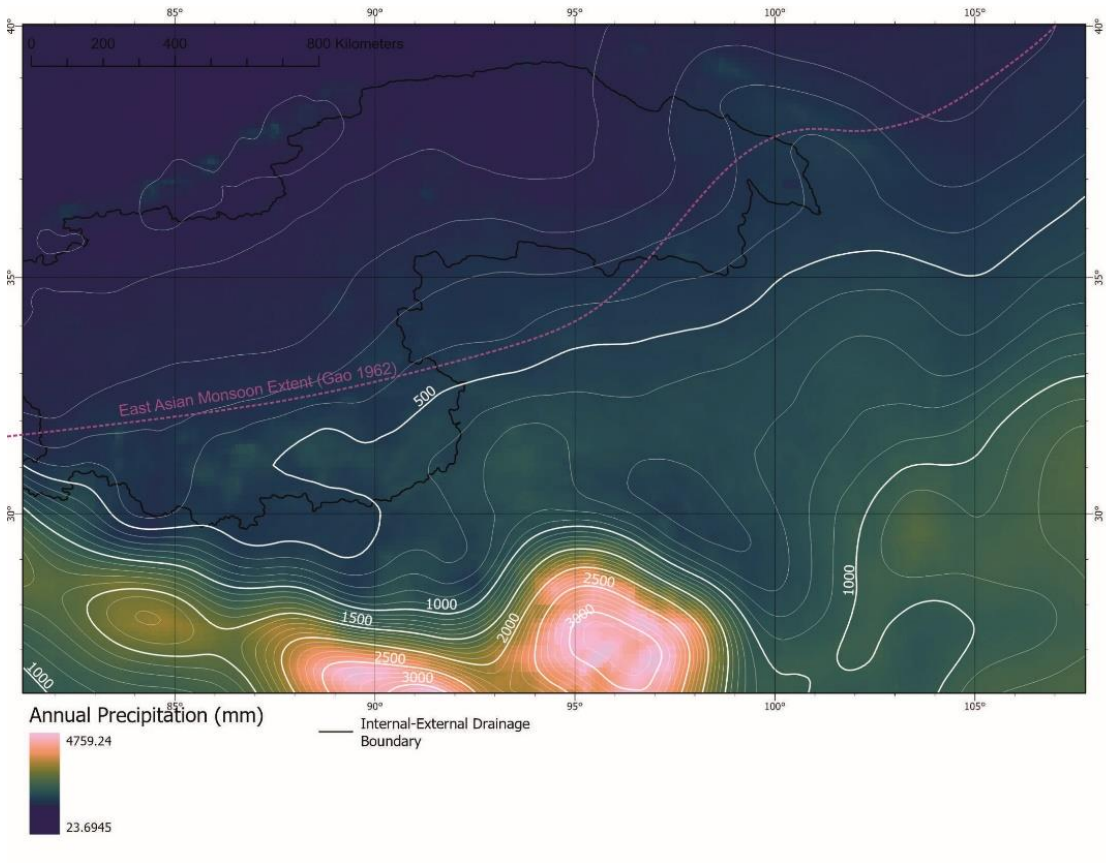

Figure 3.3: Map showing the precipitation across the Tibetan Plateau. The map shows the same spatial extent as Figure 3.1a. The internal-external drainage boundary is shown for reference. Data are mean annual precipitation for 2000-2018, taken from the GPM. Contours show the 100 mm intervals of precipitation and 500 mm intervals are shown in bold. The east Asian summer monsoon extent of Gao (1962) is shown.

typically indicates rapid uplift rates but can also be controlled by underlying lithology and precipitation. HI was calculated using TecDEM software (Shahzad and Gloaguen, 2011).

3.2.2 Surface Roughness

Surface roughness (SR; Figure 3.5) shows the variability of the topography (Grohmann et al., 2010). This is calculated as the standard deviation of slope within each drainage basin, as used in chapter 2. High SR represents a variable surface which may be due to rock uplift, or river incision.

3.2.3 Elevation-Relief Ratio

The elevation-relief ratio (ZR; Figure 3.6) is calculated for each drainage basin as:

$$ZR = \frac{Mean\ Elevation\ (m)}{Maximum\ Elevation\ (m) - Minimum\ Elevation\ (m)}$$

High ZR represents areas of both high elevation and low relief and therefore highlight plateau regions (Formento-Truglio and Pazzaglia (1998)).

3.2.4 Swath Profiles

Swath profiles condense data from a corridor onto a single profile. Seventeen profiles were drawn, of 100 km length and 30 km total width. Swaths are orthogonal to and centred on the internal-external drainage boundary (Figure 3.7), with 16 spaced evenly along this drainage boundary and 1 additional swath which was included to provide extra data in the data gap caused by outside bend of the drainage boundary (swath 3b; Figure 3.7). Mean values of elevation, precipitation, HI, SR and ZR are shown for each swath. Segmented linear regression of each profile was used to statistically define changes in trend across "breakpoints", shown by vertical lines (Figure 3.8). I set the number of breakpoints but the location of these was statistically defined and had no other manual input and could therefore be repeated by another user. The breakpoints highlighted by the vertical purple line are the breakpoints defining the change in trend of interest.

The trends of interest are those selected as highlighting a flat, plateau nature. These are, from east to west, a transition to high but not increasing elevation, a transition to low HI, a transition to low or decreasing SR and a transition to increasing ZR (Figures 3.9 - 3.13). These breakpoints were selected manually as the greatest change in trend of the multiple regression lines, to the trend of interest. A transition to decreasing precipitation is identified, which is interpreted to be the extent of the East Asian monsoon (Figure 3.13). The locations of these changes were mapped and a line of change drawn for each of the 5 variables, by manually connecting the breakpoints.

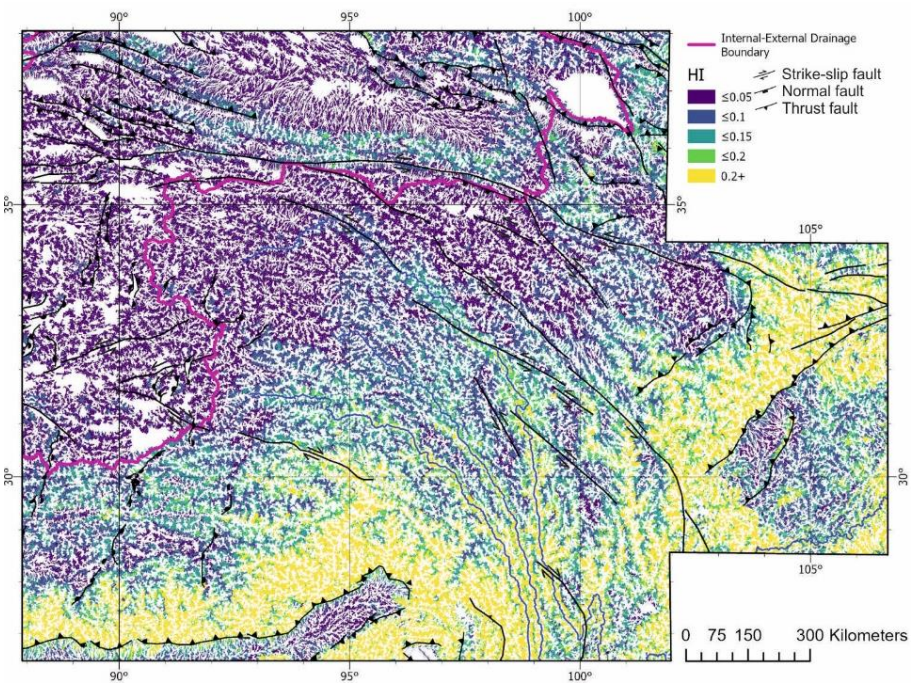

Figure 3.4: Map showing the hypsometric integral (HI) for second order drainage basins, across the plateau. The yellow colours show high HI meaning a large range of elevation within the drainage basin and the highest values occur at the plateau margin, in the regions of the Longmen Shan and Himalaya and along the major river valleys. The purple colours show low HI and are found in the internally drained region and to also to the east and south of the internal-external drainage boundary.

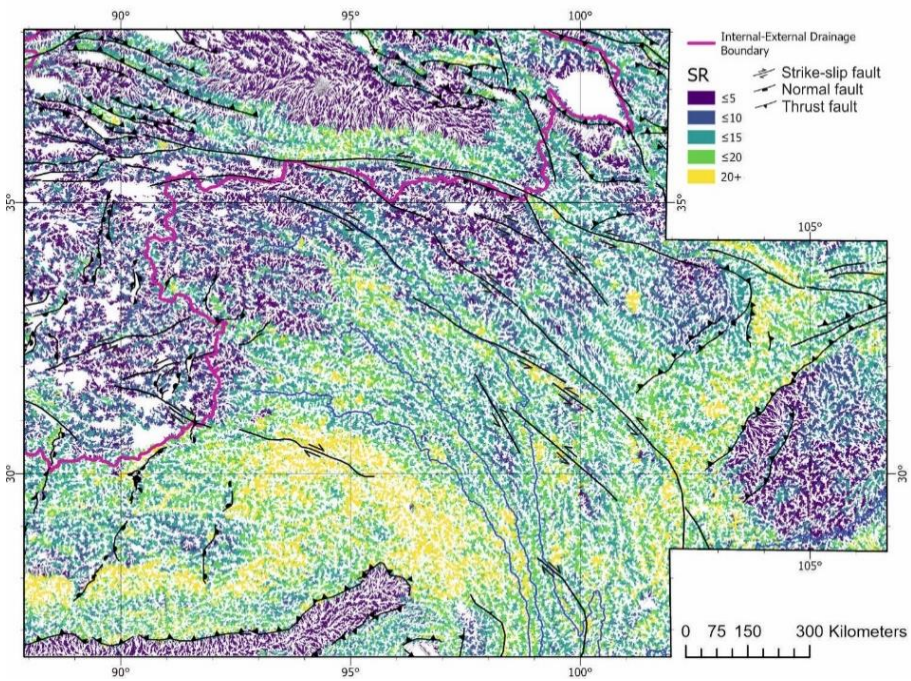

Figure 3.5: Map showing the surface roughness (SR) for second order drainage basins, across the plateau, calculated as the standard deviation of slope. The yellow colours show high SR meaning a rougher surface within the drainage basin and the highest values occur at the plateau margin, in the regions of the Longmen Shan and Himalaya and along the major river valleys. The purple colours show low SR and therefore a flatter landscape and are found in the internally drained region and to also to the east of the internal-external drainage boundary.

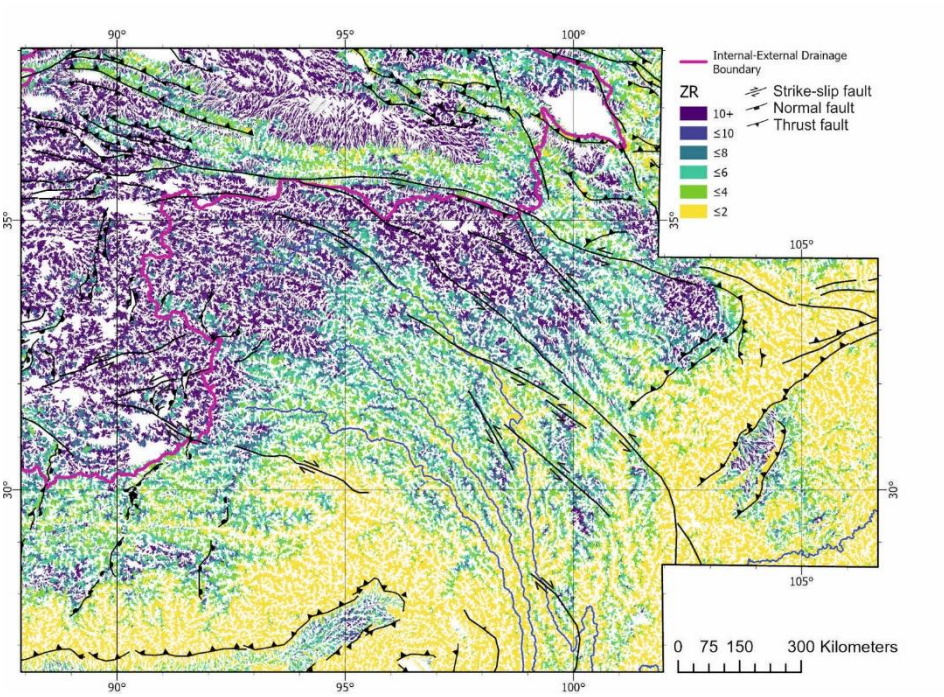

Figure 3.6: Map showing the elevation-relief ratio (ZR) for second order drainage basins, across the plateau. The purple colours show high ZR and therefore a flatter landscape and are found in the internally drained region and to also to the east of the internal-external drainage boundary.

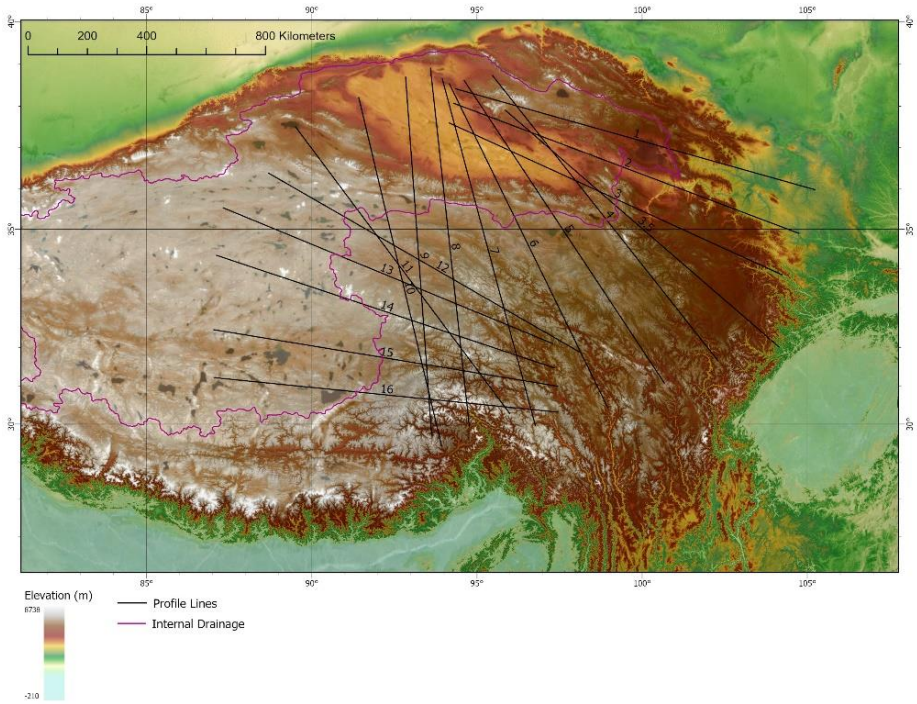

Figure 3.7: Map showing the location of the swath profiles drawn through the data. Each line represents the centre of the swath. The profiles are 30 km in width and 1000 km in length. They are centred and orthogonal to the internal-external drainage boundary shown in purple.

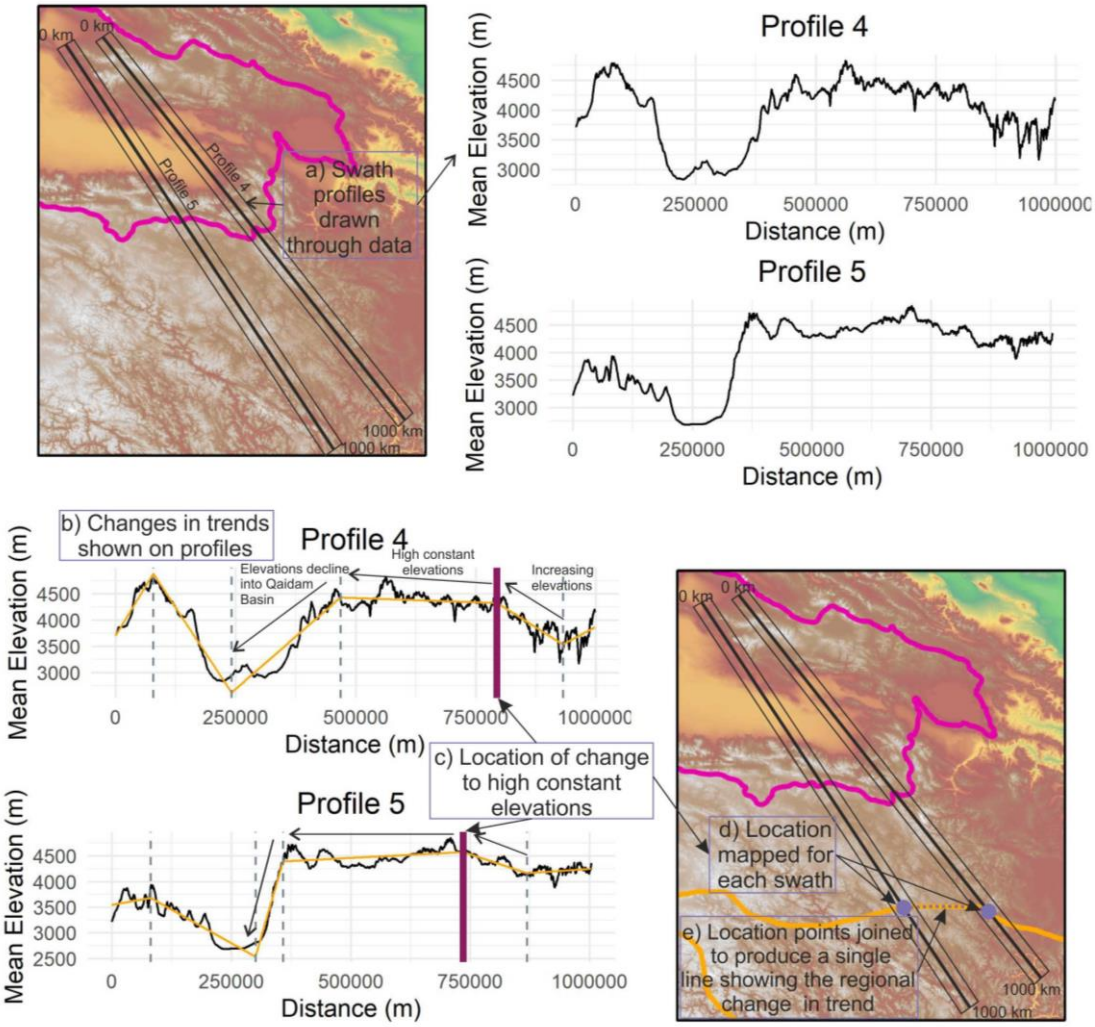

Figure 3.8: An annotated example of how the lines of change in the landscape are identified using swaths and then mapped. An example of identifying a change in elevation trend is shown. The process is the same for the geomorphic indices and precipitation data.

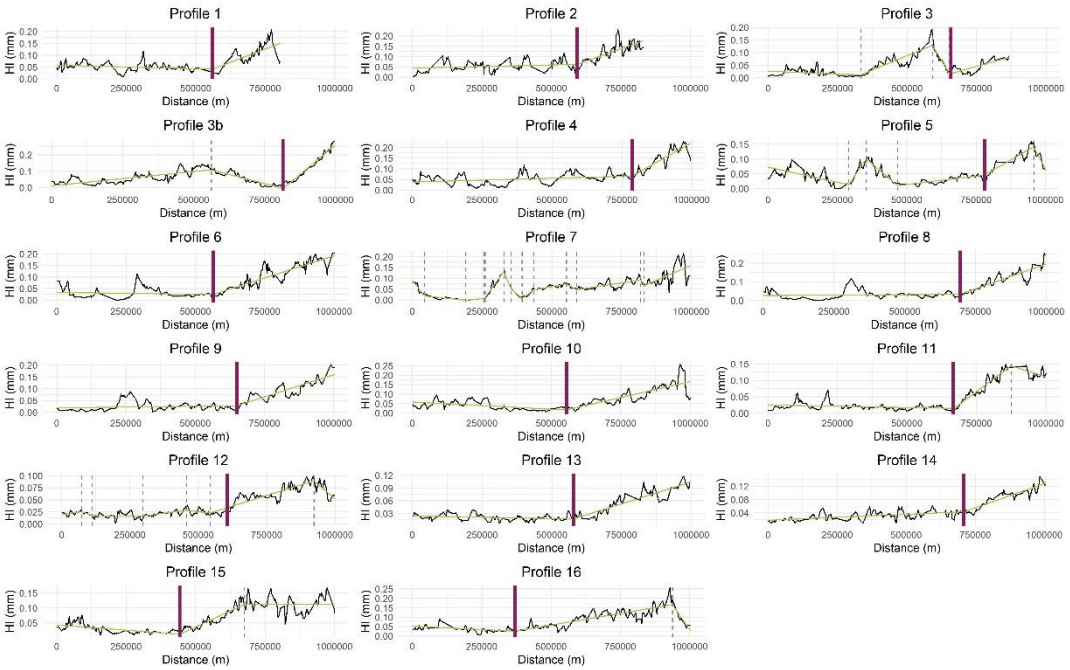

Figure 3.9: Swath profiles of mean HI taken from swath profiles of 1000 km length and 30 km width. The profiles are drawn from ˜NW-˜SE. The green line shows the multiple regression best fit lines and the vertical dashed lines the changes in trend. Low HI is seen in the central plateau and the purple vertical line marks the extent of low HI.

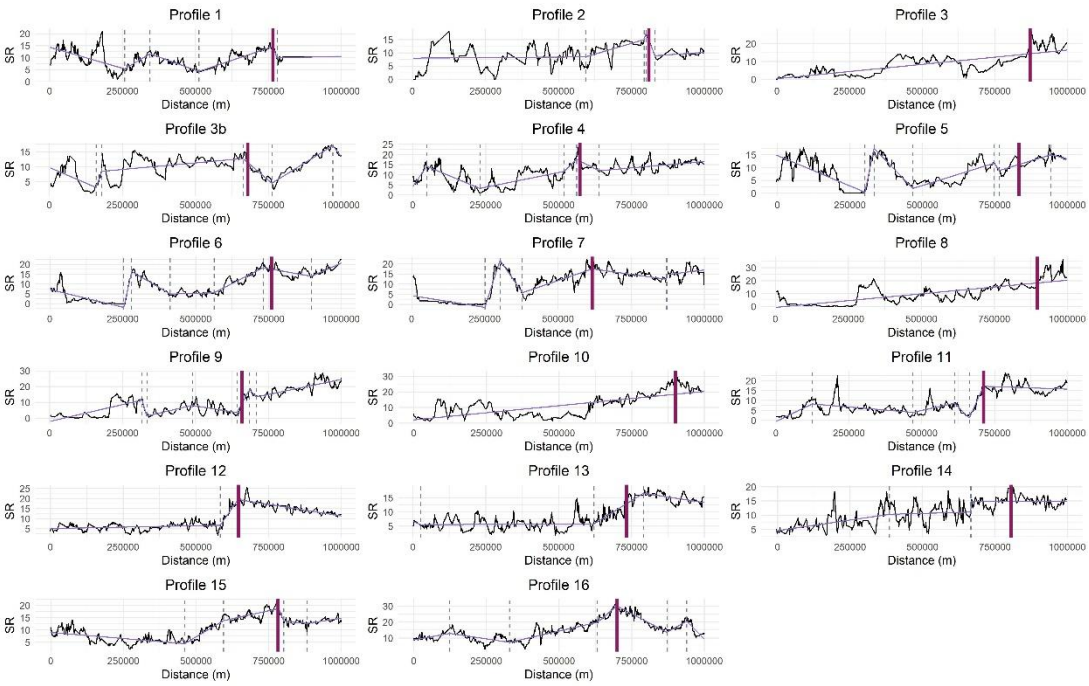

Figure 3.10: Swath profiles of mean SR taken from swath profiles of 1000 km length and 30 km width. The profiles are drawn from ˜NW-˜SE. The thin purple line shows the multiple regression best fit lines and the vertical dashed lines the changes in trend. Low SR is seen in the central plateau and the purple vertical line marks the extent of low SR.

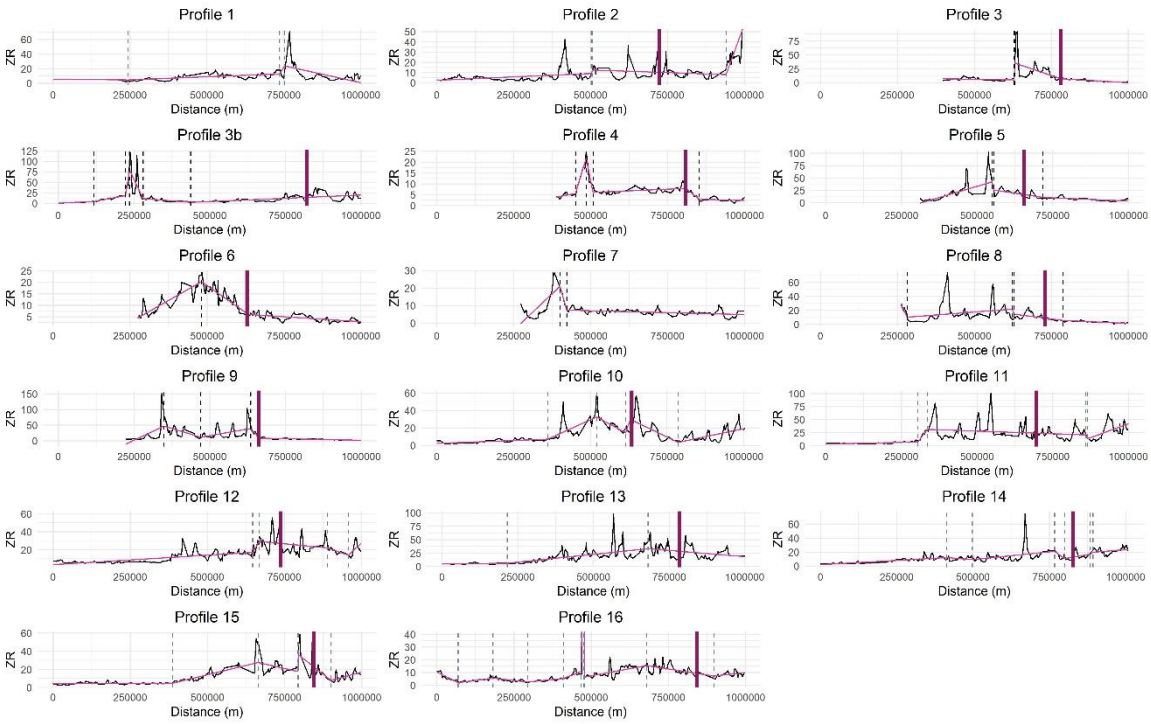

Figure 3.11: Swath profiles of mean ZR taken from swath profiles of 1000 km length and 30 km width. The profiles are drawn from ˜NW-˜SE. The thin pink line shows the multiple regression best fit lines and the vertical dashed lines the changes in trend. High ZR is seen in the central plateau and the purple vertical line marks the extent of high ZR.

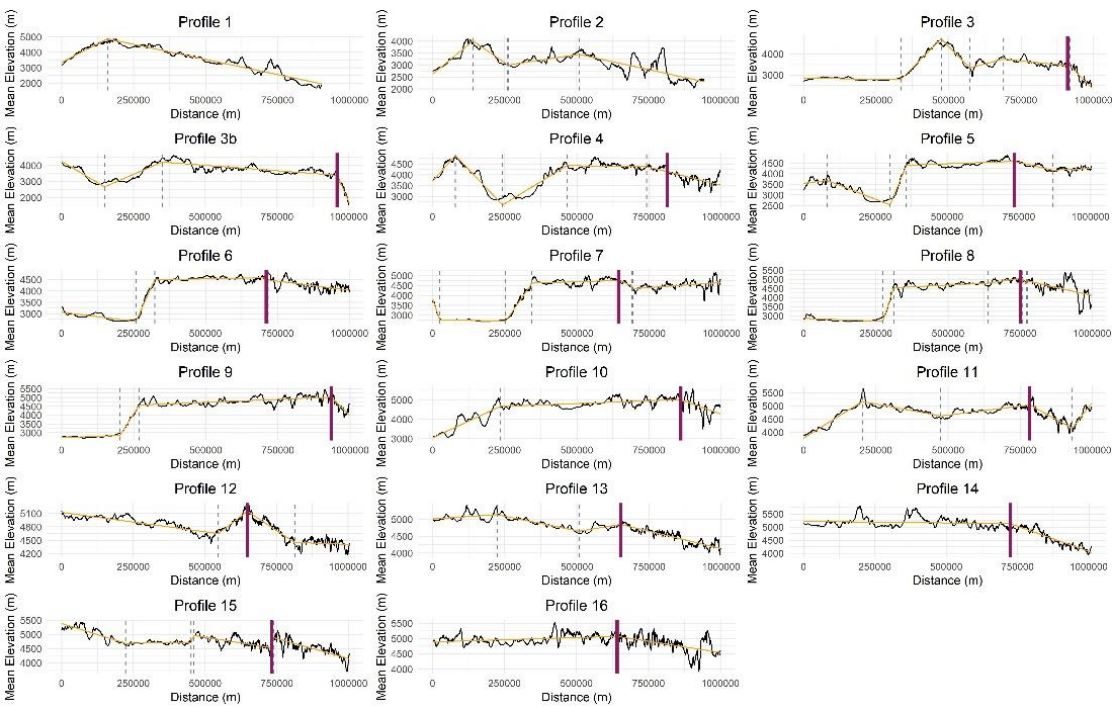

Figure 3.12: Swath profiles of mean elevation taken from swath profiles of 1000 km length and 30 km width and from the 90 m SRTM data. The profiles are drawn from ˜NW-˜SE. The yellow line shows the multiple regression best fit lines and the vertical dashed lines the changes in trend. High elevation and flat topography is seen in the central plateau and the purple vertical line marks the extent of this, where it is seen.

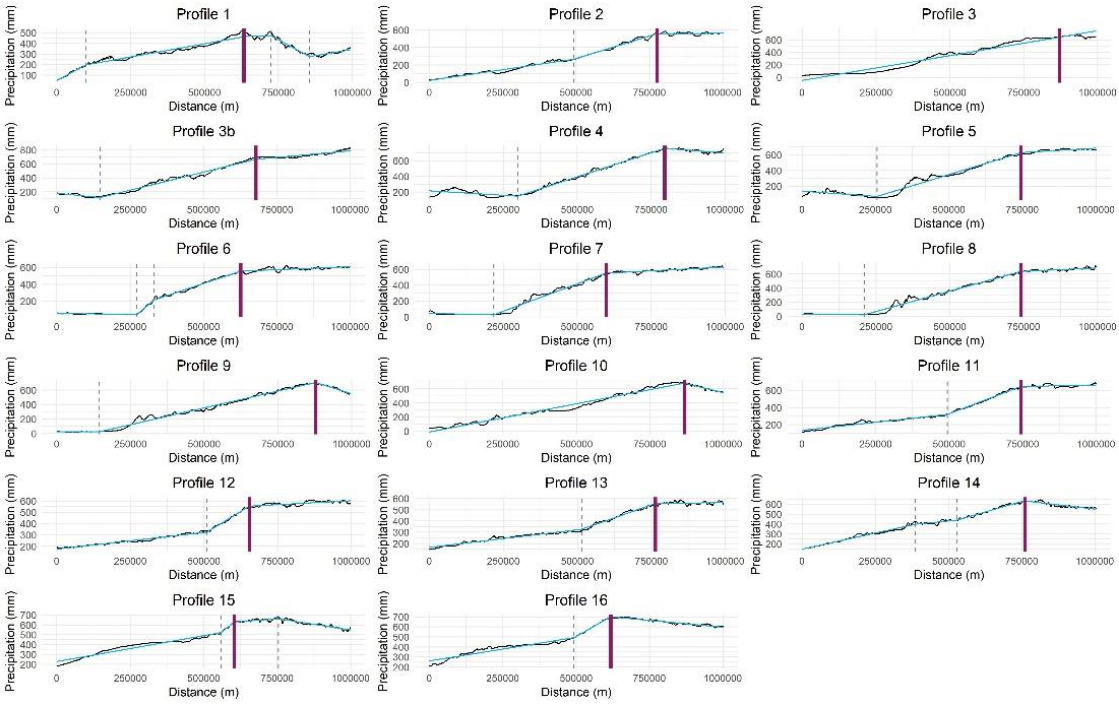

Figure 3.13: Swath profiles of mean annual precipitation taken from swath profiles of 1000 km length and 30 km width and using GPM data. The profiles are drawn from ˜NW-˜SE. The blue line shows the multiple regression best fit lines and the vertical dashed lines the changes in trend. Precipitation declines towards the central plateau and the purple vertical line marks the extent of low HI.

3.2.5 Thermochronology and Erosion Rate Data

I use a compilation of thermochronology ages from the central and eastern Tibetan Plateau from 44 individual studies (Arne et al. 1997; Ansberque et al.. 2018; Chen et al., 2019; Clark et al., 2004; Cook et al., 2013; Dai et al., 2013; Deng et al., 2018; Godard et al., 2009; Haider et al., 2013; Hetzel et al., 2011; Jolivet et al., 2015; Kirby et al., 2002; Lai et al., 2007; Leng et al., 2018; H. Li et al., 2019; Li et al., 2012; Liu-Zeng et al., 2018; Lu et al., 2015; McRivette et al., 2019; Nie et al., 2018; Ouimet et al., 2010; Replumaz et al., 2020; Rohrmann et al., 2012; Tan et al., 2014; Tan et al., 2017a; Tan et al., 2019; Tang et al., 2018; Y. Tian et al., 2013; Tian et al., 2014a; Tian et al., 2014b; Tian et al., 2015; Wang et al., 2007; E. Wang et al., 2012; S. Wang et al., 2012; L. Wang et al., 2013; Wang et al., 2018; Wang et al., 2019; Wilson et al., 2011; Xu et al., 2000; Zhang et al., 2016; Zhang et al., 2019; Y.Z. Zhang et al., 2017; Y. Zhang et al., 2015), partially compiled by H. Li et al., (2019). The dataset includes apatite and zircon fission track and apatite and zircon (U-Th)/He dating. By making assumptions about geothermal gradients, the times at which the minerals pass through the blocking temperature associated with each technique can be converted into exhumation ages and therefore long-term rates. The thermochronology age data points are concentrated in th eastern Tibetan Plateau, within the Longmen Shan and the major river basins including the three gorges of the Salween, Mekong and Yangtze, with less data in the central Tibetan Plateau and very sparse

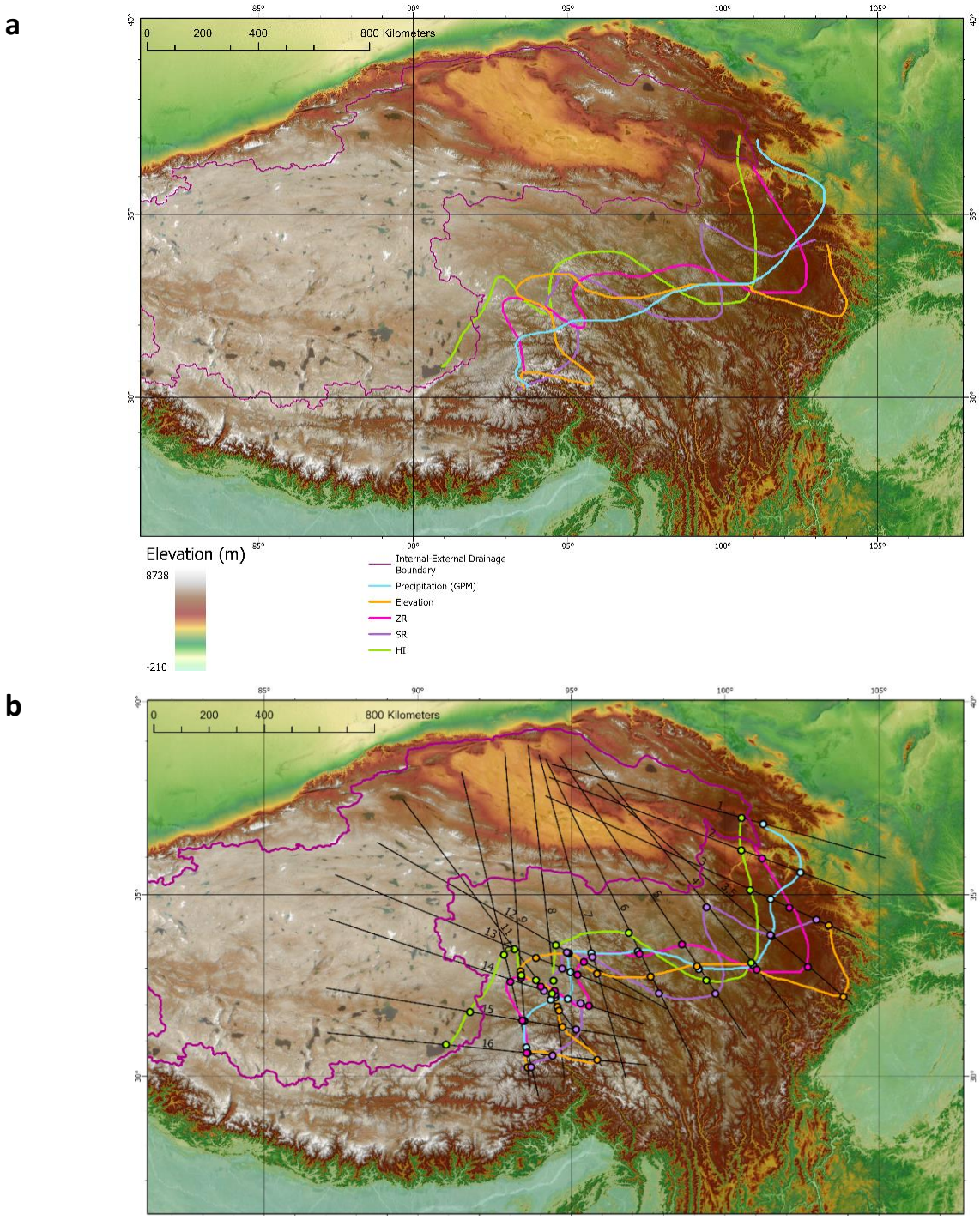

Figure 3.14: a) The locations of the changes in trend to the lower relief landscape in the plateau interior, shown by the coloured lines. The spatial changes in the geomorphic indices, raw elevation data and mean annual precipitation are all grouped and aligned. This area is referred to as the landscape transition. b) The locations of the changes in trend are shown by the coloured lines as in a). In addition the individual coloured points show the locations of trend identified as the breakpoints in Figures 3.9 – 3.13. From these the curved coloured lines are drawn. The locations of the swath profiles are also shown and these are centred on and orthogonal to the internal-external drainage boundary and are equally spaced.

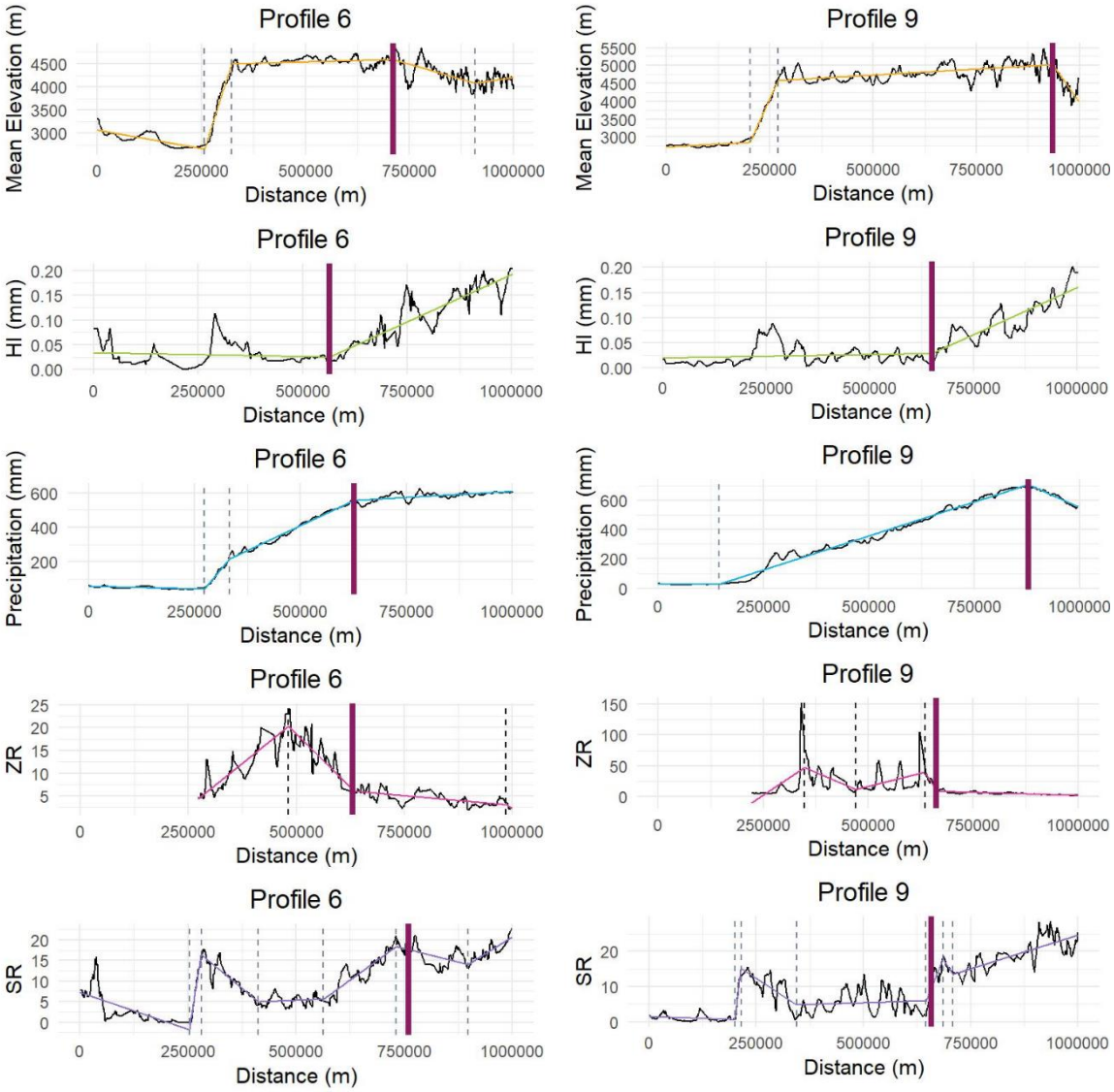

Figure 3.15: Examples of the swath profiles produced. The profiles are drawn from ˜NW to ˜SE and are 1000 km in length and 30 km in width. The coloured lines show the multiple regression best fit lines and the dashed vertical lines show the locations of trend changes. The purple vertical line shows the change, from the plateau margin to the interior, to constant high elevation, low HI, declining mean annual precipitation (GPM dataset), increased ZR and declining SR. The swaths shown are from profiles 6 and 9 and the locations of these are shown in Figure 3.7.

data between 92 and 97 °E. We therefore additionally consider detrital thermochronology data for this region (Duvall et al., 2012), which usefully covers the region with fewest bedrock data.

Modern erosion rate data are compiled from 9 studies (Lal et al., 2004; Harkins et al., 2007; Ouimet et al., 2009; Godard et al., 2010; Liu-Zeng et al., 2011; Henck et al., 2011; Strobl et al., 2012; Li et al., 2014 and Ansberque et al., 2015). These data are primarily derived from cosmogenic isotope dating and are representative of Kyr timescales.

3.3 Results

3.3.1 Results of Geomorphic Analysis

Figures 3.4 – 3.6 show the HI, SR and ZR values respectively, plotted by drainage basin, as described in section 3.2. Relatively high HI, SR and low ZR values are found in the major river channels and at the plateau margins, including in the Longmen Shan. Relatively low HI and SR and high ZR values are seen in the internally drained central plateau but these values also occur to the east of the internal-drainage boundary. The values do not appear to be controlled by faulting.

This work aims to identify the areas of the flattest plateau landscape to inform our understanding of the Tibetan Plateau formation. The transition lines drawn (Figure 3.14) represent a change in trend on the swath profiles from east to west showing: a transition from increasing to constant high elevations; a transition from decreasing to constant low HI; a transition to low or declining SR and a transition from low to increasing ZR. These transition lines are spatially grouped (Figure 3.15) and all are aligned with a ˜NE-SW trend (Figure 3.14). Together, they form a broad transition zone in the landscape, to the north west of which is high elevation with a smooth landscape, whereas the region to the south east is steeper and more incised. The transition zone is to the east of the internal-external drainage boundary. It is also to the east of the easternmost active normal faults in the plateau interior, which is roughly located at the boundary between internal and external drainage (Figure 3.14). The zone cross cuts major faults (Figure 3.1a). The landscape transition zone therefore does not appear to be controlled by active faulting or first order drainage morphology.

The changes in trend of the elevation and geomorphic index data are spatially consistent with the location of the decline in precipitation (Figures 3.13, 3.14). Analysis of the annual precipitation data by swath profile shows the westward decline in precipitation across this study area, as seen in map view (Figure 3.3). In addition, the swath profiles show that this decrease is not gradual but shows a sharp change in trend from constant or increasing precipitation in the east to a declining precipitation, marked by the vertical purple lines in Figure 3.13. This decline in precipitation continues westwards for over 500 km. I suggest that this mapped line represents the western limit of the East Asian Monsoon. I therefore suggest that the transition in the plateau landscape is controlled by the western extent of the East Asian Monsoon.

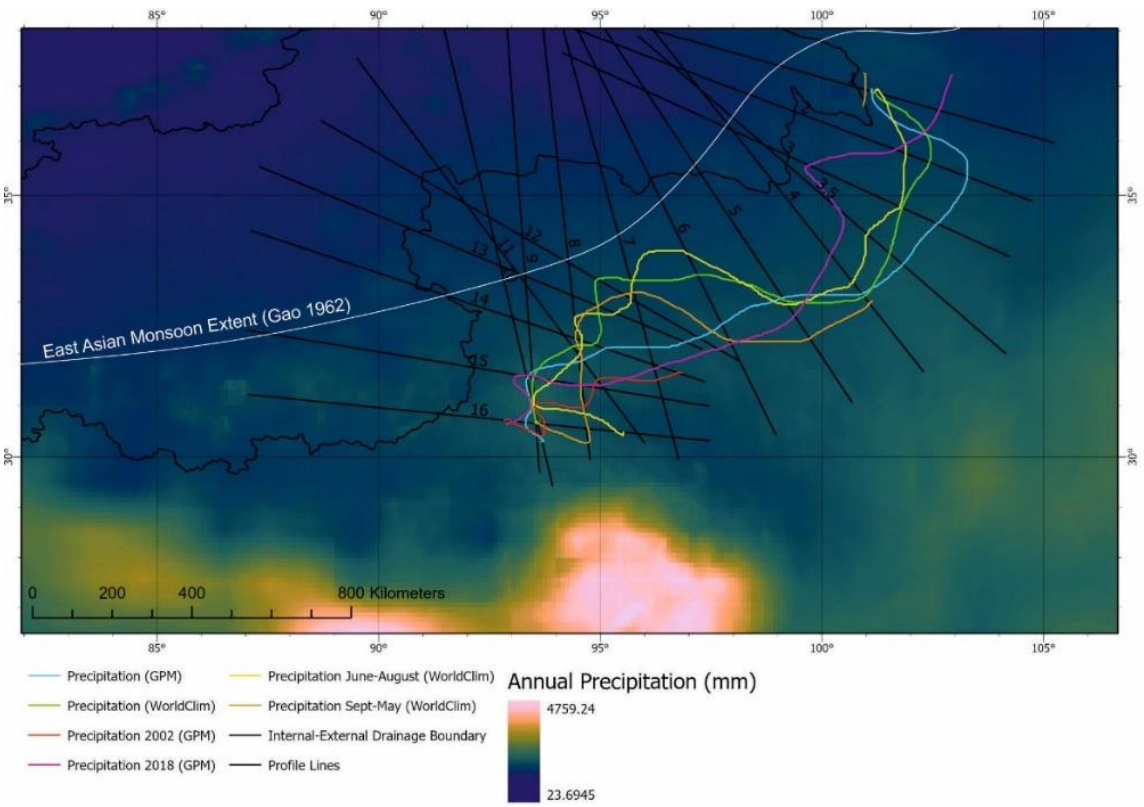

Figure 3.16: A comparison of different precipitation records, with the WorldClim dataset shown as the map background. The changes in trend were identified using the same method as described. The comparison includes two different datasets, the GPM record as shown in Figure 3.13 and 3.14 and which represents the mean annual precipitation from 2001-2018 and the WorldClim v2 record of precipitation from 1970-2000. Further comparison is made between the GPM record for the wettest and driest years in the region, 2018 and 2002 respectively. The wettest and driest years were selected by sampling random points within the area (98.8°E, 33°N and 97.5°E, 32.5°N). Finally, a comparison is made between the summer monsoon months precipitation (June-August) and the non-monsoonal months (September-May). In each case the precipitation lines are seen to occur in a broadly similar location: although the precipitation amount varies, the location of the monsoon extent appears to be largely consistent. Each of the datasets suggests that the monsoon extent is to the east of the commonly drawn line of Gao (1962).

The method of identifying a trend change in precipitation data using swath profiles is used to compare different precipitation data (Figure 3.16). This includes comparisons of the GPM and WorldClim datasets. Monsoonal rainfall is concentrated in the months of June, July and August and therefore the analysis of data for these months only is shown. Outside of these three months, the change in trend of the precipitation swaths is less pronounced and in some cases is not present but is largely in the same spatial location when present. The precipitation pattern of the wettest (2018) and driest (2002) years in the GPM dataset are also shown to occur in a broadly similar zone. In each case the precipitation decline, which we suggest to be the extent of the East Asian Monsoon, is to the east or southeast of the location where the monsoon limit is commonly drawn (Figures 3.3, 3.16; Gao 1962; Chen et al., 2010; Long et al., 2010).

3.3.2 Thermochronology

West of 95° E, thermochronology dates are clustered between ˜40 and ˜75 Ma (Figures 3.17, 3.18), with sparse data showing ages of ˜12 Ma. Catchment wide thermochronology data, from detrital grains sampling basins between 94 - 104° longitude show catchment mean ages of 20 - 40 Ma and minimum of 12 Ma (Duvall et al., 2012). East of 98° E there has been continued exhumation through the last >100 Ma, with clusters of ages at ˜40 Ma and in the last 25 Ma. The probability distribution plot (Figure 3.19) for this region, within the monsoon limit, shows a prominent peak in the last 25 Ma which is not present in the regions to the west but is partially present in the detrital data.

The scatter plot and boxplot in Figure 3.20 show the thermochronology data, grouped according to location relative to the landscape transition zone. The internally drained region is considered

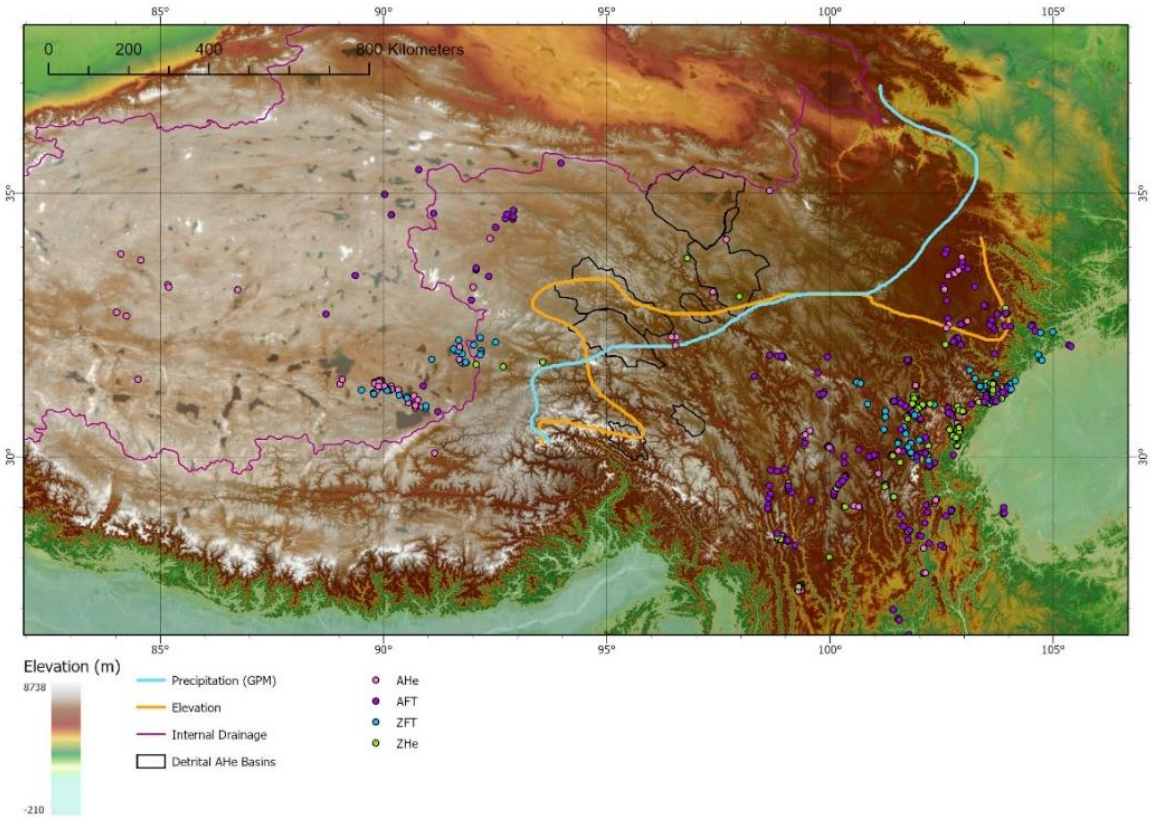

Figure 3.17: Map showing the location of thermochronology data, taken from published studies. The colours represent the method. The black outlines show the drainage basins from which detrital grains were analysed by Duvall et al., (2012). The elevation and precipitation lines, from Figure 3.14 are shown for reference.

separately to allow for comparison. The figure shows the exhumation pattern of the internally drained region and the externally drained region to the north west of the landscape transition zone to be similar (min = 13.9 Ma, median = 58.5 Ma and min = 14.7 Ma, median = 48.9 Ma respectively).

The area to the southeast of the landscape transition zone shows a wider range of thermochronology ages, including a much lower minimum age (min = 0.80 Ma, median = 15.95 Ma). Figure 3.21, shows the same dataset but instead divided by the areas defined by Clark et al., (2006) as remnant plateau surfaces and non-remnant surfaces. In addition, erosion rate values to the north and west of the area studied by Clark et al., (2006) are included as "plateau". This figure shows that the central plateau and remnant surfaces show no thermochronology ages younger than ˜20 Ma, whereas the non-remnant surface shows a much greater range.

3.3.3 Erosion Rate

Modern erosion rate data, compiled from 9 studies, show low erosion rates in the internally drained plateau (median = 0.01 mm/yr) and low rates in the area to the northwest of the landscape transition zone (median = 0.04 mm/yr). Figure 3.22 shows these erosion rate data divided by the landscape transition zone described in this study, as in Figure 3.20. To the south and east of the landscape transition zone there is a larger range in exhumation rates (median = 0.18 mm/yr, IQR = 0.24 mm/yr). From west to east, the change from low erosion rates to a greater range of erosion rates occurs at ˜97° E, which is coincident with the landscape transition zone identified in this study.

The internally drained region and the externally drained region to the north west of the landscape transition zone has low erosion rates (median = 0.01 mm/yr and 0.036 mm/yr). The area to the south east of the landscape transition zone shows a greater range of erosion rates and a higher average rate (median = 0.18). Figure 3.23 shows the distribution of erosion rates divided as in Figure 3.21. This figure shows that the plateau and remnant surfaces have similar, low erosion rates (median = 0.03 mm/yr and 0.05 mm/yr respectively), whereas the non-remnant surfaces, as actively eroding river valleys, have a larger range of erosion rates (median = 0.21 mm/yr, IQR = 0.245 mm/yr).

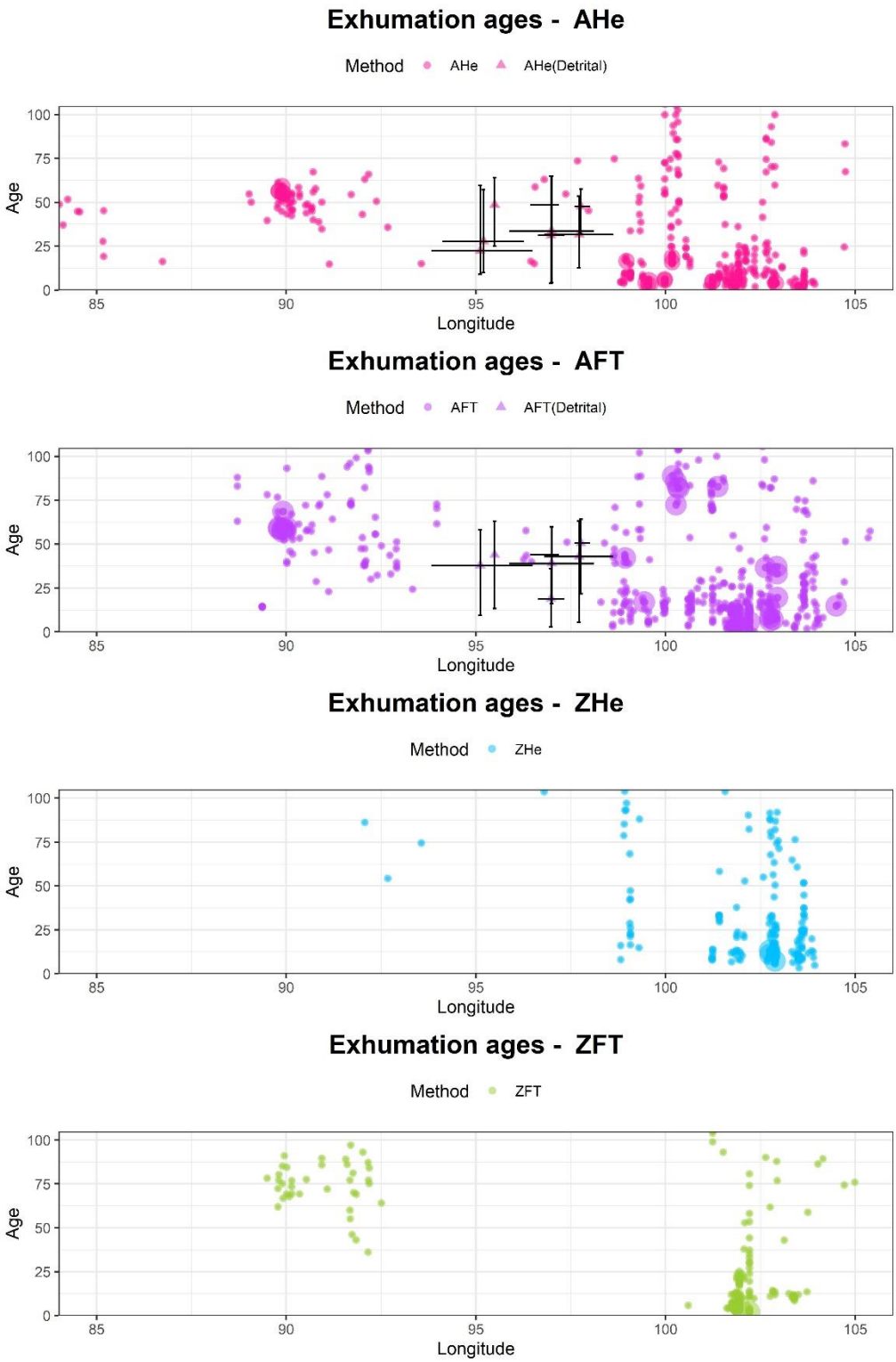

Figure 3.18: Scatter plots of the published thermochronology compilation, shown divided by method. The error bars represent the detrital data of Duvall et al., (2012) representing the spatial extent of the drainage basins and the range of data within each basin. Larger circles represent multiple values.

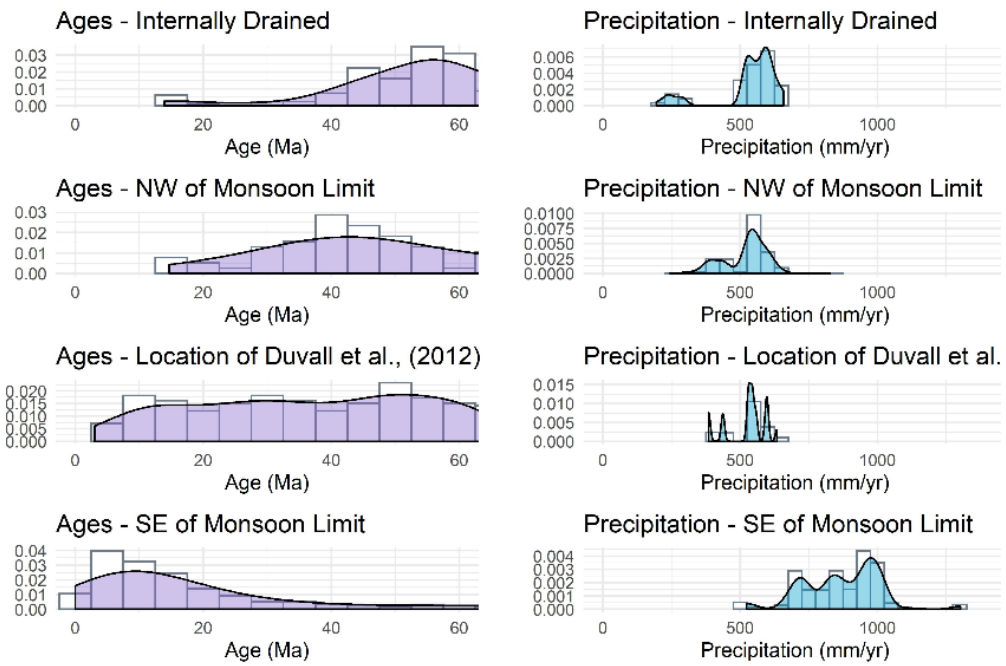

Figure 3.19: a) Probability distribution curves of the thermochronology dataset and b) annual precipitation, divided by location relative to the internal-external drainage boundary and the landscape transition boundary. The detrital dataset and the area to the south east of the landscape transition show exhumation throughout the time period shown, with the area to the south east showing a peak in ages in the last 15 Ma. The areas to the north west of the landscape transition show no thermochronology ages in the last 15 Ma.

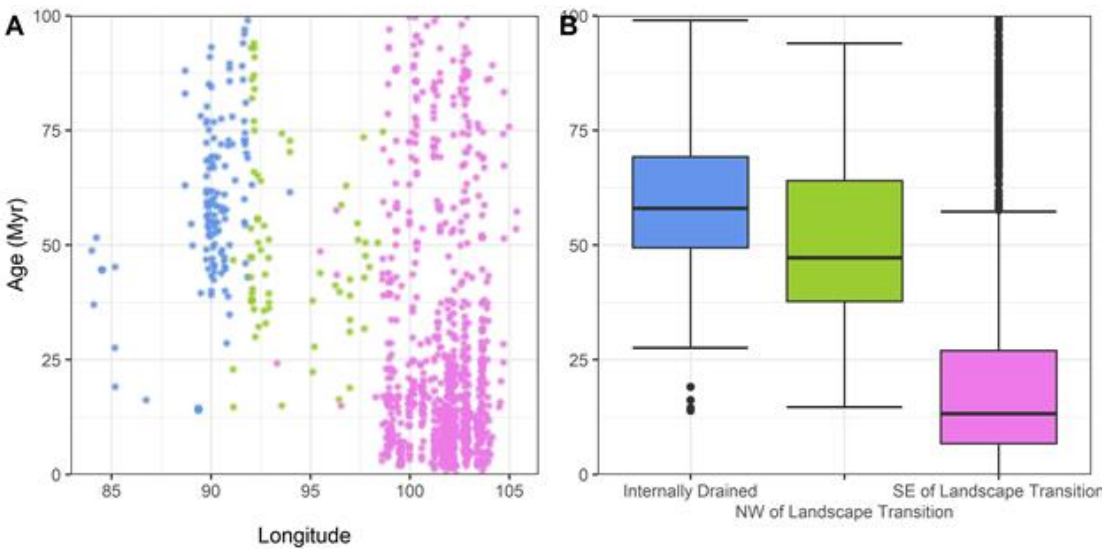

Figure 3.20: a) Scatter graph and b) boxplots showing thermochronology data, coloured according to location relative to the internal-external drainage boundary and the landscape transition. The areas to the north and west of the landscape transition shows no thermochronology ages in the last 14 Ma suggesting the area was high elevation and low relief by this time. To the south east of the landscape transition there are thermochronology ages throughout the last 50 Ma, suggesting a long-lived margin and a cluster of ages in the last 25 Ma which we attribute to increased erosion due to increased precipitation after the East Asian Monsoon onset and intensification. Whiskers represent data within 1.5 * IQR of the data, the box represents the first and third quartiles and the central line represents the median.

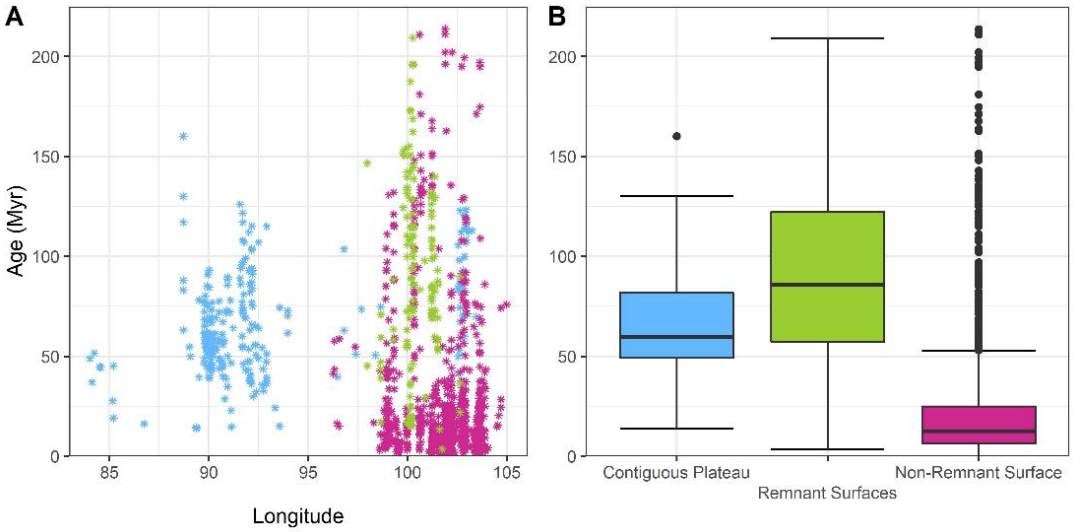

Figure 3.21: a) Scatter graph and b) boxplots showing thermochronology ages coloured by location relative to the landscape described by Clark et al., (2005). The area between the remnant surfaces shows ages throughout the past 200 Ma and a clustering of ages in the last 25 Ma, whereas the remnant surfaces and contiguous plateau to the north and west shows no ages in the past 20 Ma. I suggest the remnant surfaces were low relief surfaces formed at high elevations. I suggest the cluster of Miocene exhumation in the non-remnant surfaces is due to increased exhumation to due to the onset of the Miocene monsoon. Whiskers represent data within 1.5 * IQR of the data, the box represents the first and third quartiles and the central line represents the median.

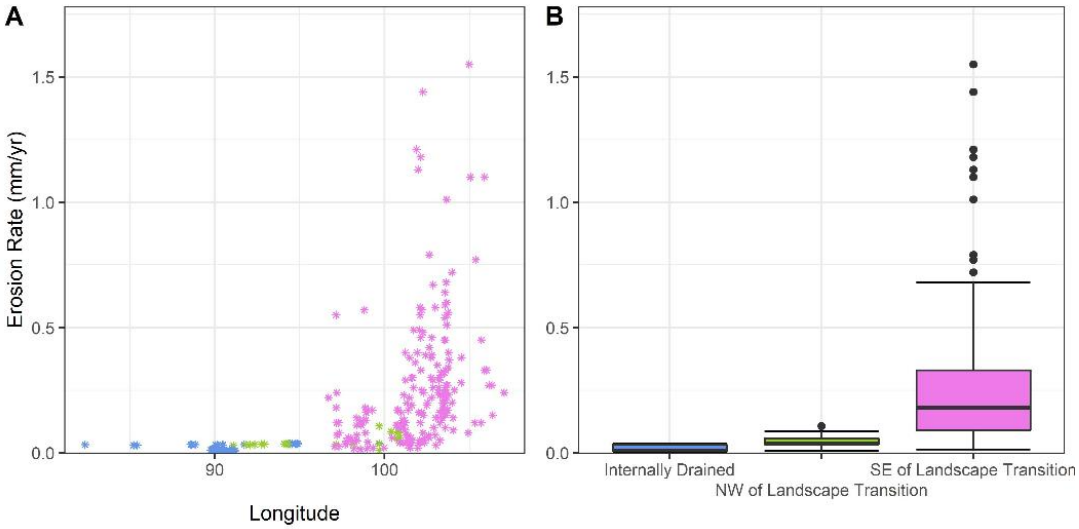

Figure 3.22: a) Erosion rate scatter and b) boxplot showing Erosion rate data, coloured according to location relative to the internal-external drainage boundary and the landscape transition. c) shows the erosion rate data with a limited y axis. The areas to the north west of the landscape transition has low erosion rates and the area to the south east has a larger range of erosion rates. The higher erosion rates only occur in the area which experiences the summer monsoon precipitation. Whiskers represent data within 1.5 * IQR of the data, the box represents the first and third quartiles and the central line represents the median.

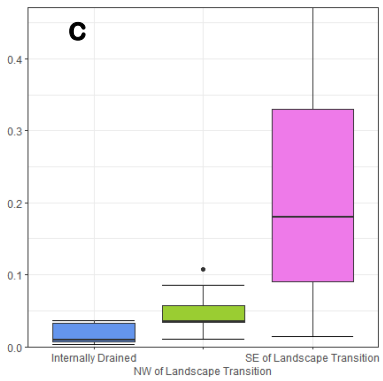

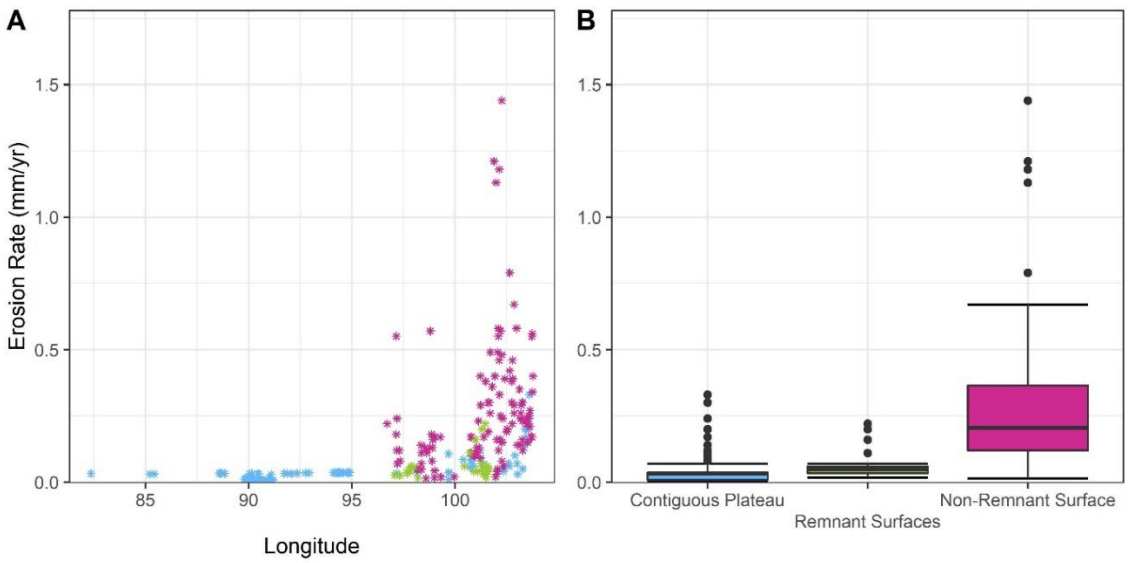

Figure 3.23: a) Scatter graph and b) boxplots showing erosion rate coloured by location relative to the landscape described by Clark et al., (2005): The areas between the remnant surfaces show the highest erosion rates. Whiskers represent data within 1.5 * IQR of the data, the box represents the first and third quartiles and the central line represents the median.

3.4 Discussion

The transition zone identified in the Tibetan landscape trends roughly ENE-WSW. This landscape change is not coincident with strike slip faulting in the region, which trends largely NNW-SSE (Figure 3.1a) and also crosscuts the Tibetan Plateau terranes. The landscape change is also near-orthogonal to the major rivers in the region, i.e. the Mekong, Salween and Yangtze (Figure 3.1a). The identified zone of landscape change therefore has no apparent structural or drainage-divide control.

In terms of exhumation, the channel flow model would predict an increase in exhumation in the central plateau at 12-10 Ma, moving outwards towards the margins over time, tracking surface uplift. The thermochronology age probability distribution curves indicate no west-to-east wave of exhumation (Figure 3.19). The area to the west of the landscape transition, towards the plateau interior, shows no significant exhumation in the past 15 Ma. The increase in exhumation is confined to the region to the east of the landscape transition zone. The channel flow model also suggests that prior to uplift at 12-10 Ma the eastern Tibetan Plateau had low relief and was at low elevations. Thermochronology data would therefore be predicted to show little exhumation until the time of uplift. This is not the case: the data show that exhumation of eastern Tibet has been occurring throughout the past >100 Ma (Figure 3.18). I therefore conclude that the channel flow hypothesis cannot fully explain the landscape transition and thermochronology data presented here. The long-lived exhumation at the eastern margin of the Tibetan Plateau is consistent with a long-lived

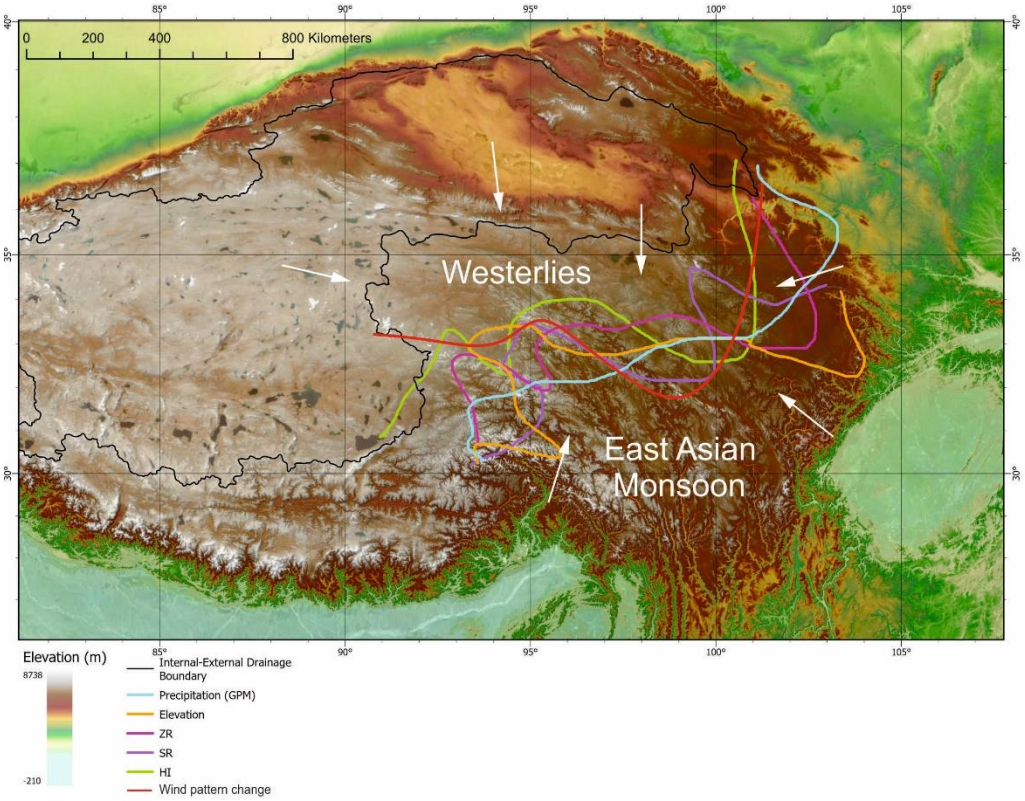

Figure 3.24: Map showing the direction of wind systems in the area, with the major systems the East Asian Monsoon and the westerlies. The red line shows the boundary between these systems, produced following Dong et al. (2017) and this is seen to correspond with the landscape transition shown in this study.

plateau margin and is therefore consistent with a model of Pre-Miocene growth (e.g. Rowley and Currie, 2006).

The precipitation change which corresponds to the landscape transition (Figure 3.14) is the extent of summer monsoon precipitation (see Section 3.3a). Beyond this limit, to the west of the line, the climate system is controlled by westerlies (Figure 3.24; Dong et al., 2017). Figures 3.19 and 3.20 show the spread of ages within 3 regions of study: the internally drained region, the externally drained region to the NW of the landscape transition and the externally drained region to the SE of the landscape transition and therefore within the area of summer monsoonal precipitation. A cluster of thermochronology ages at 25 Ma is present in the incised area to the east of the landscape transition, within the monsoon limit but no equivalent peak in ages occurs in the non-incised areas beyond the monsoon limit (Figure 3.20). This increased exhumation can therefore be attributed to the intensification of the East Asian Monsoon in the Early Miocene, consistent with palaeoclimatic data for this time (Guo et al., 2002; 2008). This spatial correlation of the more incised

modern landscape and increased exhumation since the Miocene suggests that the western extent of monsoonal precipitation has remained largely static since the Miocene.

During the Early-Middle Miocene the East Asian Monsoon intensified, as evidenced by increased loess deposits, indicating strong winter winds from 22Ma (Guo et al., 2002), flora in the Central Tibetan Plateau throughout the Miocene (Wu et al., 2008), increased sedimentation rates in the South China Sea between 11-16 Ma (Clift et al., 2002), changesin terrestrial ecosystems shown by stable isotopes also from the South China Sea at 11-16 Ma (Jia et al., 2003) and increased exhumation in the upper and middle Mekong in the time of the Mid Miocene Climatic Optimum (MMCO) from 17-14 Ma (Nie et al., 2018). The Asian Monsoon systems are related to global climate. Northern hemisphere cooling weakens the Asian Summer Monsoons (Chiang and Friedman, 2012) whereas southern hemisphere cooling enhances it by strengthening the Australian High, leading to the Intertropical Convergence Zone (ITCZ) moving northwards (Xue et al., 2003; Rohling et al.,2009). Antarctic ice sheet extent controls the monsoon systems by altering eustatic sea level (Y. Sun et al., 2015) and lowering the global temperature, leading to colder Pacific sea surface and therefore lower evaporation and precipitation (Nie et al., 2017) and by changing the cross-equatorial pressure gradient and latent heat release (Clemens et al., 2008). Miocene monsoon intensification has been linked to low CO_2 levels due to Antarctic glaciation (R. Zhang et al., 2015; Ao et al., 2016). The East Asian monsoon system and associated exhumation and weathering act as a positive climate feedback at the time of Antarctic glaciation: Antarctic glaciation leads to a strengthened monsoon system, leading to more erosion and therefore higher levels of CO_2 drawdown by silicate weathering (Raymo and Ruddiman, 1992) and therefore cooler global temperatures. Global studies suggest that the rivers of the eastern Tibetan Plateau erode and transport ˜50 % of the sediment from the India-Eurasia collision (Milliman and Syvitski, 1992) and the Tibetan Plateau produces an estimated 20 % of the global silicate weathering (Hilley and Porder, 2008). This suggests that the monsoon intensification and subsequent erosion of the eastern plateau accounts for about 10 % of global weathering. This would suggest that the large-scale exhumation of the eastern Tibetan Plateau due to monsoon intensification therefore has large potential climatic impacts. However, another study suggests that the Three Rivers region of the Eastern Tibetan Plateau is responsible 0.6 % of global atmospheric CO_2 consumption and 0.4 % of global continental area (Noh et al., 2009) suggesting a much lower global climatic impact. Therefore, the extent of the climatic impacts of the exhumation of the area are unclear.

Published modern day erosion rates (Figure 3.22) are low (>0.1 mm/yr) in the central plateau and are much more variable in the eastern plateau, from very low rates up to 1.5 mm/yr. The higher

erosion rates only occur in the area of the incised landscape, within the area of summer monsoonal precipitation. Low erosion rates occur across the entire study region and in areas with all levels of precipitation but high erosion rates only occur in areas with above ˜600 mm annual precipitation (Figure 3.25). High erosion rates also only occur in areas of high SR (SR > 12) and at elevations below 5000 m. There is no clear correlation of erosion rate with HI (Figure 3.25). In order to make the comparison to erosion rate SR and HI are spatially smoothed using a moving window approach, rather than calculated for each basin, as many of the erosion rate points are from the hillslopes and river channels, which were excluded from the basins (Chapter 2, Section 2.2). This spatial smoothing may account for the poor correlation with HI, but not for the difference in correlation patterns between HI and SR. The comparison with erosion rate and precipitation suggests a potential climate-linked erosion threshold but this would need to be tested elsewhere. More data are needed for the region of sparse data, between the central and eastern plateau, to test this relationship.

In order to compare the modern-day erosion rates to the long-term exhumation rate, the thermochronology data from the last 50 Ma was converted to produce long-term erosion rates. Assuming a geothermal gradient of 25°C/km and closure temperatures for AHe, AFT, ZHe and ZFT of 65°, 105°, 180° and 240° respectively (Reiners et al., 2005, Yameda et al., 1995) simple erosion rates were calculated. Although this method is simplified and very low erosion rates are excluded, due to restricting the age range used to the last 50 Myr, the results are comparable to the modern erosion rates. Low erosion rates occur to the north west of the landscape transition and high erosion rates occur to the south east of the transition, in the area which experiences monsoon precipitation. These rates derived from each thermochronology technique and the published erosion rate data have very similar erosion rates within each area (Figure 3.26). This suggests that the erosion rates are comparable to the long-term exhumation rate. The modern-day rate appears to be more than high enough to achieve the long-term exhumation (e.g. 0.5 mm/yr over 20 Myr would give 10 km of exhumation).

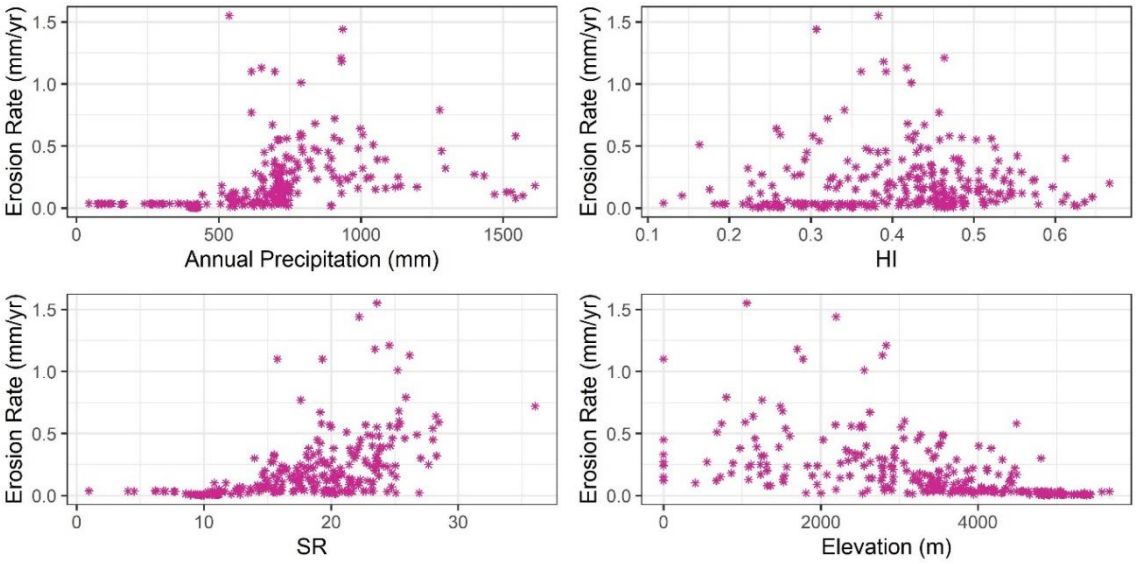

Figure 3.25: Scatter plots showing the mean annual precipitation, HI, SR and elevation at the location where each erosion rate data point is taken. Low erosion rates occur in areas of low and high precipitation but higher erosion rates (> 0.1 mm/yr) only occur in areas of higher rainfall (> 450 mm/yr).

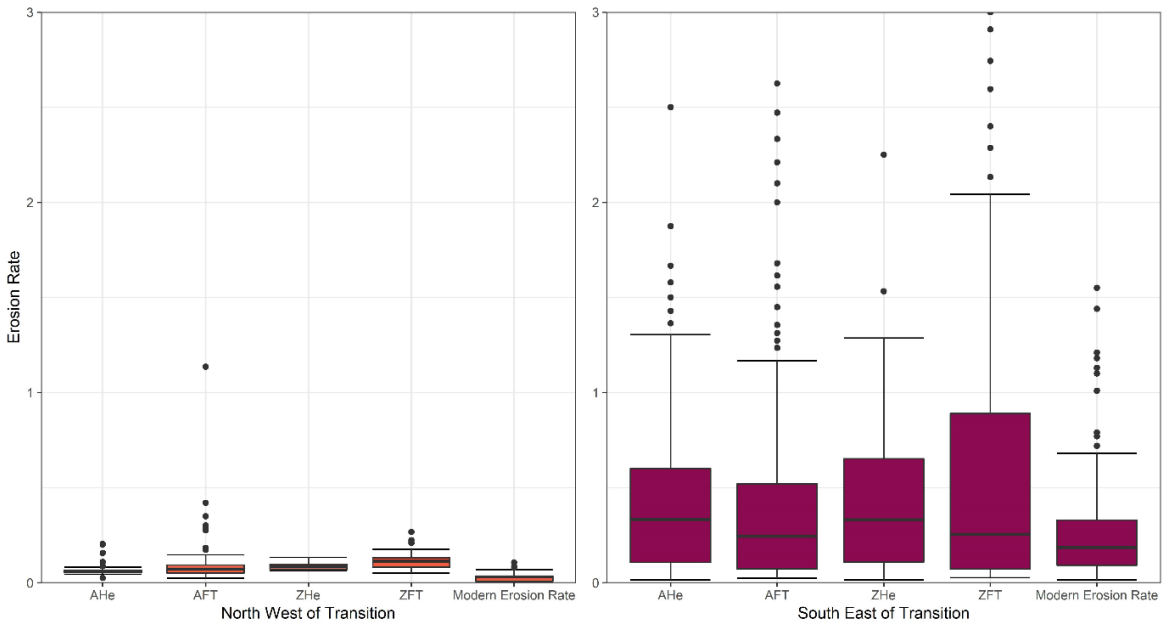

Figure 3.26: Boxplots showing published modern erosion rates and simple erosion rates estimated from the published thermochronology data. Whiskers represent data within 1.5 * IQR of the data, the box represents the first and third quartiles and the central line represents the median.

Figure 3.21 show that the contiguous plateau and the areas identified by Clark et al., (2006) as remnant plateau surfaces show a similar pattern of exhumation through time. This is consistent with the model of Pre-Miocene plateau growth followed by monsoon driven incision, as the model

predicts the interfluves, or “non-remnant surfaces” to be exhumed by the actively eroding rivers. This is also seen to occur in the modern-day erosion rate data (Figure 3.23): the contiguous plateau and remnant surfaces show much lower erosion rates (median = 0.03 mm/yr and = 0.05 mm/yr respectively) than the non-remnant surfaces towards the eastern plateau margin (median = 0.21 mm/yr).

If the Miocene monsoon extent is consistent with the modern-day monsoon extent, as is suggested by the thermochronology data, the location is likely to have been controlled by the Miocene landscape. The central Tibetan Plateau in the Miocene is thought to have been high elevation (Rowley and Currie 2006), low relief (Han et al., 2019; Law and Allen, 2020) and internally drained (Wu et al., 2008) during the Miocene. The high elevation plateau would lead to low atmospheric pressure and precipitation would be focussed on the plateau margins.

The extent of the Miocene internal drainage (from 23.5 Ma to 13.5 Ma; Wu et al., 2008, 2014) is spatially coincident with the incised-non-incised transition. This therefore suggests that the non-incised landscape, to the NW of the zone of landscape change, is a relict of the Miocene landscape. The modern day internal-external drainage divide is further west than in the Miocene. This westward migration of the divide indicates that increased stream power of the rivers draining the eastern plateau, likely to be due to increased precipitation due to monsoon intensification, has caused the rivers to cut into the plateau, a maximum of 500 km west of the monsoon limit. The modern-day extent of internal drainage is spatially coincident with the extent of normal faulting within the plateau interior. This coincidence may be due to faulting dissecting the drainage basins. The active normal faulting may be preventing further westward migration of the internal drainage boundary.

3.5 Conclusions

The broad location of a change in landscape from flat in the central plateau to more varied in the southern and eastern plateau is identified. This change in landscape occurs in the same location as a north-westward decline in precipitation. I suggest this is a more accurate location of the extent of the East Asian Monsoon high precipitation than previously defined. Geomorphic data, precipitation, erosion rate data and thermochronology age data all change across this transition region. Since the Miocene, high erosion rates have only occurred in the region of the modern day East Asian Summer Monsoon. I conclude that intensification of the East Asian Monsoon, beginning at ˜25 Ma, led to incision and exhumation of the high Tibetan Plateau landscape which had been formed before this time. Incision took place by the major rivers draining the region, including the

Mekong, Salween and Yangtze. A record of the early plateau has been preserved in the landscape, with plateau remnants preserved in the interfluve regions of eastern Tibet. Changing climate has therefore been a major control on the landscape of the Central and Eastern Tibetan Plateau since the Early Miocene. The combined exhumation and geomorphic data support early plateau growth and do not show evidence for late Tibetan Plateau uplift by channel flow.

Chapter 4: Geomorphic indices compared to underlying structure and strain rate in fold-and-thrust belts

4.1 Introduction

This chapter presents work comparing different fold-and-thrust belts and collisional systems. These include areas from the India-Eurasia collision, the Arabia-Eurasia collision and the retroarc fold-and-thrust belt above the Andean subduction zone. For the India-Eurasia collision the study area is the Himalaya, along with the Qilian Shan as discussed in Chapter 2. The length of the Zagros mountain belt is studied, which has been formed by the Arabia-Eurasia collision. Finally, the central Andes, in the region of the Puna plateau is studied. In each area the geomorphic indices of Hypsometric Integral (HI), Surface Roughness (SR) and Elevation Relief ratio (ZR) are calculated, as introduced in Chapter 2. These indices are then compared to the inferred underlying structure of each area, based on published studies. The indices are also compared to crustal strain rate calculated from the global GPS velocity database compiled by Kreemer et al., (2014).

These areas were selected to give a broad comparison of the links between geomorphology, underlying structure and strain rate in active collision zones, with the climatic differences also considered. The fold-and-thrust belts provide varied examples (Figure 4.1a). For example, the Himalaya, Qilian Shan and Central Andes are suggested to accommodate deformation on an underlying detachment (e.g. Stevens and Avouac, 2015; Allen et al., 2017; Brooks et al., 2011), whereas in the Zagros mountain belt strain is accommodated on discrete thrust faults (e.g. Allen et al., 2013). The study of the Central Andes allows comparison between continent-continent collision zones and ocean-continent subduction. The climatic characteristics also vary between the areas, with the Qilian Shan and the Eastern cordillera of the Central Andes being much drier than the Himalaya. There are also differences in climatic gradients. For example, the precipitation gradient of the Himalaya is mostly orthogonal to the mountain belt, in the style of typical orographic precipitation. However, the Qilian Shan also shows an along strike precipitation gradient, from drier in the west to wetter in the east.

The aim of the work is to compare the relationships between underlying structure and geomorphology (Figure 4.1b), as a strong relationship was found in the Qilian Shan (Chapter 2; Figure 2.24). This relationship showed high HI, high SR and low ZR values above the locked portion of the underlying detachment thrust (seismogenic faulting in the upper crust), with a distinct transition to low HI, low SR and high ZR above the creeping portion of the detachment (ductile

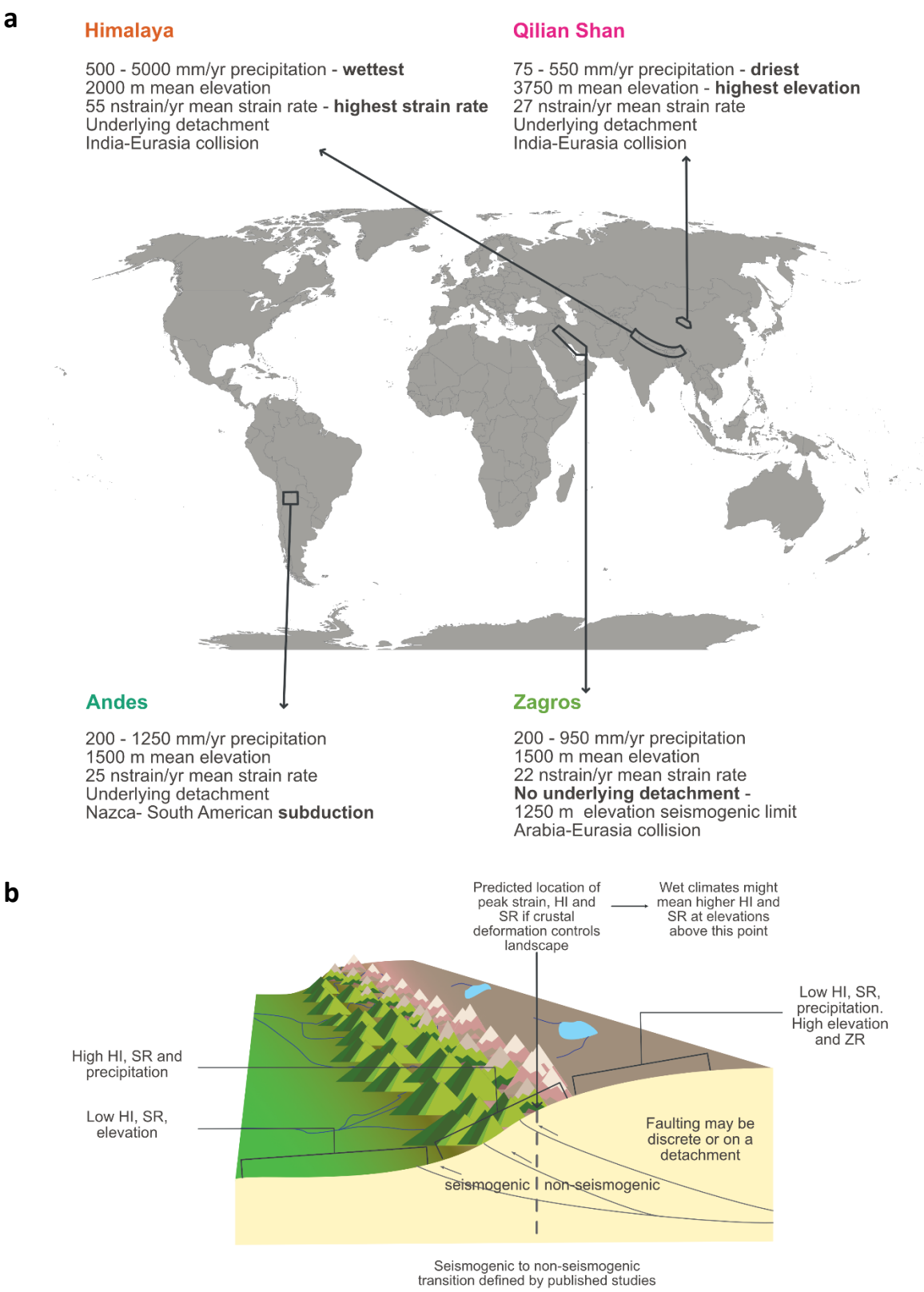

Figure 4.1: a) Location map showing an overview of the four areas studied and b) a stylised mountain belt showing the expected relationship between the landscape and underlying tectonic structure.

deformation deeper in the lower crust). The Himalaya and Eastern Cordillera of the central Andes are suggested to also accommodate deformation on an underlying detachment and the extent of the locked portion of these detachments have been studied by elastic dislocation modelling of geodetic data. This allows for a simple comparison of the pattern of geomorphic indices in these areas and also the Qilian Shan. The pattern of geomorphic indices in the Zagros Mountains is also of interest as although the deformation is accommodated on discrete thrust faults rather than an underlying detachment, seismicity has been observed only to occur below the 1250 m contour (Nissen et al., 2011; Allen et al., 2013). Therefore, a comparison can be made between the landscapes of these two different tectonic deformation parameters: the extent of potentially seismogenic locking on a detachment and the extent of seismogenic thrusting. Variation of results is analysed in terms of the structure of the underlying detachment, climatic variations and lithological variations. The crustal strain rate is also calculated in order to compare the geomorphic indices to a tectonic control. No modelling is used in the calculation of strain rate, as models introduce assumptions into the analysis, such as structures. This method therefore allows us to compare simply between the different regions. If crustal deformation style controls landscape, then high HI and SR would occur over the area of brittle deformation and low HI and SR and high ZR over the area of ductile deformation. A precipitation control on landscape would be predicted to show high HI and SR and low ZR values coupled with high precipitation (Figure 4.1b).

4.2 Methods

4.2.1 Geomorphic Indices

The geomorphic indices of HI, SR and ZR are calculated for second order drainage basins, following the methods described in Chapter 2. Swath profiles are drawn through the datasets at equal intervals, orthogonal to the shortening directions. The width of the swath profiles is 30 km. Quadrats are drawn above the frontal thrust in each region and the maximum, minimum, median and IQR of the data within these areas are used to produce boxplots (more detail is given in Chapter 5, section 5.2). The results are compared to elevation (3 arc second SRTM) and mean annual precipitation (WorldClim, v2). Integrated relief is calculated as in Chapter 2, Section 2.4a. This is calculated as the area under the curve of the elevation range swath profiles, which are the maximum-minimum elevation along the swath. Obaid and Allen (2019) introduce this metric to describe the variation in relief along the Zagros mountain belt and they suggest that a variation in integrated relief of < 25 % is low.

4.2.2 Strain Rate

Crustal strain rates were calculated using GPS data taken from the Kreemer et al., (2014) global compilation, which was used to create the Global Strain Rate Model v2. This study uses GPS data in a Eurasian reference frame (Himalaya, Qilian Shan and Zagros) and a South American reference frame (Andes). Data were filtered to remove datapoints with uncertainty >2 mm/yr, with the exception of the Andes, where no data were removed due to sparse data coverage. Where stations have multiple values in the same geographic location the most accurate data were used, selected as the smallest variance in east and north vectors. The number of GPS velocities used for each area is shown in Table 4.1 and the number of datapoints used at each stage of the quality filtering stage shown.

Location (min.long./max.long./min.lat./max.lat.)	Number of reported GPS velocities within study region	Number GPS velocities with an error < 2mm/yr	Number of GPS velocities after duplicated sites removed
Tibetan Plateau 72/108/24/41	1659	1562	1137
Qilian Shan 94/103/36/41	231	230	146
Himalaya 72/97/25/37	518	438	365
Zagros 40/59/25/40	553	536	360
Andes -69.5/-62/-28/-20	55	No stations removed	43

Table 4.1: Number of GPS velocity data points for each fold-and-thrust belt studied at each stage of data filtering.

Strain rate was calculated using open-source, python-based software StrainTool (https://github.com/DSOlab/StrainTool) based on the method of calculation used by Shen et al., (2015), which calculates values weighted by GPS uncertainty and distance between stations. This weighting factor used in the algorithm can be varied. A weighting value of 24 is used throughout this study, as a smaller weighting value e.g. 6 or 12, with smaller spatial smoothing, leads to large jumps in the

calculated strain values, whereas a high value e.g. 48 leads to a large amount of smoothing, reducing the accuracy of the values for comparison to the geomorphic indices in this study (Figure 4.2). A weighting value of 24 was also used by other studies as they also found this gives the best balance between smoothing and discrete jumps in strain rate patterns (Shen et al., 2015; Palano et al., 2018; Ojo et al., 2021). Strain crosses show the directions of the principal extensional and contractual strain rate at each 0.5° interval for the Qilian Shan, Zagros and Andes and each 1° interval for the Tibetan Plateau. Maps show the second invariant of the strain rate tensor (˜magnitude of strain rate, referred to as the second invariant of strain rate), rotation rate, dilation and shear strain, calculated for points at 0.1° intervals with units in nanostrain/year. The 0.1 ° interval for calculation produces a smooth result and calculating for a denser grid would not change the values calculated, as the data input is much less than 0.1 °. The GPS network used is dense and the strain rate patterns and maps produced are similar to published results (Kreemer et al., 2014). In the areas of study, additional GPS measurements have not changed our understanding of shortening on fold-and-thrust belts over the last decade. The maximum, minimum, median and IQR values of the second invariant of strain rate are extracted from the calculated 0.1 ° grid, for each quadrat, in order to produce boxplots: the strain rate is calculated using the surrounding GPS data points, not just those that lie within each quadrat. Strain rate was calculated rather than crustal shortening across the mountain belt. This is because crustal shortening is calculated between two GPS points, whereas the approach used in this study to calculate strain rate uses spatial weighting of multiple GPS points to calculate the strain rate at each grid point. This gives a more spatially accurate result.

4.3 Himalaya

4.3.1 Introduction

4.3.1.1 Location

The Himalaya were formed by the India-Eurasia collision, (see Chapter 2). This work studies the landscape of the entire length of the mountain range. Deformation is thought to be accommodated on the Main Himalayan Thrust (MHT) which is a north-dipping detachment. The surface expression of MHT is the Main Frontal Thrust (MFT) which defines the southern limit of the Himalaya. The other major thrust faults, from south to north are the Main Boundary Thrust (MBT) and the Main Central Thrust (MCT), with the extensional South Tibetan Detachment (STD) further north (Figure 4.3; Yin, 2006).

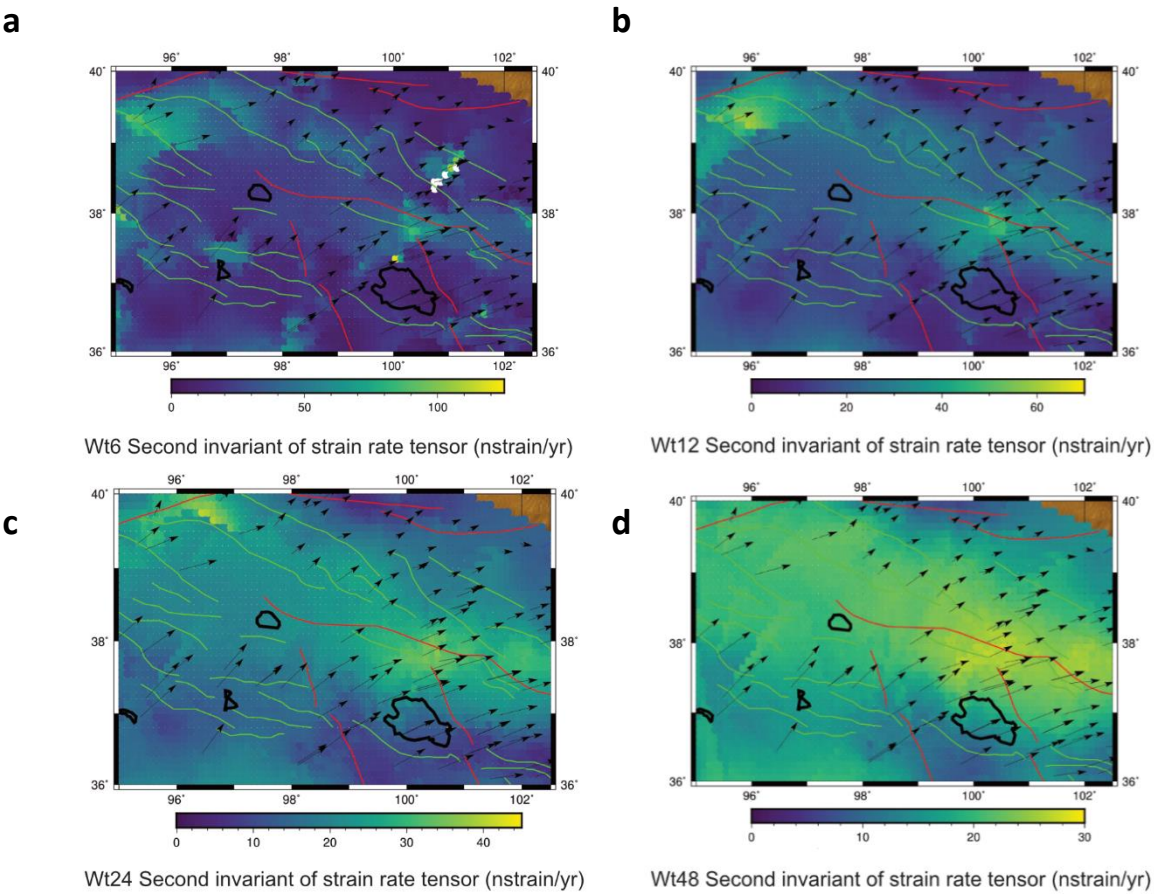

Figure 4.2: The second invariant of strain rate, calculated using StrainTool for the Qilian Shan. The weighting of the distance from GPS stations is calculated as a) 6, b) 12, c) 24, d) 48. Smaller weightings produce less smoothing but can produce large changes in values over a small distance, whereas the large weighting values produce large smoothing but no large jumps in data. A weighting of 24 is used throughout this work as a balance between these two factors.

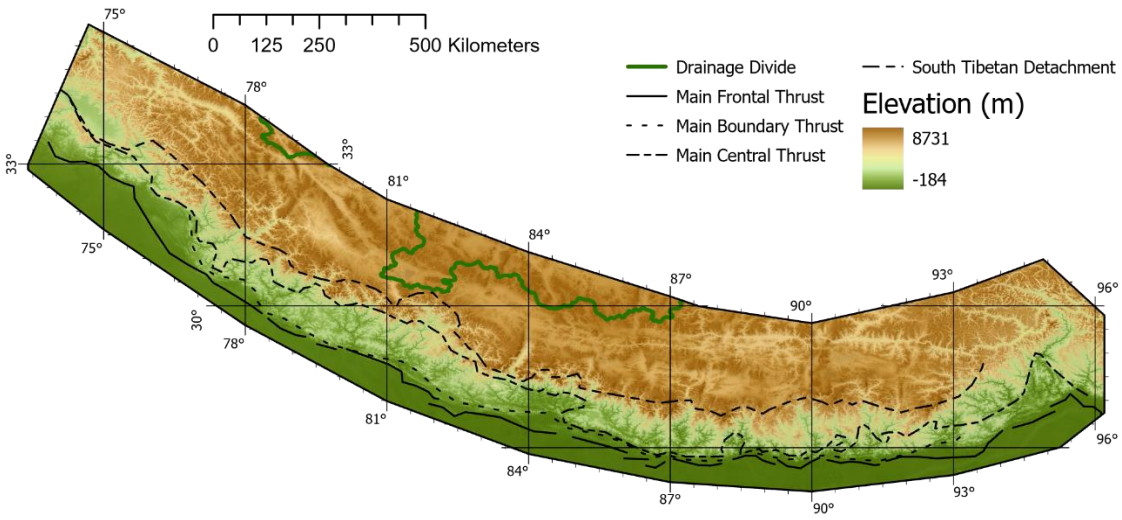

Figure 4.3: Elevation map of the area of Himalaya studied using 3 arc second SRTM data. Major fault traces are shown (Yin, 2006).

Deformation on the MHT is locked in the shallow crust and creeping at depth. This transition from locked to creeping has been modelled using geodetic data. Stevens and Avouac (2015) modelled the slip rate and coupling on the MHT across the Himalaya using interseismic geodetic displacements, InSAR and micro-seismicity data. Their work suggests that the MHT is fully locked along the length of the Himalaya, to ˜100 km ±20 km downdip and they found that this location is consistent with geodesy, seismicity and topography. The transition from locked to creeping is sharp, apart from in the very west of the Himalaya, where the transition is broader and more diffuse. The locked-creeping transition roughly intersects the 350°C isotherm defined by Herman et al., (2010). Lindsey et al., (2018) modelled geodetic data for the Nepal region of the Himalaya, with the model independent of micro-seismicity, to identify the extent of the locked portion of the MHT. The extent of the locked portion is consistent with a band of micro-seismicity and the inferred location of a ramp in the MHT (Pandey et al., 1995). The structure of the MHT is likely to be more complex than shown by these models, for example, studies of micro-seismicity following the 2015 Gorkha earthquake suggest that slip occurs on a duplex structure at ˜15 - 20 km depth (Mendoza et al., 2019).

4.3.1.2 Climate

The climate of the Himalaya is dominated by intense summer precipitation due to the Indian Summer Monsoon. The NW Himalaya is also affected by westerlies and the E Himalaya by the East Asian Summer Monsoon (Burbank et al., 2012 and references within). In the central Himalaya 70 % of the annual precipitation is received in the summer months, declining to the East and West. The Himalaya show intense orographic precipitation (Figure 4.4). Moisture is mainly transported from

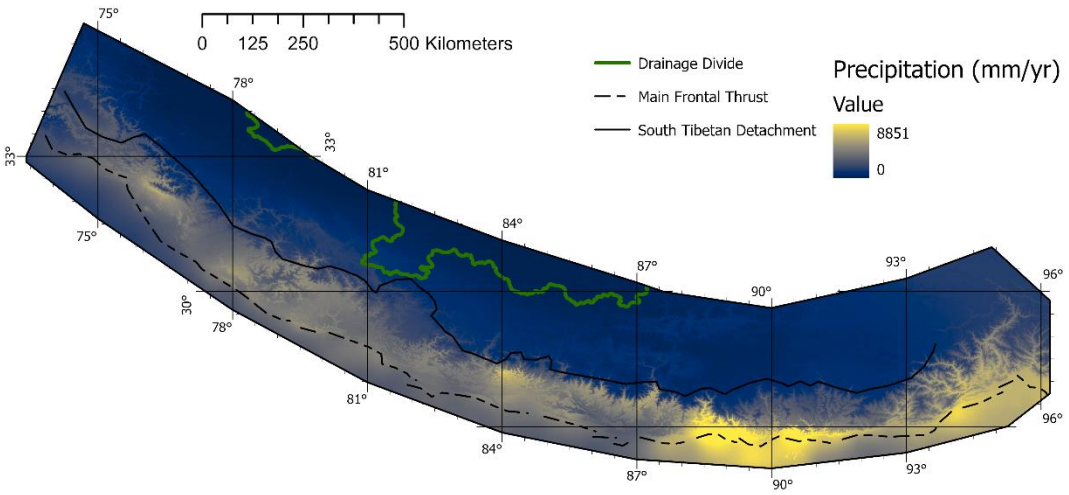

Figure 4.4: Map of annual precipitation in the Himalaya (World Clim v2). The internal-external drainage divide is shown in green.

the south, with intense rainfall concentrated on the steep slopes of the Himalaya and little precipitation to the north of the mountain chain, within the Tibetan Plateau. Glacial processes also occur in the Himalaya. A large portion of discharge in the High Himalaya is produced by snowmelt. This climatic gradient leads to a distinct erosion gradient, where precipitation and erosion rates are seen to be coupled (Bookhagen and Burbank, 2010).

4.3.1.3 Previous studies

Three physiographic transitions have been defined as PT1, PT2 and PT3 from north to south by Hodges et al., (2000). PT1 corresponds to the STD which defines the transition between the Tibetan Plateau and the Himalaya (Figure 4.3). PT3 corresponds to the MFT. PT2 is more variable and is not entirely spatially consistent with a major fault but is within the Himalayan range, typically 10-20 km south of the MCT.

The sensitivity of the landscape of the Himalaya has been noted by many studies of tectonic geomorphology. These studies show along strike variation in the Himalayan landscape (Duncan et al., 2003), a peak in k_{sn} and monsoonal precipitation at the PT2 boundary, suggested to show an active thrust (Hodges et al., 2004), use of chi analysis and k_{sn} to show the lateral extent of an active fault (Sinclair et al., 2017) and use of hypsometric integrals to show the location of maximum uplift at the Eastern Himalayan Syntaxis (Zhang et al., 2020). Tectonic geomorphology is also used to suggest the extent of the locked portion of the MHT using k_{sn} (Cannon and Murphy, 2014) and changes in relief and k_{sn} along swath profiles (Morell et al., 2015). Studies conclude that the underlying lithology is not a major control on landscape (Zhang et al., 2020; Cannon and Murphy, 2014).

There have been many studies which show the variation in erosion rates across the Himalaya. In general, these show lower rates in the Lesser Himalaya (e.g. < 0.55 mm/yr Godard et al., 2014), increased rates at the PT2 transition (e.g. ˜1 mm/yr, Godard et al., 2014) and higher rates on the southern flanks of the Higher Himalaya (e.g. 2-3 mm/yr, Godard et al., 2014). Erosion rates are found to be well correlated with channel steepness in the Central Himalaya (Morell et al., 2015, r^2 = 0.77) although a weaker correlation is found between erosion rates and slope, relief and channel steepness in the Eastern Syntaxis (Yang et al., 2018, r^2 = 0.16, 0.34, 0.28 respectively). Variation in the correlations is likely as both erosion rates and geomorphology are affected by multiple factors, such as rock uplift rates, rock erodibility, landsliding and the climatic impact on erosion rates.

4.3.2 Results

4.3.2.1 Overview

Maps of HI, SR and ZR calculated for second order drainage basins are shown in Figure 4.5. Sixteen quadrats 150x150 km in size are drawn at evenly spaced intervals along the Himalayan front, above the MFT (Figure 4.6). Sixteen swath profiles are drawn through the centre of these quadrats, 300 km in length, from ˜south to ˜north (Figure App.1, referred to as H1-H16). Geomorphic data, annual precipitation data and elevation data are included, along with modelled coupling by Stevens and Avouac (2015). The black vertical lines represent the MFT and STD, the dotted lines represent the area of the quadrats, the green dashed line represents the location of internal drainage, the shaded pink area represents the location of the locking-creeping transition as calculated by Lindsey et al., (2018) and shaded blue area represents the location of slip of the Gorkha earthquake.

4.3.2.2 Geomorphic Index Maps

HI, SR and ZR results for the Himalaya (Figure 4.5) on a broad scale show the low relief, lower elevations of the Himalayan foreland, shown in purple colours (HI < 0.2; SR < 6; ZR > 1.75) with a marked change in landscape across the MFT. The Tibetan Plateau interior, north of the STD shows low HI, high ZR and mid-low SR (HI < 0.2; SR < 12; ZR > 1.75). This boundary is also of the highest peaks of the Himalaya. The highest SR values (SR > 15) occur along the boundary between the highest Himalaya and the Tibetan Plateau. The highest HI values (HI > 0.4) occur to the south of this, within the fold-and-thrust belt.

4.3.2.3 Boxplots

The 16 boxplots (Figure 4.6) show an increase in precipitation variation (increase in IQR) from west to east along the Himalaya, although mean precipitation remains largely constant with a peak at H11. Median and mean HI and SR increase from west to east. The second invariant of strain rate is highest in the central Himalaya (H5-11) and lowest in the eastern (H1-4) and western (H12-16) Himalaya.

4.3.2.4 Strain Maps

The calculated strain rate values are shown in Figure 4.7 for the entire Tibetan Plateau. Strain crosses for the Himalaya show range parallel shortening with largest values in the centre. The Himalaya have a negative dilation rate along the range, with positive dilation (extension) only occurring in the Tibetan Plateau. Positive rotation rate (clockwise rotation) values also occur along

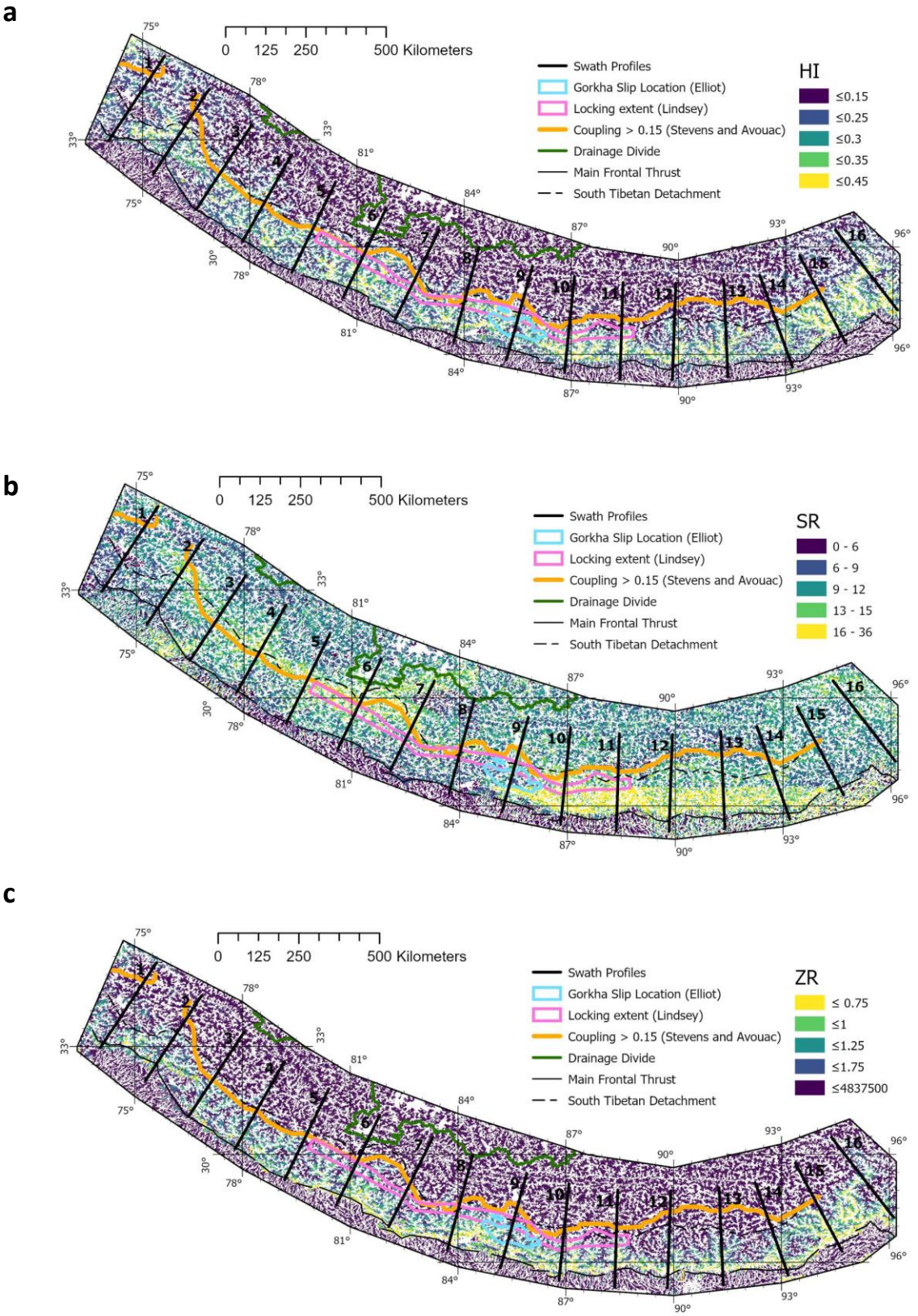

Figure 4.5: Maps of a) HI, b) SR and c) ZR calculated for second order drainage basins in the Himalaya. The location of slip in the Gorkha earthquake is shown in pale blue and the locking extents calculated by Lindsey et al., (2018) and Stevens and Avouac (2015) are shown in pink and orange respectively.

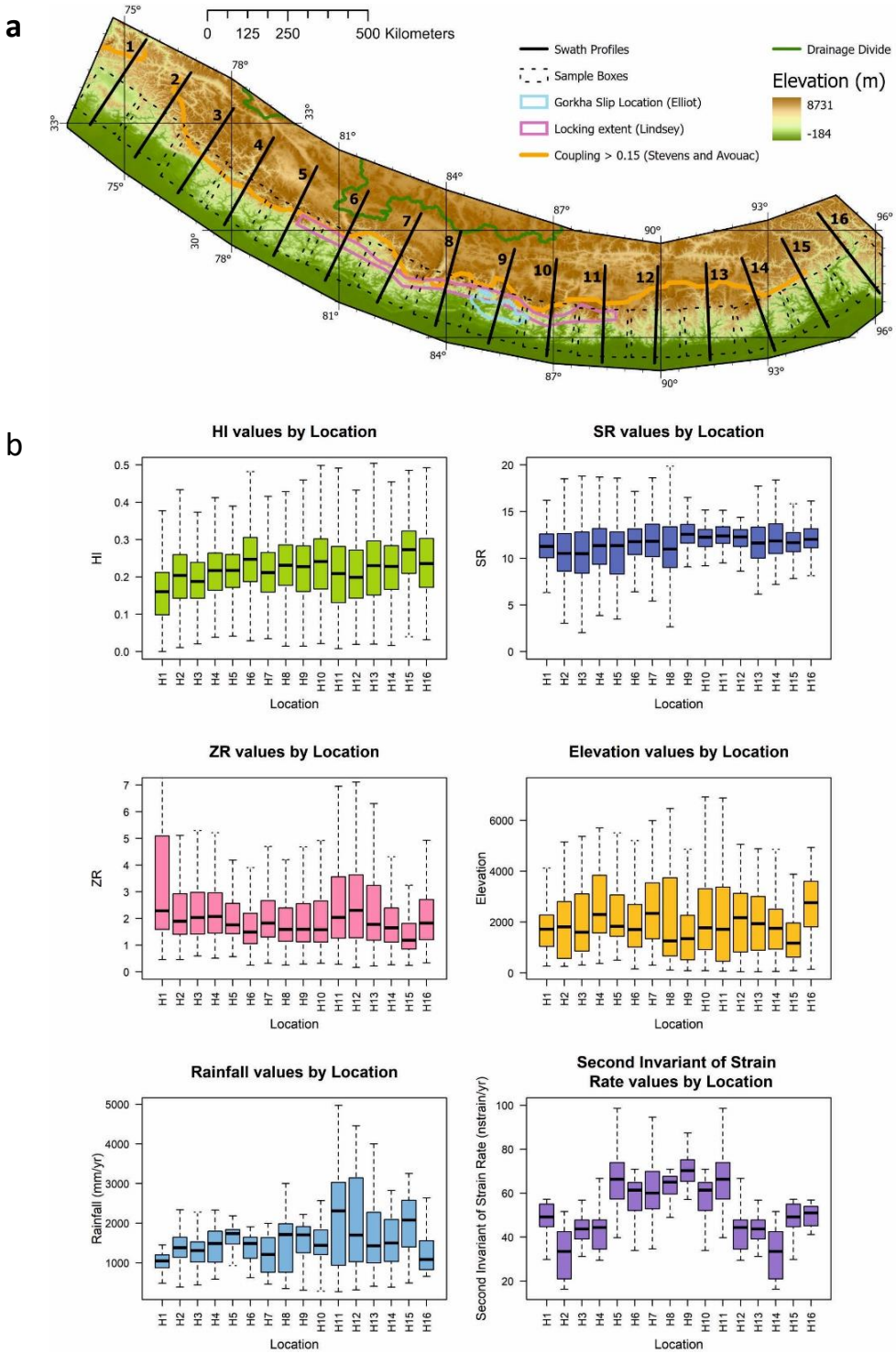

Figure 4.6: a) map of the Himalaya, showing the location of the quadrats by dashed lines and the swath traces in black, which are 300 km in length and are located through the centre of the quadrats. As in Figure 4.5 the location of slip in the Gorkha earthquake is shown in pale blue and the locking extents calculated by Lindsey et al., (2018) and Stevens and Avouac (2015) are shown in pink and orange respectively. b) boxplots for the Himalaya, showing elevation, annual precipitation, second invariant of strain rate and geomorphic indices. The boxplots represent the mean, upper and lower quartiles and range of values. The r^2 of correlation between mean precipitation and SR is 0.14 and between mean precipitation and HI is 0.12.

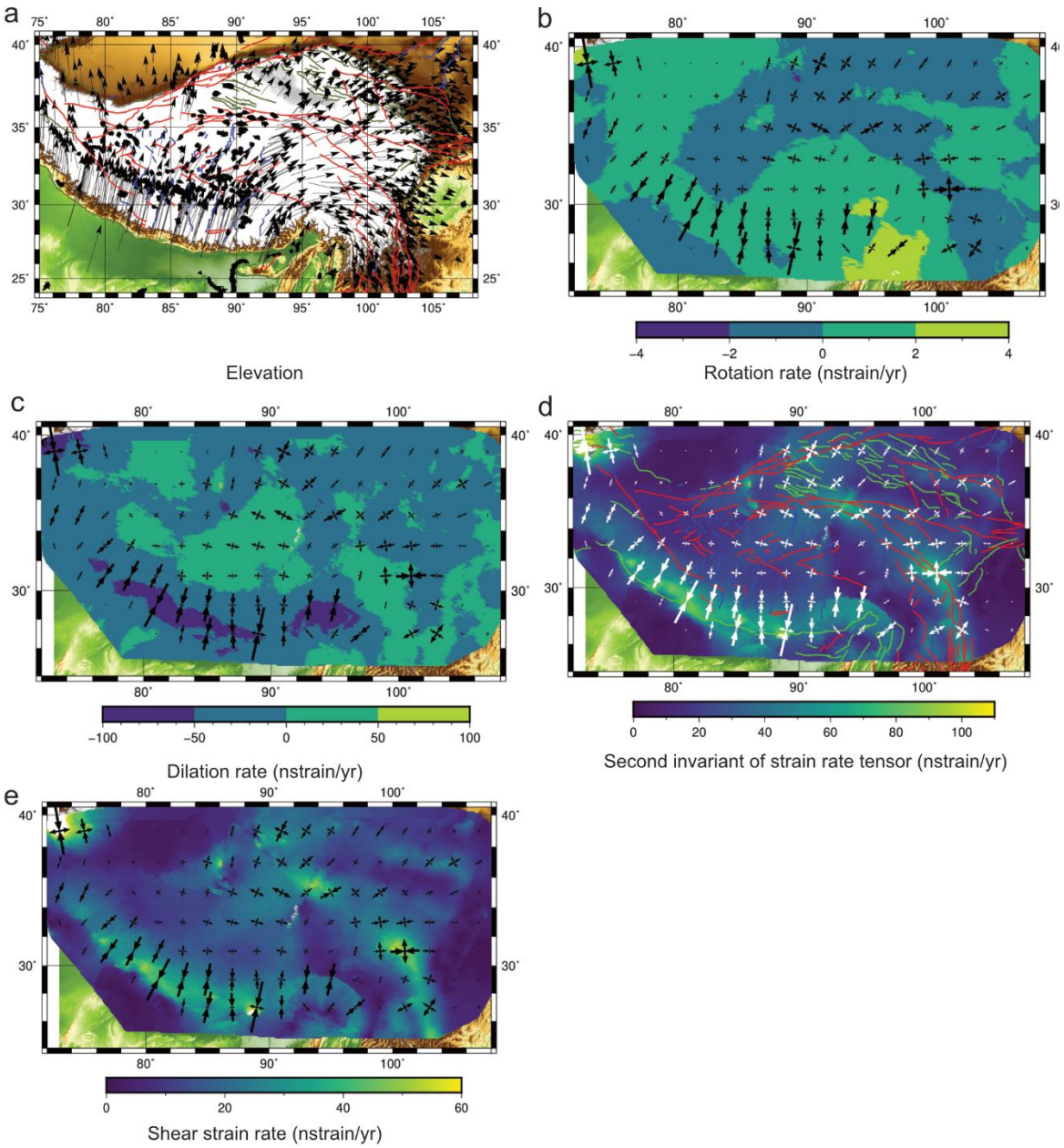

Figure 4.7: Strain rate maps for the Tibetan Plateau, including the Himalaya, showing a) GPS data points used, major faults and elevation b) rotation rate and principal strain axes in black, c) dilation rate and principal strain axes, d) second invariant of strain rate tensor, major faults and principal strain axes, e) shear strain rate and principal strain axes.

the entire Himalaya but the highest positive values occur at the Eastern Syntaxis. Shear strain rate is highest in the central Himalaya (> 50 nstrain/yr). The highest values (> 40 nstrain/yr) for the second invariant of strain rate in the Tibetan Plateau occur along the Himalaya and the highest values (> 100 nstrain/yr) in the region of or to the north of the MFT. There is further discussion of the strain rate of the Tibetan Plateau in Chapter 5.

4.3.2.5 Swath Profiles

By eye, the trends in the swath profiles (Figure App.1) show that the HI and elevation range are largely instep and ZR inversely so (peaks in elevation range correspond to peaks in HI and lows in ZR). SR is also reasonably well coupled to the elevation range (relief) and HI data, although the highest peaks in SR and the beginning of declining values into the plateau are ˜30 km further north than the peaks and beginning of declining HI values. In each swath the orographic rainfall gradient is clear, with the precipitation curve declining where the elevation starts to increase. The integrated relief, for each swath profile, for each mountain belt is shown in Table 4.2. The integrated relief for the Himalayas is variable from east to west along the Himalaya, with the highest values in swath H4 and the lowest in swath H1.

The second invariant of strain rate is included on Figure App.1. A peak in this strain rate in the swath profiles corresponds to a peak in HI in swaths H3, H4, H6-9, H12, H12, H15 and H16; a peak in SR in swaths H3, H5, H8-12; a peak in annual precipitation in swaths H2-5, H7-11 and a decline in coupling in swaths H3, H5, H6, H8-10, H12-15. These show that the highest strain rate occurs in the central Himalaya, in swaths H5-11 and it is in this central area where the clearest visual spatial correlation between the second invariant of strain rate and geomorphic indices, precipitation and coupling from the Stevens and Avouac (2015) model occurs.

4.3.3 Discussion

Previous geomorphological studies in the area conclude that the underlying lithology is not a major control on landscape (Cannon and Murphy 2014; Zhang et al., 2020). In this work the geomorphic indices are interpreted to show variations in tectonic and/or climate related erosion. Glacial erosion is also likely to be controlling the landscape morphology of the high Himalaya. The along strike gradient in Himalayan precipitation, which increases from west to east, may partially control the geomorphic indices: there is a small but variable increase in median SR and HI from west to east (Figure 4.6). However, the precipitation curves in the swath profiles do not show peaks corresponding to each peak in HI and SR, instead the peak is where elevation increases. The peaks

Integrated Relief (km^2)				
Swath Number	Himalaya	Qilian Shan	Andes	Zagros
1	440	321	282	343
1.5			229	
2	501	302	235	184
2.5			163	
3	497	241	200	294
4	629	282		215
5	554	195		222
6	454	288		277
7	461			242
8	462			213
9	430			213
10	501			200
11	475			
12	561			
13	506			
14	507			
15	501			
16	501			
Mean	499	272	222	240
Maximum	629	321	282	343
Minimum	430	195	163	184
Standard Deviation	48	42	39	47
% Difference from Minimum	46	64	73	86

Table 4.2: Integrated relief of each swath profile, in km^2.

in HI and SR further to the north are therefore not precipitation controlled. There is no apparent correlation between the integrated relief and the precipitation or elevation (Table 4.2; Figure 4.6).

The coupling on the detachment underlying the Himalaya, as calculated by Stevens and Avouac (2005), is shown as a curve in the swath profiles (Figure App.1). This allows us to compare the trends in the geomorphic data to the location of the decline in coupling. In most swaths the decline in coupling is clear. Stevens and Avouac (2015) describe a sharp transition from locked to creeping behaviour at ˜100 km downdip from the surface trace of the Main Frontal Thrust. However, in the Western Himalaya they show the transition from fully coupled to fully uncoupled to be much wider and more diffuse, occurring at ˜150 km downdip from the emergent fault trace. The coupling decline in swaths H14 and H15 in the Western Himalaya is not steep and therefore comparisons

are not easily made to the geomorphic data (Figure App.1). The same is true for swath H2 in the eastern Himalaya. The patterns of geomorphic indices are complicated, as shown by the swath profiles. In general, relief (relief = maximum-minimum elevation along the swath, also referred to as the elevation range) mainly decreases where coupling is < 0.5; SR mainly decreases where coupling is < 0.25; HI mainly decreases where coupling is between 1 and 0.75 and ZR mainly begins to increase where coupling is ˜0.25.

The highest HI values (HI > 0.4) are concentrated above the locked or coupled portion of the MHT, to the south of the line where coupling > 0.15, shown in orange (Figure 4.5a). The seismogenic to non-seismogenic transition (degree of coupling) is not a discrete zone (as shown by the slope of the coupling swaths; Figure App.1). A coupling value of 0.15 is arbitrary but it is chosen as coupling values of < 0.15 occur over a broad region down dip of the fault. The decline in HI values, shown clearly in Figure App.1, occurs in the location where coupling begins to decrease. Therefore, HI begins to decrease northwards where the change from locked to creeping behaviour occurs on the MHT, as shown by both the Stevens and Avouac (2015) curve and the shaded area defined by Lindsey et al., (2018). The exception to this pattern is in swath H11, where a large peak in HI occurs to the north of the MFT and the northwards decline in HI begins to the south of the locked-creeping transition. This is likely to be due to extremely high HI values occurring in the wettest part of the Himalayan range.

The highest SR values occur at the boundary between the Himalaya and Tibetan Plateau, further north than the highest HI values (Figure 4.5b). This is the PT1 transition identified by Hodges et al., (2000). This relationship may be due to the SR being more sensitive of the highest slopes, whereas the HI is more sensitive to a large range of elevation values, or high SR values being due to glaciation. SR mostly declines northwards, with the decline beginning in the region of declining coupling (Figure App.1; Stevens and Avouac, 2005), where the fault is partially creeping and partially locked. HI declines where the fault ceases to be fully locked. The exceptions to this pattern are swaths H4, H6, H7 and H12 where SR declines northwards where the MHT is fully creeping and H3 where SR does not show a clear decline.

The lowest ZR values (ZR < 0.75) are also located above the locked portion of the MHT (Figure 4.5c). A sustained northwards increase in ZR begins in each swath at the locked-creeping transition (Figure App.1).

The second invariant of strain rate is included on Figure App.1. A peak in strain rate in the swath profiles corresponds to a peak in HI in swaths H3, H4, H6-9, H12, H12, H15 and H16 a peak in SR in

swaths H3, H5, H8-12; a peak in annual precipitation in swaths H2-5, H7-11 and a decline in coupling in swaths H3, H5, H6, H8-10, H12-15. The highest strain rate occurs in the central Himalaya, in swaths H5-11 (Figure 4.6). It is in this central area where the clearest visual spatial correlation between second invariant of strain rate and geomorphic indices, precipitation and coupling from the Stevens and Avouac (2015) model is seen.

Therefore, overall, the pattern of HI, SR and ZR in the Himalaya is correlated with the transition from locked to creeping behaviour on the MHT. These results are consistent with the extent of the locked portion also being the extent of seismicity, pulsed uplift and landsliding. The high elevation and low relief surface to the north of the orange line, marks the area overlying creeping behaviour on the detachment. The second invariant of strain rate broadly matches the landscape and the coupling but the peaks in geomorphic indices do not always match peaks in the strain rate: this may be due to the spatial smoothing which occurs in the calculation of the strain rate, meaning that it may not be appropriate to compare these two measures.

Previous studies show complementary results. For example, there is a correlation between coupling and channel steepness (Cannon and Murphy, 2014) as well as between coupling and HI and SR in this study (Figure App.1). The basin wide geomorphic indices identify active faulting and correlate to relief (Figure 4.5; Morell et al., 2015). High values of channel steepness calculated by Morell et al., 2015 and Hodges et al., 2003 occur in the same spatial location as values of high HI and SR in Figure 4.5.

4.4 Qilian Shan

4.4.1 Introduction

The patterns of geomorphic indices (HI, SR, ZR as well as k_{sn}) are described for the Qilian Shan in Chapter 2. The study concluded that the overall geomorphic pattern was controlled primarily by the underlying structure. The north to south change from high HI and SR and low ZR coincides spatially with the change from locked to creeping behaviour on an underlying detachment. This locked-creeping transition is spatially coincident with the strike-slip Haiyuan Fault (Allen et al., 2017).

4.4.2 Results

4.4.2.1 Geomorphic Index Maps

Six quadrats 100 x 100 km in size are drawn from WNW to ESE along the Qilian Shan range. These quadrats are located between the frontal thrusts of the Qilian Shan and the internal drainage boundary and therefore this considers the fold-and-thrust belt rather than the foreland or plateau region (Figure 4.8). This is comparable to the quadrats studied in the other fold-and-thrust belts in this study. Six swath profiles are drawn from ˜NNE to ˜SSW, 30 km in width and 350 km in length (Figure App.2), with swath QS1 in the West and QS6 in the East. The dotted vertical lines show the area included in the quadrats, the vertical green dashed line the extent of internal drainage and the vertical black line the location of the Haiyuan Fault. In summary, high HI and SR occur above the locked portion of the underlying detachment (Figure App.2; to the left of the solid black vertical lines in the swaths).

4.4.2.2 Boxplots

Boxplots, using data from the 6 100 x 100 km quadrats shown are shown in Figure 4.8. These show the east-to-west decline in annual precipitation. There is no east-to-west trend in the HI and SR data. The second invariant of strain rate is highest in quadrat Q5 and lowest in quadrat Q2.

4.4.2.3 Strain Rate Maps

Strain rate maps for the Qilian Shan are shown in Figure 4.9. The outlines of the two major lakes in the area are shown. The larger is Qinghai Lake and the smaller is Hala Lake. Strain rate crosses show the NE-SW shortening direction across the Qilian Shan range. High values of the second invariant of strain rate occur in the northern margin of the Qilian Shan fold-and-thrust belt, with the highest values (> 30 nstrain/yr) concentrated in the region to the north of Qinghai Lake, near to the location of the Haiyuan Fault. The map of dilation rate shows positive values (extension) in the region to the south of Qinghai Lake and compression in all other areas, with the lowest values (< -15 nstrain/yr) at the mountain front to the north of Hala Lake. Rotation rate is negative (anticlockwise) in the northern Qilian Shan and positive in the southern Qilian Shan. High shear strain rate (> 20 nstrain/yr) occurs near to the 2 major strike slip faults, the Altyn Tagh Fault to the NW of the range and the Haiyuan Fault in the centre of the range.

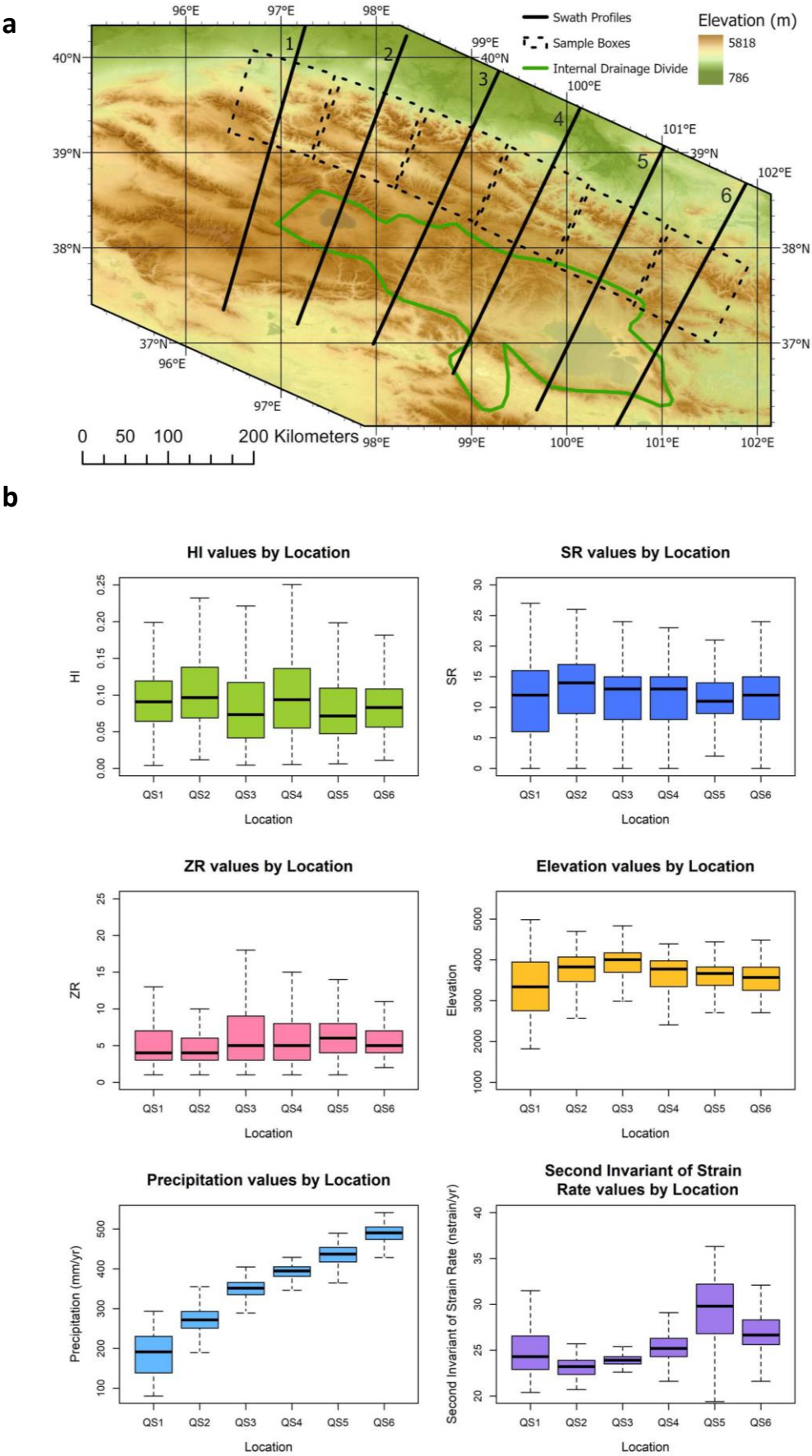

Figure 4.8: a) Qilian Shan location map showing the internal-external drainage divide in green and the location of the quadrats used in the analysis. b) boxplots for the Qilian Shan, showing elevation, annual precipitation, second invariant of strain rate and geomorphic indices. The boxplots represent the mean, upper and lower quartiles and range of values. The r^2 of correlation between mean precipitation and SR is 0.02 and between mean precipitation and HI is 0.35.

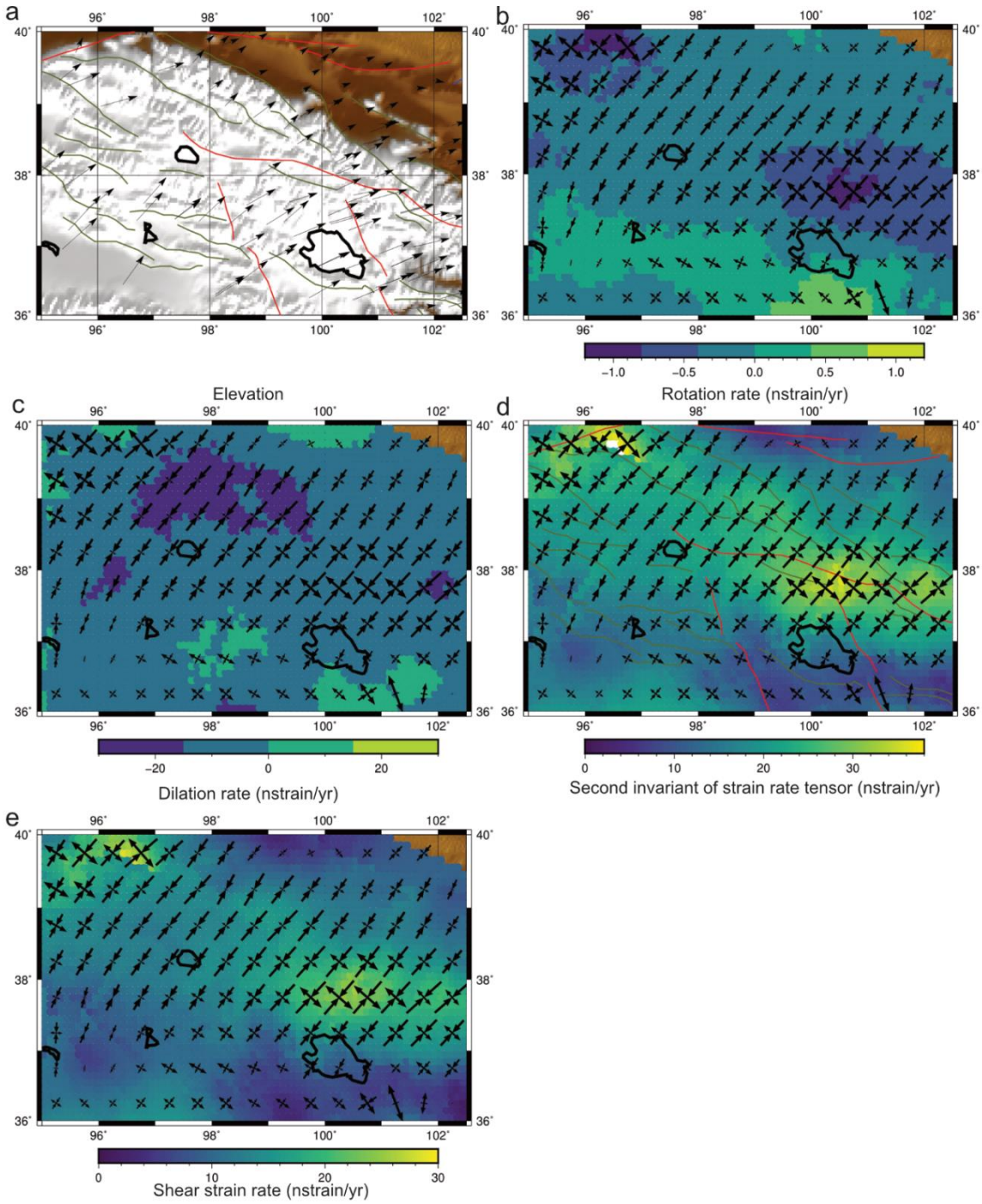

Figure 4.9: Strain rate maps for the Qilian Shan with lake outlines in black showing a) elevation and GPS points used b) rotation rate and principal strain axes in black, c) dilation rate and GPS points used, d) second invariant of strain rate, major faults and principal strain axes, e) shear strain rate and principal strain axes.

4.4.2.4 Swath Profiles

A detailed description of seven different swaths drawn through the area is given in Chapter 2 including a description of changes in HI, SR, ZR, elevation and precipitation. The second invariant of strain rate is compared to the geomorphic indices, annual precipitation and elevation in Figure App2. The highest peaks in strain rate in the swath profiles corresponds to a peak in HI in swaths

QS1-3 and QS5; a peak in SR in swaths QS1 and QS3-5 and a southward change to continued high in annual precipitation in swaths QS2-6. The location of the peak in strain rate and the location of the Haiyuan Fault are broadly similar in swaths QS4-6 but not in the more western swaths. This is most likely due to the degree of smoothing between the spatially dispersed GPS datapoints used in the calculation of strain rate. The integrated relief for the Qilian Shan is highest in swaths QS1 and QS2 and lowest in swaths QS3-5 (Table 4.2 in Section 4.3.2.5).

4.4.3 Discussion

The descriptions and interpretations of the patterns identified in the geomorphic indices (HI, SR, ZR as well as k_{sn}) are described in detail for the Qilian Shan in the Chapter 2. The study concluded that the overall geomorphic pattern is controlled primarily by the underlying structure, rather than underlying lithology or precipitation. The integrated relief does not appear to be related to precipitation (Table 4.2 in Section 4.3.2.5; Figure 4.8). The highest integrated relief is in swath QS1. This is the only swath which does not include the internally drained, low relief central plateau. The north to south change from high HI and SR and low ZR coincides spatially with the change from locked to creeping behaviour modelled on an underlying detachment. The location of the change from locked to creeping behaviour occurs at the location of the strike-slip Haiyuan Fault, shown by the vertical black line in swaths QS2-Q5 (Figure App.2). High HI and SR values occur to the left of this line, meaning to the NE of the Haiyuan Fault. The east of the Qilian Shan, in the region of swath QS6, is the only profile that does not show the clear pattern of high HI and SR and low ZR above the locked portion of detachment only. This is due to the thrust-parallel drainage in the region, which creates a distinct morphology (discussed further in Chapter 2). The change from high HI and SR and low ZR is roughly coincident with high values of the second invariant of strain rate (Figure App.2) but this relationship is not as clear as that between the locked-creeping transition at the Haiyuan Fault and the geomorphology. This could be due to spatial smoothing in the calculation of strain rate.

4.5 Andes

4.5.1 Introduction

4.5.1.1 Location

The Andes are formed by the subduction of the Nazca Plate under the South American Plate, forming the long Andean mountain chain and plateau. The central Andes, at ˜20°S is over 800 km

wide and has the highest elevations (> 4km) and thickest crust (> 60km) of any modern-day subduction zone (Assumpção et al., 2013). The area of focus for this work is the Central Andes between 20 and 26°S (Figure 4.10). The area is formed of the Western and Eastern Cordillera (fold-and-thrust belts) with the internally drained Puna Basin in the centre. To the north of the Puna Basin is the internally drained Altiplano Basin, which is higher elevation and lower relief than the Puna (Barnes and Ehlers, 2009). Together the basins form a large composite plateau called the Altiplano-Puna Plateau, which is 3.8-4.5 km high, 1800 km long and 350-400 km wide. It is low relief and has experienced low erosion rates of < 0.02 mm/yr both in the modern day and since the Miocene (Karátson et al., 2012; Bookhagen and Strecker, 2012). It is the only modern-day tectonic plateau formed by ocean-continent subduction and is the second largest tectonic plateau globally, following the Tibetan Plateau (Barnes and Ehlers, 2009; Garzione et al., 2017).

Orogen-normal shortening began in the Eocene, with deformation propagating eastward and southward and uplift of the plateau began in the Miocene, at the peak of plate convergence (Deeken et al., 2006). Deformation of the Santa Barbara region of the Eastern Cordillera, which is to the east of the Puna Plateau is thick-skinned, with high angle reverse faults, whereas the Sub-Andean belt, which borders the Altiplano basin shows thin-skinned deformation (Kley and Monaldi, 1998). The crust of the Altiplano-Puna Plateau is largely aseismic, with a few strike-slip and extensional events in the Altiplano region (Devlin et al., 2012). Most seismicity is concentrated in the Eastern Cordillera (Devlin et al., 2012).

Geodetic data have been continuously collected for the past ˜30 years in the central Andes. Modelling of this geodetic data suggests that the subduction interface accounts for ˜90 % of convergence (Bevis et al., 2001). Models have suggested that an underlying, west-dipping detachment, locked between 10 and 50 km depth, is present in the Central Andes. This detachment accounts for the remaining convergence at a rate of > 10 mm/yr. Brooks et al. (2011) and Weiss et al. (2016) studied ˜17 - 23°S latitude and did not consider the subduction interface in their modelling, due to the distance from the interface. The work of McFarland et al., (2017) is further south, between latitudes of 23 and 25°S and considered both locking on the subduction interface and deformation along a basal, west-dipping detachment. Their work also concluded that the proportion of strain accommodated at the subduction interface is likely to be as low as 70 % and the remaining strain is accommodated on the west-dipping detachment. McFarland et al., (2017) showed that the extent of the locked portion is coincident with the extent of micro-seismicity and

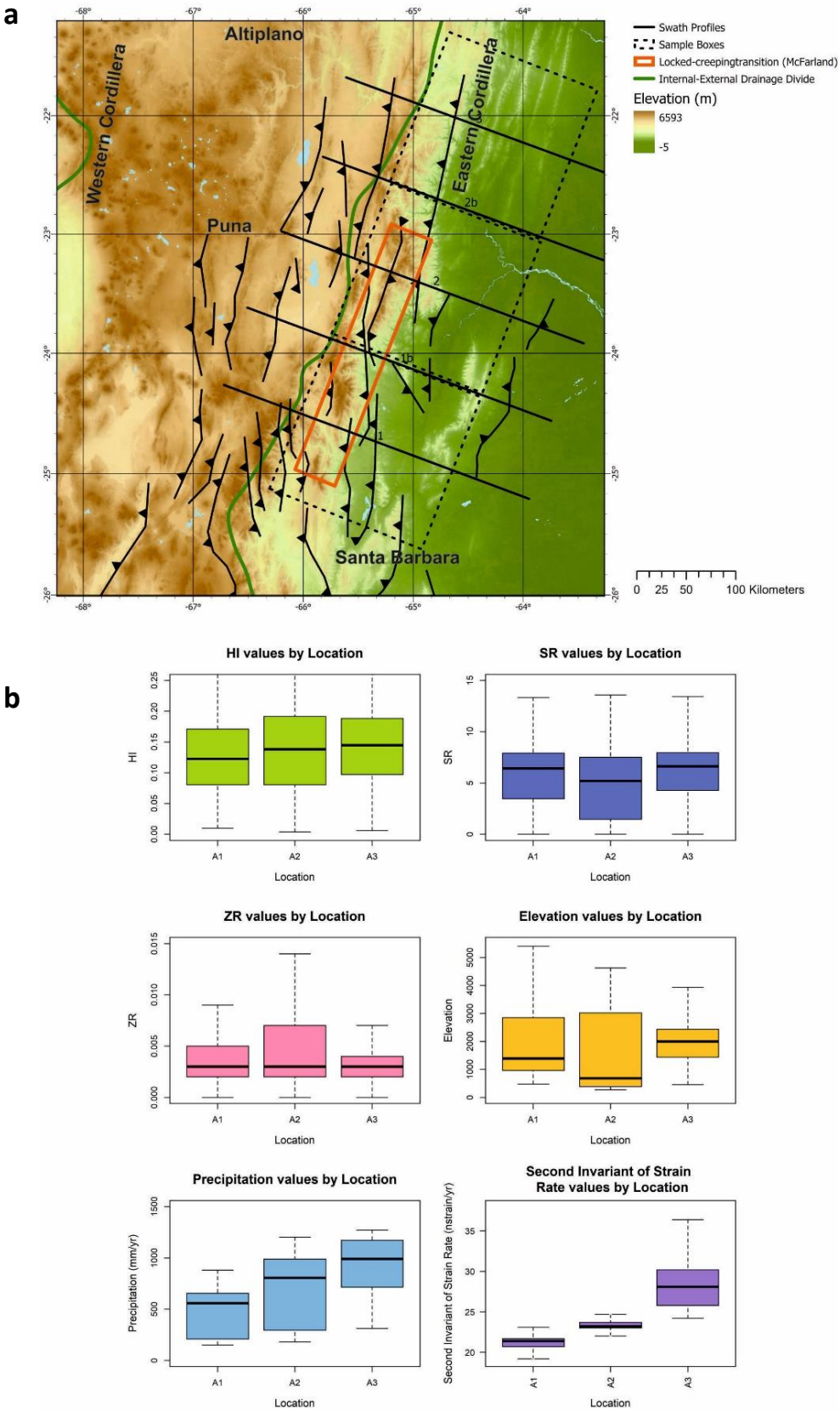

Figure 4.10: a) map of the Andes, showing the location of the sample quadrats by dashed lines and the swath traces in black, which are 300 km in length and are located both through the centre of the quadrats and in between the quadrats. b) boxplots for the Andes, showing data from south to north. These show elevation, annual precipitation, second invariant of the strain rate and geomorphic indices. The boxplots represent the mean, upper and lower quartiles and range of values. The r^2 of correlation between mean precipitation and SR and HI is not calculated due to having only three datapoints.

a possible change in the geotherm, with cooler temperatures and a steeper geotherm in the east, which may favour stick and slip behaviour.

4.5.1.2 Climate

Climate has played an important role in Andean development. A large precipitation gradient due to topography creates a large erosional gradient. Uplift of the Eastern and Western Cordillera formed orographic barriers leading to arid conditions in the Altiplano-Puna. Aridity led to defeat of the fluvial systems. This internal drainage means erosion and deposition occurs within these basins, giving them their low relief topography (Alonso et al., 2006). Evaporite deposition beginning in the Miocene in the Puna and low exhumation rates are evidence of an arid climate (Strecker et al., 2007 and references within). The orographic barrier of the Eastern Cordillera now receives > 750 mm/yr precipitation in this region, at 23-25 °S and the moisture-shielded Puna receives < 200 mm/yr. Precipitation is seasonal, with > 55 % falling in the summer months of November-February in the Puna Basin (Figure 4.11). Wet periods have induced landsliding and slumping on windward flanks and these may be related to enhanced El Niño Southern Oscillation (ENSO) periods (Trauth et al., 2003).

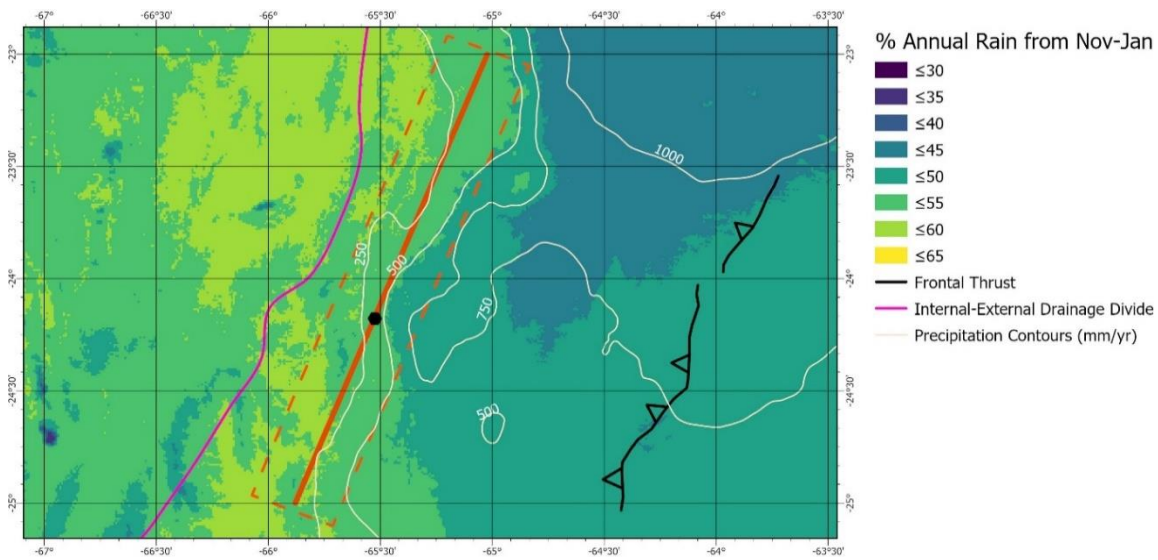

Figure 4.11: Map of seasonal precipitation in the Andes (World Clim v2), showing the percentage of rain that falls in the summer months of November to January. The internal-external drainage divide is shown in pink, the frontal trust in black. The location of the locked-creeping transition as defined by McFarland et al., (2017) is shown by the black dot and this transition is projected to the north and south, shown by the solid orange line, with the dashed orange line representing error. This is also shown in Figure 4.10.

4.5.1.3 Previous geomorphic work

Geomorphic studies have been carried out across the Andes, although not specifically in the area of study. The geomorphology has given insight into both tectonic and climatic processes. Hypsometry is found to correlate well with modern erosion rates in the North-Central Andes (5-20 °S; Lowman and Barros, 2014). Mountain front sinuosity and valley-shape ratios calculated in the South-Central Andes (23-28 °S) highlight Quaternary-recent surface deformation from mountain-front thrust faults (Daxberger and Riller, 2015). Channel steepness calculations on the Western Cordillera (18.5-22 °S) suggest 1 km surface uplift in the last 10 Ma (Hoke et al., 2007). Stream power, calculated using precipitation data and upstream area, is related to erosion rates in the Central Andes (21-29 °S) up to a threshold of 0.2 mm/yr erosion rate, above which rate non-fluvial transport and sediment availability is a more dominant control (Bookhagen and Strecker, 2012). This work also shows channel slopes to vary with precipitation. The region to the east of the Puna Plateau is an area of transient drainage, where the marginal basins have alternated between being internally and externally drained. This history of drainage reorganisation may have altered the landscape in the region. It is suggested that these basins have never been fully incorporated into the plateau due to variations in tectonic displacement (Alonso et al., 2006). These variations allow the fluvial systems to stay connected to or easily reconnect to the foreland, while the high precipitation gradient focuses erosion on the windward slopes, leading to headward erosion and promoting stream capture.

4.5.2 Results

4.5.2.1 Overview

Maps of HI, SR and ZR as calculated for second order drainage basins are shown in Figure 4.12. Three 150 x 150 km square quadrats are drawn along the strike of the Andes. Three swath profiles 30 km wide and 300 km long were drawn through the centre of these quadrats, between the frontal thrusts and plateau (Swaths A1-A3; Figure App.3). It should be noted that the swaths are drawn from east to west, to allow for easier comparison to the other fold-and-thrust belts in this study, as this means that the foreland is located consistently at the left-hand side of the swath profiles. The extent of the quadrats are shown on the swath profiles by dotted black lines. Two additional swath profiles were drawn between the quadrats to give more data (swaths A1b and A2b; Figure App.3). The green vertical dashed lines represent the location of the internal-external drainage boundary. The location of the locked-creeping transition on the underlying detachment, as defined by McFarland et al., (2017) is shown by the shaded area on the swaths.

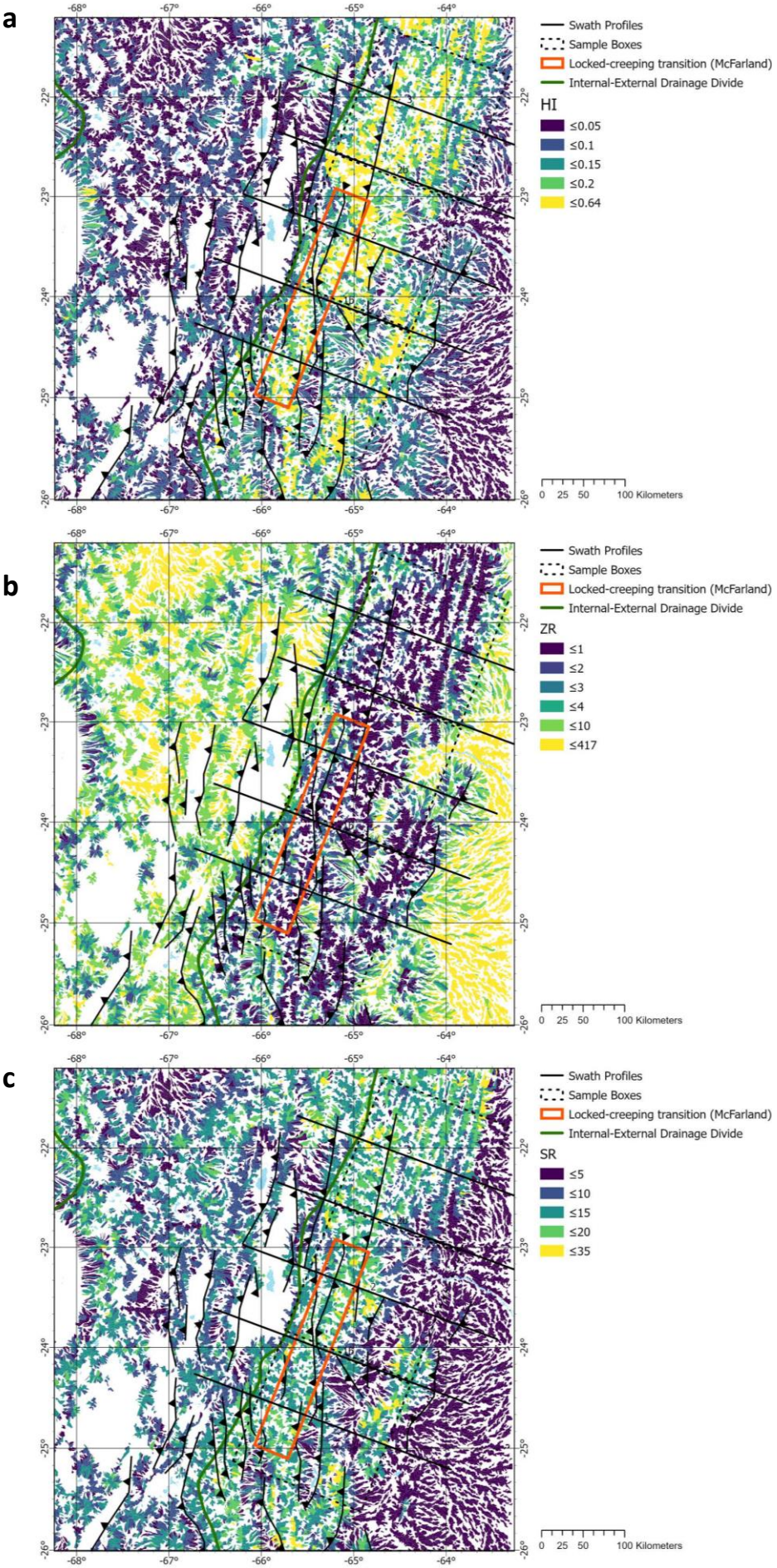

Figure 4.12: Maps of a) HI, b) SR and c) ZR calculated for second order drainage basins for the Andes. Swath profile traces, thrust fault traces and the location of the locked-creeping transition (McFarland et al., 2017) are shown.

4.5.2.2. Geomorphic Index Maps

Low SR values (SR < 15; Figure 4.12b) occur in the Andean foreland and in the internally drained Puna plateau, meaning these areas exhibit low relief. High SR values (SR > 20) are concentrated in the Eastern Cordillera and in the hanging wall of the frontal thrust fault. Low HI values (HI < 0.1; Figure 4.12a) occur in the internally drained plateau and to the east of the Santa Barbara range. High HI values (HI > 0.15) occur across the Santa Barbara Range. High ZR values (ZR > 4), indicating high elevation and low relief landscapes, occur in the internally drained Puna basin and to the east of the frontal thrust of the Eastern Cordillera (Figure 4.12c). Low ZR (ZR < 3) occurs in the area of the Eastern Cordillera.

4.5.2.3 Boxplots

The distribution of precipitation shown in the boxplots of the Andes data (Figure 4.10) shows the along-strike precipitation gradient in this area of the central Andes, which is wettest in the north. SR, ZR and elevation show no correlation with the precipitation, as there is no north-south gradient in the data. HI shows a northwards increase in the median HI values but this is very slight (0.12 to 0.13). The boxplots show that the second invariant of strain rate increases from south to north. This strain rate gradient varies in the same direction as the precipitation gradient. There is a small south-north increase in HI but no trend in the other geomorphic indices or in the distribution of elevation.

4.5.2.4 Strain Rate Maps

Strain Rate maps for the Andes are shown in Figure 4.13. The strain arrows show that shortening is east-west throughout the area. Dilation rate is positive across this area of the Andes, with the lowest values (< 10 nstrain/yr) in the mountain front of the Eastern Cordillera. Rotation rate is positive in the north of the area and negative in the south. The shear strain rate is 10-20 nstrain/yr in the mountain front, with lower values above the plateau (<10 nstrain/yr). The second invariant of strain rate is 20-30 nstrain/yr in the mountain front, with lower values above the plateau (<20 nstrain/yr).

4.5.2.5 Swath Profiles

HI, SR and the maximum-minimum elevation curves are well matched, with the data peaking in the same locations in the swath profiles. Low ZR values correspond to these HI and SR peaks (Figure

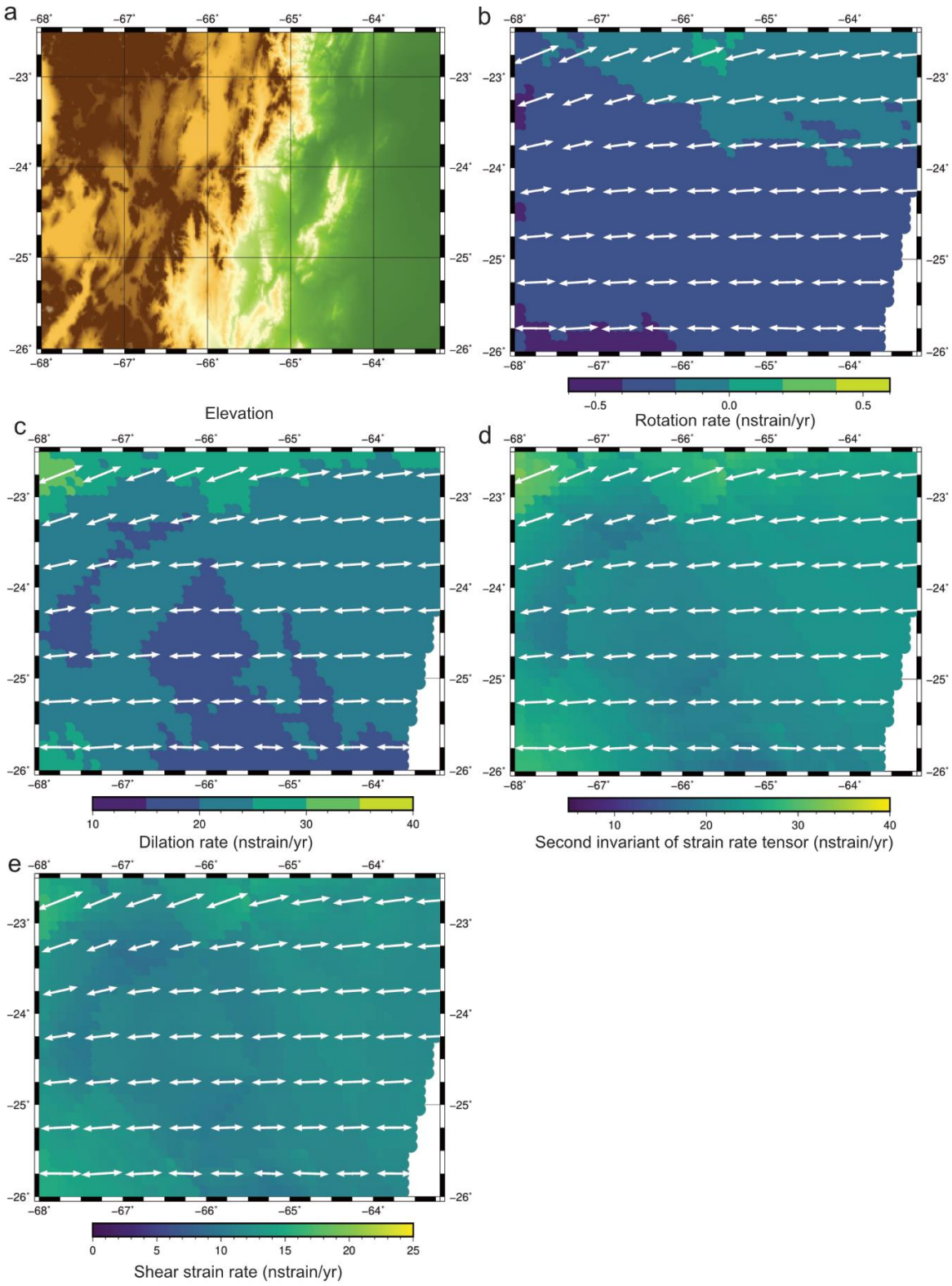

Figure 4.13: Strain rate maps for the Andes showing a) elevation b) rotation rate and principal strain axes in white, c) dilation rate and principal strain axes, d) second invariant of strain rate, major faults and principal strain axes, e) shear strain rate and principal strain axes.

App.3). In each profile the decline in HI and SR and increase in ZR occurs within the externally drained region, rather than at the internal-external drainage boundary. Swaths A1, A1b and A2 allow for comparison to the locked-creeping transition as defined by McFarland et al., (2017). In swaths A1 and A1b the location of this transition corresponds to the location of the start of a continued decline in HI and SR and an increase in ZR. In swath A2 this location is further to the east than the suggested location of the locked creeping transition. The integrated relief is highest in the SW of this region of the Andes, decreasing to the NE (Table 4.2 in Section 4.3.2.5).

Along the swath profiles the second invariant of strain rate declines towards the west in swaths A1 and A1b, with highest strain rate (> 23 nstrain/yr) in the foreland of the Eastern Cordillera (Figure App.3). The largest peaks in HI and SR occur where strain rate is low (<22 nstrain/yr). In swaths A2 and A2b the second invariant of strain increases to the west. Peaks in HI, SR and relief occur where strain begins to increase westward (>23 nstrain/yr) but the highest strain values (>25 nstrain/yr) occur further to the west of these peaks, at higher elevations. In swath A3 the second invariant of strain peaks in the centre of the swath (>29 nstrain/yr), in the same location as the peak in HI and slightly to the east of the peak in SR.

4.5.3 Discussion

Deformation in this area of the Andes is thought to be accommodated on a west dipping detachment, the surface expression of which is the frontal thrusts of the Eastern Cordillera. The orange box on the maps (Figures 4.12 and 4.14) and the shaded area on the swath profiles represents the location of the locked-creeping transition on this detachment, as modelled by McFarland et al., (2017). The extent of the creeping portion occurs to the west of the identified line (Figures 4.14 and 4.15) and the locked portion of the fault occurs between this location and the frontal thrust.

There is a change in geomorphic indice values across this locked-creeping transition. This includes a change to sustained low HI and SR and high ZR values above the creeping portion of the fault (Figure App.3). In swaths A1 and A1b the location of the locked-creeping transition (McFarland et al., 2017) corresponds to the location of the start of a continued decline in HI and SR and an increase in ZR. In swath A2 this location is ˜10 km further to the east than the suggested location of the locked creeping transition. This pattern is not clear-cut. Part of this may relate to the uncertainty in the geodetic modelling, as this is projected from the central black point. Also, the downdip

transition from locked to creeping behaviour is unlikely to be linear and is also likely to occur over a wide area. The precipitation across these swaths is similar and therefore this difference is unlikely to be climatically controlled.

Previous studies show that in this region of the Andes channel slopes vary with precipitation (Bookhagen and Strecker, 2012) but comparisons of mean geomorphic indices and precipitation along the Andes do not show a correlation (Figure 4.10). This may be due to studies being on varying scales, meaning there may be localised correlations between precipitation and geomorphic indices, but no or weak correlations across a larger area. Geomorphic indices in this and other studies (channel steepness, mountain front sinuosity, valley shape) show active faulting (Daxberger and Riller, 2015; Hoke et al., 2007). The integrated relief (Table 4.2) decreases to the NE and the precipitation and strain rate increase to the NE, suggesting that the integrated relief is not controlled by these factors.

In each profile the decline in HI and SR and increase in ZR occurs within the externally drained region, rather than at the internal-external drainage boundary (Figure App.3). This suggests that the geomorphic transition is not controlled by the drainage patterns. I conclude that the geomorphic indices are at least partly controlled by the underlying structure, with the east to west transition in the landscape roughly coincident with the change of behaviour on the underlying detachment.

The calculation of crustal strain rate uses all GPS measurements in the region but these are much sparser than for the other study areas (Table 4.1). There is no consistent relationship between the second invariant of strain rate and the geomorphic indices (Figures 4.12 and 4.15). In swath 3 the peak in the second invariant of strain rate (magnitude of strain) occurs in the same location as the peak in HI and SR but in the four swaths to the south there is no clear relationship. This may be because the variation in strain rate is very low across the region, for example the range of values in swaths 1, 1b and 2b is < 2 nstrain/yr (Figure 4.10).

4.6 Zagros

4.6.1 Introduction

4.6.1.1 Location

The Zagros fold-and-thrust belt is one of the largest and most active globally (Mouthereau et al., 2012). It is 1800 km in length and spans from the south-eastern Turkey to southern Iran (Vera and

Gines, 2009). The fold-and-thrust belt was formed by the collision of the Arabian and Eurasian plates. This current collision reactivated faults formed by past compressional and extensional events in the region, initiated by the closure of the Neo-Tethys (Stern and Johnson, 2010). The Arabian plate is currently moving northwards at a rate of ˜16-26 mm/yr, shown by GPS measurements (Vernant et al., 2004). The Zagros is composed of folded sedimentary cover from the Arabian plate and underlying basement. The timing of initial collision is debated, with suggestions of the Late Cretaceous (Mazhari et al., 2009), Early Miocene (Fakhari et al., 2008; Okay et al., 2010) and the Mid-Late Miocene (Guest et al., 2006).

The structure of the Zagros is complex but is largely composed of "whaleback" folds which trend NW-SE in most of the range, gradually changing to an east-west trend in the south of the mountain range. The regional topography (Figure 4.14) shows a steep north-eastward increase in elevation from sea level across the fold-and-thrust belt, to peak elevations of ˜4000 m. Thrust seismicity and geodetically-detected shortening indicate active crustal deformation at lower elevations (<1250 m). The Turkish-Iranian Plateau lies northeast of the Zagros and is characterised by low relief, little convergence and rare strike-slip seismicity. A marked cut-off in thrust seismicity occurs at 1250 m elevation, with rare thrust seismicity above this elevation (Nissen et al., 2011). Elevations continue to rise beyond this elevation but with little evidence of upper-crustal shortening (Allen et al., 2013). This thrust limit has been suggested to be caused by variations in the strength and depth of the underlying basement (Nissen et al., 2011), or by the thicker, higher elevation crust suppressing the seismicity (Allen et al., 2013).

The Zagros is divided into different zones, known as embayments and salients (arcs), based on variations in elevation, exhumation and relief (from NW to SE: Kirkuk embayment; Pusht-e kuh arc; Dezful embayment; Fars arc; Figure 4.14) along its 1800 km length. The deformation front is linear along the length of the Zagros, with the exception of a curved front in the Fars region in the SE. Along the length of the Zagros, structures such as the Mountain Front Fault are not continuous, with the exception of the High Zagros Fault, which separates the High Zagros Zone and the Zagros Simply Folded Zone.

Deformation in the Zagros is not considered to be accommodated by an underlying detachment but by discrete and relatively steep thrust faults (>30°). This is in contrast to the Himalaya, Qilian Shan and Andes considered in this chapter. Instead, the geomorphic indices are compared to the location of the 1250 m elevation seismogenic cut-off.

a

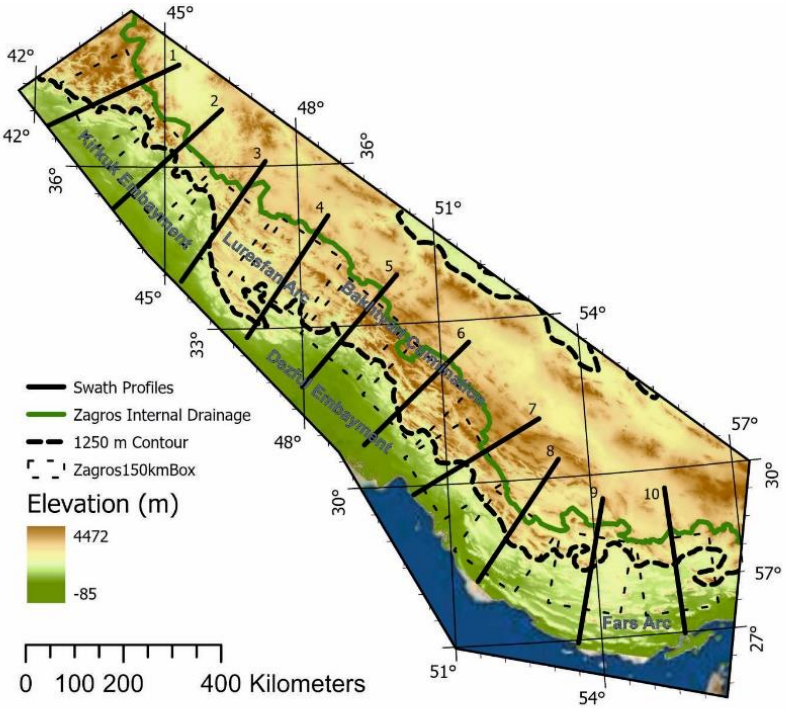

b

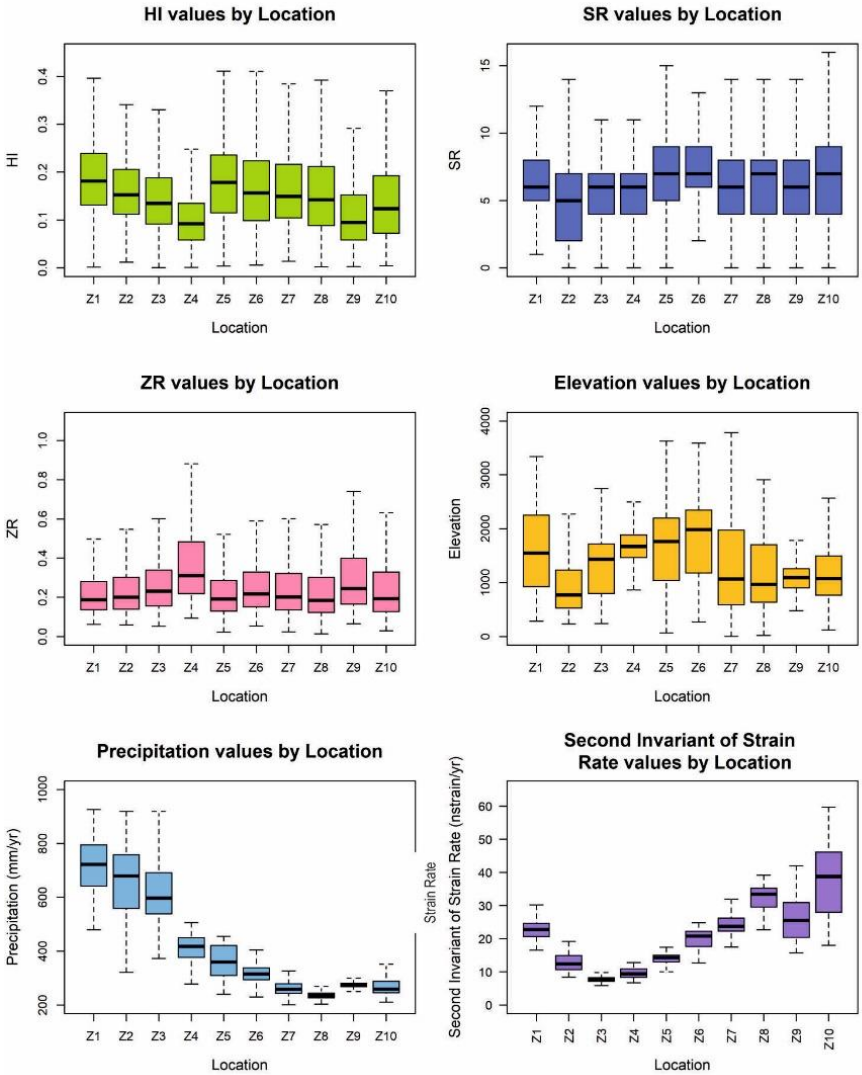

Figure 4.14: a) map of the Zagros, showing the location of the sample quadrats by dashed lines and the swath traces in black, which are 300 km in length and are located through the centre of the quadrats. b) boxplots for the Zagros, showing elevation, annual precipitation, second invariant of strain rate and geomorphic indices, from north to south. The boxplots represent the mean, upper and lower quartiles and range of values. The r^2 of correlation between mean precipitation and SR is 0.30 and between mean precipitation and HI is 0.09.

4.6.1.2 Climate

The Zagros is largely arid (Figure 4.15), with very low annual precipitation (< 400 mm/yr) in the Turkish-Iranian Plateau and the Fars region (SE Zagros) compared to the NW Zagros (> 600 mm/yr).

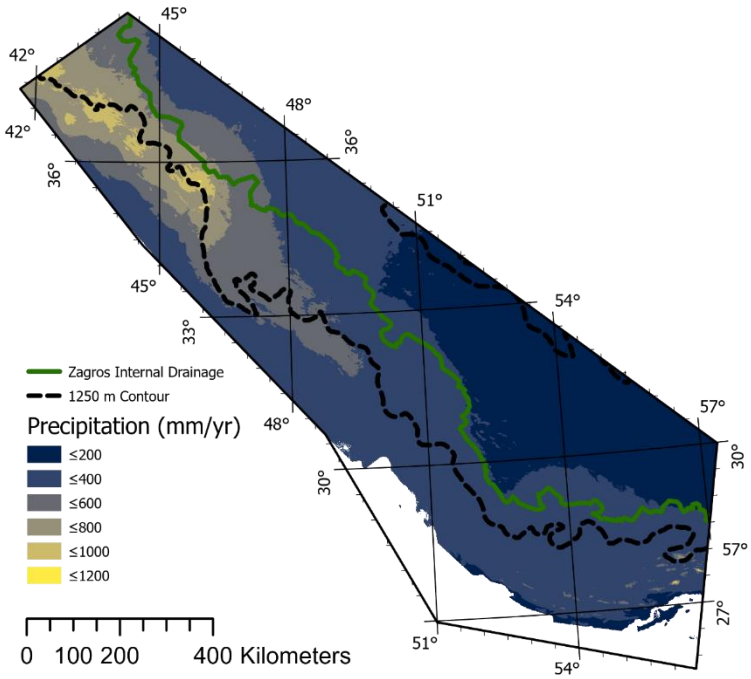

Figure 4.15: Annual precipitation in the Zagros (World Clim v2).

4.6.1.3 Previous geomorphic studies

Previous work by Obaid and Allen (2019) calculated the regional HI in a similar way to the method used in this chapter. HI shows a limited correlation to lithology and therefore lithology is considered a second order control. In general, HI values are correlated to the regional thrust seismicity cut-off at 1250 m but in the wetter areas high HI values continue above this elevation and in the driest areas the high HI values do not reach this elevation. Obaid and Allen (2019) therefore concluded a strong correlation between climate and HI. Their analysis of channel steepness shows a similar but less sharp pattern. In the Lurestan Arc the k_{sn} and relief are correlated but are not correlated with precipitation (Basilici et al., 2020). High HI and SR occur in anticlines in the hanging wall of the frontal thrust at ˜44 °E (Zebari et al., 2019).

4.6.2 Results

4.6.2.1 Overview

The geomorphic indices of HI, SR and ZR, calculated for second order drainage basins are shown in Figure 4.16. Ten swaths of 30 km width and 300km length are drawn at equal intervals along the length of the Zagros, with Z1 in the NW and Z10 in the SE. The profiles are roughly orthogonal to the deformation front. The swath profiles show variations in elevation, precipitation, second invariant of strain rate, HI, SR and ZR from the foreland into the plateau (Figure App.4). Ten 150 x 150 km quadrats are drawn centred on these swaths, between the deformation front and the internal-external drainage divide which is assumed to roughly define the location of the plateau (Figure 4.14). Data are sampled within these quadrats, with boxplots produced (Figure 4.14). Data are compared to the 1250 m contour as this has been identified as the limit of seismogenic thrusting (Allen et al., 2013).

4.6.2.2 Maps

High HI and SR values (HI > 0.3; SR > 0.4) broadly occur to the SW of the 1250 m contour and low HI and SR and high ZR values occur to the NE of the 1250 m contour (HI > 0.2, SR > 3, ZR < 3). In the NW of the region and in the location of the Dezful and Bakhtyari regions the high values continue beyond 1250 m contour, into the mountain interior. In the SE of the region the opposite pattern occurs: high values only occur at elevations lower than 1250 m. This pattern is shown clearly in the swath profiles (Figure App.4).

4.6.2.3 Boxplots

The boxplots (Figure 4.14b) show the median, the upper and lower quartile and the range of values. The locations of the quadrats are shown in Figure 4.14a and the extent of the quadrats are also shown on the swath profiles by vertical dotted lines (Figure App.4). The boxplots show the precipitation variation along the Zagros, from wettest in the NW to driest in the SE clearly. Elevation and SR values appear to have no relationship to precipitation as there is no trend in the data values from NW to SE. Within the wettest three areas (Z1-3) there is a correlation between precipitation and HI and ZR, with the wettest area (Z1) showing the highest HI values and lowest ZR values. This trend also occurs in swaths Z4-Z10 although the decline in HI and increase in ZR is less clear. However, the HI and ZR values are comparable to those in swaths Z1-Z3, so overall there is no clear relationship between precipitation and the geomorphic indices. The second invariant of strain rate

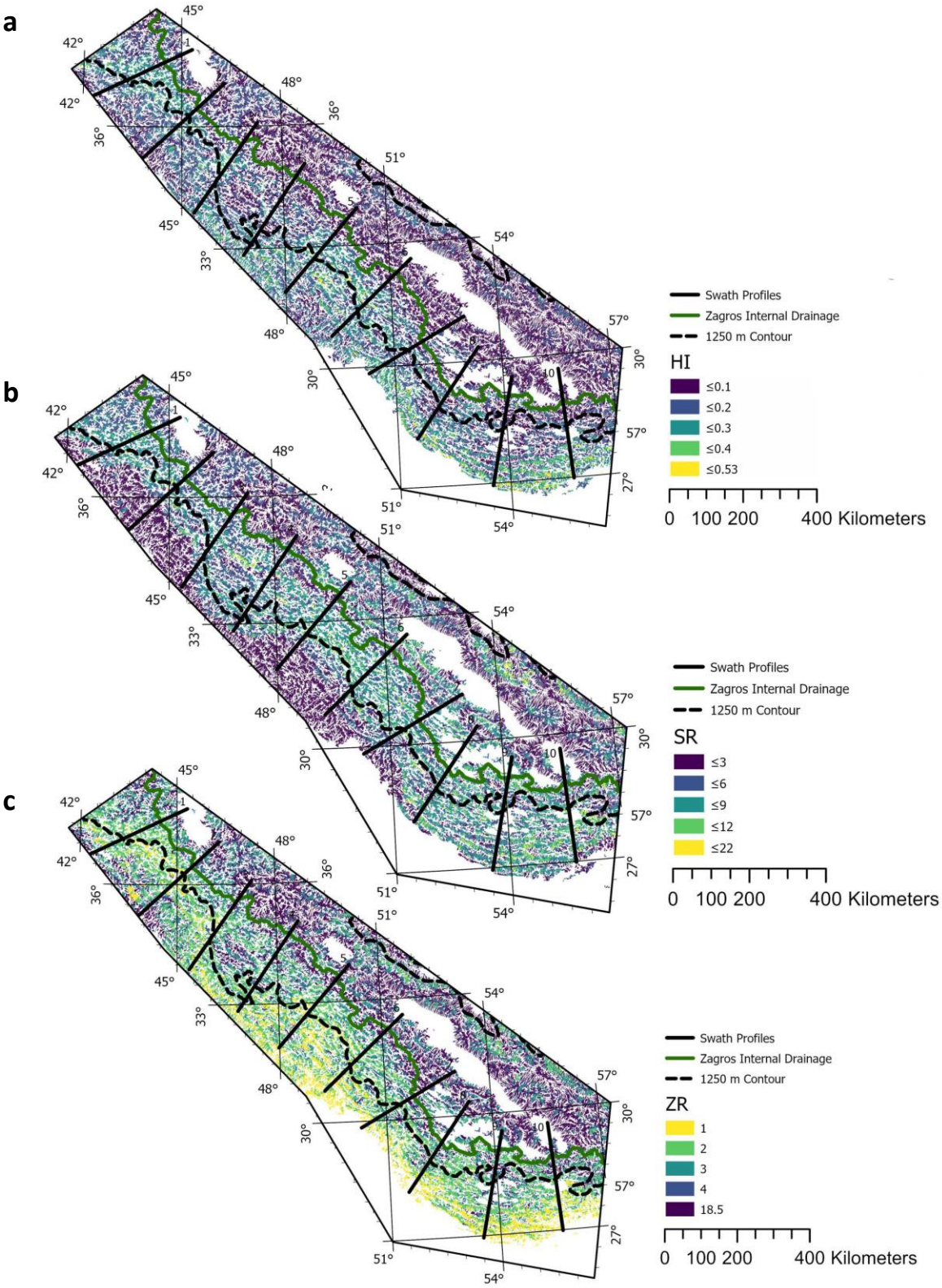

Figure 4.16: Maps of a) HI, b) SR and c) ZR calculated for second order drainage basins in the Zagros. The location of the 1250 m contour, the internal-external drainage boundary and the swath profile traces are shown.

increases from Z3-10 and again there is no clear trend in these swaths in the geomorphic indices. In swaths Z1-3 both HI and the second invariant of strain decrease.

4.6.2.4 Strain Rate Maps

Strain rate maps for the Zagros are shown in Figure 4.17. The strain rate pattern of the Zagros varies along strike. In the SE of the range the highest second invariant of strain rate values (> 60 nstrain/yr) in the Zagros occur at low elevations, near sea level. In this region rotation rate is negative, shear strain rate is high (> 20 nstrain/yr) and dilation rate is low east of 55° (< 50 nstrain/yr). In the NW Zagros, second invariant of strain rate is lower (< 25 nstrain/yr), rotation rate is positive (< 1 deg/Myr), shear strain rate is low (< 20 nstrain/yr) and dilation rate is negative. Positive dilation occurs in some areas of the plateau. Strain crosses show rotation, from north-south in the NW to NE-SW at ˜50° to near N-S at 56°.

4.6.2.5 Swath Profiles

HI, SR, ZR and elevation range show similar profiles throughout the Zagros, with peaks in HI, SR and elevation range corresponding to low ZR (Figure App.4). In the wettest region, in swath Z1, elevations and HI and SR values continue to rise above the 1250 m elevation contour (solid black line) and begin to decline at the location of the internal drainage boundary (green line). In swaths Z2, Z4-8 and Z10 HI and SR values start to decrease beyond the 1250 m contour and ZR values start to increase. Swath Z3 also shows a decline in SR beyond the 1250 m contour but also has a localised peak in HI. Swath Z9, in the driest part of the Zagros has low HI and SR values below elevations of 1250 m, with these low values continuing into the plateau interior, in comparison to the equally dry values of swath Z10, where the swath trends are more similar to the central range. The integrated relief (Table 4.2 in Section 4.3.2.5) is highest in swath Z1 (343 km^2), lowest in swath 2 (184 km^2) and overall there is a southwards decline in integrated relief in swaths Z3-10 (200-294 km^2).

Variation in the second order of strain rate along swath profiles is shown in Figure App.4. They show the highest values in the southern Zagros (note that the strain rate swaths y-axes have variable scales) and the lowest strain rate in swath Z3 in the northern Zagros. This is the opposite pattern to precipitation: the highest annual precipitation occurs in the northern Zagros. In swaths Z1-3 the second invariant of strain rate is seen to increase from the foreland into the plateau interior, whereas in swaths Z5-10 strain rate decreases from the foreland and in Z4 the strain rate is variable. In swaths Z5-10, where strain rate decreases into the plateau interior, the beginning of

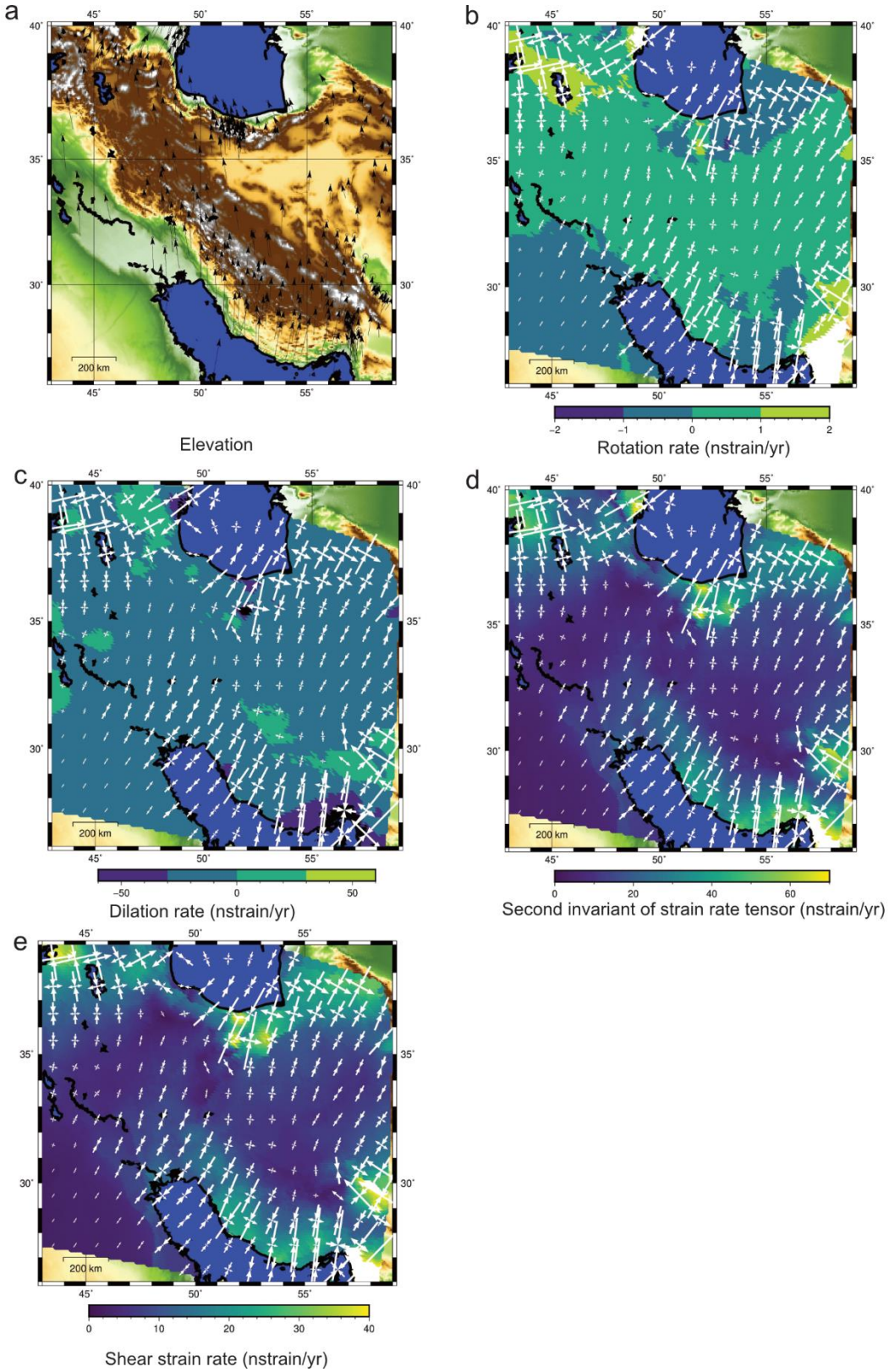

Figure 4.17: Strain rate maps for the Zagros showing a) GPS data points used and elevation b) rotation rate and principal strain axes in white, c) dilation rate and principal strain axes, d) second invariant of strain rate and principal strain axes, e) shear strain rate and principal strain axes.

the decline in strain rate is matched by: a peak in HI in swaths Z5, Z6 and Z8-10, the beginning of a sustained high in SR in swaths Z5-10 and a peak in annual precipitation in swaths Z5-10.

4.6.3 Discussion

The maps of geomorphic indices and the swath profiles show the geomorphic indices to have similar patterns across the Zagros (Figures 4.17 and 4.20). High HI and SR and low ZR values occur between the foreland and up to the 1250 m contour. This is the region which has seismogenic thrusting. Beyond this elevation, low HI and SR values and high ZR values highlight a plateau morphology. Therefore, as in the Qilian Shan (Chapter 2) the geomorphic indices are sensitive to underlying structure, particularly picking out the location of seismogenic activity.

However, this pattern does vary along strike. In the wettest region in the Kirkuk Embayment in the NW Zagros high HI and SR values continue above the 1250 m contour (Figures 4.19 and 4.20). In this region, the area above the 1250 m is tectonically non-seismogenic but geomorphically is not a plateau. In the driest region, the Fars in the SE, low HI and SR and high ZR values occur below 1250 m elevation. This area is therefore geomorphically plateau-like but in terms of tectonics is not part of the plateau as it is seismically active. These results are in agreement with those of Obaid and Allen (2019) who concluded that the wet climate of the NW Zagros and the dry climate of the SE Zagros are a strong control on geomorphology in these areas. Overall, the geomorphic indices in the Zagros are well correlated to the seismogenic limit but in the extreme wettest (>750 mm/yr precipitation) and driest (<400 mm/yr) areas climate is a stronger control. There are few other studies of tectonic geomorphology of the Zagros and these are localised. The geomorphic index patterns presented here (Figure App.4) match well to those of other studies, with areas of high HI and SR corresponding to areas of high HI, k_{sn} and relief identified in the Lurestan Arc (Zebari et al., 2019; Basilici et al., 2020; Figures 4.17 and 4.20). Precipitation and integrated relief are also related (Table 4.2; Figure 4.14). From swaths Z3-10 there is an overall decline in integrated relief and precipitation and the highest integrated relief and highest precipitation both occur in Z1.

Strain rate can be broadly compared to the change from seismogenic to non-seismogenic behaviour at 1250 m elevation (Figure App.4). In swaths Z2-4 strain rate starts to increase from 1250 m elevation; in swaths Z5-7 strain rate starts to decrease from 1250 m elevation and in swaths Z1 and Z8-10 there is no clear correlation between the second invariant of strain rate and the 1250 m elevation contour. This poor correlation between the 1250 m elevation of the landscape and the strain rate in the area may be due to the two factors being unrelated but may also be due to the degree of smoothing in the strain rate data due to the way that strain rate is calculated between

dispersed GPS stations. Highest strain rate occurs in the SE Zagros and lowest in the NW. There is no apparent correlation between the second invariant of strain rate values and the geomorphic indices values along the strike of the Zagros.

In conclusion, the landscape of the Zagros is related to the 1250 m elevation contour and therefore is likely to be controlled by the extent of seismic thrust activity (Figure App.4). In much of the Zagros there is a correlation between the calculated second order of strain rate and the geomorphic indices in terms of changes in trend along the swath profiles. However, there is no apparent correlation with the magnitude of the strain rate. For example, low second order of strain rate in the northern Zagros corresponds to HI and SR values which are average for the Zagros (Figure 4.14). Annual precipitation also shows no correlation with geomorphic indices along the range but in some locations variations in the landscape can be explained by precipitation extremes.

4.7 Discussion

The geomorphic indices in this study provide complementary results to other published studies, including those using different techniques such as analysis of channel profiles and mountain front sinuosity (e.g. Hodges et al., 2004; Bookhagen and Strecker 2012; Cannon and Murphy, 2015; H. Zhang et al., 2017; Obaid and Allen, 2019; Zebari et al.,2019; Basilici et al., 2020). In this thesis I calculate geomorphic indices across the entire mountain belts, which is different from many of these studies, which focus on smaller regions. This also allows comparison between the areas, which is carried out and discussed in Chapter 5.

4.7.1 Geomorphology and climatic, lithological and drainage controls

Representative swaths from each range studied are shown side by side to allow for easier comparison to show the general trends for each range (Figure 4.18). With the exception of the Zagros, there is no clear correlation in each of the ranges between the precipitation and the geomorphic indices, with low correlations between mean HI and precipitation (r^2 0.09 - 0.35) and mean SR and precipitation (r^2 0.02 - 0.14) and a lack of visual correlation in the boxplot trends suggesting that precipitation is not a first order control on the landscapes (Figures 4.6, 4.9, 4.12, 4.17). In general, the swath profiles show the peaks in precipitation occur where elevations increase at the mountain front but peaks in HI and SR occur at higher elevations. The effect of underlying lithology on the geomorphology is not analysed in this study because in each area previous studies have concluded that lithology is a secondary control on landscape (e.g. Zhang et

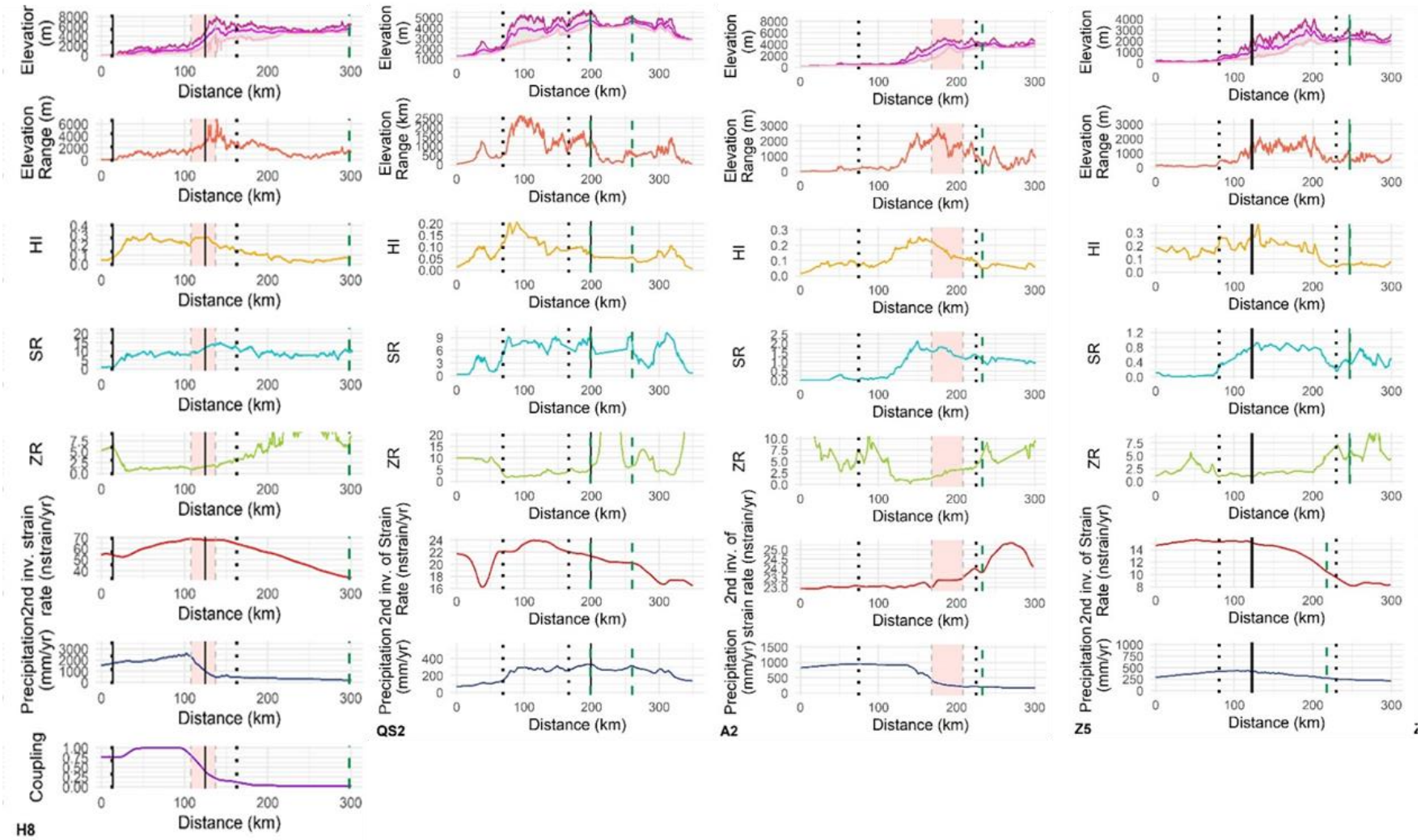

Figure 4.18: Examples of a swath from the centre of each range studied to allow for comparison (Himalaya swath 8 from Figure App.1, Qilian Shan swath 2 from Figure App.2 Zagros swath 5 from Figure App.3 and Andes swath 2 from Figure App.4).

al., 2020; Cannon and Murphy, 2014; Obaid and Allen, 2019; Chapter 2). Drainage patterns can have a major impact on the landscape. In each swath profile, with the exception of QS6 (Figure App.2) as discussed in Chapter 2, rivers drain from the plateau interior, across the thrust belts and to the foreland. Where the swaths cross the internal-external drainage divides the locations are shown by vertical green lines (Figures 4.7, 4.10, 4.15. 4.20). The relationship between internal-drainage, landscape and the underlying detachment in the Qilian Shan is discussed in more detail in the Chapter 2. In the Himalaya, Andes and Zagros the divide occurs at much higher elevations than the landscape change and the HI and SR values are low on either side of the divide. The changes in landscape identified in this study are therefore due to underlying structure rather than drainage morphology. This result shows that internal drainage helps to create a plateau morphology but is not a requirement: plateau landscapes can form in areas of external drainage.

Table 4.1 (Section 4.3.2.5) shows that the percentage variation of integrated relief ranges from 46 % to 86 %, with the smallest variation in the Himalaya and the largest variation in the Zagros. This variation is much higher than Obaid and Allen (2019) found for the Zagros (< 25 %), including a higher integrated relief in this study for the Zagros (86 %). The reason for the high variation in the Zagros in this study is the high integrated relief value for swath Z1, which is outside of the region studied in Obaid and Allen (2019) and is the wettest area in the Zagros, with an average strain rate. Variation in integrated relief along each range may be related to precipitation. For example, there is a decline in precipitation and integrated relief from swath 1- 10 in the Zagros, although the opposite pattern in the Qilian Shan where precipitation increases to the east (QS6), but the integrated relief decreases. This may be because profile QS1 is in an entirely externally drained region, whereas the other swaths include the low relief, internally drained, central plateau region. The differing variations between precipitation and integrated relief results suggest that variation may be controlled by a factor other than precipitation. This could be due to the river incision, which may be partially controlled by precipitation but also by the drainage pattern. For example, drainage parallel to or cross cutting thrust faulting was shown produce different landscapes in the Qilian Shan in Chapter 2, as well as the internally drained areas having lower integrated relief. The integrated relief is included for interest and could be compared to other ranges, such as non-active ranges.

4.7.2 Geomorphology and strain rate

The second invariant of strain rate is compared to the geomorphic indices in each location (Figures 4.7, 4.10, 4.15, 4.20). In the Qilian Shan high second invariant of strain rate values occur in the region where HI and SR begin to decrease and ZR increase; in the Himalaya the peak in strain rate

generally occurs where HI and SR begin to decrease and ZR increase; in the Zagros the relationship between the second invariant of strain rate and geomorphology varies along the length of the mountain chain; in the Andes the strain rate varies very little across the range but in the northern part of the study area the highest second invariant of strain rate occurs where HI and SR peak and ZR is low. Therefore, the second invariant of strain rate broadly compares to the landscape in active fold-and-thrust belts. However, the correlation is not clear enough to be able to interpret the change in strain rate in terms of underlying structure or changes from seismogenic to non-seismogenic deformation. This variable relationship may be due to data sparsity or the way that changes in strain rate reflect diffuse variations in underlying structure – e.g. the transition from locked to creeping behaviour taking place along a zone of a detachment thrust rather than an abrupt transition.

4.7.3 Geomorphology and underlying structure

In each of the locations I demonstrate a link between the underlying structure of the fold-and-thrust belt and the geomorphic indices. In each location, above the creeping part of the underlying detachment (for the Qilian Shan, Himalaya and Andes) or the non-seismogenic zone (for the Zagros) there is low HI, low SR and high ZR (Figures 4.5, 4.7, 4.10, 4.14, 4.15, 4.19, 4.20). The trend changes overlying the change from locked to creeping behaviour are to declining HI and SR (Himalaya, Andes, Zagros) or low HI and SR (Qilian Shan) and increased ZR (all areas). The change in the geomorphic indices across the structural boundaries therefore varies. Low HI, low SR and high ZR values indicate flat landscapes, with the high ZR values indicating that the area is both high elevation and low relief. In each region these values define the location of plateau-like landscapes. Although the underlying structures vary, particularly between those areas with an underlying detachment and those without, the results suggest that the deformation is similar. Both sets of areas show non-seismogenic deformation which is encouraging plateau formation. There are likely to be many factors in this relationship, but the simplest explanation is that the lack of earthquakes means that there is no pulsed uplift and no earthquake-driven landsliding. Above the locked portion of the detachments and within the zone of seismogenic thrusting in the Zagros high values of HI and SR and low ZR occur (Figures = Figures 4.7 4.10, 4.15, 4.20). This is likely to be due to uplift encouraging river incision as well as earthquake-driven mass movement, meaning the landscapes in this region change more rapidly.

Although this pattern is seen in most of the swath profiles, there are some exceptions. Swath QS6 shows a different morphology to the others in the Qilian Shan (Figure App.2). This is due to a distinct drainage pattern, with major river valleys orthogonal to the swath profile in this area, rather than

parallel to in the other swaths, which has created wider valleys. In the Qilian Shan the change from locked-creeping behaviour is correlated with a change to sustained low HI and SR values, whereas in the other regions, the locked-creeping transition is defined by a gentle decline in HI and SR values. In the Himalaya there is an offset between the peaks in HI and SR, seen most clearly in Figure App.1, with the SR peaks consistently further north, towards the plateau interior. In the other fold-and-thrust belts there is no offset between the HI and SR curves. Possible reasons for the offset in the Himalaya are that the elevations in the High Himalaya are more extreme than the other areas, giving large slope variations, or may be due to the suggested complexities of the underlying detachment which is suggested to contain one or more ramps (e.g. Mendoza et al., 2019). In the Andes, the westward decline in HI and SR towards the plateau interior occurs at the westward uncertainty limit for the locked-creeping transition (Figures 4.14, 4.15). This may be due to model uncertainties but may also be due to the dip of the detachment: the Andes detachment has the shallowest dip (Andes 4°, Himalaya 10°, Qilian Shan 17°) and therefore the zone over which the deformation behaviour changes may be wider at the surface. Finally, precipitation variations along the Zagros are seen to disrupt spatial coincidence of the non-seismogenic and plateau landscapes seen elsewhere, creating an offset between geomorphic changes and the seismogenic limit. Low precipitation areas see plateau formation occurring in the seismogenic region and in the wettest areas plateaus form well above the seismogenic limit (Figure 4.16).

4.8 Conclusion

This study concludes that patterns in the geomorphology of fold-and-thrust belts provides additional evidence for understanding the underlying structure of areas, backing up conclusions drawn from modelling of geodetic data. There is a strong correlation between the change in deformation style from locked to creeping and the change in landscape from incised to plateau-like. However, additional landscape-controlling factors such as localised thrust faulting, drainage configuration and precipitation mean that the landscapes alone cannot be used to define the underlying structure.

Chapter 5: Does the rain or the strain shape the mountain chain? Correlations between climate, tectonics and landscape

5.1 Introduction

The aim of this chapter is to assess the relationship of present-day tectonics and climate to the landscape of fold-and-thrust belts. In Chapter 4 I assessed the landscape using swath profiles and mapping of geomorphic indices across individual fold-and-thrust belts, to assess the relationship of landscape to the underlying tectonic structure. The chapter focussed on identifying common variations in geomorphology, strain and climate orthogonal to the mountain ranges and also variations along each range. One conclusion of this work was that there is no clear relationship between precipitation or strain rate control on the geomorphic indices within each range, both in the boxplots of quadrats or along swath profiles. In this chapter comparisons are made between the ranges. The local structures are not considered as this is covered in Chapter 4, but instead the impact of the regional crustal shortening (second invariant of strain rate) and the regional climate (precipitation and glaciation) on landscape (represented by HI and SR).

The analysis in this work builds on the work of Champagnac et al., (2012) who compared climate, landscape and crustal shortening for mountain belts across the world. They conclude that less than 25 % of topographic relief is due to crustal shortening alone and up to 50 % is due to measures of tectonics and climate (latitude, annual precipitation and crustal shortening). The work presented in this chapter uses more restricted areas of the fold-and-thrust belt (between the plateau and frontal thrust), rather than the entire range as used in the study by Champagnac et al., (2012). The analysis in this chapter gives multiple data points for each range by using quadrats and uses more detailed geomorphic analysis rather than relief only.

The areas studied in this work are the Qilian Shan introduced in Chapter 2, the Himalaya, Andes and Zagros introduced in Chapter 4, with the addition of the Longmen Shan (Figure 5.1). The Longmen Shan is a NE-SW trending range at the eastern margin of the Tibetan Plateau. The area is steep, with active faulting and is seismically active (e.g. 2008 M_w7.9 Wenchuan earthquake; Burchfiel et al., 2008), despite low shortening rates (1-3 mm/yr; Shen et al., 2005). The Longmen Shan, therefore, provides an interesting comparison to the other ranges in this study, for example, the Himalaya are also high elevation but with a much higher strain rate. Data are also extracted from the eastern Tibetan Plateau, with four quadrats on either side of the monsoon-controlled landscape transition identified in Chapter 3. These data are considered separately because the

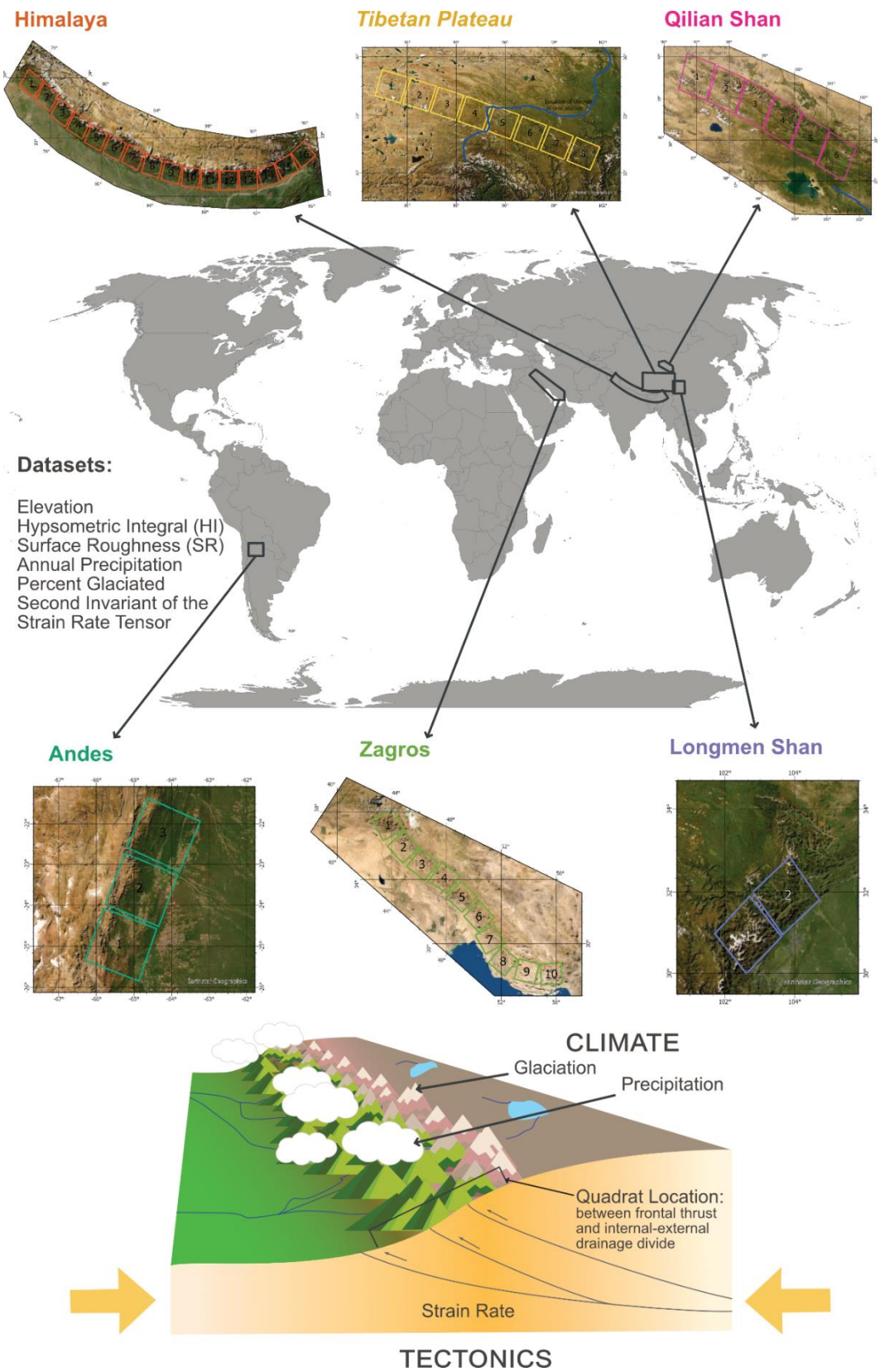

Figure 5.1: Location map with satellite images labelled with the location of the quadrats used. Satellite images also show the landscape vegetation cover. Cartoon shows the climatic and tectonic factors used in the study and the location of the quadrats drawn, between the frontal thrust and the internal-external drainage divide.

other areas in this study are fold-and-thrust belts with plateau excluded, whereas the analysis of the Tibetan Plateau is entirely within the plateau. The comparison is also across the internal-external drainage divide, therefore the landscape has a varying base level. The comparison of the eastern Tibetan Plateau therefore may not be of statistical value, but is shown for interest. Satellite imagery in Figure 5.1 shows the variation in vegetation cover between the areas which gives an indication of the climate variation.

This comparison of climate, tectonics and landscape uses data on decadal timescales. The landscape data is taken from the SRTM mission, strain rate is calculated from decadal geodetic records and annual precipitation averaged over 3 decades. The study therefore compared these factors on similar timescales, which is rare in work of this kind (e.g. Bermúdez et al., 2012). Although using decadal timescales means that comparisons are between near-modern day climate, tectonics and landscape there is still the issue of landscape response time: landscapes respond to changes tectonics and climate over time and therefore result from conditions which may be different from the current conditions. This needs to be taken into account when comparing the factors.

5.2 Methods

The geomorphic datasets used in this study are the elevation and the SR and HI (methods described in Chapter 2). In the Qilian Shan the fluvial base level is above sea level, so the elevation used in this study is corrected to a common base level, by removing 2000 m elevation from Qilian Shan elevations. Climate datasets used are the mean annual precipitation (WorldClim v.2) and the percentage of land covered by glaciers, calculated from the global GLIMs dataset (Global Land Ice Measurements from Space glacier database, updated 2020). The proxy for tectonics is the second invariant of the strain rate tensor (later referred to as the second invariant of strain rate or simply the strain rate), which is an approximation of the magnitude of strain rate; the method is described in Chapter 4.

In this comparison, mean and standard deviation of data are taken from quadrats spaced evenly along each mountain belt, above the frontal thrusts and below the plateaux. The quadrats are 150 x 150 km in size apart from the Qilian Shan where quadrats are 100 x 100 km due to the smaller scale of this range. The locations of the swaths are shown in Figure 5.1. HI and SR are calculated for individual drainage basins and the value of each drainage basin within the quadrats is used in analysis. Elevation and precipitation data are raster format and the data points used in the analysis are the values at the centre of each drainage basin. Strain rate is calculated as a grid of points spaced 0.1 ° apart and each point within the quadrat is used in the analysis. The 0.1 ° grid size

produces an accurate map of strain rate, with a smooth variation which is spatially comparable to that of other studies (Kreemer et al., 2014; Stevens and Avouac, 2005). A denser grid would not produce a different strain rate pattern due to the number and distribution of GPS stations. The strain rate is calculated using all GPS data points, not just those that lie within the quadrats. An example of the datasets used in each quadrat is shown in Figure 5.2. Boxplots show the distribution of values in Figures 4.6, 4.8, 4.10 and 4.14.

5.3 Results

5.3.1 Pearson's Correlation Coefficients and Data Distribution

Pearson's correlation coefficient is a measure of the linear correlation between datasets and does not assume a causation effect. Therefore, the r value does not vary if x and y axes are swapped. Values of 0 show no linear correlation and of 1 a perfect correlation, regardless of slope. Scatterplots and variable distribution curves show the relationship between the datasets. Comparison is made between each of the variables (Figure 5.3). There is a positive correlation between each variable, with the strongest correlations between the second invariant of strain rate and precipitation ($r = 0.75$), second invariant of strain rate and glaciation ($r = 0.72$), second invariant of strain rate and SR ($r = 0.72$), SR and precipitation ($r = 0.79$), HI and precipitation ($r = 0.81$) and HI and SR ($r = 0.81$). These high values highlight the inter-dependency of the variables considered, for example, glaciation and strain rate should not be directly related, therefore the positive correlation may be due to an additional factor, such as elevation. Glaciation values are skewed to low and 0 values and SR shows a bimodal distribution.

5.3.2 Linear Regression

Linear regression shows the strength of the relationship between the different factors, as shown in Figure 5.4. The plots are ordered from highest r^2 values in the top left to lowest in the bottom right. Due to the inter-dependency of the variables the x and y axes cannot always be the dependent and independent variables. In each plot the scatter points represent mean values within the quadrats, of elevation, annual precipitation, HI, SR and the second invariant of strain rate. The colours represent the fold-and-thrust belt from which the data are taken and ellipses represent the 95 % confidence limit, where there is enough data for this to be calculated.

The results show positive relationships between each variable. The r^2 values are relative, but values > 0.5 are considered strong correlations, > 0.35 medium correlations and < 0.35 weak correlations in this work. For each r^2 value the p-values are < 0.01. Overall, annual precipitation shows a strong

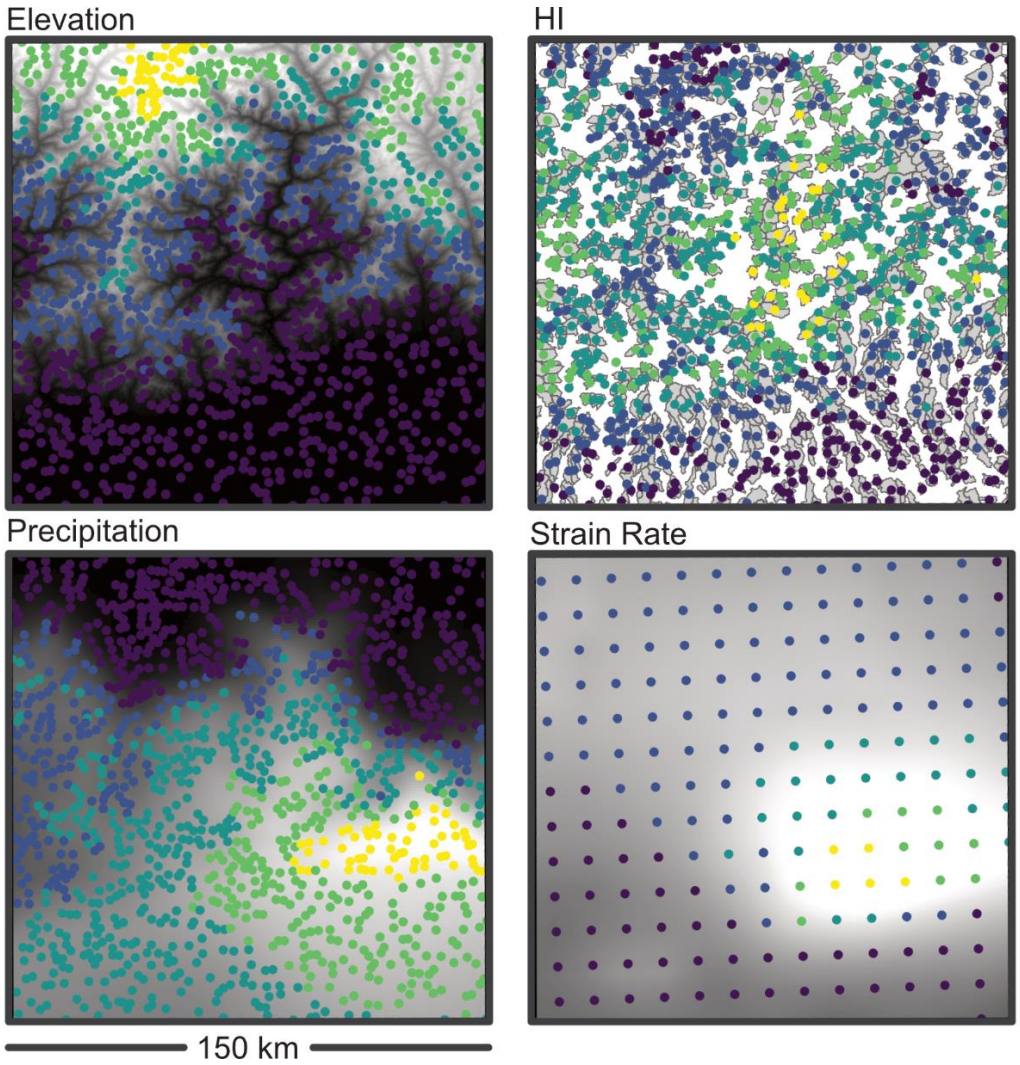

Figure 5.2: Map showing the different datasets used in the chapter for an example quadrat (quadrat 11 from the Himalaya). The mean and standard deviation are calculated for each quadrat using the datapoints shown. HI data are calculated for second order basins and elevation and precipitation data are the values at the centre of these basins. Strain rate is taken from the raw calculated data which are a grid of points 0.1° apart (~ 11 km). The coloured points show the variation of values within the quadrat, in each case there are 5 equally spaced colour intervals ranging from 66 – 6876 for elevation, 0.008-0.49 for HI, 270 – 4975 for precipitation and 40 – 134 for strain rate. The background of each map show from top to bottom: the elevation data; the individual basins from which HI is calculated; the precipitation data and a raster of strain rate which is created from the strain rate grid to allow a visual comparison to the other datasets.

positive relationship with the other variables ($r^2 > 0.55$) apart from a weak positive correlation with the percentage of glaciation and the elevation ($r^2 < 0.34$). Precipitation is strongly correlated with HI, SR and the second invariant of strain rate ($r^2 > 0.55$). The second invariant of strain rate is positively correlated with precipitation, SR, glaciation and HI ($r^2 > 0.38$). HI is most strongly correlated with precipitation ($r^2 = 0.64$) and with the second invariant of strain rate ($r^2 = 0.38$). SR is

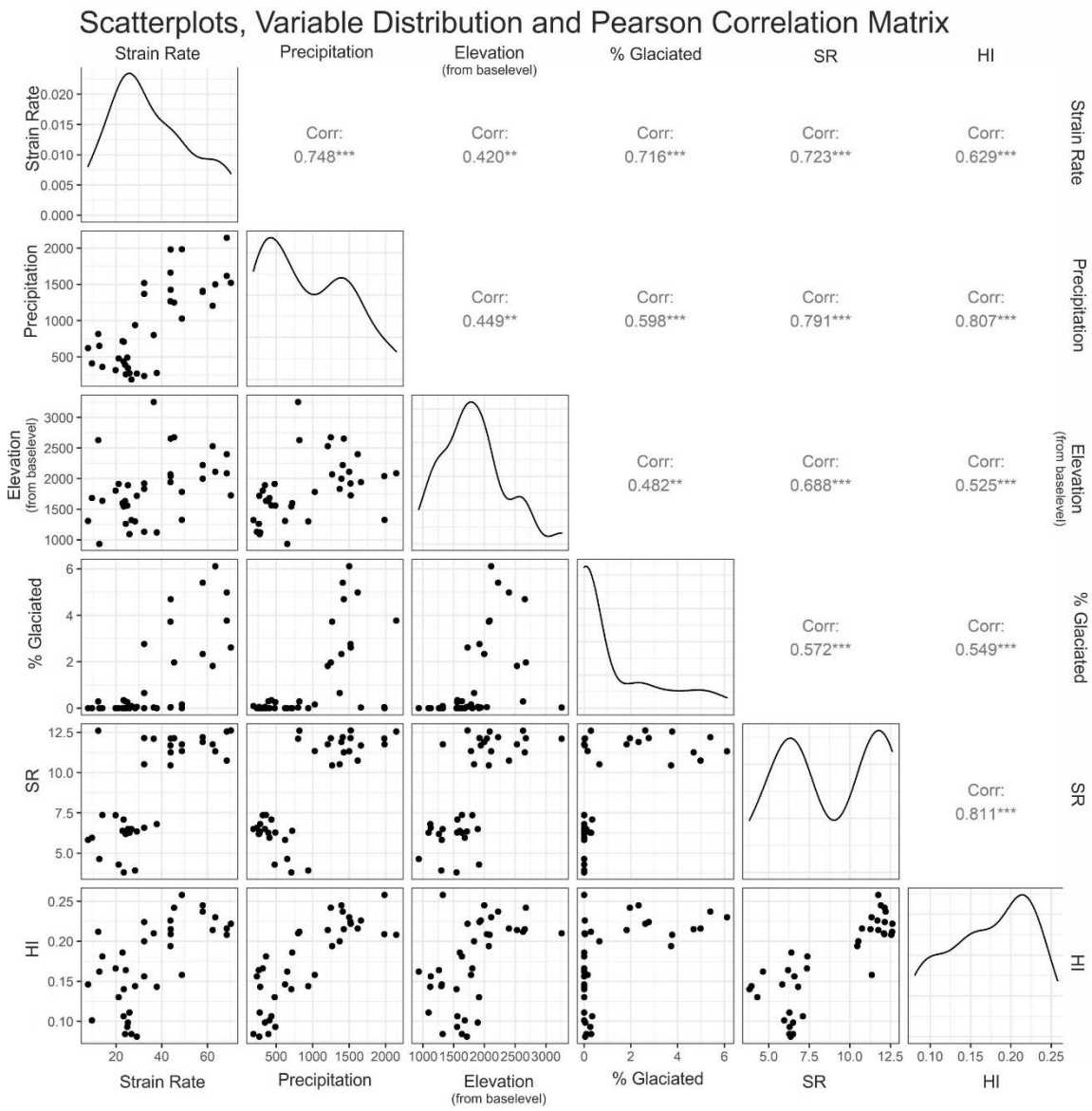

Figure 5.3: A correlation matrix showing scatterplots for each pair of variables (to the bottom left of the diagonal), Pearson's corelation values for each pair of variables (to the top right of the diagonal) and probability distribution curves for each variable (along the diagonal).

most strongly correlated with precipitation ($r^2 = 0.62$), second invariant of strain rate ($r^2 = 0.51$) and elevation ($r^2 = 0.46$). Glaciation shows weaker correlations with the other variables ($r^2 < 0.31$) as does elevation ($r^2 < 0.25$).

5.3.3 Multiple Linear Regression

Multiple linear regression is used to look for significant relationships between the geomorphic indices and the other variables. HI and SR are considered separately as dependant variables and

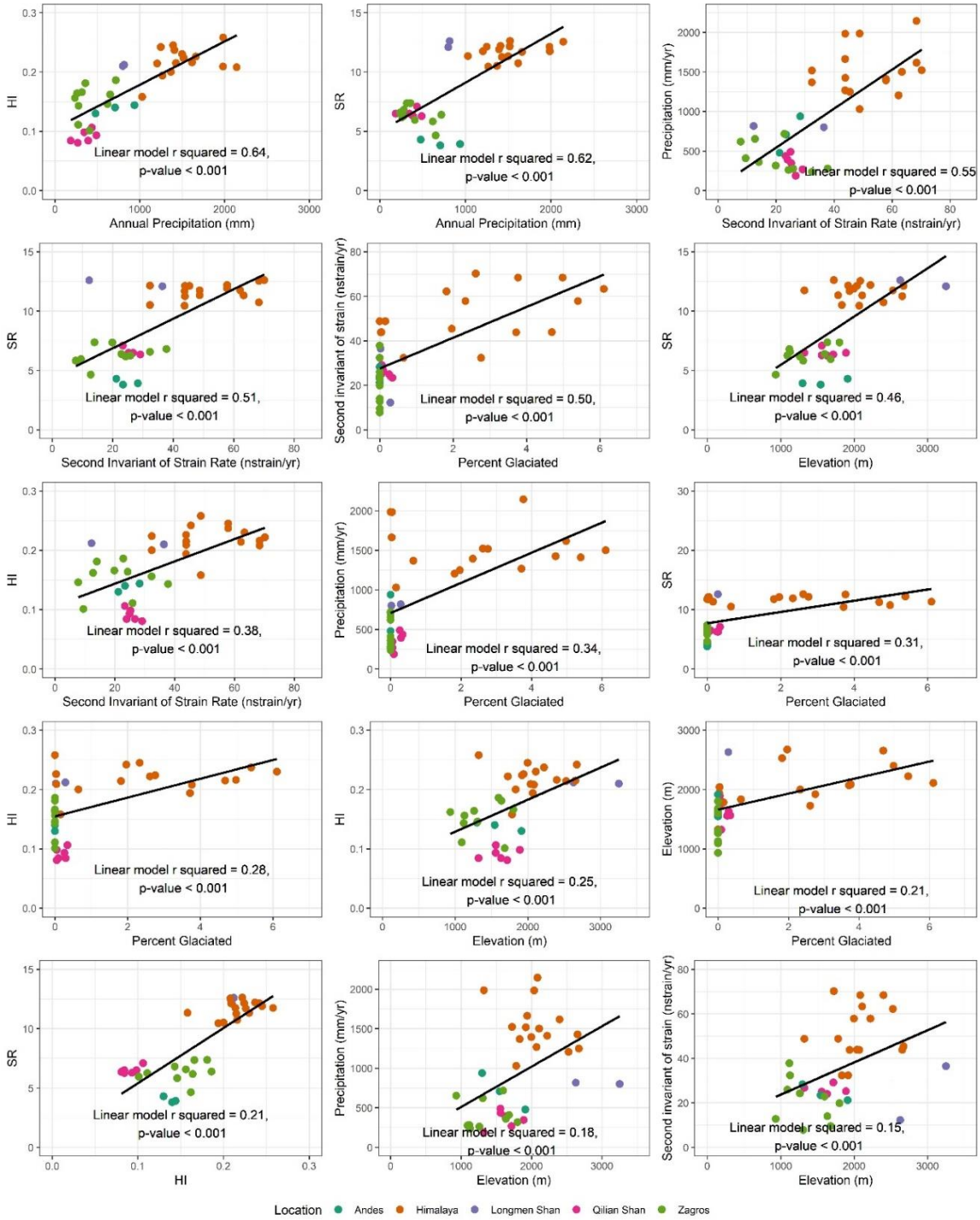

Figure 5.4: Scatterplots showing correlations between HI, SR, elevation, mean annual precipitation, glaciation and the second invariant of the strain rate tensor. Colours represent the different mountain belts and ellipses represent the 95 % confidence limit. The graphs are order of highest r^2 from linear regression, in the top right corner, to lowest in the bottom left.

are compared to the variables of strain rate, precipitation, elevation and glaciation. The independent variables are not collinear (Pearson's correlation r < 0.8 for each variable pair; Figure

5.3). Correlations appear linear, although the correlations with glaciation are more complicated due to the number of non-glaciated regions (% glaciation = 0).

Precipitation and elevation (p value < 0.01) and second invariant of strain rate (p value < 0.1) are significant predictors of SR. Multiple linear regression suggests that these factors account for 77 % of variation in SR (p < 0.01). Precipitation is a significant predictor of HI (p value < 0.01), but no other variable has significant p values. Linear regression suggests that precipitation accounts for 64 % of variation in HI (p < 0.01). However, these values are overestimates, as linear regression assumes that the variables are entirely independent of other factors, but this is unlikely to be true: for example, precipitation is partially controlled by elevation, which may in turn be controlled by strain rate.

5.3.4 Geomorphic indices, precipitation and second invariant of strain rate

The multiple linear regression shows that precipitation is a significant predictor of both HI and SR and the second invariant of strain rate is also a significant predictor of SR and shows a strong correlation with HI (Figure 5.4). These 4 factors are of interest in assessing the relative importance of tectonics and climate on controlling fold-and-thrust belt morphology and are shown in Figure 5.5. The error bars are 1 standard deviation from the mean within each quadrat. Elevation is not shown as this has a weak correlation with HI ($r^2 = 0.25$).

HI is positively correlated to the second invariant of strain and annual precipitation. Values for the Qilian Shan and Andes are clustered, but the other ranges show a larger spread of data. The highest values of HI, strain and precipitation are in the Himalaya, but these values plot in a similar location to values from the other fold-and-thrust belts, which suggests that the factors are truly linearly related (compare with SR, below). HI shows a stronger correlation with the annual precipitation than the strain rate.

SR is also positively correlated to the second invariant of strain and the annual precipitation and the correlation between SR and precipitation is strongest. The Himalaya and Longmen Shan have the highest SR values and the Himalaya have the highest precipitation and strain. These two locations have distinct SR, strain and precipitation values compared to the other regions in this dataset. It is, therefore, not clear if there is only an apparent linear trend because of the data gap between the Himalaya/Longmen Shan and the other ranges, although within the individual ranges there are positive correlations between SR and precipitation and strain rate, suggesting the overall trend may be truly linear. The data point representing the SW Longmen Shan point has high SR values, but low strain rate, which is an outlier in this dataset.

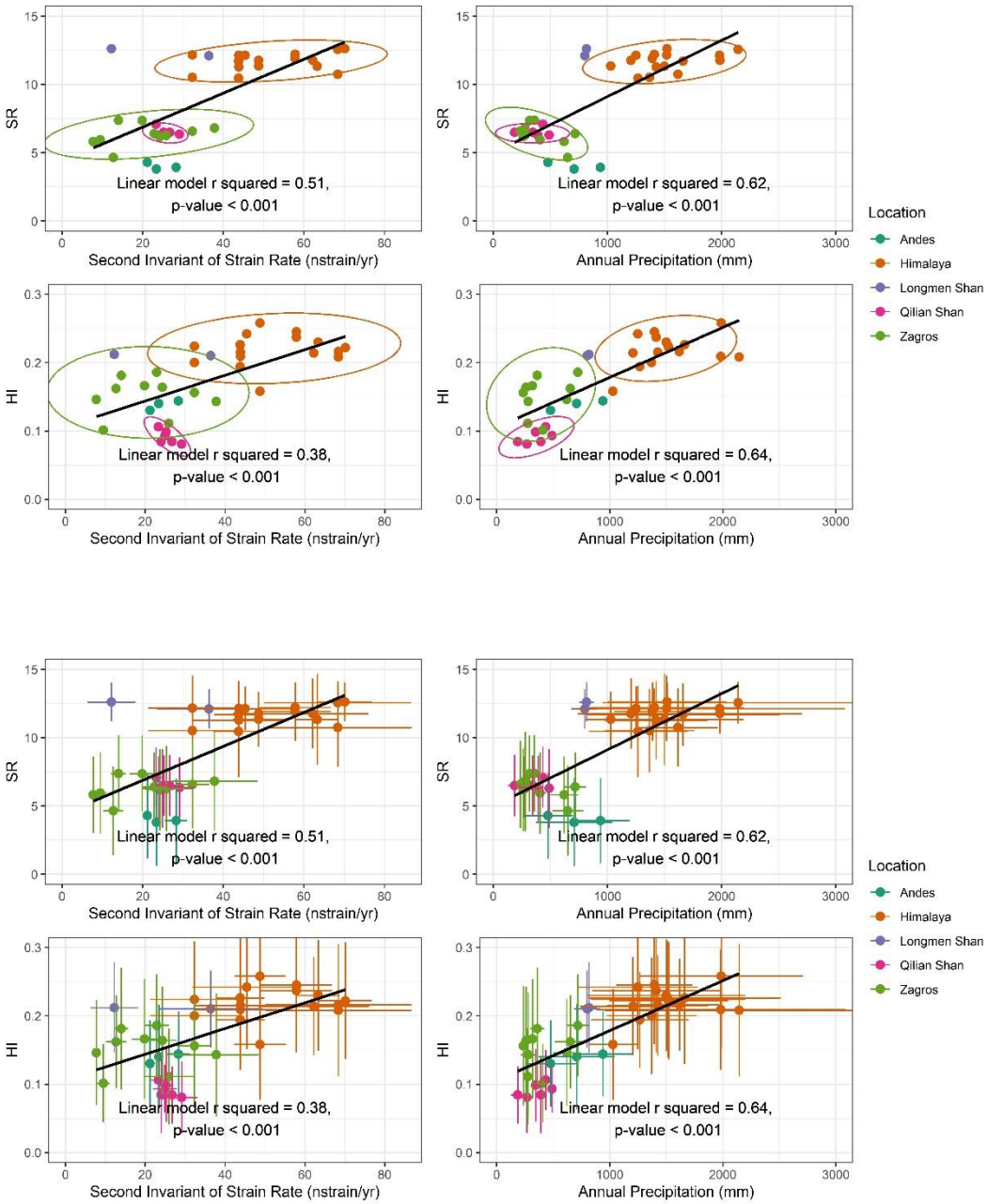

Figure 5.5: Correlations between HI and SR and annual precipitation and second invariant of the strain rate tensor showing a) 95 % confidence ellipses and b) error bars representing one standard deviation from the mean. The equations of the best fit lines are: SR and strain rate y = 0.12x + 4.4; SR and precipitation y = 0.004x + 5.0; HI and strain rate y = 0.002x + 0.11; HI and precipitation y = 0.00007x + 0.11.

5.3.5 Eastern Tibetan Plateau

The landscapes of fold-and-thrust belts and plateau are distinctly different (e.g. Liu-Zeng et al., 2008). In each of the fold-and-thrust belts considered, the area which is included in the quadrat analysis is the area of active thrusting and steep slopes, between the foreland and plateau. The Tibetan Plateau is an area of overall high elevation, low relief and no active thrusting and uplift.

Deformation in the eastern Tibetan Plateau is accommodated on strike slip faults and the central Tibetan Plateau is experiencing extension (Y. Li et al., 2015; Chapter 3, Figure 3.1a). The landscape is composed of high elevation low relief surfaces in the interfluves, dissected by major river valleys (Clark et al., 2004). Maps of strain rate for the Tibetan Plateau are shown in Chapter 4, in Figure 4.7. The central plateau, where extension occurs, has a low second invariant of strain rate. Towards the eastern Tibetan Plateau there is a high second invariant of strain rate, along the strike slip faults and the area is under extension, as shown by a positive dilation rate.

A comparison of values of the eastern Tibetan Plateau with the fold-and-thrust belts is included for interest. As the landscapes of fold-and-thrust belts and plateau are different the analysis is included separately to that in sections 3.1 to 3.4. Eight quadrats are drawn through the central and eastern Tibetan Plateau, with 4 to the west and 4 to the east of the line of landscape change introduced in Chapter 3 and shown in Figure 5.1. The values of mean HI, SR, second invariant of strain and annual precipitation are included in Figure 5.6.

Values of SR against the second invariant of strain rate for the eastern Tibetan Plateau plot in a similar location to the trend from the other locations but show very dispersed values. SR values

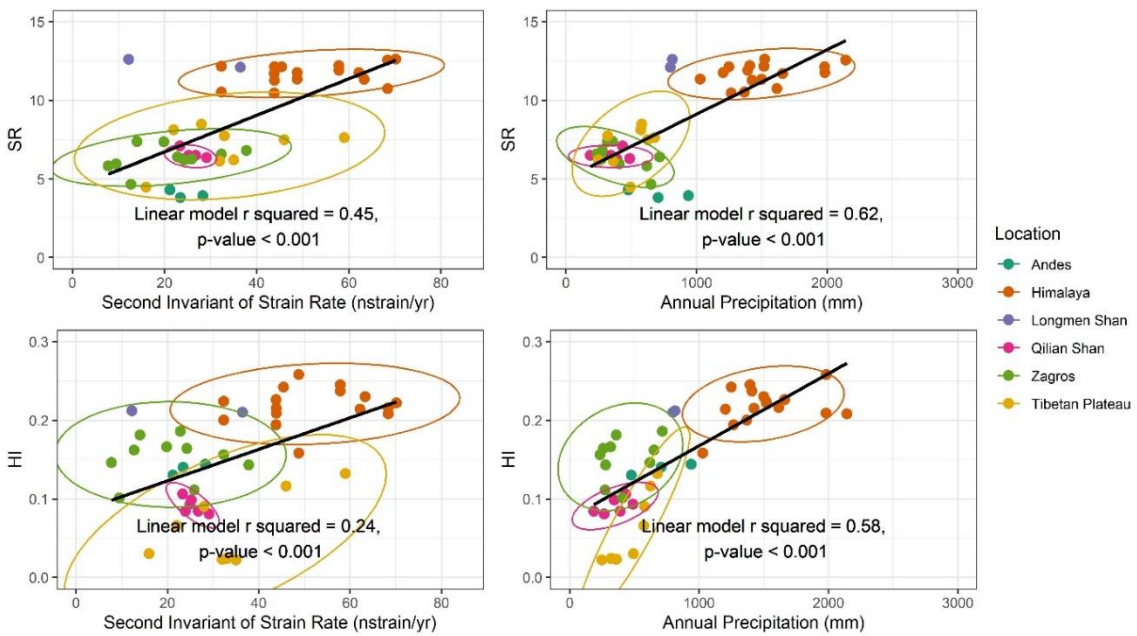

Figure 5.6: Correlations between HI and SR and annual precipitation and second invariant of strain, with 95 % confidence ellipses and linear line of best fit, including data from the eastern Tibetan Plateau.

appear to be similar to the other areas of lower precipitation, plotting in a similar location to the

Qilian Shan, Zagros and Andes. There is a large variation in strain rate across this area of the Tibetan Plateau and the HI values are consistently lower than for areas of similar strain rate in the actively shortening fold-and-thrust belts. There is a steeper gradient in the positive relationship between the HI and annual precipitation for the eastern Tibetan Plateau compared to the overall pattern for the fold-and-thrust belts.

SR values in the eastern Tibetan Plateau are therefore similar to the active fold-and-thrust belts studied, in terms of relative precipitation and strain rate. However, HI values are much lower for the plateau than the fold-and-thrust belts. The lowest HI values are those from the central, dry plateau. There may be various factors explaining why the SR values are more consistent with the fold-and-thrust belts than the HI values, but a likely factor is the existence of major river valleys in this region.

5.4 Discussion

There is a positive correlation between each climatic, tectonic and landscape variable considered. Precipitation is a significant predictor of both SR and HI, with the strongest correlation between the geomorphic indices and precipitation (for HI $r^2 = 0.64$ with p-value < 0.001 and $r = 0.81$; for SR $r^2 = 0.62$ with p-value < 0.001 and $r = 0.79$). There is a weaker correlation between the geomorphic indices and glaciation (for HI $r^2 = 0.28$ with p-value < 0.001 and $r = 0.55$; for SR $r^2 = 0.31$ with p-value < 0.001 and $r = 0.37$). There are medium-strong correlations between the geomorphic indices and strain rate for (HI $r^2 = 0.38$ with p-value < 0.001 and $r = 0.63$; for SR $r^2 = 0.51$ with p-value < 0.001 and $r = 0.72$). Therefore, the analysis shows that both the climate and tectonics are controls on landscape, as is shown worldwide (e.g. Ferrier et al., 2013; D'Arcy and Whittaker, 2014), but that the climate, particularly the precipitation, may be a greater factor than strain rate.

Landscapes are largely driven by erosion rate, mainly due to fluvial erosion (Whipple et al., 2004). The strong positive correlation between precipitation and geomorphic indices is comparable to results of a positive correlation between erosion rate (thermochronology-derived or decadal) and precipitation as shown by many studies including in the Himalaya (Thiede et al., 2004; Adams et al., 2020), Cascades (Reiners et al., 2003), New Zealand (Jiao et al., 2017) and worldwide (Herman et al., 2013). However, in the individual belts in Chapter 5, weak to no visual relationships are found between the geomorphic indices and precipitation in the boxplots (Figures 4.6, 4.8, 4.10, 4.14) and peaks in precipitation along swath profiles occur at the location of the largest increase in elevation, showing orographic effects, rather at locations of peaks in HI or SR. Other studies also find no or a weak correlation between precipitation and erosion rates in the Himalaya (Burbank et al., 2003;

Godard et al., 2014) and the Qilian Shan (Pan et al., 2010). These results show the complexity of the tectonic-climatic-erosion rate systems.

In the eastern Tibetan Plateau, I suggest that build-up of low relief, plateau topography occurred as a result of prolonged crustal shortening in dry climate conditions, then increased precipitation at the time of monsoon intensification (>20 Ma) led to increased exhumation rates, which continue to the present day. A similar effect might be seen in this global comparison: tectonic uplift is important to set up landscapes, because it creates elevation via isostasy, but above a threshold, precipitation becomes an important factor (> 600 mm/yr in the eastern Tibetan Plateau). Jiao et al., (2017) also showed that tectonics is important for setting up the regional exhumation pattern in New Zealand, but both strong tectonic deformation and efficient erosion are required to maintain rapid exhumation rates.

The simple correlation of factors presented here does not account for all complexities in the tectonic-climate-landscape system. For example, the pattern of faulting and deformation are not considered and this is shown in Chapters 2 and 4 to partially control the landscape. Climate factors such as temperature and seasonality are important. For example, temperature affects erosion rates and storminess and seasonality affect the likelihood of erosion events such as landslides (Burbank and Anderson, 2001). The effect of changing variables over different timescales is also not considered. A landscape which has experienced prolonged unchanging variables will evolve differently to one which is experiencing changing climate or tectonic conditions. This study compares the modern precipitation and strain rate to the modern landscape, but this does not account for the response time of landscapes to adapt to changing conditions, which may be on a Kyr to low (< 3) Myr timescale (Huntington et al., 2006; Hobley et al., 2010). Strong correlations may suggest that the climatic and tectonic conditions have remained largely steady allowing the landscape to respond, that the landscape has responded rapidly to changing climatic or tectonic factors, or that tectonic or climate variations have not varied spatially.

The results of Chapter 3 suggest that the eastern Tibetan Plateau was at high elevations before the Miocene. The intensification of the monsoon leads to incision and erosion of the plateau, with the rivers biting into the plateau. The trend of correlation between HI and annual precipitation in the Tibetan Plateau is much steeper than for the fold-and-thrust belts (Figure 5.6), meaning HI varies more over a smaller range of precipitation. A possible explanation for this is that the monsoon precipitation creates much higher relief, due to high erosion in the area of high precipitation. Therefore, areas within the monsoon limit have a higher HI than those outside the monsoon limit.

5.5 Conclusion

HI, SR and the second invariant of strain rate are calculated in Chapter 4 and correlations between these factors in different fold-and-thrust belts are studied here. There is a positive correlation between these factors and annual precipitation, elevation and the percentage of glaciation. Strong correlations of interest are those between precipitation and the strain rate respectively with HI and SR. These correlations give insight into the relative importance of tectonics and climate in the landscape of active fold-and-thrust belts. This study concludes that climate is a greater control on landscape than tectonics (r^2 = 0.62 – 0.64 with p-value < 0.001 and a positive correlation r = 0.79 - 0.81, compared to r^2 = 0.38 – 0.51 with p-value < 0.001 and a positive correlation r = 0.63 - 0.72; Figures 5.3 and 5.5), although the variables considered are not completely independent. However, the result does suggest that the climate is a stronger control on landscape than the strain. This result has potential to be extended in the future, to other active regions. The analysis is briefly extended to the eastern Tibetan Plateau which also shows a similar result.

Chapter 6: Discussion, Suggestions for Further Work and Conclusions

6.1 Discussion

6.1.1 Tectonic Geomorphology

Throughout the thesis, multiple methods of analysing the regional tectonic geomorphology are used. The results show the good functionality of geomorphic indices in highlighting active faulting (Chapter 2), potentially highlighting the location of a seismogenic-non-seismogenic transition (Chapters 2 and 4), identifying regional changes in the landscape (Chapter 3) and allowing a more global comparison of landscapes in different fold-and-thrust belts (Chapter 5).

In Chapter 2, multiple methods and different ways of using the same methods are introduced. Calculation of regional geomorphic indices e.g. HI, SR, ZR can be carried out within individual drainage basins or over the entire region using a moving window approach. Calculation by basin is preferred, as this minimises smoothing over geomorphic and tectonic boundaries. The margins of basins are not random, but reflect tectonic and lithological factors such as the location of active faults and stratigraphic boundaries. This is seen as an advantage rather than a problem but needs to be kept in mind when making either visual or numerical analyses of the results. HI and SR are used to assess fold-and-thrust belts and both techniques show complementary results, with some variation. In some areas, there are differences between the location of high or low HI and SR regions. For example, in Chapter 4, HI correlates consistently with the change in deformation style, with SR also correlating well, apart from in the Himalaya where high SR values occur at higher elevations than the deformation transition from locked to creeping behaviour on the underlying thrust. This offset between HI and SR is likely to be due to the highest SR values occurring at the highest peaks. Differences in the geomorphic indices may therefore give further information about landscapes.

In Chapters 3-5, these regional geomorphic indices of HI, SR and ZR are used rather than commonly used stream channel measures such as k_{sn} (slope area analysis) which is calculated in Chapter 2, or chi analysis or the identification of knickpoints (e.g. Kirby and Whipple, 2012; Perron and Royden, 2013). Benefits of using channel profile analysis are that they have been shown to be highly sensitive to tectonic perturbations (Whittaker, 2012), are drivers of landscape systems and set the boundary conditions for hillslopes and therefore are the mechanism by which climate and tectonic signals are transferred to the entire landscape (Whipple, 2004; Hurst et al., 2013). However, the fold-and-thrust belts studied in this thesis have been extensively analysed using these methods,

with results complementary to the results presented in this thesis. For example, channel steepness (k_{sn}) and HI calculated in the Himalaya give a largely complementary pattern of values, but k_{sn} does not pick out the Main Frontal Thrust and South Tibetan Detachment as clearly as HI (Obaid, 2018). Cannon and Murphy (2014) find a negative relationship between k_{sn} and degree of coupling on the underlying thrust in the Himalaya, as calculated by Stevens and Avouac (2015), which is complementary to the results of HI and SR shown in the Himalaya swath profiles in Chapter 4. Knickpoints in the Himalaya are found to occur in high relief areas (Duncan et al., 2003). Across the Zagros, k_{sn} and HI patterns are also found to be complementary (Obaid and Allen, 2019) and knickpoints across the range do not highlight active faulting, apart from in two localised regions. Knickpoints also occur both above and below the 1250 m seismogenic limit (Obaid, 2018; Nissen et al., 2011). Knickpoints calculated across the Qilian Shan, calculated by H. Zhang et al., (2017) show a broad correlation to the geomorphic indices (discussed in Chapter 2) and k_{sn} analysis shows similar results to the geomorphic indices calculated on a basin scale in Chapter 2. In the Central Andes extensive analysis of river channels identifies multiple knickpoints related to tectonic uplift (Hoke et al., 2007). These results suggest that the use of the basin-scale geomorphic indices are a valid approach for analysing landscapes in tectonically active areas, providing a useful alternative to channel-based approaches. A benefit of a basin-wide approach is that it uses data from a larger area, including hillslopes. Basin-wide techniques also have the benefit of making better comparisons to non-river datasets. This includes raster data such as precipitation and point data such as thermochronology ages and erosion rates, as the datasets do not have to be spatially smoothed and extrapolated, or collapsed onto the nearest river profile. Basin-wide geomorphic indices identified a landscape transition in the eastern Tibetan Plateau, but changes have not previously been identified in channel long profiles through the region. River channel measurements and knickpoint calculation are also highly dependent on DEM resolution and quality (Schwanghart and Scherler, 2017), whereas resolution was not found to alter the regional geomorphic indices in this work (Chapter 2).

The landscapes of tectonically active areas are controlled by a large variety of independent and interdependent factors. These are tectonic factors such as active faults, crustal strain and shortening and deformation, climatic factors such as precipitation, seasonality and glaciation and erosion factors such as drainage pattern, erosion rates and lithology. These factors may vary on different timescales, for example, the monsoon intensification discussed in Chapter 3 shows that a change in climate can rapidly change exhumation patterns. In order to understand the processes shaping these tectonically active regions, it is necessary to consider this wide variety of factors. The geomorphic index results show that, although there are a wide variety of controls on landscape, it

is possible to identify multiple factors. For example, in Chapters 2 and 4 individual faults, drainage divides and underlying structure and deformation style of the mountain belts are each shown to have an effect on geomorphic indices. Looking at different scales also reveals different controls. For example, comparison between different areas shows climatic control on landscape which is not seen within individual mountain belts and swaths (Chapter 5). Geomorphic indices should also be visualised in different ways. Map views can help to show general patterns and also individual features such as changes in values across faults and drainage divides. Use of data swath profiles gives a picture of trends in data which are not always obvious in map view, although, as they smooth data they cannot show the discrete changes across features in the same way as the maps.

6.1.2 Tectonic Understanding

The geomorphic indices have helped in tectonic understanding. They are shown to be sensitive to active faulting, with changes in geomorphic indices occurring across active traces, as has also been found in previous studies (Boulton and Whittaker, 2009; Gao et al., 2016; Nennewitz et al., 2018). The methods have been applied to differing tectonic settings, as the scale, deformation style and formation of the different mountain belts studied differ.

Results in Chapters 2 and 4 show geomorphic indices can give greater confidence in, or constraints on models of crustal deformation or strain rate. Higher HI and SR and lower ZR occur over locked, seismogenic faults and lower HI, lower SR and higher ZR occur over non-seismogenic, ductily-deforming crust. The extent of seismogenic thrusting has been compared with geomorphic indices (Obaid and Allen, 2019) and the work presented here extends this work. Confidence in defining a seismogenic to non-seismogenic transition is important for hazard planning as this can constrain the area of likely earthquakes and seismically induced landslides.

Plateau formation occurs in high elevation crust with low shortening rates. Plateaux are often internally drained basins, with internal drainage aiding the formation of low relief as material is eroded from and deposited into the same basin (Burbank and Anderson, 2001). Internal drainage formation is also aided by active faulting disrupting the drainage network (Burbank and Anderson, 2001), which is seen in the Qilian Shan and the Tibetan Plateau (Chapters 2 and 3). Throughout this thesis, changes in values of geomorphic indices show the location of a change from flat, high elevation plateau morphology to more incised and rugged landscapes. The extent of the geomorphic plateau is not the same as the extent of internal drainage (200-500 km apart in the Tibetan Plateau, >150 km in the Himalaya, 0 - 100 km in the Qilian Shan and Zagros and 20 – 50 km in the Andes). These changes are shown particularly clearly in the swath profiles in Chapter 4 or the

maps in Chapter 3. This suggests that although internal drainage aids plateau formation, it is not required.

6.1.3 Climate and Tectonics

Climate and tectonics both affect landscapes and are interlinked, making it difficult to determine the relative importance of each driver (Champagnac et al., 2012). Within the individual ranges studied, there are no strong visual correlations between mean geomorphic indices and precipitation. In individual swaths, the precipitation is largely related to elevation (orographic precipitation), rather than the geomorphic indices. I conclude that the precipitation is not a major factor controlling landscapes within the mountain belts, because precipitation does not clearly correlate to landscape changes. In all cases I look at changes in trend on swath profiles or relative values on maps and boxplots. This is not to say that climate has no effect on landscape, but more simply that the precipitation is not the overriding factor e.g. in the Qilian Shan there is E-W variation in precipitation along the mountain belt and little E-W variation in deformation style and strain rate, yet there is no apparent correlation between landscape and annual precipitation. This may be due to the response time of the landscape to changing climate conditions. In each fold-and-thrust belt there is no clear positive correlation between mean HI and precipitation and mean SR and precipitation, with the scatter plot figures showing clustering of values from each location. This lack of correlation is useful as this means that non-climatically forced changes can be identified in the profiles, for example across a fault or as a result of a drainage divide or change in deformation style, as discussed above.

It is only when the mountain belts are considered together that correlations between mean HI and precipitation and geomorphic indices occur (Chapter 5). This is likely to be due to the relatively low variations in precipitation within the mountain ranges compared to between them. A lack of correlation within the ranges may also be due to the other factors controlling morphology (tectonics, drainage, lithology and other climatic factors). In the comparison the greater number of data points may cause these factors to form scatter within each belt, without concealing the main trend between the belts. Therefore, on different scales the apparent relative impact of different tectonic and climatic forcings may vary.

The correlations between the climatic, tectonic and geomorphic variables in this work suggest that the climate (namely annual precipitation) is a greater control on landscape than tectonics. Few studies have quantified the relative controls of tectonics and climate on modern landscapes. Champagnac et al., (2012) used a global study with conclusions in line with this work: climate can

account for landscape relief more than tectonics (less than 25 % of topographic relief is due to crustal shortening and up to 50 % is due to measures of tectonics and climate (latitude, annual precipitation and shortening)). Jiao et al., (2017) show highest exhumation in New Zealand where both tectonic deformation and precipitation are high, but areas of low tectonic deformation can still produce high exhumation rates in glaciated areas. However, Bermúdez et al., 2012 suggested that elevation in mountain belts is tectonically supported with no need for climate forcing. Clearly further work needs to be done in quantifying and untangling these factors. The work in Chapter 5 contributes to this understanding by using a range of factors at a decadal timescale rather than comparing to modelled exhumation rates calculated from thermochronology (Herman et al., 2013; Jiao et al., 2017) and is one of the few studies to include multiple mountain ranges (e.g. Jiao et al., 2017 in New Zealand and Bermúdez et al., 2012 in the Venezuelan Andes).

Comparison of published erosion rate to calculated geomorphic indices show no to weak correlation in the eastern Tibetan Plateau (r^2 0.02 – 0.4) and Qilian Shan (r^2 0.34 – 0.53). Published comparisons show varied results: no correlation of denudation rate to relief in Taiwan (Dadson et al., 2003) and a strong correlation between exhumation and relief in the Andes (Bermúdez et al., 2012). These varied results and low correlations may be due to the different timescales on which factors are measured.

The relationship between erosion rates (decadal, or thermochronology-derived) and precipitation (decadal) varies globally, with some studies show strong correlations (Herman et al., 2013; Jiao et al., 2017; Reiners et al., 2003; Thiede et al., 2004; Adams et al., 2020) and others showing weak to no correlation (Burbank et al., 2003; Godard et al., 2014; Pan et al., 2010). Published erosion rates show a distinct pattern of low erosion rates in eastern Tibet (< 0.1 mm/yr) east of 95° and where precipitation rates are below 450 mm/yr and a range of low to high erosion rates to the west in areas with higher precipitation. High erosion rates are attributed to the extent of the East Asian Summer Monsoon. This may not be the only cause: there may be a threshold in a control. This may be a threshold in the annual precipitation, or a related factor such as the amount of precipitation in individual storm events, or surface runoff. In the Andes, stream power (precipitation and upstream area) is related to erosion up to an erosion rate threshold of 0.2 mm/yr but above this non-fluvial transport and sediment availability are more dominant controls (Bookhagen and Strecker, 2012). These two results may be complementary and suggest that such erosion rate thresholds may occur globally.

Results of Chapter 3 and published work suggested that the eastern Tibetan Plateau was at high elevations by the pre-Miocene and monsoon-driven erosion occurred by ˜25 Ma (Rowley and

Currie, 2006; Ao et al., 2016; Zhang et al., 2018; Kapp and DeCelles, 2019) to create the modern-day morphology described in Chapter 3. Jiao et al., (2017) has also suggested a similar mechanism in New Zealand: tectonics set up the regional exhumation pattern, but both strong tectonic deformation and efficient erosion from precipitation are needed to maintain high exhumation rates. This may partially explain why precipitation is more strongly correlated with landscape than strain rate (Chapter 5) as each mountain belt studied has been uplifted for a long duration and precipitation may now be now modulating erosion rate, although they are still actively shortening. Tectonics builds up landscape for potential erosion, but erosion rate, exhumation, river incision and therefore landscape morphology depend on precipitation.

6.2 Conclusions

Geomorphic indices have been used successfully in this study to understand processes in fold-and-thrust belts, enhancing understanding based on previous geomorphology studies and other approaches (Chapters 2 and 4). The geomorphic indices of HI, SR and ZR are shown to be sensitive to climatic and tectonic controls. Geomorphic indices are particularly useful in evaluating models of crustal deformation when integrated with information such as active faulting, drainage patterns and climate data. Seismic to non-seismic transitions in crustal deformation defined by published studies are also identified using geomorphic indices.

Seismic to non-seismic transitions in crustal deformation style are seen in the geomorphic data for each fold-and-thrust belt studied, although tectonic and climatic settings and tectonic structure varies. Seismic to non-seismic transitions and active faulting are identified using swath profiles spaced along mountain belts in the Qilian Shan, Himalaya, Andes and Zagros. These settings vary in terms of climate and mountain belt scale as well as tectonic setting (continent-continent collision: Qilian Shan, Himalaya and Zagros; ocean-continent subduction: Andes) and deformation style (shorting accommodated on a detachment: Qilian Shan, Himalaya, Andes; shorting accommodated on discrete thrusts: Zagros). Identification of a landscape change over the seismic to non-seismic transitions strengthens our confidence in understanding the structures and therefore strengths our understanding of the mountain belt-landscape systems.

A monsoon-controlled landscape transition in the central-eastern Tibetan Plateau is identified using geomorphic indices, precipitation, erosion rates and thermochronology ages (Chapter 3). This monsoon control has occurred since monsoon intensification at 25 Ma. This result is used to analyse suggested Tibetan Plateau uplift mechanisms and is consistent with a model of pre-Miocene growth.

Comparison between the geomorphic indices values for different mountain belts and climatic and tectonic factors suggests that both climate and strain rate control the landscape of fold-and-thrust belts, with strong positive correlations. This work tentatively suggests that climate (precipitation) is a stronger control on these landscapes than tectonics (strain rate) and this work can be extended further.

The relationship between precipitation and geomorphic indices varies in the different geographic locations studied in this thesis and at different scales. A positive correlation between precipitation and geomorphic indices occurs when comparing between different fold-and-thrust belts (Chapter 5). However, within individual fold-and-thrust belts no strong precipitation control on geomorphic indices is seen in boxplots and along swath profiles (Chapter 4). This lack of correlation is particularly clear in the Qilian Shan where there is a distinct east-west variation in precipitation which is orthogonal to the shortening direction but there is no east-west variation in the geomorphic indices (Chapter 2). This may be because of the scale of the comparison: climate varies much more between different locations than within them. In the eastern Tibetan Plateau a strong precipitation control on landscape is inferred (Chapter 3).

6.3 Suggestions for Further Work

A landscape evolution model could be usefully integrated into Chapter 3 to show that the monsoon can drive incision and exhumation to produce the exhumation and erosion rates in the datasets and the modern-day landscape.

Comparison could be extended to other areas for example, areas without plateaux, less tectonically active areas, wetter areas or other tectonic settings. Examples could include the Greater Caucasus range which is a relatively narrow, tectonically active belt, or the Pyrenees which has similar dimensions to the Greater Caucasus but has been tectonically inactive for millions of years.

Channel profile analysis techniques could be applied to the fold-and-thrust belts studied using a consistent approach. However, such analysis has already been extensively carried out in the areas studied in this thesis, and results are consistent with those of the geomorphic indices calculated in basins in this thesis, so results are unlikely to provide a new insight.

There is very little thermochronology data between 94 and 98 ° E in the Tibetan Plateau. This is the location of the landscape change identified in Chapter 3. If more data was collected in this region this could be used to confirm the conclusions of this work: a distinct change in thermochronology age pattern occurs across the landscape change, with the area within the monsoon limit

experiencing significant exhumation since monsoon intensification, but the area beyond experiencing little or no exhumation.

Further comparison of erosion rate data to precipitation or to surface runoff or stream power could be carried out in the area of the Tibetan Plateau and the other areas studied, to identify if there is a threshold controlling erosion rates, and if this threshold is global or variable between regions.

Multiple regression of the three factors considered (strain rate, annual precipitation, % glaciation) can account for up to 77% of SR and 64% of HI, caveats discussed in Chapter 5. There could be inclusion of other factors such as lithology, temperature, seasonal precipitation, surface runoff, denudation, tectonic shortening or strain rate calculated in different ways.

Appendix

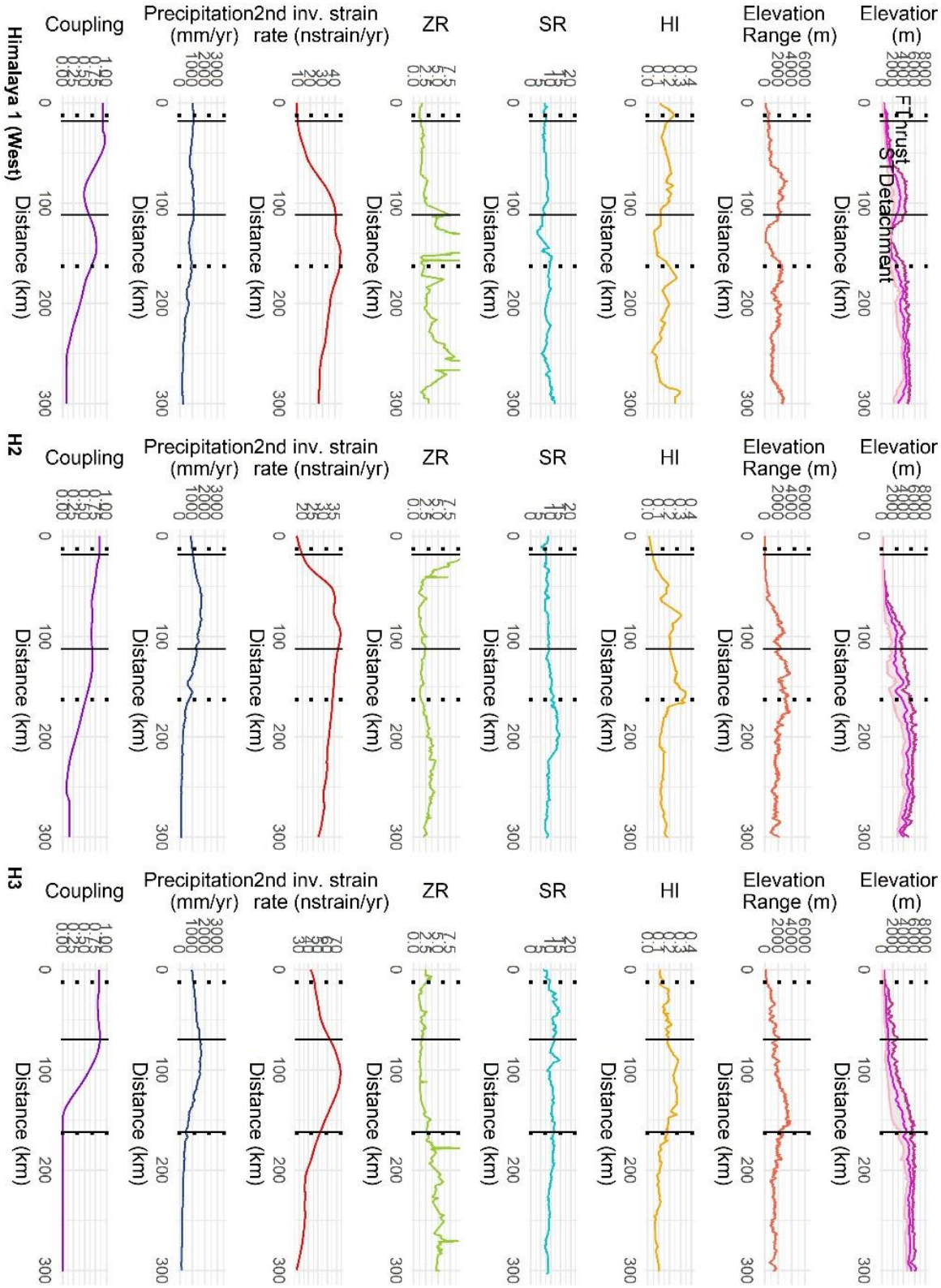
Elevation (m)
Elevation Range (m)
HI
SR
ZR
2nd inv. strain rate (nstrain/yr)
Precipitation (mm/yr)
Coupling
Distance (km)
FT
Thrust
ST
Detachment
Himalaya 1 (West)
H2
H3

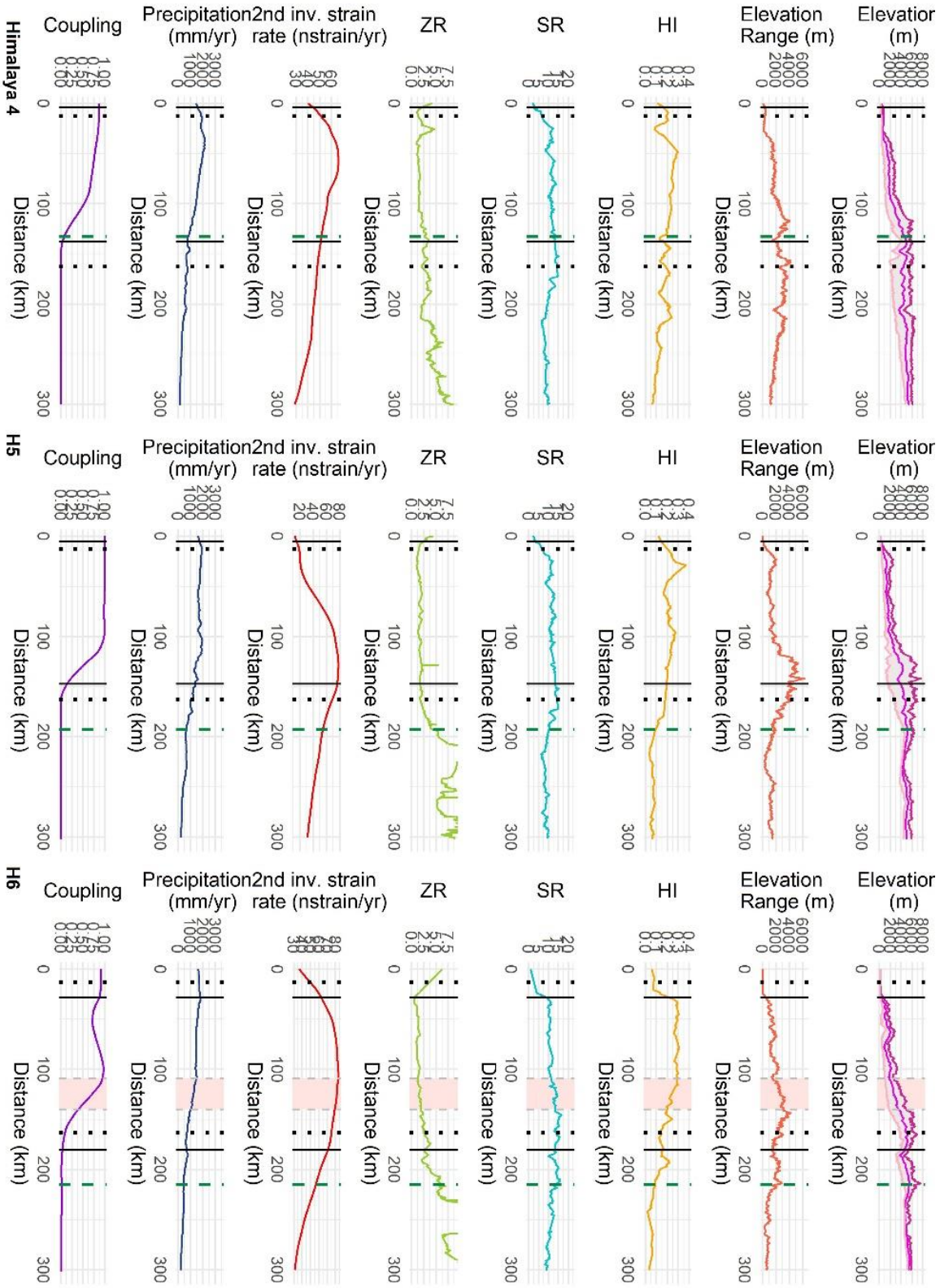
Elevation (m)
Elevation Range (m)
HI
SR
ZR
2nd inv. strain rate (nstrain/yr)
Precipitation (mm/yr)
Coupling
Distance (km)
Himalaya 4
H5
H6

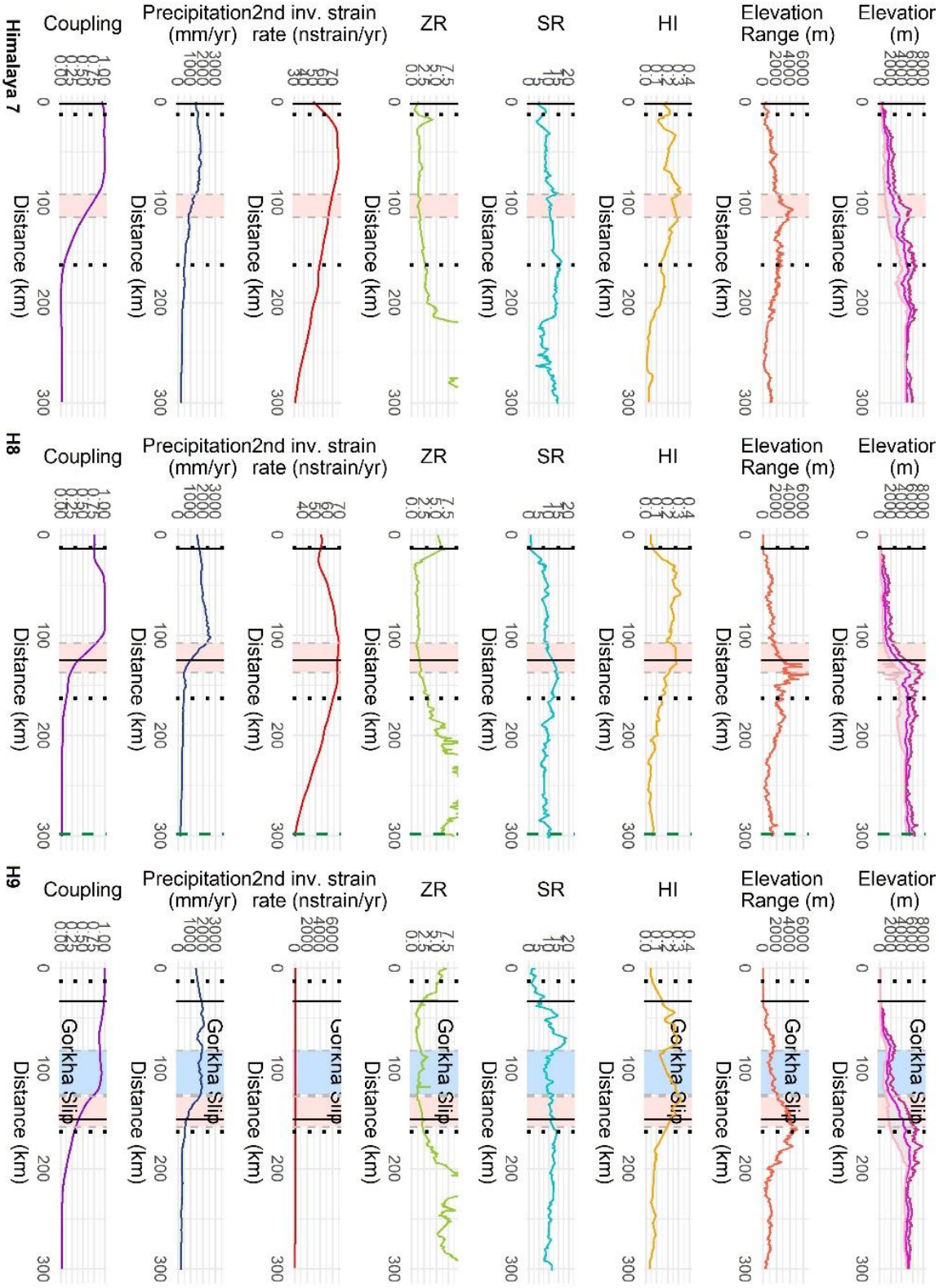
Elevation (m)
Elevation Range (m)
HI
SR
ZR
2nd inv. strain rate (nstrain/yr)
Precipitation (mm/yr)
Coupling
Distance (km)
Gorkha Slip
Himalaya 7
H8
H9

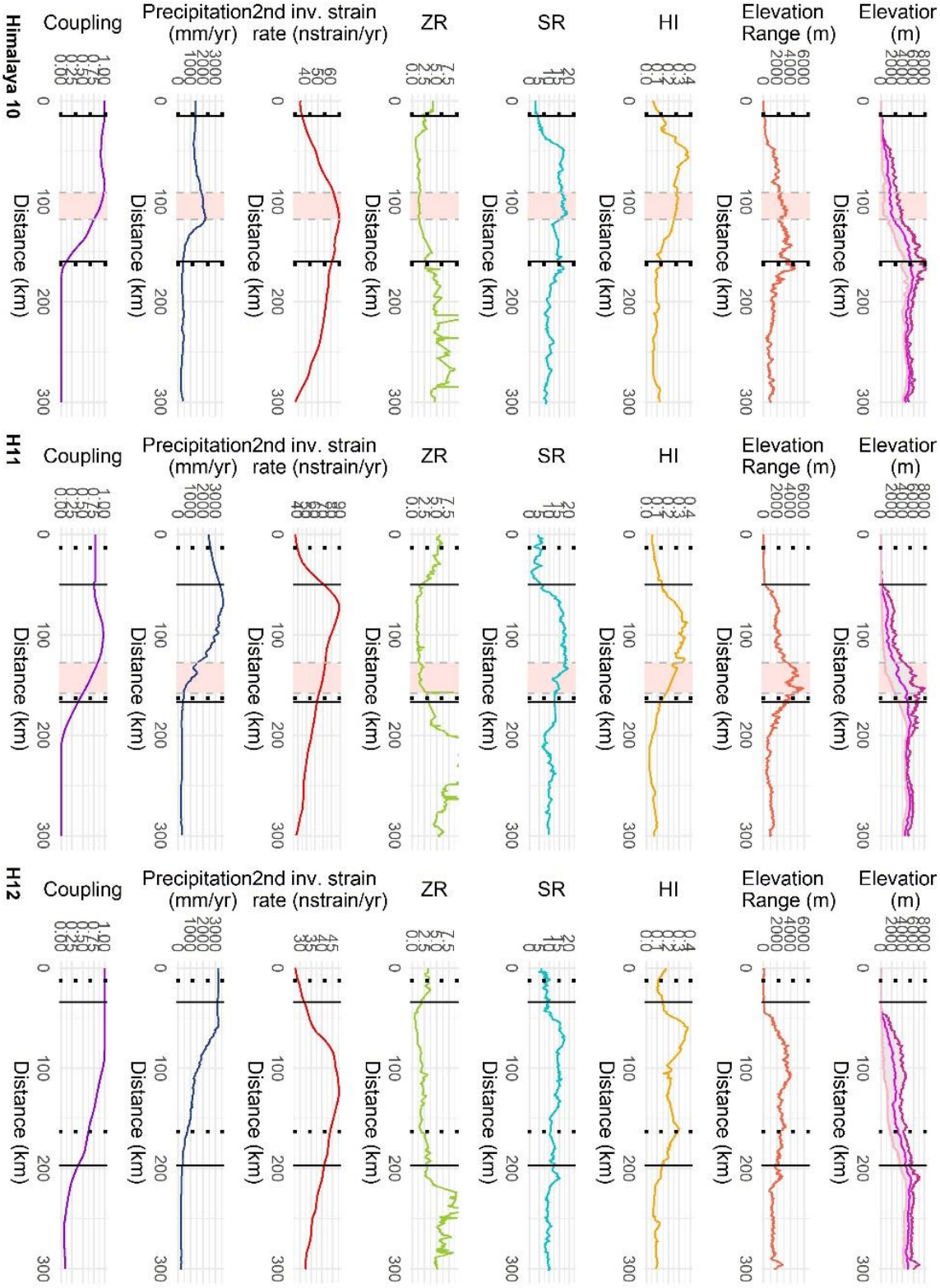
Elevation (m)
Elevation Range (m)
HI
SR
ZR
2nd inv. strain rate (nstrain/yr)
Precipitation (mm/yr)
Coupling
Distance (km)
Himalaya 10
H11
H12

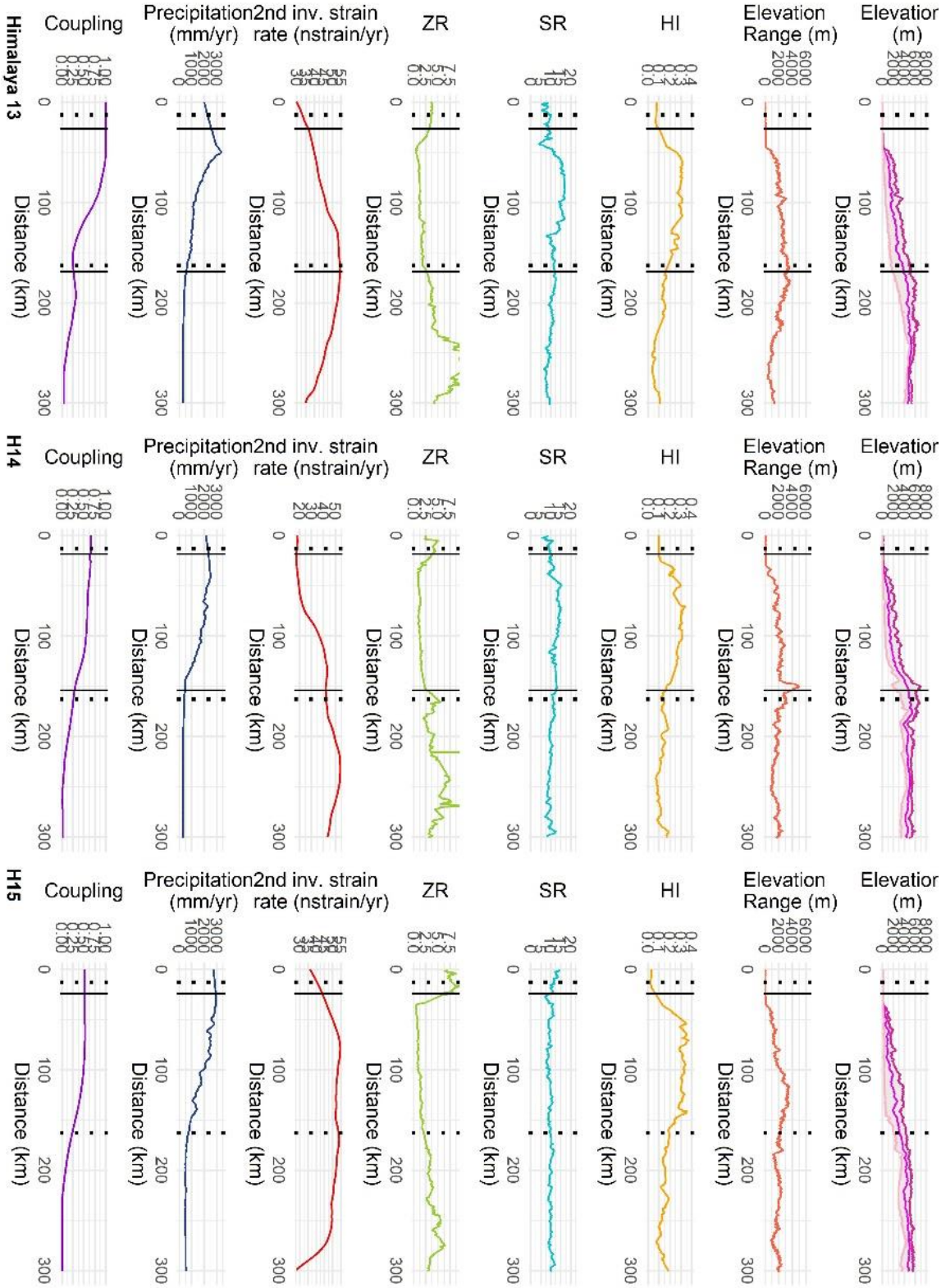
Elevation (m)
Elevation Range (m)
HI
SR
ZR
2nd inv. strain rate (nstrain/yr)
Precipitation (mm/yr)
Coupling
Distance (km)
Himalaya 13
H14
H15

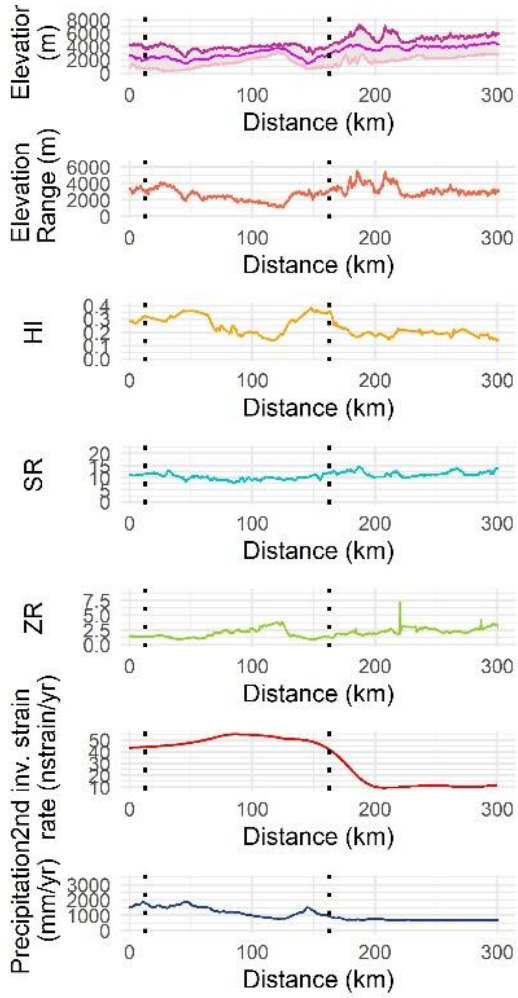

Figure App.1: Sixteen swath profiles, from east to west across the Himalaya, 300 km in length, locations of which are shown in Figure 4.6. For each swath the elevation, relief, HI, SR, ZR, annual precipitation and second invariant of strain rate are shown, calculated for 30 km width swaths and the Stevens and Avouac (2015) calculated coupling extent is shown for swaths H1-H15. Black dotted vertical lines show the extent of the quadrats, solid black lines show the location of fault traces, dashed green lines show the location of the internal-external drainage divide, the shaded pink area show the extent of creeping as calculated by Lindsey et al., (2018) and the shaded blue the extent of the slip on the 2015 Gorkha earthquake.

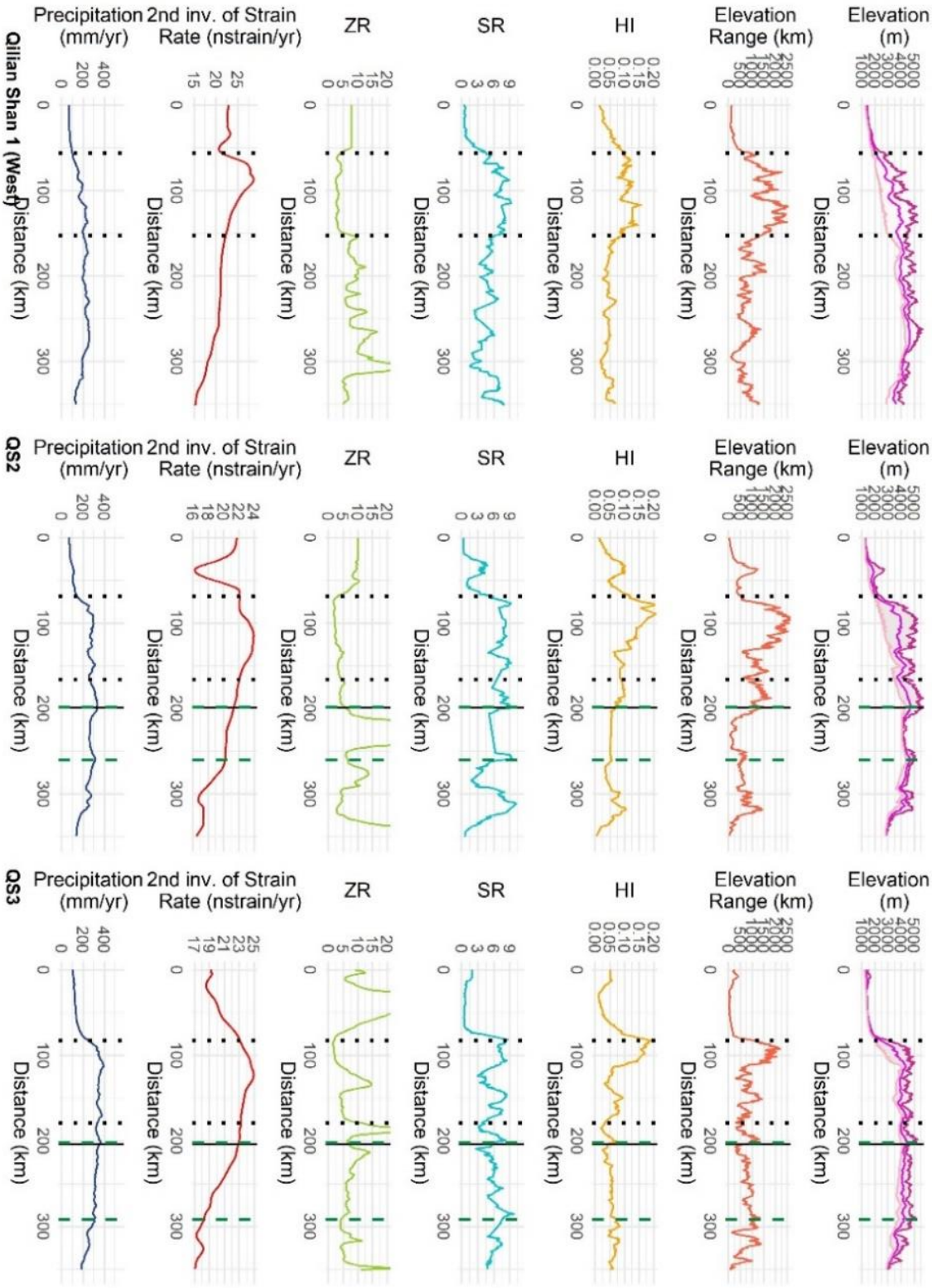
Qilian Shan 1 (West)
QS2
QS3
Elevation (m)
Elevation Range (km)
HI
SR
ZR
2nd inv. of Strain Rate (nstrain/yr)
Precipitation (mm/yr)
Distance (km)

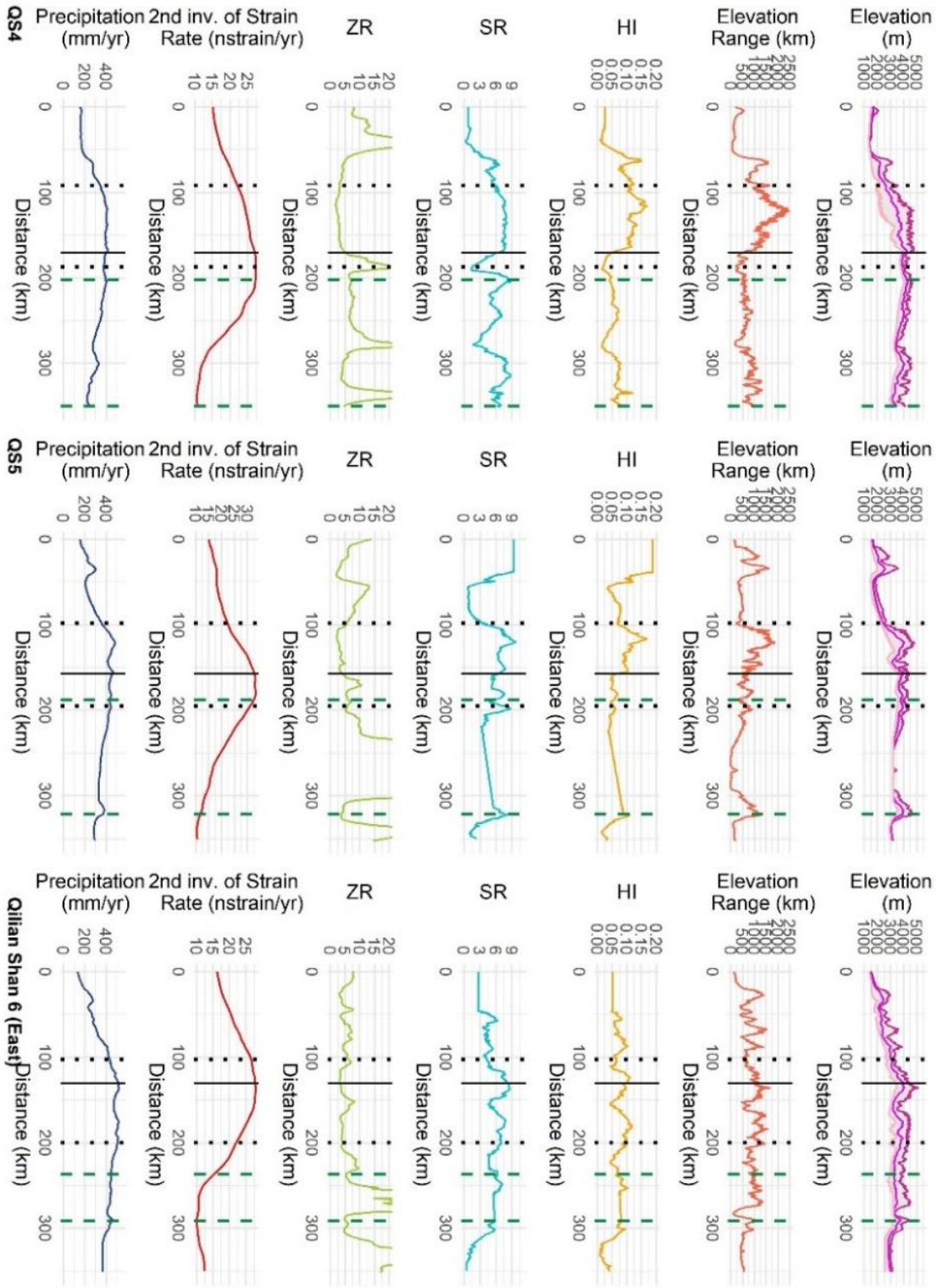

Figure App.2: Six swath profiles, from east to west across the Qilian Shan, 300 km in length. The locations are shown in Figure 4.9 and HI, ZR, SR and precipitation maps in Figures 2.12, 2.14, 2.15 and 2.3. For each swath the elevation, relief, HI, SR, ZR, annual precipitation and second invariant of strain rate are shown, calculated for 30 km width. Black dotted vertical lines show the extent of the quadrats, solid black lines show the location of Haiyuan Fault and dashed green lines show the location of the internal-external drainage divide.

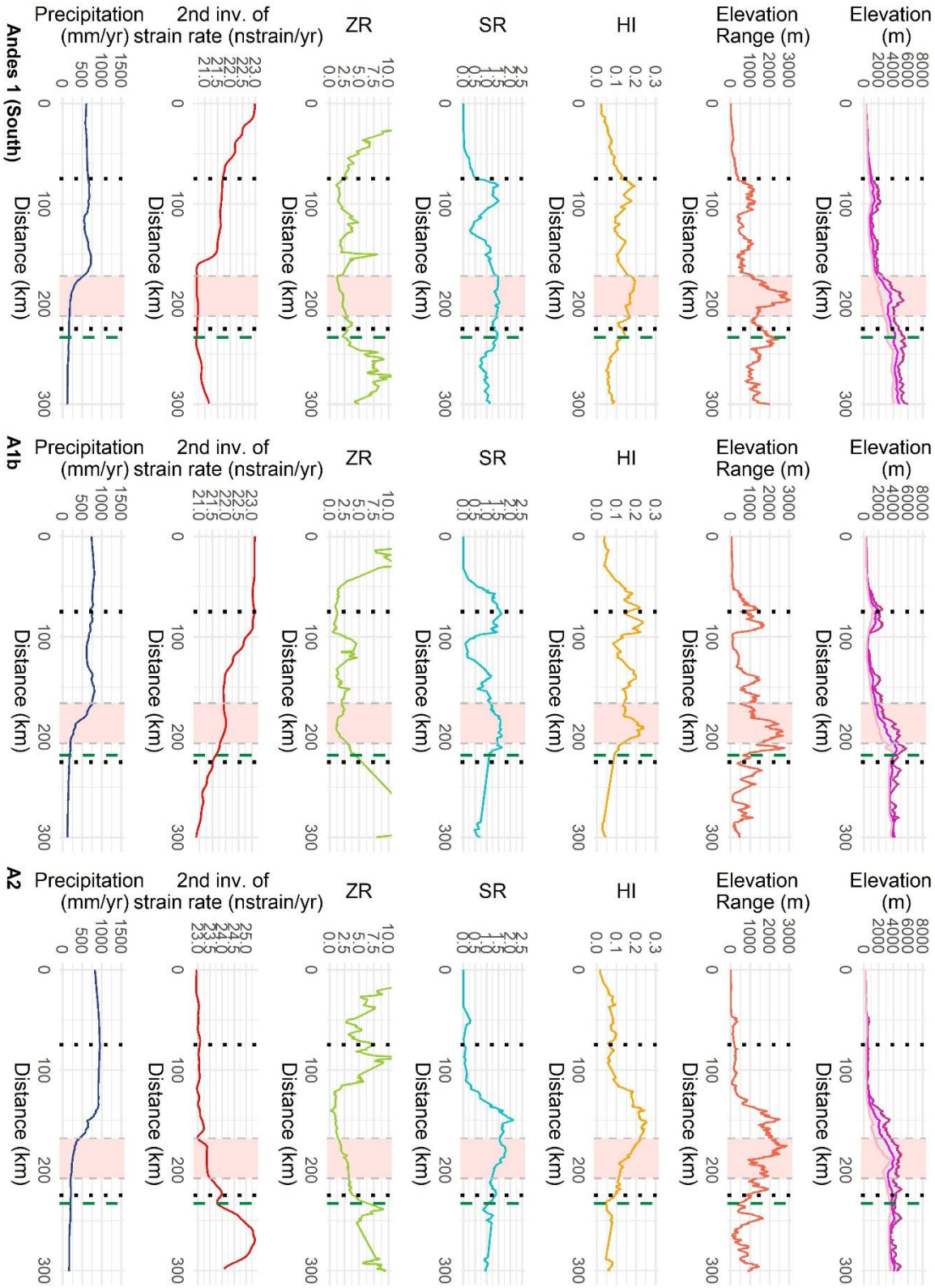
Andes 1 (South)
A1b
A2
Precipitation (mm/yr)
2nd inv. of strain rate (nstrain/yr)
ZR
SR
HI
Elevation Range (m)
Elevation (m)
Distance (km)

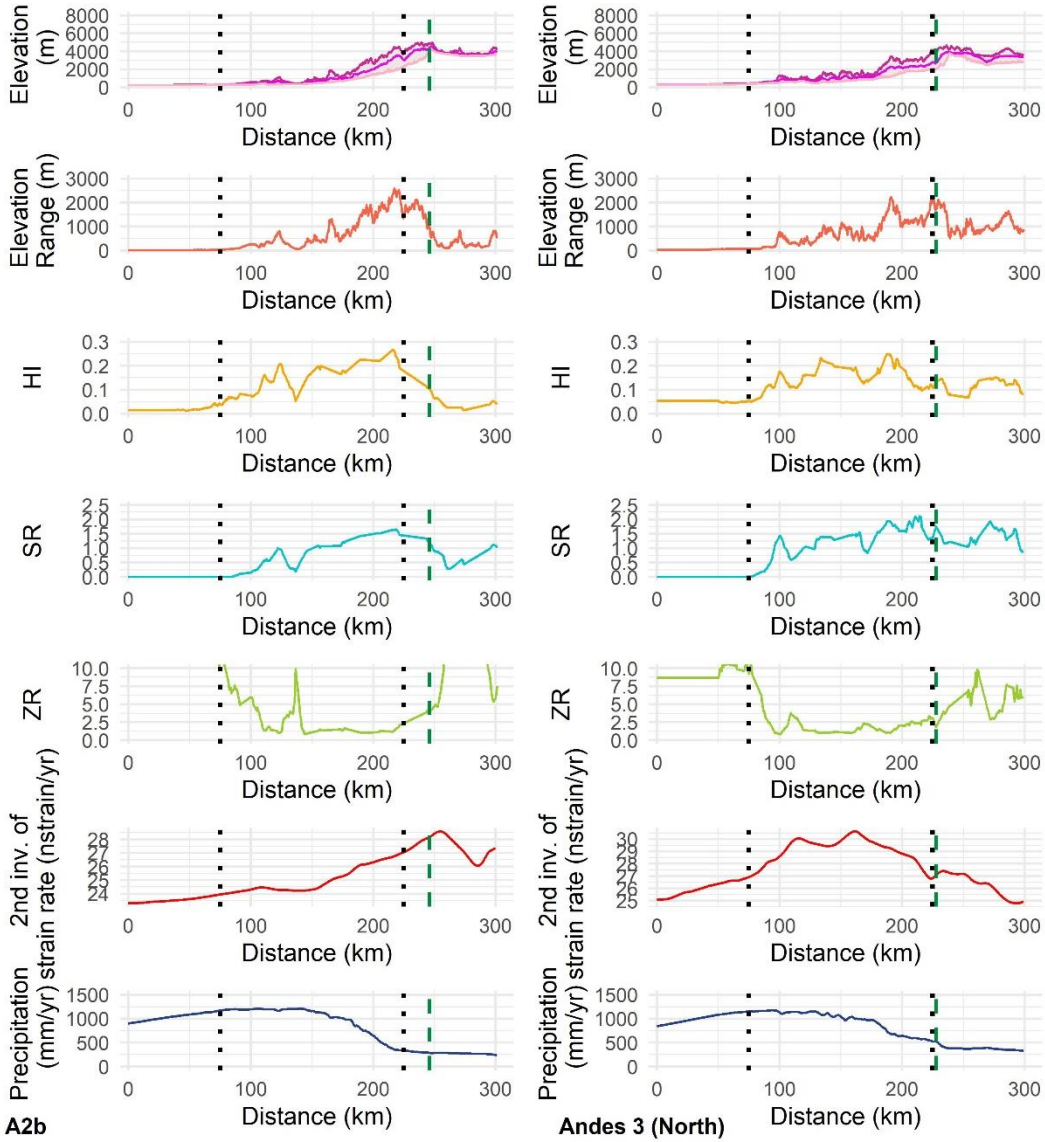

Figure App.3: Five swath profiles in the Andes, 300 km in length, with profiles drawn from A1 in the south to A3 in the north, shown on Figure 4.12. Note that the profiles are drawn from east to west across the range, to allow easier comparison to the other ranges (this means that elevation increases from left to right in each swath profile). For each swath the elevation, relief, HI, SR, ZR, annual precipitation and second invariant of the strain rate are shown, calculated for 30 km width swaths. Black dotted vertical lines show the extent of the quadrats, solid black lines show the location of fault traces, dashed green lines show the location of the internal-external drainage divide and the shaded pink area shows the locked-creeping transition defined by McFarland et al., (2017).

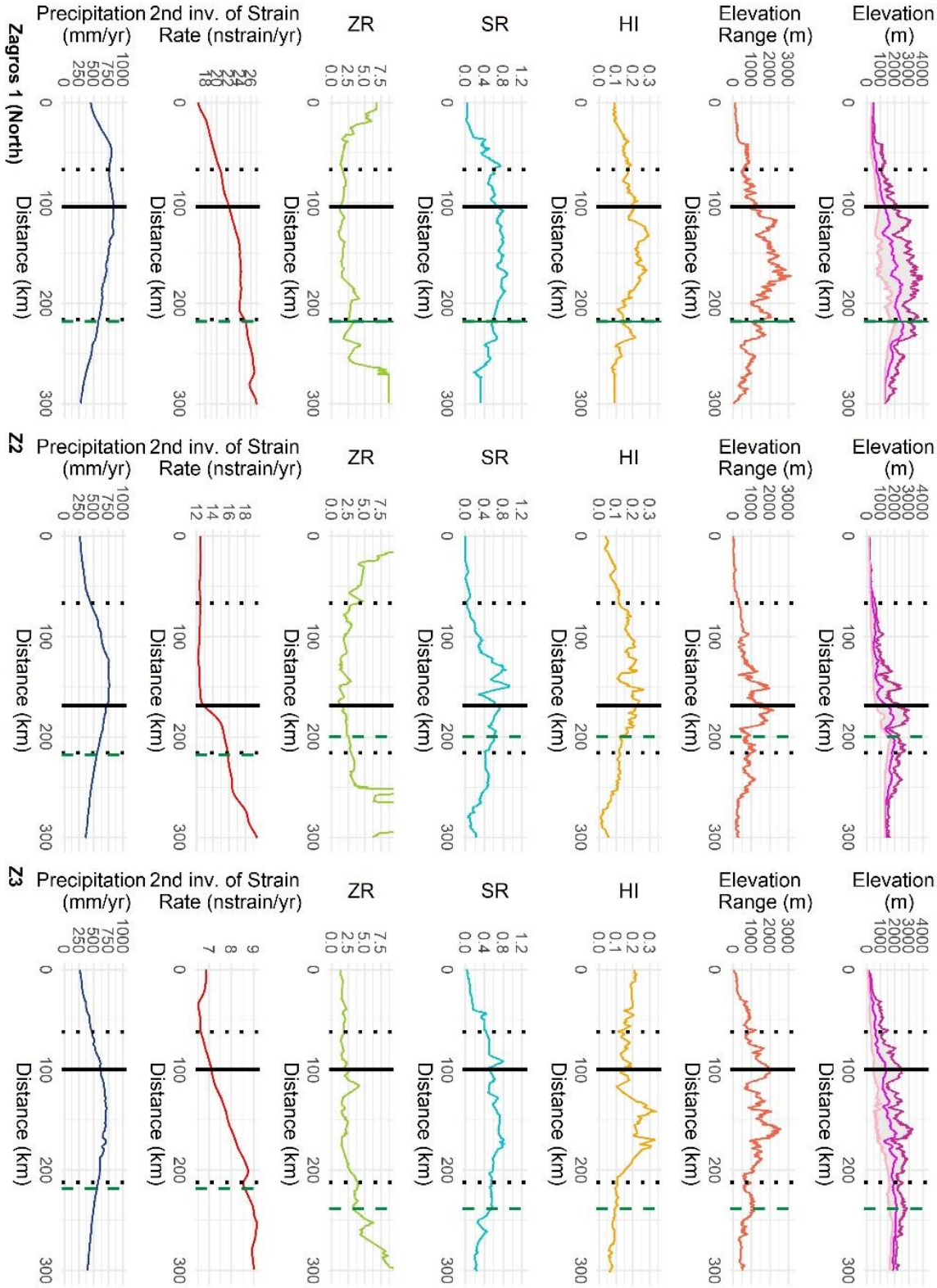
Zagros 1 (North)
Z2
Z3
Elevation (m)
Elevation Range (m)
HI
SR
ZR
2nd inv. of Strain Rate (nstrain/yr)
Precipitation (mm/yr)
Distance (km)

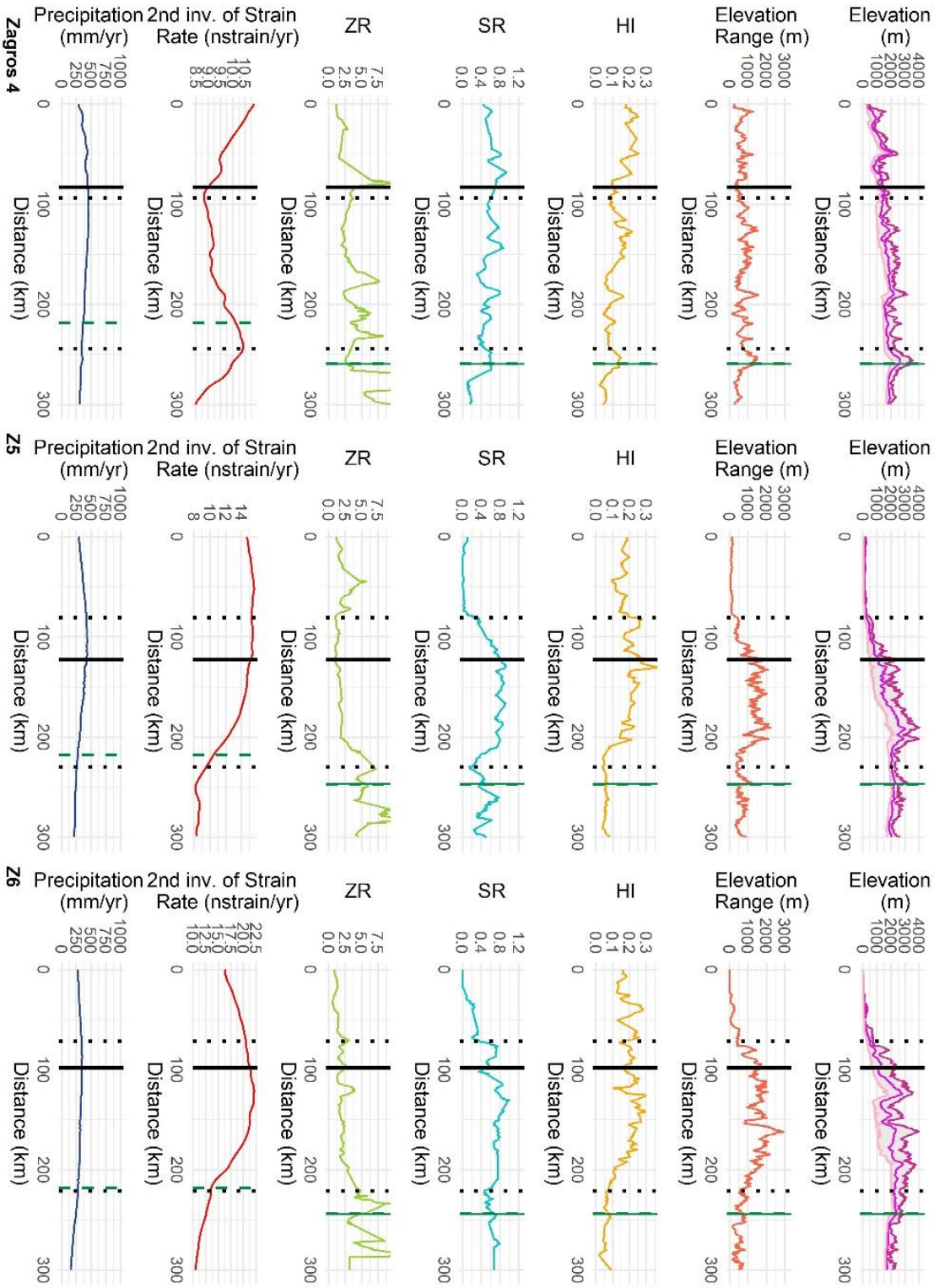
Zagros 4
Z5
Z6
Elevation (m)
Elevation Range (m)
HI
SR
ZR
2nd inv. of Strain Rate (nstrain/yr)
Precipitation (mm/yr)
Distance (km)

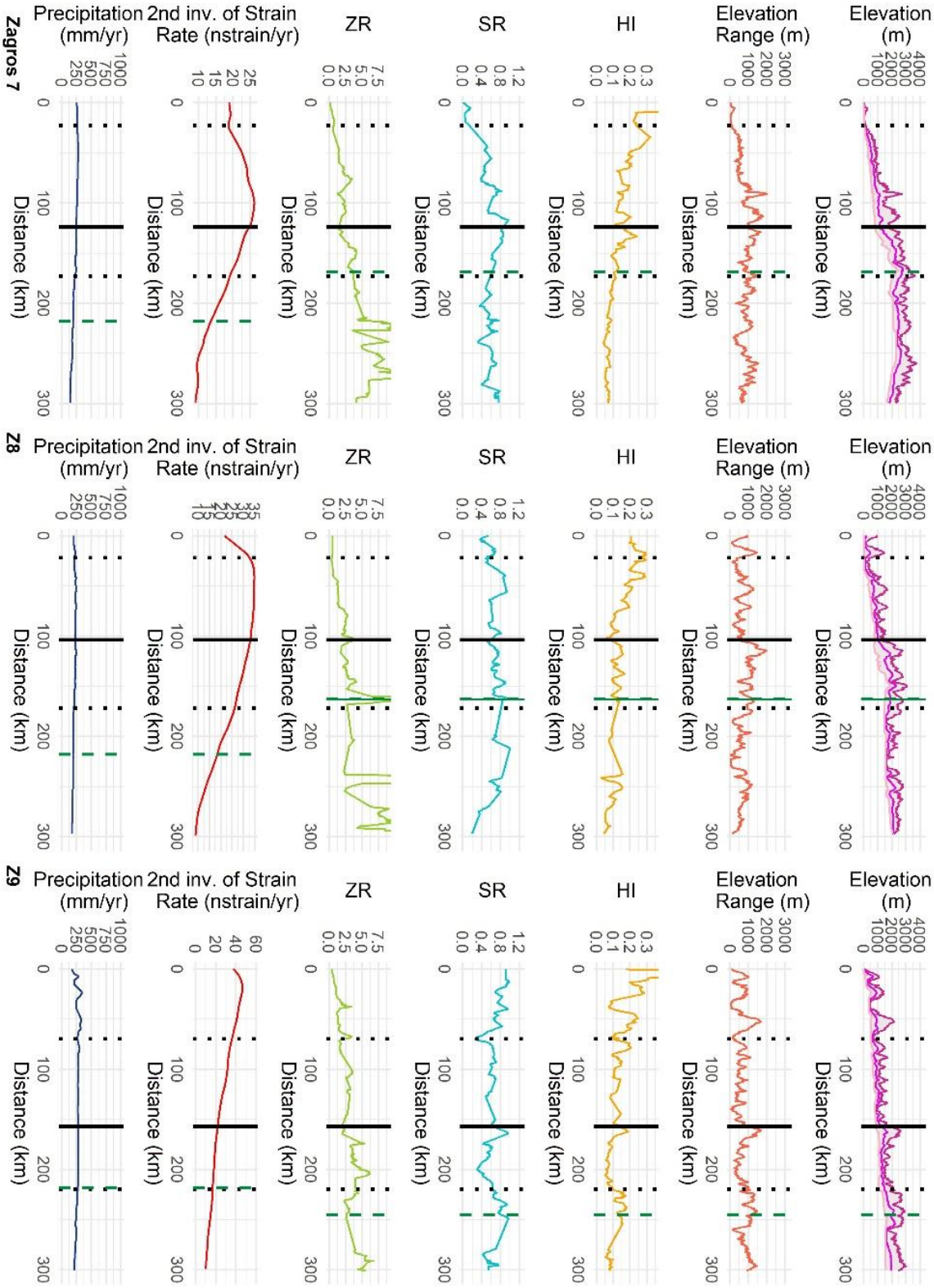
Zagros 7
Z8
Z9
Elevation (m)
Elevation Range (m)
HI
SR
ZR
2nd inv. of Strain Rate (nstrain/yr)
Precipitation (mm/yr)
Distance (km)

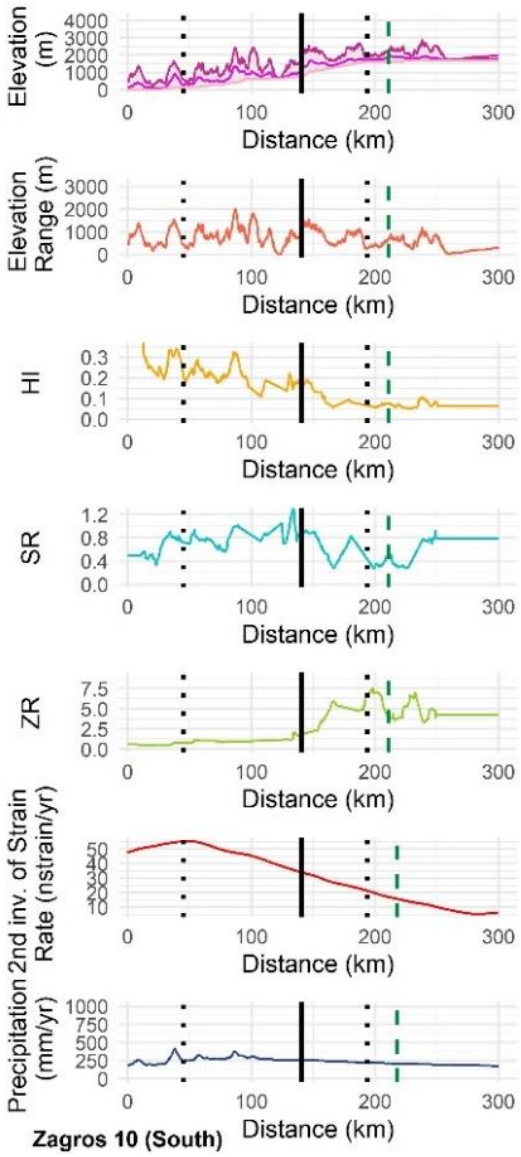

Figure App.4: Ten swath profiles, from north to south along the Zagros, 300 km in length, the locations of which are shown in Figure 4.17. For each swath the Elevation, relief, HI, SR, ZR, annual precipitation and second invariant of strain rate is shown, calculated for 30 km width. Black dotted vertical lines show the extent of the quadrats, solid black lines show the location of the 1250 m contour and dashed green lines show the location of the internal-external drainage divide.

References

Acosta, V.T., Schildgen, T.F., Clarke, B.A., Scherler, D., Bookhagen, B., Wittmann, H., von Blanckenburg, F. and Strecker, M.R., 2015. Effect of vegetation cover on millennial-scale landscape denudation rates in East Africa. Lithosphere, 7, 408-420.

Adams, B.A., Whipple, K.X., Forte, A.M., Heimsath, A.M. and Hodges, K.V., 2020. Climate controls on erosion in tectonically active landscapes. Science advances, 6, 3166.

Allen, M.B., Saville, C., Blanc, E.J.-P., Talebian, M., Nissen, E., 2013. Orogenic plateau growth: expansion of the Turkish-Iranian Plateau across the Zagros fold-and-thrust belt. Tectonics, 32, 171–190.

Allen, M.B., Walters, R.J., Song, S., Saville, C., De Paola, N., Ford, J., Hu, Z. and Sun, W., 2017. Partitioning of oblique convergence coupled to the fault locking behaviour of fold-and-thrust belts: Evidence from the Qilian Shan, northeastern Tibetan Plateau. Tectonics, 36, 1679-1698.

Alonso, R.N., Bookhagen, B., Carrapa, B., Coutand, I., Haschke, M., Hilley, G.E., Schoenbohm, L., Sobel, E.R., Strecker, M.R., Trauth, M.H. and Villanueva, A., 2006. Tectonics, climate, and landscape evolution of the southern central Andes: the Argentine Puna Plateau and adjacent regions between 22 and 30 S. In The Andes (265-283). Springer, Berlin, Heidelberg.

An, Z., Kutzbach, J.E., Prell, W.L. and Porter, S.C., 2001. Evolution of Asian monsoons and phased uplift of the Himalaya–Tibetan plateau since Late Miocene times. Nature, 411, 62-66.

Andronicos, C.L., Velasco, A.A. and Hurtado Jr, J.M., 2007. Large-scale deformation in the India-Asia collision constrained by earthquakes and topography. Terra Nova, 19, 105-119.

Ansberque, C., Godard, V., Bellier, O., De Sigoyer, J., Liu-Zeng, J., Xu, X., Ren, Z., Li, Y. and ASTER Team, 2015. Denudation pattern across the Longriba fault system and implications for the geomorphological evolution of the eastern Tibetan margin. Geomorphology, 246, 542-557.

Ansberque, C., Godard, V., Olivetti, V., Bellier, O., de Sigoyer, J., Bernet, M., Stübner, K., Tan, X.B., Xu, X.W., Ehlers, T.A., 2018. Differential exhumation across the Longriba fault system: implications for the eastern Tibetan plateau. Tectonics, 37, 663–679.

Ao, H., Roberts, A.P., Dekkers, M.J., Liu, X., Rohling, E.J., Shi, Z., An, Z. and Zhao, X., 2016. Late Miocene–Pliocene Asian monsoon intensification linked to Antarctic ice-sheet growth. Earth and Planetary Science Letters, 444, 75-87.

Arne, D., Worley, B., Wilson, C., Chen, S.F., Foster, D., Luo, Z.L., Liu, S.G. and Dirks, P., 1997. Differential exhumation in response to episodic thrusting along the eastern margin of the Tibetan Plateau. Tectonophysics, 280, 239-256.

Assumpção, M., Feng, M., Tassara, A., and Julià, J., 2013. Models of crustal thickness for South America from seismic refraction, receiver functions and surface wave tomography. Tectonophysics, 609, 82–96.

Barnes, J.B., and Ehlers, T.A., 2009. End member models for Andean Plateau uplift. Earth-Science Reviews, 97, 105–132.

Basilici, M., Ascione, A., Megna, A., Santini, S., Tavani, S., Valente, E. and Mazzoli, S., 2020. Active deformation and relief evolution in the western Lurestan region of the Zagros mountain belt: new insights from tectonic geomorphology analysis and finite element modeling. Tectonics, 39, 6402.

Bermúdez, M.A., van der Beek, P.A. and Bernet, M., 2013. Strong tectonic and weak climatic control on exhumation rates in the Venezuelan Andes. Lithosphere, 5, 3-16.

Bevis, M., Kendrick, E., Smalley Jr, R., Brooks, B., Allmendinger, R. and Isacks, B., 2001. On the strength of interplate coupling and the rate of back arc convergence in the central Andes: An analysis of the interseismic velocity field. Geochemistry, Geophysics, Geosystems, 2.

Bi, H., Zheng, W., Ge, W., Zhang, P., Zeng, J. and Yu, J., 2018. Constraining the distribution of vertical slip on the South Heli Shan Fault (northeastern Tibet) from high-resolution topographic data. Journal of Geophysical Research: Solid Earth, 123, 2484-2501.

Blisniuk, P.M., Hacker, B.R., Glodny, J., Ratschbacher, L., Bi, S., Wu, Z., McWilliams, M.O. and Calvert, A., 2001. Normal faulting in central Tibet since at least 13.5 Myr ago. Nature, 412, 628-632.

Bookhagen, B. and Burbank, D.W., 2010. Toward a complete Himalayan hydrological budget: Spatiotemporal distribution of snowmelt and rainfall and their impact on river discharge. Journal of Geophysical Research: Earth Surface, 115.

Bookhagen, B. and Strecker, M.R., 2012. Spatiotemporal trends in erosion rates across a pronounced rainfall gradient: Examples from the southern Central Andes. Earth and Planetary Science Letters, 327, 97-110.

Boulton, S.J. and Whittaker, A.C., 2009. Quantifying the slip rates, spatial distribution and evolution of active normal faults from geomorphic analysis: Field examples from an oblique-extensional graben, southern Turkey. Geomorphology, 104, 299-316.

Bowman, D., King, G. and Tapponnier, P., 2003. Slip partitioning by elastoplastic propagation of oblique slip at depth. Science, 300, 1121-1123.

Brooks, B.A., Bevis, M., Whipple, K., Arrowsmith, J.R., Foster, J., Zapata, T., Kendrick, E., Minaya, E., Echalar, A., Blanco, M. and Euillades, P., 2011. Orogenic-wedge deformation and potential for great earthquakes in the central Andean backarc. Nature Geoscience, 4, 380-383.

Burbank, D.W. and Anderson, R.S., 2001. Tectonic geomorphology. Blackwell Science.

Burbank, D.W., Blythe, A.E., Putkonen, J., Pratt-Sitaula, B.G.A.B.E.T., Gabet, E., Oskin, M., Barros, A. and Ojha, T.P., 2003. Decoupling of erosion and precipitation in the Himalayas. Nature, 426, 652-655.

Burbank, D.W., Bookhagen, B., Gabet, E.J. and Putkonen, J., 2012. Modern climate and erosion in the Himalaya. Comptes Rendus Geoscience, 344, 610-626.

Burchfiel, B.C., Royden, L.H., Van der Hilst, R.D., Hager, B.H., Chen, Z., King, R.W., Li, C., Lü, J., Yao, H., and Kirby, E., 2008. A geological and geophysical context for the Wenchuan earthquake of 12 May 2008, Sichuan, People's Republic of China. GSA Today, 18, 7.

Bush, M.A., Saylor, J.E., Horton, B.K. and Nie, J., 2016. Growth of the Qaidam Basin during Cenozoic exhumation in the northern Tibetan Plateau: Inferences from depositional patterns and multiproxy detrital provenance signatures. Lithosphere, 8, 58-82.

Cannon, J.M. and Murphy, M.A., 2014. Active lower crustal deformation and Himalayan seismic hazard revealed by stream channels and regional geology. Tectonophysics, 633, 34-42.

Cannon, J.M., Murphy, M.A. and Taylor, M., 2018. Segmented strain accumulation in the High Himalaya expressed in river channel steepness. Geosphere, 14, 1131-1149.

Champagnac, J.D., Molnar, P., Sue, C. and Herman, F., 2012. Tectonics, climate, and mountain topography. Journal of Geophysical Research: Solid Earth, 117.

Chen, F.H., Chen, J.H., Holmes, J., Boomer, I., Austin, P., Gates, J.B., Wang, N.L., Brooks, S.J. and Zhang, J.W., 2010. Moisture changes over the last millennium in arid central Asia: a review, synthesis and comparison with monsoon region. Quaternary Science Reviews, 29, 1055-1068.

Chen, X., Yuan, W., Xu, J., Wang, K., Yuan, E. and Feng, Z., 2019. Tectonic activities in Dongshangen polymetallic ore district, eastern Kunlun Mountains, Qinghai-Tibet Plateau: Evidences from fission track thermochronology. Ore Geology Reviews, 112, 103065.

Cheng, F., Garzione, C.N., Mitra, G., Jolivet, M., Guo, Z., Lu, H., Li, X., Zhang, B., Zhang, C., Zhang, H. and Wang, L., 2019. The interplay between climate and tectonics during the upward and outward growth of the Qilian Shan orogenic wedge, northern Tibetan Plateau. Earth-Science Reviews, 198, 102945.

Cheng, F., Jolivet, M., Dupont-Nivet, G. Wang, L. Yu, X. J. and Guo, Z. J., 2015. Lateral extrusion along the Altyn Tagh Fault, Qilian Shan (NE Tibet): Insight from a 3D crustal budget, Terra Nova, 27, 416–425.

Chiang, J.C. and Friedman, A.R., 2012. Extratropical cooling, interhemispheric thermal gradients, and tropical climate change. Annual Review of Earth and Planetary Sciences, 40.

Clark, M.K. and Royden, L.H., 2000. Topographic ooze: Building the eastern margin of Tibet by lower crustal flow. Geology, 28, 703-706.

Clark, M.K., Farley, K.A., Zheng, D., Wang, Z. and Duvall, A.R., 2010. Early Cenozoic faulting of the northern Tibetan Plateau margin from apatite (U–Th)/He ages. Earth and Planetary Science Letters, 296, 78-88.

Clark, M.K., House, M.A., Royden, L.H., Whipple, K.X., Burchfiel, B.C., Zhang, X., Tang, W., 2005. Late cenozoic uplift of southeastern Tibet. Geology, 33, 525–528.

Clark, M.K., Royden, L.H., Whipple, K.X., Burchfiel, B.C., Zhang, X. and Tang, W., 2006. Use of a regional, relict landscape to measure vertical deformation of the eastern Tibetan Plateau. Journal of Geophysical Research: Earth Surface, 111.

Clark, M.K., Schoenbohm, L.M., Royden, L.H., Whipple, K.X., Burchfiel, B.C., Zhang, X., Tang, W., Wang, E. and Chen, L., 2004. Surface uplift, tectonics, and erosion of eastern Tibet from large-scale drainage patterns. Tectonics, 23.

Clemens, S.C., Prell, W.L., Sun, Y., Liu, Z. and Chen, G., 2008. Southern Hemisphere forcing of Pliocene δ18O and the evolution of Indo-Asian monsoons. Paleoceanography, 23.

Clift, P., Lee, J.I., Clark, M.K. and Blusztajn, J., 2002. Erosional response of South China to arc rifting and monsoonal strengthening; a record from the South China Sea. Marine Geology, 184, 207-226.

Cook, K.L., Royden, L.H., Burchfiel, B.C., Lee, Y.H., Tan, X., 2013. Constraints on cenozoic tectonics in the southwestern Longmen Shan from low-temperature thermochronology. Lithosphere 5, 393–406.

Dadson, S.J., Hovius, N., Chen, H., Dade, W.B., Hsieh, M.L., Willett, S.D., Hu, J.C., Horng, M.J., Chen, M.C., Stark, C.P. and Lague, D., 2003. Links between erosion, runoff variability and seismicity in the Taiwan orogen. Nature, 426, 733-736.

Dai, J.G., Wang, C.S., Hourigan, J., Santosh, M., 2013a. Insights into the early Tibetan plateau from (U–Th)/He thermochronology. Journal of the Geological Society 170, 917–927.

D'Arcy, M. and Whittaker, A.C., 2014. Geomorphic constraints on landscape sensitivity to climate in tectonically active areas. Geomorphology, 204, 366-381.

Daxberger, H. and Riller, U., 2015. Analysis of geomorphic indices in the southern Central Andes (23–28 S): Evidence for pervasive Quaternary to Recent deformation in the Puna Plateau. Geomorphology, 248, 57-76.

Deeken, A., Sobel, E.R., Coutand, I., Haschke, M., Riller, U. and Strecker, M.R., 2006. Development of the southern Eastern Cordillera, NW Argentina, constrained by apatite fission track thermochronology: From early Cretaceous extension to middle Miocene shortening. Tectonics, 25.

Deng, B., Liu, S.G., Jiang, L., Zhao, G.P., Huang, R., Li, Z.W., Li, J.X., Jansa, L., 2018. Tectonic uplift of the Xichang basin (SE Tibetan plateau) revealed by structural geology and thermochronology data. Basin Research, 30, 75–96.

Devlin, S., Isacks, B.L., Pritchard, M.E., Barnhart, W.D., and Lohman, R.B., 2012, Depths and focal mechanisms of crustal earthquakes in the central Andes determined from teleseismic waveform analysis and InSAR. Tectonics, 31.

Dielforder, A., Hetzel, R. and Oncken, O., 2020. Megathrust shear force controls mountain height at convergent plate margins. Nature, 582, 225-229.

Dietrich, W.E., Bellugi, D.G., Sklar, L.S., Stock, J.D., Heimsath, A.M. and Roering, J.J., 2003. Geomorphic transport laws for predicting landscape form and dynamics. Prediction in Geomorphology, 135, 103-132.

Domínguez-González, L., Andreani, L., Stanek, K.P. and Gloaguen, R., 2015. Geomorpho-tectonic evolution of the Jamaican restraining bend. Geomorphology, 228, 320-334.

Dong, Z., Hu, G., Qian, G., Lu, J., Zhang, Z., Luo, W. and Lyu, P., 2017. High-altitude aeolian research on the Tibetan Plateau. Reviews of Geophysics, 55, 864-901.

Duncan, C., Masek, J. and Fielding, E., 2003. How steep are the Himalaya? Characteristics and implications of along-strike topographic variations. Geology, 31, 75-78.

Duvall, A., Clark, M.K., Kirby, E., Farley , K.A., Craddock, W.H., Li, C.Y. and Yuan, D.Y. 2013. Low-temperature thermochronometry along the Kunlun and Haiyuan Faults, NE Tibetan Plateau: Evidence for kinematic change during late-stage orogenesis. Tectonics, 32, 1190-1211.

Duvall, A.R., Clark, M.K., Avdeev, B., Farley, K.A. and Chen, Z., 2012. Widespread late Cenozoic increase in erosion rates across the interior of eastern Tibet constrained by detrital low-temperature thermochronometry. Tectonics, 31.

Elliott, J. R., R. J. Walters, P. C. England, J. A. Jackson, Z. Li, and B. Parsons (2010), Extension on the Tibetan Plateau: Recent normal faulting measured by InSAR and body wave seismology, Geophysical Journal International, 183, 503–535.

England, P. and Houseman, G., 1986. Finite strain calculations of continental deformation: 2. Comparison with the India-Asia collision zone. Journal of Geophysical Research: Solid Earth, 91, 3664-3676.

England, P. and Houseman, G.A., 1988. The mechanics of the Tibetan Plateau. Philosophical Transactions of the Royal Society of London. Series A, Mathematical and Physical Sciences, 326, 301-320.

England, P. and Houseman, G., 1989. Extension during continental convergence, with application to the Tibetan Plateau. Journal of Geophysical Research: Solid Earth, 94, 17561-17579.

Fakhari, M.D., Axen, G. J., Horton, B.K., Hassanzadeh, J., Amini, A. , 2008. Revised age of proximal deposits in the Zagros foreland basin and implication for Cenozoic evolution of the High Zagros. Tectonophysics, 451, 170–185.

Ferrier, K.L., Huppert, K.L. and Perron, J.T., 2013. Climatic control of bedrock river incision. Nature, 496, 206-209.

Fick, S.E. and Hijmans, R.J., 2017. WorldClim 2: new 1-km spatial resolution climate surfaces for global land areas. International Journal of Climatology, 37, 4302-4315.

Formento-Trigilio, M.L. and Pazzaglia, F.J., 1998. Tectonic geomorphology of the Sierra Nacimiento: Traditional and new techniques in assessing long-term landscape evolution in the southern Rocky Mountains. The Journal of Geology, 106, 433-454.

Gao, M., Zeilinger, G., Xu, X., Tan, X., Wang, Q. and Hao, M., 2016. Active tectonics evaluation from geomorphic indices for the central and the southern Longmenshan range on the Eastern Tibetan Plateau, China. Tectonics, 35, 1812-1826.

Gao, Y.X., 1962. On some problems of Asian monsoon. In: Gao, Y.X. (Ed.), Some Questions about the East Asian Monsoon. Science Press, Beijing, 1–49.

Garzione, C.N., McQuarrie, N., Perez, N.D., Ehlers, T.A., Beck, S.L., Kar, N., Eichelberger, N., Chapman, A.D., Ward, K.M., Ducea, M.N. Lease, R.O., Poulsen, C.J., Wagner, L.S., Saylor J.E., Zandt, G., Horton, B.K., 2017. Tectonic evolution of the Central Andean plateau and implications for the growth of plateaus. Annual Review of Earth and Planetary Sciences, 45, 529-559.

Gaudemer, Y., Tapponnier, P., Meyer, B., Peltzer, G., Shunmin, G., Zhitai, C., Huagung, D. and Cifuentes, I., 1995. Partitioning of crustal slip between linked, active faults in the eastern Qilian Shan, and evidence for a major seismic gap, the 'Tianzhu gap', on the western Haiyuan Fault, Gansu (China). Geophysical Journal International, 120, 599-645.

Geng, H., Pan, B., Huang, B., Cao, B. and Gao, H., 2017. The spatial distribution of precipitation and topography in the Qilian Shan Mountains, northeastern Tibetan Plateau. Geomorphology, 297, 43-54.

GLIMS and NSIDC (2005, updated 2020): Global Land Ice Measurements from Space glacier database. Compiled and made available by the international GLIMS community and the National Snow and Ice Data Center, Boulder CO, U.S.A. DOI:10.7265/N5V98602

Godard, V., Bourlès, D.L., Spinabella, F., Burbank, D.W., Bookhagen, B., Fisher, G.B., Moulin, A. and Léanni, L., 2014. Dominance of tectonics over climate in Himalayan denudation. Geology, 42, 243-246.

Godard, V., Lavé, J., Carcaillet, J., Cattin, R., Bourlès, D. and Zhu, J., 2010. Spatial distribution of denudation in Eastern Tibet and regressive erosion of plateau margins. Tectonophysics, 491, 253-274.

Godard, V., Pik, R., Lavé, J., Cattin, R., Tibari, B., De Sigoyer, J., Pubellier, M., Zhu, J., 2009. Late cenozoic evolution of the central Longmen Shan, eastern Tibet: insight from (U-Th)/He thermochronometry. Tectonics, 28, 5009.

Grohmann, C.H., Smith, M.J. and Riccomini, C., 2010. Multiscale analysis of topographic surface roughness in the Midland Valley, Scotland. IEEE Transactions on Geoscience and Remote Sensing, 49, 1200-1213.

Groves, K., Saville, C., Hurst, M.D., Jones, S.J., Song, S. and Allen, M.B., 2020. Geomorphic expressions of collisional tectonics in the Qilian Shan, north eastern Tibetan Plateau. Tectonophysics, 788, 228503.

Guest, B., Stockli, D.F., Grove, M., Axen, G.J., Lam, P.S., Hassanzadeh, J., 2006. Thermal histories from the central Alborz Mountains, northern Iran: Implications for the spatial and temporal distribution of deformation in northern Iran. Geological Society of America Bulletin 118, 1507–1521.

Guo, Z.T., Ruddiman, W.F., Hao, Q.Z., Wu, H.B., Qiao, Y.S., Zhu, R.X., Peng, S.Z., Wei, J.J., Yuan, B.Y. and Liu, T.S., 2002. Onset of Asian desertification by 22 Myr ago inferred from loess deposits in China. Nature, 416, 159-163.

Guo, Z.T., Sun, B., Zhang, Z.S., Peng, S.Z., Xiao, G.Q., Ge, J.Y., Hao, Q.Z., Qiao, Y.S., Liang, M.Y., Liu, J.F. and Yin, Q.Z., 2008. A major reorganization of Asian climate by the early Miocene. Climate of the Past, 4.

Haider, V., Dunkl, I., von Eynatten, H., Ding, L., Frei, D., Zhang, L.Y., 2013. Cretaceous to Cenozoic evolution of the northern Lhasa Terrane and the early paleogene development of peneplains at Nam Co, Tibetan plateau. Journal of Asian Earth Sciences, 70, 79–98.

Han, J., Gasparini, N.M. and Johnson, J.P., 2015. Measuring the imprint of orographic rainfall gradients on the morphology of steady-state numerical fluvial landscapes. Earth Surface Processes and Landforms, 40, 1334-1350.

Han, Z., Sinclair, H.D., Li, Y., Wang, C., Tao, Z., Qian, X., Ning, Z., Zhang, J., Wen, Y., Lin, J. and Zhang, B., 2019. Internal drainage has sustained low-relief Tibetan landscapes since the early Miocene. Geophysical Research Letters, 46, 8741-8752.

Harkins, N., Kirby, E., Heimsath, A., Robinson, R. and Reiser, U., 2007. Transient fluvial incision in the headwaters of the Yellow River, northeastern Tibet, China. Journal of Geophysical Research: Earth Surface, 112.

Henck, A.C., Huntington, K.W., Stone, J.O., Montgomery, D.R. and Hallet, B., 2011. Spatial controls on erosion in the Three Rivers Region, southeastern Tibet and southwestern China. Earth and Planetary Science Letters, 303, 71-83.

Herman, F., Copeland, P., Avouac, J.P., Bollinger, L., Mahéo, G., Le Fort, P., Rai, S., Foster, D., Pêcher, A., Stüwe, K. and Henry, P., 2010. Exhumation, crustal deformation, and thermal structure of the Nepal Himalaya derived from the inversion of thermochronological and thermobarometric data and modeling of the topography. Journal of Geophysical Research: Solid Earth, 115.

Herman, F., Seward, D., Valla, P.G., Carter, A., Kohn, B., Willett, S.D. and Ehlers, T.A., 2013. Worldwide acceleration of mountain erosion under a cooling climate. Nature, 504, 423-426.

Hetzel, R., 2013. Active faulting, mountain growth, and erosion at the margins of the Tibetan Plateau constrained by in situ-produced cosmogenic nuclides. Tectonophysics, 582, 1-24.

Hetzel, R., Dunkl, I., Haider, V., Strobl, M., von Eynatten, H., Ding, L., Frei, D., 2011. Peneplain formation in southern Tibet predates the India-Asia collision and plateau uplift. Geology 39, 983–986.

Hetzel, R., Tao, M., Stokes, S., Niedermann, S., Ivy-Ochs, S., Gao, B., Strecker, M.R. and Kubik, P.W., 2004. Late Pleistocene/Holocene slip rate of the Zhangye thrust (Qilian Shan, China) and implications for the active growth of the northeastern Tibetan Plateau. Tectonics, 23.

Hilley, G.E. and Porder, S., 2008. A framework for predicting global silicate weathering and CO2 drawdown rates over geologic time-scales. Proceedings of the National Academy of Sciences, 105, 16855-16859.

Hobley, D.E., Sinclair, H.D. and Cowie, P.A., 2010. Processes, rates, and time scales of fluvial response in an ancient postglacial landscape of the northwest Indian Himalaya. Bulletin, 122, 1569-1584.

Hodges, K.V., Hurtado, J.M. and Whipple, K.X., 2001. Southward extrusion of Tibetan crust and its effect on Himalayan tectonics. Tectonics, 20, 799-809.

Hodges, K.V., Wobus, C., Ruhl, K., Schildgen, T. and Whipple, K., 2004. Quaternary deformation, river steepening, and heavy precipitation at the front of the Higher Himalayan ranges. Earth and Planetary science letters, 220, 379-389.

Hoke, G.D., Isacks, B.L., Jordan, T.E., Blanco, N., Tomlinson, A.J. and Ramezani, J., 2007. Geomorphic evidence for post-10 Ma uplift of the western flank of the central Andes 18 30′–22 S. Tectonics, 26.

Hoke, G.D., Liu-Zeng, J., Hren, M.T., Wissink, G.K. and Garzione, C.N., 2014. Stable isotopes reveal high southeast Tibetan Plateau margin since the Paleogene. Earth and Planetary Science Letters, 394, 270-278.

Horton, B. K., G. Dupont-Nivet, J. Zhou, G. L. Waanders, R. F. Butler, and J. Wang (2004), Mesozoic-Cenozoic evolution of the Xining-Minhe and Dangchang basins, northeastern Tibetan Plateau: Magnetostratigraphic and biostratigraphic results. Journal of Geophysical Research, 109.

Hu, X., Pan, B., Kirby, E., Li, Q., Geng, H. and Chen, J., 2010. Spatial differences in rock uplift rates inferred from channel steepness indices along the northern flank of the Qilian Mountain, northeast Tibetan Plateau. Chinese Science Bulletin, 55, 3205-3214.

Huntington, K.W., Blythe, A.E. and Hodges, K.V., 2006. Climate change and Late Pliocene acceleration of erosion in the Himalaya. Earth and Planetary Science Letters, 252, 107-118.

Hurst, M.D., Mudd, S.M., Attal, M. and Hilley, G., 2013. Hillslopes record the growth and decay of landscapes. Science, 341, 868-871.

Jia, G., Peng, P.A., Zhao, Q. and Jian, Z., 2003. Changes in terrestrial ecosystem since 30 Ma in East Asia: Stable isotope evidence from black carbon in the South China Sea. Geology, 31, 1093-1096.

Jiao, R., Herman, F. and Seward, D., 2017. Late Cenozoic exhumation model of New Zealand: Impacts from tectonics and climate. Earth-science reviews, 166, 286-298.

Jolivet, M., Roger, F., Xu, Z.Q., Paquette, J.L., Cao, H., 2015. Mesozoic-cenozoic evolution of the Danba Dome (Songpan Garzê, east Tibet) as inferred from La-Icpms U-Pb and fission-track data. Journal of Asian Earth Sciences, 102, 180–204.

Kapp, P. and DeCelles, P.G., 2019. Mesozoic–Cenozoic geological evolution of the Himalayan-Tibetan orogen and working tectonic hypotheses. American Journal of Science, 319, 159-254.

Kapp, P., DeCelles, P.G., Gehrels, G.E., Heizler, M. and Ding, L., 2007. Geological records of the Lhasa-Qiangtang and Indo-Asian collisions in the Nima area of central Tibet. Geological Society of America Bulletin, 119, 917-933.

Kapp, P., Murphy, M.A., Yin, A., Harrison, T.M., Ding, L. and Guo, J., 2003. Mesozoic and Cenozoic tectonic evolution of the Shiquanhe area of western Tibet. Tectonics, 22.

Karátson, D., Telbisz, T. and Wörner, G., 2012. Erosion rates and erosion patterns of Neogene to Quaternary stratovolcanoes in the Western Cordillera of the Central Andes: an SRTM DEM based analysis. Geomorphology, 139, 122-135.

Kearey, P., Klepeis, K.A. and Vine, F.J., 2013. Global tectonics. John Wiley & Sons.

Keller, E.A. and Pinter, N., 1996. Active tectonics. Prentice Hall.

Kirby, E. and Ouimet, W., 2011. Tectonic geomorphology along the eastern margin of Tibet: Insights into the pattern and processes of active deformation adjacent to the Sichuan Basin. Geological Society, London, Special Publications, 353, 165-188.

Kirby, E., Reiners, P.W., Krol, M.A., Whipple, K.X., Hodges, K.V., Farley, K.A., Tang, W.Q., Chen, Z.L., 2002. Late cenozoic evolution of the eastern margin of the Tibetan plateau: inferences from 40ar/39ar and (U-Th)/He thermochronology. Tectonics, 21, 1–20.

Kirby, E. and Whipple, K., 2001. Quantifying differential rock-uplift rates via stream profile analysis. Geology, 29, 415-418.

Kirby, E., Whipple, K.X., Tang, W. and Chen, Z., 2003. Distribution of active rock uplift along the eastern margin of the Tibetan Plateau: Inferences from bedrock channel longitudinal profiles. Journal of Geophysical Research: Solid Earth, 108.

Kirby, E. and Whipple, K.X., 2012. Expression of active tectonics in erosional landscapes. Journal of Structural Geology, 44, 54-75.

Kley, J., and Monaldi, C.R., 1998, Tectonic shortening and crustal thickness in the Central Andes: How good is the correlation? Geology, 26, 723–726.

Korup, O. and Weidinger, J.T., 2011. Rock type, precipitation, and the steepness of Himalayan threshold hillslopes. Geological Society, London, Special Publications, 353, 235-249.

Kreemer, C., Blewitt, G. and Klein, E.C., 2014. A geodetic plate motion and Global Strain Rate Model. Geochemistry, Geophysics, Geosystems, 15, 3849-3889.

Kutzbach, J.E., Prell, W.L. and Ruddiman, W.F., 1993. Sensitivity of Eurasian climate to surface uplift of the Tibetan Plateau. The Journal of Geology, 101, 177-190.

Lacombe, O. and Bellahsen, N., 2016. Thick-skinned tectonics and basement-involved fold–thrust belts: insights from selected Cenozoic orogens. Geological Magazine, 153, 763-810.

Lai, Q.Z., Ding, L., Wang, H.W., Yue, Y.H., Cai, F.L., 2007. Constraining the stepwise migration of the eastern Tibetan plateau margin by apatite fission track thermochronology. Science in China Series D: Earth Sciences, 50, 172–183.

Lal, D., Harris, N.B., Sharma, K.K., Gu, Z., Ding, L., Liu, T., Dong, W., Caffee, M.W. and Jull, A.J.T., 2004. Erosion history of the Tibetan Plateau since the last interglacial: constraints from the first studies of cosmogenic 10Be from Tibetan bedrock. Earth and Planetary Science Letters, 217, 33-42.

Law, R. and Allen, M.B., 2020. Diachronous Tibetan Plateau landscape evolution derived from lava field geomorphology. Geology, 48, 263-267.

Lease, R., Burbank, D.W., Clark, M.K., Farley, K.A., Zheng, D.W. and Zhang, H.P., 2011. Middle Miocene reorganization of deformation along the northeastern Tibetan Plateau. Geology, 39, 359–362.

Leng, C.B., Cooke, D.R., Hou, Z.Q., Evans, N.J., Zhang, X.C., Chen, W.T., Danišík, M., McInnes, B.I.A., Yang, J.H., 2018. Quantifying exhumation at the giant Pulang porphyry Cu-Au deposit using U-Pb-He dating. Economic Geology, 113, 1077–1092.

Li, H.A., Dai, J.G., Xu, S.Y., Liu, B.R., Han, X., Wang, Y.N. and Wang, C.S., 2019. The formation and expansion of the eastern Proto-Tibetan Plateau: Insights from low-temperature thermochronology. Journal of Asian Earth Sciences, 183, 103975.

Li, Q., Pan, B., Gao, H., Wen, Z. and Hu, X., 2019. Differential rock uplift along the northeastern margin of the Tibetan Plateau inferred from bedrock channel longitudinal profiles. Journal of Asian Earth Sciences, 169, 182-198.

Li, S., Currie, B.S., Rowley, D.B. and Ingalls, M., 2015. Cenozoic paleoaltimetry of the SE margin of the Tibetan Plateau: Constraints on the tectonic evolution of the region. Earth and Planetary Science Letters, 432, 415-424.

Li, Y., Li, D., Liu, G., Harbor, J., Caffee, M. and Stroeven, A.P., 2014. Patterns of landscape evolution on the central and northern Tibetan Plateau investigated using in-situ produced 10Be concentrations from river sediments. Earth and Planetary Science Letters, 398, 77-89.

Li, Y., Shan, X., Qu, C., Zhang, Y., Song, X., Jiang, Y., Zhang, G., Nocquet, J.M., Gong, W., Gan, W. and Wang, C., 2017. Elastic block and strain modeling of GPS data around the Haiyuan-Liupanshan fault, northeastern Tibetan Plateau. Journal of Asian Earth Sciences, 150, 87-97.

Li, Y., Wang, C., Dai, J., Xu, G., Hou, Y. and Li, X., 2015. Propagation of the deformation and growth of the Tibetan–Himalayan orogen: A review. Earth-Science Reviews, 143, 36-61.

Li, Z.W., Liu, S., Chen, H., Deng, B., Hou, M., Wu, W. and Cao, J., 2012. Spatial variation in Meso-Cenozoic exhumation history of the Longmen Shan thrust belt (eastern Tibetan Plateau) and the adjacent western Sichuan basin: Constraints from fission track thermochronology. Journal of Asian Earth Sciences, 47, 185-203.

Liang, S., Gan, W., Shen, C., Xiao, G., Liu, J., Chen, W., Ding, X. and Zhou, D., 2013. Three-dimensional velocity field of present-day crustal motion of the Tibetan Plateau derived from GPS measurements. Journal of Geophysical Research: Solid Earth, 118, 5722-5732.

Lindsey, E.O., Almeida, R., Mallick, R., Hubbard, J., Bradley, K., Tsang, L.L., Liu, Y., Burgmann, R. and Hill, E.M., 2018. Structural control on downdip locking extent of the Himalayan megathrust. Journal of Geophysical Research: Solid Earth, 123, 5265-5278.

Liu, R., Allen, M.B., Zhang, Q., Du, W., Cheng, X., Holdsworth, R.E. and Guo, Z., 2017. Basement controls on deformation during oblique convergence: Transpressive structures in the western Qaidam Basin, northern Tibetan Plateau. Lithosphere, 9, 583-594.

Liu, X. and Yin, Z.Y., 2002. Sensitivity of East Asian monsoon climate to the uplift of the Tibetan Plateau. Palaeogeography, Palaeoclimatology, Palaeoecology, 183, 223-245.

Liu-Zeng, J., Tapponnier, P., Gaudemer, Y. and Ding, L., 2008. Quantifying landscape differences across the Tibetan plateau: Implications for topographic relief evolution. Journal of Geophysical Research: Earth Surface, 113.

Liu-Zeng, J., Wen, L., Oskin, M. and Zeng, L., 2011. Focused modern denudation of the Longmen Shan margin, eastern Tibetan Plateau. Geochemistry, Geophysics, Geosystems, 12.

Liu-Zeng, J., Zhang, J.Y., McPhillips, D., Reiners, P., Wang, W., Pik, R., Zeng, L.S., Hoke, G., Xie, K.J., Xiao, P., 2018. Multiple episodes of fast exhumation since cretaceous in southeast Tibet, revealed by low-temperature thermochronology. Earth Planetary Science Letters, 490, 62–76.

Long, H., Lai, Z., Wang, N. and Li, Y., 2010. Holocene climate variations from Zhuyeze terminal lake records in East Asian monsoon margin in arid northern China. Quaternary Research, 74, 46-56.

Lowman, L.E. and Barros, A.P., 2014. Investigating links between climate and orography in the central Andes: Coupling erosion and precipitation using a physical-statistical model. Journal of Geophysical Research: Earth Surface, 119, 1322-1353.

Lu, L., Zhao, Z., Wu, Z.H., Qian, C., Ye, P.S., 2015. Fission track thermochronology evidence for the cretaceous and paleogene tectonic event of nyainrong microcontinent. Tibet. Journal of the Geological Society of China: Acta Geologica Sinica, English Edition, 89, 133–144.

Magni, V., Allen, M.B., van Hunen, J. and Bouilhol, P., 2017. Continental underplating after slab break-off. Earth and Planetary Science Letters, 474, 59-67.

Mazhari, S. A., Bea, F., Amini, S., Ghalamghash, J., Molina, J. F., Montero, P., Scarrow, J.H. and Williams, I.S., 2009. The Eocene bimodal Piranshahr massif of the Sanandaj–Sirjan Zone, NW Iran: a marker of the end of the collision in the Zagros orogen. Journal of the Geological Society 166, 53-69.

McFarland, P.K., Bennett, R.A., Alvarado, P. and DeCelles, P.G., 2017. Rapid Geodetic Shortening Across the Eastern Cordillera of NW Argentina Observed by the Puna-Andes GPS Array. Journal of Geophysical Research: Solid Earth, 122, 8600-8623.

McRivette, M.W., Yin, A., Chen, X. and Gehrels, G.E., 2019. Cenozoic basin evolution of the central Tibetan plateau as constrained by U-Pb detrital zircon geochronology, sandstone petrology, and fission-track thermochronology. Tectonophysics, 751, 150-179.

Mendoza, M.M., Ghosh, A., Karplus, M.S., Klemperer, S.L., Sapkota, S.N., Adhikari, L.B. and Velasco, A., 2019. Duplex in the Main Himalayan Thrust illuminated by aftershocks of the 2015 M w 7.8 Gorkha earthquake. Nature Geoscience, 12, 1018-1022.

Mériaux, A.S., Tapponnier, P., Ryerson, F.J., Xiwei, X., King, G., Van der Woerd, J., Finkel, R.C., Haibing, L., Caffee, M.W., Zhiqin, X. and Wenbin, C., 2005. The Aksay segment of the northern Altyn Tagh fault: Tectonic geomorphology, landscape evolution, and Holocene slip rate. Journal of Geophysical Research: Solid Earth, 110.

Meyer, B., P. Tapponnier, L. Bourjot, F. Metivier, Y. Gaudemer, G. Peltzer, G. Shunmin, and C. Zhitai, 1998, Crustal thickening in Gansu-Qinghai, lithospheric mantle subduction, and oblique, strike-slip controlled growth of the Tibet plateau. Geophysical Journal International, 135, 1–47.

Miao, Y., Herrmann, M., Wu, F., Yan, X. and Yang, S., 2012. What controlled Mid–Late Miocene long-term aridification in Central Asia?—Global cooling or Tibetan Plateau uplift: A review. Earth-Science Reviews, 112, 155-172.

Milliman, J.D. and Syvitski, J.P., 1992. Geomorphic/tectonic control of sediment discharge to the ocean: the importance of small mountainous rivers. The Journal of Geology, 100, 525-544.

Molnar, P., and Lyon-caen H., 1989. Fault plane solutions of earthquakes and active tectonics of the Tibetan Plateau and its margins, Geophysical Journal International, 99, 123–153.

Montgomery, D.R., 2001. Slope distributions, threshold hillslopes, and steady-state topography. American Journal of science, 301, 432-454.

Montgomery, D.R., Balco, G. and Willett, S.D., 2001. Climate, tectonics, and the morphology of the Andes. Geology, 29, 579-582.

Montgomery, D.R. and Brandon, M.T., 2002. Topographic controls on erosion rates in tectonically active mountain ranges. Earth and Planetary Science Letters, 201, 481-489.

Moosdorf, N., Cohen, S. and von Hagke, C., 2018. A global erodibility index to represent sediment production potential of different rock types. Applied Geography, 101, 36-44.

Morell, K.D., Sandiford, M., Rajendran, C.P., Rajendran, K., Alimanovic, A., Fink, D. and Sanwal, J., 2015. Geomorphology reveals active décollement geometry in the central Himalayan seismic gap. Lithosphere, 7, 247-256.

Mouthereau, F., Lacombe, O., Vergés, J., 2012. Building the Zagros collisional orogen: timing, strain distribution and the dynamics of Arabia/Eurasia plate convergence. Tectonophysics 532, 27–60.

Mudd, S.M., Attal, M., Milodowski, D.T., Grieve, S.W. and Valters, D.A., 2014. A statistical framework to quantify spatial variation in channel gradients using the integral method of channel profile analysis. Journal of Geophysical Research: Earth Surface, 119, 138-152.

Nennewitz, M., Thiede, R.C. and Bookhagen, B., 2018. Fault activity, tectonic segmentation, and deformation pattern of the western Himalaya on Ma timescales inferred from landscape morphology. Lithosphere, 10, 632-640.

Nie, J., Garzione, C., Su, Q., Liu, Q., Zhang, R., Heslop, D., Necula, C., Zhang, S., Song, Y. and Luo, Z., 2017. Dominant 100,000-year precipitation cyclicity in a late Miocene lake from northeast Tibet. Science advances, 3.

Nie, J., Ruetenik, G., Gallagher, K., Hoke, G., Garzione, C.N., Wang, W., Stockli, D., Hu, X., Wang, Z., Wang, Y. and Stevens, T., 2018. Rapid incision of the Mekong River in the middle Miocene linked to monsoonal precipitation. Nature Geoscience, 11, 944-948.

Nissen, E. Tatar, M., Jackson, J. A., Allen, M. B., 2011.New views on earthquake faulting in the Zagros fold-and-thrust belt of Iran. Geophysical Journal International 186, 928–944.

Noh, H., Huh, Y., Qin, J. and Ellis, A., 2009. Chemical weathering in the Three Rivers region of Eastern Tibet. Geochimica et Cosmochimica Acta, 73, 1857-1877.

Obaid A.K., 2018. Tectonic and fluvial geomorphology of the Zagros fold-and-thrust belt, Durham theses, Durham University.

Obaid, A.K. and Allen, M.B., 2019. Landscape expressions of tectonics in the Zagros fold-and-thrust belt. Tectonophysics, 766, 20-30.

Ojo, A.O., Kao, H., Jiang, Y., Craymer, M. and Henton, J., 2021. Strain Accumulation and Release Rate in Canada: Implications for Long-Term Crustal Deformation and Earthquake Hazards. Journal of Geophysical Research: Solid Earth, 126.

Okay, A. I., Zattin, M., Cavazza, W., 2010. Apatite fission-track data for the Miocene Arabia-Eurasia collision. Geology 38, 35–38.

Ouimet, W., Whipple, K., Royden, L., Reiners, P., Hodges, K., Pringle, M., 2010. Regional incision of the eastern margin of the Tibetan plateau. Lithosphere, 2, 50–63.

Ouimet, W.B., Whipple, K.X. and Granger, D.E., 2009. Beyond threshold hillslopes: Channel adjustment to base-level fall in tectonically active mountain ranges. Geology, 37, 579-582.

Palano, M., Imprescia, P., Agnon, A. and Gresta, S., 2018. An improved evaluation of the seismic/geodetic deformation-rate ratio for the Zagros Fold-and-Thrust collisional belt. Geophysical Journal International, 213, 194-209.

Palumbo, L., Hetzel, R., Tao, M. and Li, X., 2011. Catchment-wide denudation rates at the margin of NE Tibet from in situ-produced cosmogenic 10Be. Terra Nova, 23, 42-48.

Pan, B.T., Geng, H.P., Hu, X.F., Sun, R.H. and Wang, C., 2010. The topographic controls on the decadal-scale erosion rates in Qilian Shan Mountains, NW China. Earth and Planetary Science Letters, 292, 148-157.

Pandey, M.R., Tandukar, R.P., Avouac, J.P., Lave, J. and Massot, J.P., 1995. Interseismic strain accumulation on the Himalayan crustal ramp (Nepal). Geophysical Research Letters, 22, 751-754.

Pang, J., Yu, J., Zheng, D., Wang, W., Ma, Y. and Wang, Y., 2019. Neogene expansion of the Qilian Shan, north Tibet: Implications for the dynamic evolution of the Tibetan Plateau. Tectonics, 38, 1018-1032.

Perron, J.T. and Royden, L., 2013. An integral approach to bedrock river profile analysis. Earth Surface Processes and Landforms, 38, 570-576.

Pike, R.J. and Wilson, S.E., 1971. Elevation-relief ratio, hypsometric integral, and geomorphic area-altitude analysis. Geological Society of America Bulletin, 82, 1079-1084.

Poblet, J. and Lisle, R.J., 2011. Kinematic evolution and structural styles of fold-and-thrust belts. Geological Society, London, Special Publications, 349, 1-24.

Qi, B., Hu, D., Yang, X., Zhang, Y., Tan, C., Zhang, P. and Feng, C., 2016. Apatite fission track evidence for the Cretaceous–Cenozoic cooling history of the Qilian Shan (NW China) and for stepwise northeastward growth of the northeastern Tibetan Plateau since early Eocene. Journal of Asian Earth Sciences, 124, 28-41.

Raymo, M.E. and Ruddiman, W.F., 1992. Tectonic forcing of late Cenozoic climate. Nature, 359, 117-122.

Reiners, P.W., 2005. Zircon (U-Th)/He thermochronometry. Reviews in Mineralogy and Geochemistry, 58, 151-179.

Reiners, P.W., Ehlers, T.A., Mitchell, S.G. and Montgomery, D.R., 2003. Coupled spatial variations in precipitation and long-term erosion rates across the Washington Cascades. Nature, 426, 645-647.

Replumaz, A., San José, M., Margirier, A., van der Beek, P., Gautheron, C., Leloup, P.H., Ou, X., Kai, C., Wang, G.C., Zhang, Y.Z. and Valla, P.G., 2020. Tectonic Control on Rapid Late Miocene—Quaternary Incision of the Mekong River Knickzone, Southeast Tibetan Plateau. Tectonics, 39.

Richardson, N.J., Densmore, A.L., Seward, D., Fowler, A., Wipf, M., Ellis, M.A., Yong, L. and Zhang, Y., 2008. Extraordinary denudation in the Sichuan Basin: Insights from low-temperature thermochronology adjacent to the eastern margin of the Tibetan Plateau. Journal of Geophysical Research: Solid Earth, 113.

Riley, S.J., DeGloria, S.D. and Elliot, R., 1999. Index that quantifies topographic heterogeneity. Intermountain Journal of Sciences, 5, 23-27.

Rohling, E.J., Liu, Q.S., Roberts, A.P., Stanford, J.D., Rasmussen, S.O., Langen, P.L. and Siddall, M., 2009. Controls on the East Asian monsoon during the last glacial cycle, based on comparison between Hulu Cave and polar ice-core records. Quaternary Science Reviews, 28, 3291-3302.

Rohrmann, A., Kapp, P., Carrapa, B., Reiners, P.W., Guynn, J., Ding, L., Heizler, M., 2012. Thermochronologic evidence for plateau formation in central Tibet by 45 Ma. Geology 40, 187–190.

Rowley, D.B. and Currie, B.S., 2006. Palaeo-altimetry of the late Eocene to Miocene Lunpola basin, central Tibet. Nature, 439, 677-681.

Royden, L.H., Burchfiel, B.C. and van der Hilst, R.D., 2008. The geological evolution of the Tibetan Plateau. Science, 321, 1054-1058.

Saylor, J.E., Quade, J., Dettman, D.L., DeCelles, P.G., Kapp, P.A. and Ding, L., 2009. The late Miocene through present paleoelevation history of southwestern Tibet. American Journal of Science, 309, 1-42.

Schwanghart, W. and Scherler, D., 2014. TopoToolbox 2–MATLAB-based software for topographic analysis and modeling in Earth surface sciences. Earth Surface Dynamics, 2, 1-7.

Schwanghart, W. and Scherler, D., 2017. Bumps in river profiles: uncertainty assessment and smoothing using quantile regression techniques. Earth Surface Dynamics, 5, 821-839.

Shahzad, F. and Gloaguen, R., 2011. TecDEM: A MATLAB based toolbox for tectonic geomorphology, Part 1: Drainage network preprocessing and stream profile analysis. Computers & Geosciences, 37, 250-260.

Shen, H. and Poulsen, C.J., 2019. Precipitation δ 18 O on the Himalaya–Tibet orogeny and its relationship to surface elevation. Climate of the Past, 15, 169-187.

Shen, X., Tian, Y., Li, D., Qin, S., Vermeesch, P. and Schwanethal, J., 2016. Oligocene-Early Miocene river incision near the first bend of the Yangze River: Insights from apatite (U-Th-Sm)/He thermochronology. Tectonophysics, 687, 223-231.

Shen, Z.K., Lü, J., Wang, M. and Bürgmann, R., 2005. Contemporary crustal deformation around the southeast borderland of the Tibetan Plateau. Journal of Geophysical Research: Solid Earth, 110.

Shen, Z.K., Wang, M., Li, Y., Jackson, D.D., Yin, A., Dong, D. and Fang, P., 2001. Crustal deformation along the Altyn Tagh fault system, western China, from GPS. Journal of Geophysical Research: Solid Earth, 106, 30607-30621.

Shen, Z.K., Wang, M., Zeng, Y. and Wang, F., 2015. Optimal interpolation of spatially discretized geodetic data. Bulletin of the Seismological Society of America, 105, 2117-2127.

Shi, C., 2019. Ages and magnitudes of base level fall and valley downcutting in ten tributaries (the Ten Kongduis) of the upper Yellow River, China. Geomorphology, 325, 29-39.

Sinclair, H.D., Mudd, S.M., Dingle, E., Hobley, D.E.J., Robinson, R. and Walcott, R., 2017. Squeezing river catchments through tectonics: Shortening and erosion across the Indus Valley, NW Himalaya. Bulletin, 129, 203-217.

Song, S., Y. Niu, L. Su, and X. Xia 2013, Tectonics of the North Qilian orogen, NW China. Gondwana Research, 23, 1378–1401.

Stern, R. J., Johnson, P., 2010. Continental lithosphere of the Arabian Plate: A geologic, petrologic, and geophysical synthesis. Earth-Science Reviews 101, 29–67.

Stevens, V.L. and Avouac, J.P., 2015. Interseismic coupling on the main Himalayan thrust. Geophysical Research Letters, 42, 5828-5837.

Strahler, A.N., 1952. Hypsometric (area-altitude) analysis of erosional topography. Geological Society of America Bulletin, 63, 1117-1142.

Strecker, M.R., Alonso, R.N., Bookhagen, B., Carrapa, B., Hilley, G.E., Sobel, E.R. and Trauth, M.H., 2007. Tectonics and climate of the southern central Andes. Annual Review of Earth Planetary Sciences, 35, 747-787.

Strobl, M., Hetzel, R., Niedermann, S., Ding, L. and Zhang, L., 2012. Landscape evolution of a bedrock peneplain on the southern Tibetan Plateau revealed by in situ-produced cosmogenic 10Be and 21Ne. Geomorphology, 153, 192-204.

Su, Q., Xie, H., Yuan, D.Y. and Zhang, H.P., 2017. Along-strike topographic variation of Qinghai Nanshan and its significance for landscape evolution in the northeastern Tibetan Plateau. Journal of Asian Earth Sciences, 147, 226-239.

Su, Q., Yuan, D., Zhang, H., Manopkawee, P., Zhan, Y., Zhang, P. and Xie, H., 2019. Geomorphic evidence for northeastward expansion of the eastern Qilian Shan, northeastern Tibetan Plateau. Journal of Asian Earth Sciences, 177, 314-323.

Sun, B., Wang, Y.F., Li, C.S., Yang, J., Li, J.F., Li, Y.L., Deng, T., Wang, S.Q., Zhao, M., Spicer, R.A. and Ferguson, D.K., 2015. Early Miocene elevation in northern Tibet estimated by palaeobotanical evidence. Scientific reports, 5, 10379.

Sun, Y., Kutzbach, J., An, Z., Clemens, S., Liu, Z., Liu, W., Liu, X., Shi, Z., Zheng, W., Liang, L. and Yan, Y., 2015. Astronomical and glacial forcing of East Asian summer monsoon variability. Quaternary Science Reviews, 115, 132-142.

Tan, X.B., Lee, Y.H., Chen, W.Y., Cook, K.L., Xu, X.W., 2014. Exhumation history and faulting activity of the southern segment of the Longmen Shan, eastern Tibet. Journal of Asian Earth Sciences, 81, 91–104.

Tan, X.B., Lee, Y.H., Xu, X.W., Cook, K.L., 2017a. Cenozoic exhumation of the Danba Antiform, eastern Tibet: evidence from low-temperature thermochronology. Lithosphere, 9, 534–544.

Tan, X.B., Xu, X.W., Lee, Y.H., Lu, R.Q., Liu, Y.D., Xu, C., Li, K., Yu, G.H., Kang, W.J., 2017b. Late cenozoic thrusting of major faults along the central segment of Longmen Shan, eastern Tibet: evidence from low-temperature thermochronology. Tectonophysics, 712, 145–155.

Tan, X.B., Liu, Y.D., Lee, Y.H., Lu, R.Q., Xu, X.W., Suppe, J., Shi, F., Xu, C., 2019. Parallelism between the maximum exhumation belt and the moho ramp along the eastern Tibetan plateau margin: coincidence or consequence? Earth and Planetary Science Letters, 507, 73–84.

Tang, C., van Asch, T.W., Chang, M., Chen, G.Q., Zhao, X.H. and Huang, X.C., 2012. Catastrophic debris flows on 13 August 2010 in the Qingping area, southwestern China: the combined effects of a strong earthquake and subsequent rainstorms. Geomorphology, 139, 559-576.

Tang, Y., Zhang, Y.P., Tong, L.L., 2018. Mesozoic-Cenozoic evolution of the zoige depression in the Songpan-Ganzi Flysch basin, eastern Tibetan plateau: constraints from detrital zircon U-Pb ages and fission-track ages of the Triassic sedimentary sequence. Journal of Asian Earth Sciences, 151, 285–300.

Tapponnier, P., Meyer, B., Avouac, J.P., Peltzer, G., Gaudemer, Y., Shunmin, G., Hongfa, X., Kelun, Y., Zhitai, C., Shuahua, C. and Huagang, D., 1990. Active thrusting and folding in the Qilian Shan, and decoupling between upper crust and mantle in northeastern Tibet. Earth and Planetary Science Letters, 97, 382-403.

Tapponnier, P., Zhiqin, X., Roger, F., Meyer, B., Arnaud, N., Wittlinger, G. and Jingsui, Y., 2001. Oblique stepwise rise and growth of the Tibet Plateau. Science, 294, 1671-1677.

Tejero, R., González-Casado, J.M., Gómez-Ortiz, D. and Sánchez-Serrano, F., 2006. Insights into the "tectonic topography" of the present-day landscape of the central Iberian Peninsula (Spain). Geomorphology, 76, 280-294.

Thiede, R.C., Bookhagen, B., Arrowsmith, J.R., Sobel, E.R. and Strecker, M.R., 2004. Climatic control on rapid exhumation along the Southern Himalayan Front. Earth and Planetary Science Letters, 222, 791-806.

Tian, X. and Zhang, Z., 2013. Bulk crustal properties in NE Tibet and their implications for deformation model. Gondwana Research, 24, 548-559.

Tian, Y., Kohn, B.P., Phillips, D., Hu, S., Gleadow, A.J. and Carter, A., 2016. Late Cretaceous–earliest Paleogene deformation in the Longmen Shan fold-and-thrust belt, eastern Tibetan Plateau margin: Pre-Cenozoic thickened crust? Tectonics, 35, 2293-2312.

Tian, Y.T., Kohn, B.P., Gleadow, A.J.W., Hu, S.B., 2013. Constructing the Longmen Shan eastern Tibetan plateau margin: insights from low-temperature thermochronology. Tectonics, 32, 576–592.

Tian, Y.T., Kohn, B.P., Gleadow, A.J.W., Hu, S.B., 2014a. A thermochronological perspective on the morphotectonic evolution of the southeastern Tibetan plateau. Journal of Geophysical Research: Solid Earth, 119, 676–698.

Tian, Y.T., Kohn, B.P., Hu, S.B., Gleadow, A.J.W., 2014b. Postorogenic rigid behaviour of the eastern Songpan-Ganze terrane: insights from low-temperature thermochronology and implications for intracontinental deformation in Central Asia. Geochemistry, Geophysics, Geosystems, 15, 453–474.

Tian, Y.T., Kohn, B.P., Hu, S.B., Gleadow, A.J.W., 2015. Synchronous fluvial response to surface uplift in the eastern Tibetan plateau: implications for crustal dynamics. Geophysical Research Letters, 42, 29–35.

Tong, K., Li, Z.W., Zhu, L., Tao, G., Zhang, Y.X., Yang, W.G. and Zhang, J.L., 2019. Fold-and-thrust deformation of the hinterland of Qilian Shan, northeastern Tibetan Plateau since Mesozoic with implications for the plateau growth. Journal of Asian Earth Sciences, 104131.

Trauth, M.H., Bookhagen, B., Marwan, N. and Strecker, M.R., 2003. Multiple landslide clusters record Quaternary climate changes in the northwestern Argentine Andes. Palaeogeography, Palaeoclimatology, Palaeoecology, 194, 109-121.

Tripati, A.K., Roberts, C.D. and Eagle, R.A., 2009. Coupling of CO2 and ice sheet stability over major climate transitions of the last 20 million years. Science, 326, 1394-1397.

Van Der Woerd, J., Xu, X., Li, H., Tapponnier, P., Meyer, B., Ryerson, F.J., Meriaux, A.S. and Xu, Z., 2001. Rapid active thrusting along the northwestern range front of the Tanghe Nan Shan (western Gansu, China). Journal of Geophysical Research: Solid Earth, 106, 30475-30504.

Vera, J. and De Gines, J., 2009. Structure of the Zagros fold and thrust belt in the Kurdistan Region, northern Iraq. Trabajos de Geología, Universidad de Oviedo, 29, 213–217.

Vernant, P., Nilforoushan, F., Hatzfel, D., Abbassi, M. R., Vigny, C., Masson, F., Nankali, H., Matinod, J., Ashtiani, A., Bayer, R., Tavakoli, F., Chery, J., 2004. Present-day crustal deformation and plate kinematics in the Middle East constrained by GPS measurements in Iran and northern Oman. Geophysical Journal International, 157, 381–398.

Wang, C., Dai, J., Zhao, X., Li, Y., Graham, S.A., He, D., Ran, B. and Meng, J., 2014. Outward-growth of the Tibetan Plateau during the Cenozoic: A review. Tectonophysics, 621, 1-43.

Wang, C.S., Zhao, X.X., Liu, Z.F., Lippert, P.C., Graham, S.A., Coe, R.S., Yi, H.S., Zhu, L.D., Liu, S., Li, Y.L., 2008a. Constraints on the early uplift history of the Tibetan plateau. National Academy of Science, USA, 105, 4987–4992.

Wang, E.C., Kirby, E., Furlong, K.P., Van Soest, M., Xu, G.Q., Shi, X., Kamp, P.J.J., Hodges, K.V., 2012a. Two-phase growth of high topography in eastern Tibet during the Cenozoic. Nature Geoscience, 5, 640.

Wang, L.C., Wei, Y.S., 2013. Apatite fission track thermochronology evidence for the mid-Cretaceous tectonic event in the Qiangtang basin, Tibet. Acta Petrologica Sinica, 29, 1039–1047.

Wang, Q., Zhang, P.Z., Freymueller, J.T., Bilham, R., Larson, K.M., Lai, X.A., You, X., Niu, Z., Wu, J., Li, Y. and Liu, J., 2001. Present-day crustal deformation in China constrained by global positioning system measurements. Science, 294, 574-577.

Wang, S.F., Jiang, G.G., Xu, T.D., Tian, Y.T., Zheng, D.W., Fang, X.M., 2012b. The Jinhe- Qinghe fault—an inactive branch of the Xianshuihe-Xiaojiang fault zone, eastern Tibet. Tectonophysics, 544, 93–102.

Wang, Y., Mooney, W.D., Yuan, X. and Okaya, N., 2013. Crustal structure of the northeastern Tibetan Plateau from the southern Tarim Basin to the Sichuan Basin, China. Tectonophysics, 584, 191-208.

Wang, Y., Ren, M.E. and Zhu, D., 1986. Sediment supply to the continental shelf by the major rivers of China. Journal of the Geological Society, 143, 935-944.

Wang, Y., Zhang, H., Zheng, D., Wenjun, Zheng, W., Zhang, Z., Wang, W. and Yu, J., 2014b. Controls on decadal erosion rates in Qilian Shan: Re-evaluation and new insights into landscape evolution in north-east Tibet. Geomorphology, 223, 117-128.

Wang, Y., Zhang, P., Schoenbohm, L.M., Zheng, W., Zhang, B., Zhang, J., Zheng, D., Zhou, R. and Tian, Y., 2018. Two-Phase Exhumation Along Major Shear Zones in the SE Tibetan Plateau in the Late Cenozoic. Tectonics, 37, 2675-2694.

Wang, Y., Zhang, X., Sun, L. and Wan, J., 2007. Cooling history and tectonic exhumation stages of the south-central Tibetan Plateau (China): Constrained by 40Ar/39Ar and apatite fission track thermochronology. Journal of Asian Earth Sciences, 29, 266-282.

Wang, Y., Zheng, D., Zhang, H., Li, C., Xiao, L., Li, Y. and Hao, Y., 2019. The distribution of active rock uplift in the interior of the western Qilian Shan, NE Tibetan Plateau: Inference from bedrock channel profiles. Tectonophysics, 759, 15-29.

Weiss, J.R., Brooks, B.A., Foster, J.H., Bevis, M., Echalar, A., Caccamise, D., Heck, J., Kendrick, E., Ahlgren, K., Raleigh, D. and Smalley Jr, R., 2016. Isolating active orogenic wedge deformation in the southern Subandes of Bolivia. Journal of Geophysical Research: Solid Earth, 121, 6192-6218.

Whipple, K.X., 2004. Bedrock rivers and the geomorphology of active orogens. Annual Review of Earth and Planetary Sciences, 32, 151-185.

Whipple, K.X., 2009. The influence of climate on the tectonic evolution of mountain belts. Nature Geoscience, 2, 97-104.

Whittaker, A.C., 2012. How do landscapes record tectonics and climate?. Lithosphere, 4, 160-164.

Whittaker, A.C. and Boulton, S.J., 2012. Tectonic and climatic controls on knickpoint retreat rates and landscape response times. Journal of Geophysical Research: Earth Surface, 117.

Whittaker, A.C., Attal, M., Cowie, P.A., Tucker, G.E. and Roberts, G., 2008. Decoding temporal and spatial patterns of fault uplift using transient river long profiles. Geomorphology, 100, 506-526.

Wilson, C.J.L., Fowler, A.P., 2011. Denudational response to surface uplift in east Tibet: evidence from apatite fission-track thermochronology. Geological Society of America Bulletin, 123, 1966–1987.

Wobus, C., Whipple, K.X., Kirby, E., Snyder, N., Johnson, J., Spyropolou, K., Crosby, B., Sheehan, D. and Willett, S.D., 2006. Tectonics from topography: Procedures, promise, and pitfalls. Special papers-geological society of America, 398, 55.

Wobus, C.W., Hodges, K.V. and Whipple, K.X., 2003. Has focused denudation sustained active thrusting at the Himalayan topographic front? Geology, 31, 861-864.

Wu, Z., Barosh, P.J., Wu, Z., Hu, D., Zhao, X. and Ye, P., 2008. Vast early Miocene lakes of the central Tibetan Plateau. Geological Society of America Bulletin, 120, 1326-1337.

Wu, Z., Yang, Y., Barosh, P.J., Wu, Z. and Zhang, Y., 2014. Tectonics and topography of the Tibetan Plateau in Early Miocene. Acta Geologica Sinica-English Edition, 88, 410-424.

Xiong, J., Li, Y., Zhong, Y., Lu, H., Lei, J., Xin, W., Wang, L., Hu, X. and Zhang, P., 2017. Latest Pleistocene to Holocene thrusting recorded by a flight of strath terraces in the eastern Qilian Shan, NE Tibetan Plateau. Tectonics, 36, 2973-2986.

Xu, G.Q., Kamp, P.J.J., 2000. Tectonics and denudation adjacent to the xianshuihe fault, eastern Tibetan plateau: constraints from fission track thermochronology. Journal of Geophysical Research: Solid Earth, 105, 19231–19251.

Xu, Q., Liu, X. and Ding, L., 2016. Miocene high-elevation landscape of the eastern Tibetan Plateau. Geochemistry, Geophysics, Geosystems, 17, 4254-4267.

Xu, X., Yeats, R.S. and Yu, G., 2010. Five short historical earthquake surface ruptures near the Silk Road, Gansu Province, China. Bulletin of the Seismological Society of America, 100, 541-561.

Xue, F., Wang, H. and He, J., 2003. Interannual variability of Mascarene high and Australian high and their influences on summer rainfall over East Asia. Chinese Science Bulletin, 48, 492-497.

Yamada, R., Tagami, T., Nishimura, S. and Ito, H., 1995. Annealing kinetics of fission tracks in zircon: an experimental study. Chemical Geology, 122, 249-258.

Yang, H., Yang, X., Huang, X., Li, A., Huang, W. and Zhang, L., 2018. New constraints on slip rates of the Fodongmiao-Hongyazi fault in the Northern Qilian Shan, NE Tibet, from the 10Be exposure dating of offset terraces. Journal of Asian Earth Sciences, 151, 131-147.

Yang, R., Fellin, M.G., Herman, F., Willett, S.D., Wang, W. and Maden, C., 2016. Spatial and temporal pattern of erosion in the Three Rivers Region, southeastern Tibet. Earth and Planetary Science Letters, 433, 10-20.

Yang, R., Herman, F., Fellin, M.G. and Maden, C., 2018. Exhumation and topographic evolution of the Namche Barwa Syntaxis, eastern Himalaya. Tectonophysics, 722, 43-52.

Yin, A., 2006. Cenozoic tectonic evolution of the Himalayan orogen as constrained by along-strike variation of structural geometry, exhumation history, and foreland sedimentation. Earth-Science Reviews, 76, 1-131.

Yin, A., Dang, Y.Q., Wang, L.C., Jiang, W.M., Zhou, S.P., Chen, X.H., Gehrels, G.E. and McRivette, M.W., 2008. Cenozoic tectonic evolution of Qaidam basin and its surrounding regions (Part 1): The southern Qilian Shan-Nan Shan thrust belt and northern Qaidam basin. Geological Society of America Bulletin, 120, 813-846.

Yin, A., Rumelhart, P.E., Butler, R., Cowgill, E., Harrison, T.M., Foster, D.A., Ingersoll, R.V., Qing, Z., Xian-Qiang, Z., Xiao-Feng, W. and Hanson, A., 2002. Tectonic history of the Altyn Tagh fault system in northern Tibet inferred from Cenozoic sedimentation. Geological Society of America Bulletin, 114, 1257-1295.

Yuan, D.Y., Champagnac, J.D., Ge, W.P., Molnar, P., Zhang, P.Z., Zheng, W.J., Zhang, H.P. and Liu, X.W., 2011. Late Quaternary right-lateral slip rates of faults adjacent to the lake Qinghai, northeastern margin of the Tibetan Plateau. Bulletin, 123, 2016-2030.

Yuan, D.Y., Ge, W.P., Chen, Z.W., Li, C.Y., Wang, Z.C., Zhang, H.P., Zhang, P.Z., Zheng, D.W., Zheng, W.J., Craddock, W.H. and Dayem, K.E., 2013. The growth of northeastern Tibet and its relevance to large-scale continental geodynamics: A review of recent studies. Tectonics, 32, 1358-1370.

Zachos, J., Pagani, M., Sloan, L., Thomas, E. and Billups, K., 2001. Trends, rhythms, and aberrations in global climate 65 Ma to present. Science, 292, 686-693.

Zhang, H., Zhang, P., Champagnac, J.D., Molnar, P., Anderson, R.S., Kirby, E., Craddock, W.H. and Liu, S., 2014. Pleistocene drainage reorganization driven by the isostatic response to deep incision into the northeastern Tibetan Plateau. Geology, 42, 303-306.

Zhang, H., Zhang, P., Prush, V., Zheng, D., Zheng, W., Wang, W., Liu, C. and Ren, Z., 2017. Tectonic geomorphology of the Qilian Shan in the northeastern Tibetan Plateau: Insights into the plateau formation processes. Tectonophysics, 706, 103-115.

Zhang, H.P., Craddock, W.H., Lease, R.O., Wang, W.T., Yuan, D.Y., Zhang, P.Z., Molnar, P., Zheng, D.W. and Zheng, W.J., 2012. Magnetostratigraphy of the Neogene Chaka basin and its implications for mountain building processes in the north-eastern Tibetan Plateau. Basin Research, 24, 31-50.

Zhang, H.P., Oskin, M.E., Liu-Zeng, J., Zhang, P.Z., Reiners, P.W., Xiao, P., 2016. Pulsed exhumation of interior eastern Tibet: implications for relief generation mechanisms and the origin of high-elevation planation surfaces. Earth and Planetary Science Letters, 449, 176–185.

Zhang, J., Sinclair, H.D., Li, Y., Wang, C., Persano, C., Qian, X., Han, Z., Yao, X. and Duan, Y., 2019. Subsidence and exhumation of the Mesozoic Qiangtang Basin: Implications for the growth of the Tibetan plateau. Basin Research, 31, 754-781.

Zhang, L., Liang, S., Yang, X. and Gan, W., 2020. Landscape evolution of the Eastern Himalayan Syntaxis based on basin hypsometry and modern crustal deformation. Geomorphology, 355, 107085.

Zhang, R., Jiang, D., Zhang, Z. and Yu, E., 2015. The impact of regional uplift of the Tibetan Plateau on the Asian monsoon climate. Palaeogeography, Palaeoclimatology, Palaeoecology, 417, 137-150.

Zhang, R., Zhang, Z. and Jiang, D., 2018. Global Cooling Contributed to the Establishment of a Modern-Like East Asian Monsoon Climate by the Early Miocene. Geophysical Research Letters, 45, 11-941.

Zhang, Y., Song, S., Yang, L., Su, L., Niu, Y., Allen, M.B. and Xu, X., 2017. Basalts and picrites from a plume-type ophiolite in the South Qilian Accretionary Belt, Qilian Orogen: Accretion of a Cambrian Oceanic Plateau? Lithos, 278, 97-110.

Zhang, Y.Z., Replumaz, A., Leloup, P.H., Wang, G.C., Bernet, M., Van Der Beek, P., Paquette, J.L., Chevalier, M.L., 2017b. Cooling history of the Gongga Batholith: implications for the xianshuihe fault and miocene kinematics of SE Tibet. Earth and Planetary Science Letters, 465, 1–15.

Zhang, Y.Z., Replumaz, A., Wang, G.C., Leloup, P.H., Gautheron, C., Bernet, M., Beek, P., Paquette, J.L., Wang, A., Zhang, K.X., Chaevalier, M.L., Li, H.B., 2015. Timing and rate of exhumation along the Litang fault system, implication for fault reorganization in southeast Tibet. Tectonics, 34, 1219–1243.

Zebari, M., Grützner, C., Navabpour, P. and Ustaszewski, K., 2019. Relative timing of uplift along the Zagros Mountain Front Flexure (Kurdistan Region of Iraq): Constrained by geomorphic indices and landscape evolution modeling. Solid Earth, 10, 663-682.

Zheng, D., Clark, M.K., Zhang, P., Zheng, W. and Farley, K.A., 2010. Erosion, fault initiation and topographic growth of the North Qilian Shan (northern Tibetan Plateau). Geosphere, 6, 937-941.

Zheng, D., Wang, W., Wan, J., Yuan, D., Liu, C., Zheng, W., Zhang, H., Pang, J. and Zhang, P., 2017. Progressive northward growth of the northern Qilian Shan–Hexi Corridor (northeastern Tibet) during the Cenozoic. Lithosphere, 9, 408-416.

Zheng, W. J., P. Z. Zhang, W. G. He, D. Y. Yuan, Y. X. Shao, D. W. Zheng, W. P. Ge, and W. Min 2013. Transformation of displacement between strike-slip and crustal shortening in the northern margin of the Tibetan Plateau: Evidence from decadal GPS measurements and late Quaternary slip rates on faults, Tectonophysics, 584, 267–280.

Zhu, D.C., Zhao, Z.D., Niu, Y., Dilek, Y., Hou, Z.Q. and Mo, X.X., 2013. The origin and pre-Cenozoic evolution of the Tibetan Plateau. Gondwana Research, 23, 1429-1454.

Zhu, L., Wang, C., Zheng, H., Xiang, F., Yi, H. and Liu, D., 2006. Tectonic and sedimentary evolution of basins in the northeast of Qinghai-Tibet Plateau and their implication for the northward growth of the Plateau. Palaeogeography, Palaeoclimatology, Palaeoecology, 241, 49-60.

Zuza, A.V., Cheng, X. and Yin, A., 2016. Testing models of Tibetan Plateau formation with Cenozoic shortening estimates across the Qilian Shan–Nan Shan thrust belt. Geosphere, 12, 501-532.

Zuza, A.V., Wu, C., Reith, R.C., Yin, A., Li, J., Zhang, J., Zhang, Y., Wu, L. and Liu, W., 2018. Tectonic evolution of the Qilian Shan: An early Paleozoic orogen reactivated in the Cenozoic. GSA Bulletin, 130, 881-925.